KU LEUVEN

ARENBERG DOCTORAL SCHOOL
Faculty of Science

Shape coexistence in the neutron-deficient mercury isotopes studied through Coulomb excitation

Nick Bree

Supervisory committee:
Prof. dr. K. Temst, chair
Prof. dr. P. Van Duppen, supervisor
Prof. dr. M. Huyse, co-supervisor
Prof. dr. G. Neyens
Prof. dr. R. Raabe
Prof. dr. P. Butler
(University of Liverpool)
Prof. dr. P.-H. Heenen
(University of Brussels, ULB)

Dissertation presented in partial fulfilment of the requirements for the degree of Doctor in Science

October 2014

Shape coexistence in the neutron-deficient mercury isotopes studied through Coulomb excitation

Nick BREE

Supervisory committee:
Prof. dr. K. Temst, chair
Prof. dr. P. Van Duppen, supervisor
Prof. dr. M. Huyse, co-supervisor
Prof. dr. G. Neyens
Prof. dr. R. Raabe
Prof. dr. P. Butler
(University of Liverpool)
Prof. dr. P.-H. Heenen
(University of Brussels, ULB)

Dissertation presented in partial fulfilment of the requirements for the degree of Doctor in Science

October 2014

ISBN 978-90-8649-769-0

D/2014/10705/77

Thank you

First of all, I would like to thank my promotors for giving me the amazing opportunity to work in fundamental research. Mark, Piet, and Riccardo, thanks for the good advices, help, and enriching ideas you provided.

Also a big thanks to the members of the doctoral jury: Gerda, Kristiaan, Paul-Henri, and Peter. The revision of this manuscript and the discussions afterwards are strongly appreciated!

A special thanks is reserved for my colleagues in Leuven and those I worked with at CERN. In particular, I would like to thank the secretaries and the IT people. To the people whom I shared an office with: thank you for supporting me and coping with my whims. Iain, Irina, Jan, Jarno, Kasia, Liam, Nele, Nikolas: thanks, you made the years in office 03.81 wonderful!

My friends in Leuven also deserve to be mentioned. Thank you for making the time I spent in Leuven unforgettable.

Eva, Michiel, Pitou, Süleyman, Susanna: we've known each other for almost twenty years, and the circle of friends is still there. Thank you for being who you are.

Finally, I would like to pay tribute to my mother and grandmother. 'Merci' for making everything worth fighting for...

Introduction

This thesis describes the analysis and results of a series of Coulomb-excitation experiments on even-even neutron-deficient mercury isotopes aimed at obtaining a more detailed description of shape coexistence. Two experimental campaigns have been undertaken in the Summer of 2007 and 2008. Pure beams of ^{182,184,186,188}Hg were produced and accelerated at the REX-ISOLDE radioactive-beam facility, located at CERN (Geneva, Switzerland). The beams were guided to collide with a stable target to induce Coulomb excitation. The scattered particles were registered by a double-sided silicon strip detector, and the emitted γ rays by the MINIBALL γ-ray spectrometer.

The motivation to study these mercury isotopes, focused around shape coexistence in atomic nuclei, is addressed in chapter 1, as well as an overview of the knowledge in this region of the nuclear chart. A theoretical description of Coulomb excitation is presented in the second chapter, while the third chapter describes the setup employed for the experiments. The fourth chapter focusses on how the raw data have been analyzed. A study of observed, characteristic mercury K X-rays is described in chapter 5. The further analysis per investigated isotope and the resulting matrix elements are presented in chapter 6. Chapter 7 gives a possible interpretation of the results, and a comparison with theoretical work.

The results of this work have been published in:

N. Bree, K. Wrzosek-Lipska, A. Petts, A. Andreyev, B. Bastin, M. Bender, A. Blazhev, B. Bruyneel, P. A. Butler, J. Butterworth, M. P. Carpenter, J. Cederkäll, E. Clément, T. E. Cocolios, A. Deacon, J. Diriken, A. Ekström, C. Fitzpatrick, L. M. Fraile, Ch. Fransen, S. J. Freeman, L. P. Gaffney, J. E. García-Ramos, K. Geibel, R. Gernhäuser, T. Grahn, M. Guttormsen, B. Hadinia, K. Hadyńska-Klek, M. Hass, P.-H. Heenen, R.-D. Herzberg, H. Hess, K. Heyde, M. Huyse, O. Ivanov, D. G. Jenkins, R. Julin, N. Kesteloot, Th. Kröll, R. Krücken, A. C. Larsen, R. Lutter, P. Marley, P. J. Napiorkowski,

R. Orlandi, R. D. Page, J. Pakarinen, N. Patronis, P. J. Peura, E. Piselli, P. Rahkila, E. Rapisarda, P. Reiter, A. P. Robinson, M. Scheck, S. Siem, K. Singh Chakkal, J. F. Smith, J. Srebrny, I. Stefanescu, G. M. Tveten, P. Van Duppen, J. Van de Walle, D. Voulot, N. Warr, F. Wenander, A. Wiens, J. L. Wood, and M. Zielińska.

Shape Coexistence in the Neutron-Deficient Even-Even $^{182-188}$Hg Isotopes Studied via Coulomb Excitation

Physical Review Letters 112, 162701 (2014)

Nederlandse samenvatting

Reeds in de klassieke oudheid werd geopperd dat materie moest bestaan uit kleine, ondeelbare deeltjes. In het begin van de twintigste eeuw beschreef Niels Bohr het *atoom* als een *kern* omringd door een *elektronenwolk*. De grootte van het atoom wordt bepaald door de uitgestrektheid van de elektronenwolk en heeft een straal van ongeveer 10^{-10} m. De atoomkern is honderdduizend keer kleiner: de kernstraal meet ongeveer 10^{-15} m. De kern of *nuclide* bestaat uit elektrisch neutrale *neutronen* en positief geladen *protonen*. Zij worden samen de *nucleonen* genoemd. Deze laatste stoten elkaar af door de *elektromagnetische* interactie. Het feit dat de atoomkern hierdoor niet uit elkaar valt wordt veroorzaakt tussen een andere wisselwerking die de protonen en neutronen bij elkaar houdt: de *sterke* interactie. Kernen met hetzelfde aantal protonen Z, maar een ander aantal neutronen N worden *isotopen* genoemd, kernen met eenzelfde aantal neutronen, maar een ander aantal protonen zijn *isotonen*. Wanneer het totale aantal nucleonen A gelijk is, maar het aantal neutronen en protonen verschilt, spreekt men van *isobaren*.

In de chemie vertonen bepaalde elementen een grote vorm van stabiliteit. De zogenaamde edelgassen zijn chemisch inert doordat zij een speciaal aantal elektronen bevatten en op die manier een gesloten elektronenschil vertonen. Net zoals deze elektronen zijn nucleonen *fermionen* en gedragen zich op eenzelfde manier. Zowel voor protonen als neutronen bestaan er *magische getallen*: wanneer de kern bestaat uit een magisch aantal protonen of neutronen is er sprake van een *schilsluiting* en vertoont de kern een zekere stabiliteit. De nucleonen bevinden zich immers in bepaalde *kwantumtoestanden*. Deze verschillende toestanden liggen qua energie dicht bij elkaar, behalve bij een schilsluiting. In dat geval is er een groot energieverschil. Als zowel het aantal protonen als neutronen een magisch getal is, spreekt men van een *dubbelmagische* kern. De *valentienucleonen* zijn de overige protonen en neutronen buiten de schilsluitingen. Wanneer een schil niet volledig gesloten is, kan men de kern ook beschrijven in functie van *nucleongaten*. De aanwezigheid van talrijke valentienucleonen of -nucleongaten kan de kern vervormen: de nucleonen vertonen *collectief* gedrag.

Deze thesis behelst de studie van vier kernen waarbij de magische getallen 82 en 126 een rol spelen. De kwikisotopen met massa 182, 184, 186 en 188 hebben alle hetzelfde aantal protonen ($Z = 80$), maar een verschillend aantal neutronen (102, 104, 106 en 108). Deze kernen zijn in die mate uniek omdat ze, wat de neutronen betreft, halfweg tussen $N = 82$ en $N = 126$ zitten.

De toestand waarin een kern zich bevindt, wordt beschreven door de *spin* en de *pariteit*. De spin I geeft aan hoeveel eenheden van *impulsmoment* de kern heeft, de *pariteit* p drukt uit of de kerntoestand spiegelsymmetrie vertoont of niet (uitgedrukt door een plus- of minteken). De notatie is dan I^p. De toestand met de kleinste energie wordt ook de *grondtoestand* van de kern genoemd. Alle mogelijke toestanden van de kern die een grotere energie hebben beschrijven het *excitatiespectrum* van de kern. In de meeste gevallen vervallen zij rechtstreeks of onrechtstreeks naar de grondtoestand. Alle gekende kernen met een even aantal protonen en neutronen (de *even-evenkernen*) hebben een 0^+ grondtoestand. In de meeste gevallen kunnen de nucleonen op verschillende manieren gekoppeld worden die een ander totaal impulsmoment opleveren. Bij even-evenkernen komt het vaak voor dat een 2^+-toestand een iets grotere energie heeft dan de grondtoestand, een 4^+-toestand een nog iets grotere, enzoverder. De constructie met groter wordende energie en impulsmoment 0^+, 2^+, 4^+,... wordt een *rotationele band* genoemd. In het geval van de kwikisotopen beschreven in deze thesis, vormen de twee protongaten (de protonschil is pas gevuld wanneer er 82 protonen aanwezig zijn) en de talrijke neutronen of neutrongaten (82 en 126 zijn de magische getallen) de *grondtoestandsband* met spin-pariteiten 0^+, 2^+, 4^+,... die kenmerkend is voor het excitatiespectrum.

Het is evenwel mogelijk dat protonparen een toestand vormen boven de $Z = 82$ schil op grote energie. De nucleonen in deze valentieruimte vormen dan opnieuw een band. Door de aantrekkende *proton-neutroninteractie* wordt de energie van de band opnieuw kleiner. Indien de energie klein genoeg is, kan deze band zelfs de grondtoestand van de kern leveren. Het fenomeen waarbij banden met verschillende configuratie een gelijkaardige energie hebben, wordt *coëxistentie* genoemd.

De interactie tussen protonen en neutronen heeft ook nog een ander verschijnsel tot gevolg: *kernvervorming*. Terwijl magische kernen (kernen met een proton- of neutronschilsluiting) kunnen beschreven worden als een bol, kunnen kernen met zowel valentieprotonen als -neutronen afwijken van deze *sfericiteit*. De meest eenvoudig te beschrijven vervorming is een uitrekking of induwing van de kern in een bepaalde richting. Wanneer de vorm van de kern beschreven kan worden als een rugbybal, heet dit een *prolate* vervorming. Als de kern de vorm heeft van een doughnut, spreekt men van een *oblate* vervorming. *Vormcoëxistentie* treedt op wanneer banden met gelijkaardige energie en verschillende configuratie gekenmerkt worden door verschillende vormen. Bovendien kan er *menging*

optreden. Bij dit fenomeen nemen twee toestanden van de kern met een gelijkaardige energie en eenzelfde spin-pariteit eigenschappen van elkaar over. Op die manier kan een toestand in een bepaalde band afwijken van vorm.

Uit vroegere studies van de kwikisotopen ^{182,184,186,188}Hg bleek dat er naast de grondtoestandsband een andere geëxciteerde band op kleine energie bestond. Er werd theoretisch voorspeld dat de grondtoestandsband een vrij kleine oblate vervorming had, terwijl de geëxciteerde band gekenmerkt werd door een grotere, prolate vervorming. De resultaten beschreven in deze thesis werden verkregen door een *Coulombexcitatie*-experiment met deze vier kernen. Bij Coulombexcitatie wordt de kern in zijn grondtoestand door een inelastische botsing met een trefschijf naar een toestand gebracht op grotere energie. De bedoeling van deze methode was tweeledig. De mate waarin bepaalde toestanden in dit proces bevolkt worden verschaft informatie over de *overgangswaarschijnlijkheden* tussen de verschillende toestanden. Deze worden uitgedrukt in $B(E2)$*-waarden*. Zo drukt bijvoorbeeld de $B(E2; 0_1^+ \rightarrow 2_1^+)$-waarde de *gereduceerde overgangswaarschijnlijkheid* uit om de kern vanuit de 0^+-grondtoestand te exciteren naar de eerste aangeslagen 2^+-toestand. De gemeten $B(E2)$-waarden kunnen dan gebruikt worden om de menging tussen bepaalde toestanden en de interactie tussen de banden in kaart te brengen. Bovendien heeft de vervorming van een toestand in vele gevallen een invloed op de mate waarin hij bevolkt wordt tijdens het Coulombexcitatieproces. Op die manier kan de vervorming van bepaalde aangeslagen toestanden rechtstreeks gemeten worden.

De ^{182,184,186,188}Hg-isotopen zijn *onstabiel*. Dat wil zeggen dat zij niet voorkomen in de natuur omdat ze na verloop van tijd verdwijnen door *radioactief* verval. Bij dit fenomeen zorgt de *zwakke interactie* ervoor dat er protonen worden omgezet in neutronen (of omgekeerd in andere gevallen) en er dus een nieuwe kern ontstaat. Om de kernen te onderzoeken moesten ze dus eerst kunstmatig aangemaakt worden. Een gevolg hiervan is dat het Coulombexcitatie-experiment *in inverse kinematica* moet gebeuren: er kan immers geen trefschijf die dik genoeg is gemaakt worden uit de kortlevende, te onderzoeken kernen. In de REX-ISOLDE-opstelling te CERN (Genéve, Zwitserland) konden er bundels van zuivere, radioactieve kwikisotopen aangemaakt worden. Een bundel van een bepaald kwikisotoop werd gemaakt door protonen met grote energie (1,4 GeV) af te schieten op gesmolten lood. Door *diffusie* en *efusie* verspreidden vervolgens de kwikatomen zich. Zij worden vervolgens geïoniseerd door botsingen in een *plasma* en door een elektrode uit de *ionenbron* getrokken. Door *massaseparatie* kon de isotoop naar keuze worden geselecteerd. De bundel werd vervolgens versneld tot een energie van 2,85 MeV per nucleon en afgevuurd op een trefschijf (^{112}Cd, ^{114}Cd, ^{107}Ag of ^{120}Sn), waarbij de verstrooide kernen na de botsing werden geregistreerd door een dubbelzijdige, gesegmenteerde siliciumdetector. In geval

van Coulombexcitatie werden de uitgestuurde γ-*stralen* die gepaard gaan met de *deëxcitatie* gedetecteerd door de *MINIBALL*-opstelling. Deze wordt gevormd door acht identieke armen, die elk bestaan uit drie zesvoudiggesegmenteerde *hyperpure-germaniumdetectoren*. Door te eisen dat de geregistreerde γ-stralen *in coincidentie* moesten zijn met een gedetecteerd deeltje in de deeltjesdetector, was het mogelijk de gebeurtenissen ten gevolge van Coulombexcitatie te isoleren.

In de analyse werden de intensiteiten van de verscheidene γ-stralen bestudeerd. Zij geven aan hoeveel deëxcitaties er gemeten werden van een bepaalde bevolkte kerntoestand naar een andere toestand met kleinere energie. Om de gevoeligheid aan de verstrooiingshoek van zowel projectiel (kwik) als doelwit te vergroten, werden alleen γ-stralen in coincidentie met twee deeltjes geselecteerd. Ook werden *karakteristieke X-stralen* van kwik met een energie van 79 KeV die gedetecteerd waren door MINIBALL, in de analyse opgenomen. Dit was noodzakelijk, vermits bepaalde overgangen (zoals de $0_2^+ \rightarrow 0_1^+$-overgang en een deel van de $2_2^+ \rightarrow 1_1^+$-overgang) niet gepaard gaan met het uitsturen van een γ-straal. Deze intensiteiten konden evenwel worden geschat door het aantal X-stralen in coincidentie met een gedetecteerd deeltje te meten.

Toestanden in de twee coëxisterende banden werden bevolkt in de ^{182,184,186}Hg-kernen. Bij ^{182}Hg en ^{184}Hg werden de gereduceerde overgangswaarschijnlijkheden opgemeten tussen de 0^+- en 2^+-toestanden van de grondtoestandsband en de 0^+-, 2^+- en 4^+-toestanden van de geëxciteerde band, zowel tussen de banden als in de banden afzonderlijk. Ook de *kwadrupoolmomenten* van de eerste en tweede aangeslagen 2^+-toestanden konden worden vastgesteld. Het teken van het kwadrupoolmoment is een rechtstreekse aanwijzing voor prolate of oblate vervorming van de kerntoestand. De analyse van de experimenten met ^{186}Hg leverde buiten de $B(E2; 0_1^+ \rightarrow 2_1^+)$- en $B(E2; 2_1^+ \rightarrow 4_1^+)$-waarde weinig extra informatie op omtrent de geëxciteerde 0^+- en 2^+-toestanden. In ^{188}Hg konden de $B(E2; 0_1^+ \rightarrow 2_1^+)$-waarde en de $B(E2; 2_1^+ \rightarrow 4_1^+)$-waarde opgemeten worden. De analyse leverde geen informatie op over de geëxciteerde band. Het kwadrupoolmoment van de eerste aangeslagen 2^+-toestand kon wel worden gemeten. De waardes van de gereduceerde overgangswaarschijnlijkheden en kwadrupoolmomenten worden getoond in tabel 7.1 in de vorm van $E2$-*matrixelementen*.

De gemeten matrixelementen werden gebruikt om de menging tussen de toestanden met dezelfde spin en pariteit te schatten, uitgaand van een eenvoudig model waarbij twee zuivere banden met verschillende vervorming onderling mengen. De berekening toonde aan dat de menging groter werd in de lichtere isotopen. Ook werden aan de hand van de *Quadrupole Sum Rules*-methode rotationele invarianten voor de eerste twee 0^+-toestanden berekend in de vier isotopen. Dit resulteerde in een lichte oblate vervorming voor de 0^+-grondtoestand. In ^{182}Hg en ^{184}Hg bleek de tweede 0^+-toestand beschreven te

kunnen worden als meer prolaat vervormd. De berekeningen werden vervolgens vergeleken met de resultaten uit twee theoretische modellen, waarbij gedeeltelijke overeenkomst werd bereikt.

Er kan besloten worden dat de structuur bij kleine energie van de neutronarme kwikkernen gekenmerkt wordt door twee banden met verschillende vervorming die onderling mengen. De theoretische modellen voorspellen de aanwezigheid van deze twee structuren met verschillende vorm. Over de exacte plaats waarop de menging dominant wordt, stemt de theorie evenwel niet overeen met de experimentele gegevens.

Contents

List of Figures

List of Tables

Chapter 1

Physics motivation

1.1 Nuclear shapes

The atomic nucleus, consisting of Z protons and N neutrons, is a quantum-mechanical many-body system, whose eigenstates are characterized by different energies, spins, and parities. However, nuclear states can also be described in terms of their shape. While nuclear shell and sub-shell closures invoke a stabilizing effect leading to sphericity, the residual interactions between protons and neutrons outside closed shells drive the nucleus to deformation. At low energy, near-degenerates nuclear states with different geometrical arrangements can occur: this phenomenon is called shape coexistence. In the region around the light lead isotopes ($Z = 82$), a substantial amount of information has been collected using a wide spectrum of experimental probes such as decay studies, optical spectroscopy studies and in-beam spectroscopy investigations [Jul01, Hey11].

When deviating from sphericity, the kind of deformation that preserves most symmetries can be achieved by pushing in or stretching out the nucleus in a certain direction. This kind of shape distortions are called quadrupole deformations. Hereby, axial symmetry (i.e. the rotation symmetry around one single axis) is conserved. However, the amount of deformation on the two sides of this axis can differ, meaning that at one side of the symmetry axis, the nucleus is more pushed in or stretched out in comparison with the other side. This is referred to as triaxiality. The simplest axially symmetric shapes are called oblate (shaped like a doughnut) and prolate (shaped like an American football) [Cas90].

Notwithstanding the vast amount of information at hand in this region of the nuclear chart, this chapter will focus solely on the mercury isotopes.

1.2 Observation of shape coexistence in mercury isotopes

The neutron-deficient mercury isotopes ($Z = 80$) serve as an illustrative example of shape coexistence [Hey11]. Already in 1972, a dramatic change in ground-state mean-square charge radius was discovered in ^{183}Hg and ^{185}Hg, when comparing to heavier mercury isotopes [Bon72]. These experimental quantities have been studied in isotope-shift measurements. When the shape of a nucleus deviates from sphericity, with either a prolate or an oblate deformation, its mean-square charge-radius will increase. The changes in mean-square charge radii for a wide range of mercury isotopes are shown in figure 1.1.

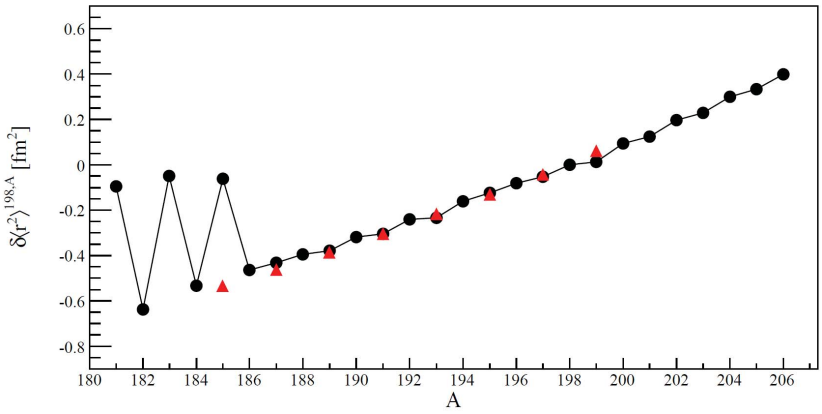

Figure 1.1: The differences in mean-square charge radii $\delta\langle r^2\rangle$ are presented for the ground states of mercury isotopes as a function of nuclear mass number A (black). In some odd-mass isotopes, the differences in mean-square charge radii are shown for an isomer with spin $\frac{13}{2}$ as well (red). ^{198}Hg serves as the reference isotope. The line connects the ground state data. These values were obtained by isotope shift measurements [Ulm86].

Further investigation probing life times in ^{184}Hg and ^{186}Hg [Rud73, Pro74] suggested a sudden increase in deformation of excited states with a spin higher

than 2. Furthermore, radioactive-decay studies on the ^{184,186,188}Hg isotopes identified coexisting bands characterized by different deformations [Ham75, Col76, Ma86]. This phenomenon was observed in ^{182}Hg as well by means of in-beam spectroscopy studies [Ma84].

1.3 Shape coexistence and energy systematics

The energy systematics of low-lying nuclear levels in the mercury isotopes can be interpreted as a manifestation of shape coexistence. The energy levels with their assigned spin and parity in function of mass number A are shown in figure 1.2.

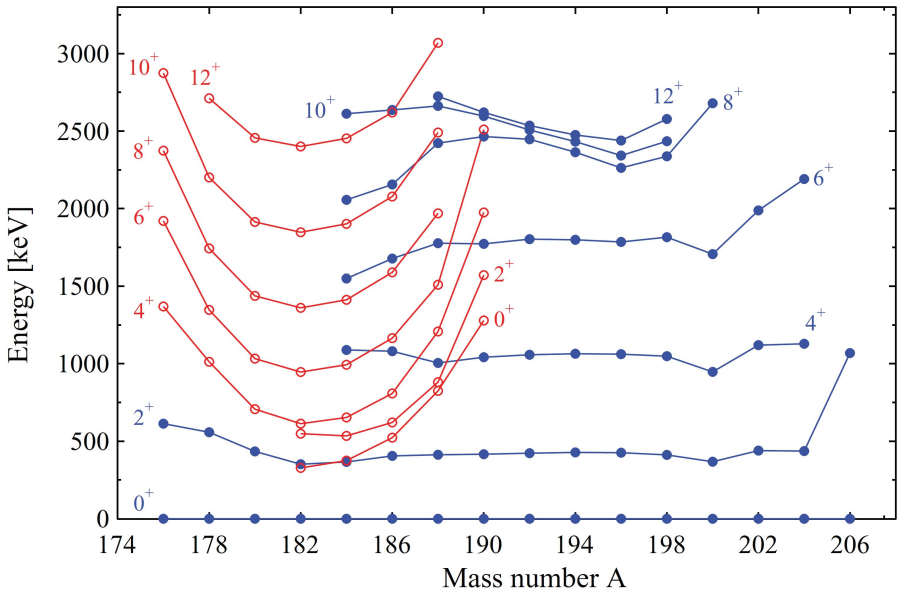

Figure 1.2: The energy systematics of low-lying positive-parity states of even-mass mercury isotopes are shown as a function of nuclear mass number A. Full blue symbols represent an assumed oblate deformation, while open red symbols show assumed intruder states having a prolate shape. This colour code is somewhat arbitrary as, as will be shown later, the character of the 2^+ states is suggested to be slightly different. These empirical values are taken from [NND].

The energies of the even-spin nuclear levels within the band built on the 0^+ ground state, are observed to remain quasi-constant. They are assumed to be characterized by an oblate deformation. However, the excited band, assumed to be of prolate nature, shifts in energy and reaches its minimum around $A = 182, 184$ [Jul01, Ric97]. This can be interpreted as the attractive proton-neutron interaction at maximum capacity, peaking at the configuration with the most neutrons or neutron holes. Since $N = 82$ and $N = 126$ indicate full neutron shell closures, the highest interaction between the valence neutrons and the excited protons in mercury can be expected to be present around $N = 104$, i.e. ^{184}Hg. The excited band in mercury has been advocated to originate form the excitation of four protons over the $Z = 82$ major shell gap, yielding six proton holes in lower-lying proton orbits [Hey11].

1.4 Ongoing investigation

Investigating shape coexistence in mercury isotopes is an ongoing process. This thesis focusses on a Coulomb-excitation study of the low-lying energy levels of the even-even mercury isotopes with mass $A = 182 - 188$. Over recent years, experiments have been performed in order to measure physical observables in these isotopes with great precision. Life times of nuclear levels have been quantified for ^{182}Hg [Gra09, Sch10], ^{184}Hg and ^{186}Hg [Gaf14], and conversion coefficients between 2^+ states as well as branching ratios connecting low-lying energy states have been determined in ^{182,184}Hg [Rap]. This recent information, together with results from older experiments, will be combined with the data acquired in the Coulomb-excitation experiments described in this thesis. The nuclear level schemes of ^{182,184,186,188}Hg of importance in this work are presented in figure 1.3.

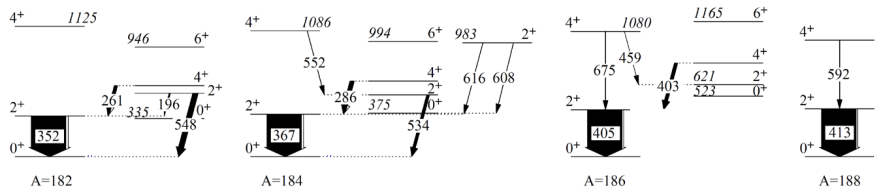

Figure 1.3: The low-lying energy levels are shown for the four even-even mercury isotopes with mass $A = 182 - 188$. The transitions detected in the Coulomb-excitation experiments are indicated by black arrows, their thicknesses representing the observed intensities.

The Coulomb-excitation experiments on the even-even $^{182-188}$Hg isotopes aim at gaining information on transition probabilities between low-lying energy states, and on their quadrupole moments. The latter ones provide direct, experimental knowledge on deformation. Hence, these experiment form a crucial factor in the expansion of insight in shape coexistence in this region of the nuclear chart.

The results deduced from this work will be compared to results from model calculations. A two-state mixing calculation will be performed [Dup90], and the quadrupole sum rules method will be used to extract information on the deformation parameters [Kum72, Cli86]. These will then be compared to calculations based on beyond mean field (BMF) [Yao13] and interacting boson models (IBM) [Gar14, Gar09, Gar11].

Chapter 2

Coulomb excitation

2.1 Introduction

This chapter aims at describing the experimental technique of Coulomb excitation. The quantum-mechanical formalism will be briefly described. Since multiple levels are populated in the experiments on the even-even $^{182-188}$Hg isotopes, higher-order effects will be discussed as well. As an example of this, the influence of the presence of a non-zero quadrupole moment of a populated state will be addressed. More in-depth information and detailed derivations can be found in [Ald75, Wal06].

2.2 An inelastic reaction

When a projectile nucleus collides with a target nucleus, the resulting scattering process is expressed by the time-dependent Schrödinger equation

$$i\hbar\frac{\partial}{\partial t}|\Psi(t)\rangle = H|\Psi(t)\rangle, \tag{2.1}$$

with the Hamiltonian

$$H = H_1 + H_2 + V(\vec{r}(t)). \tag{2.2}$$

Here H_1 and H_2 are the Hamiltonians for the free, individual nuclei, whereby one can be omitted when the corresponding particle in the chosen frame of reference is at rest. The electromagnetic interaction between the two nuclei is described by $V(\vec{r}(t))$. The scattering of a projectile and a target nucleus is depicted in figure 2.1.

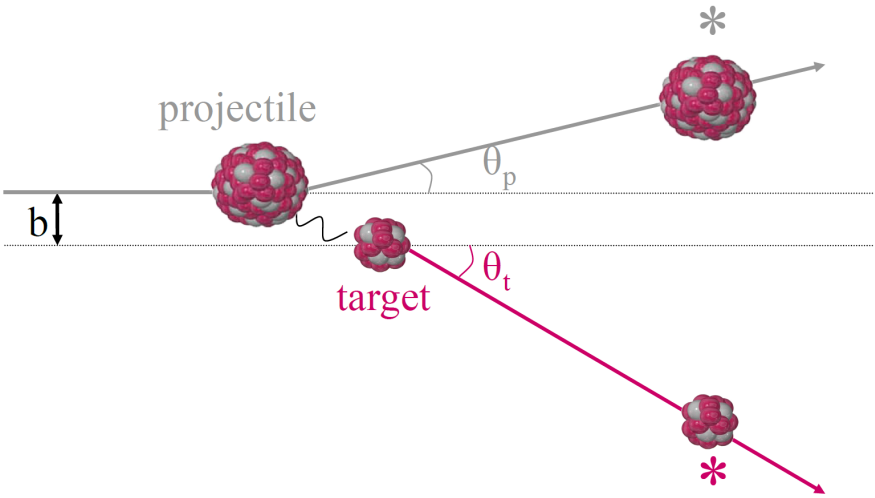

Figure 2.1: A projectile and a target nucleus collide and are scattered. The distance b is defined as the impact factor. The angles θ_p and θ_t are the scattering angles in the laboratory frame of reference.

The electromagnetic interaction can then be decomposed into its multipole-multipole interactions. The first term of these components is the monopole-monopole interaction, in which the nuclei scatter elastically. The differential cross section for scattering a nucleus elastically into an infinitesimal range covered by a solid angle $d\Omega$ is expressed by the Rutherford formula

$$\frac{d\sigma_R}{d\Omega} = \frac{1}{4}a^2 \frac{1}{\sin^4(\frac{\vartheta}{2})}, \tag{2.3}$$

where a is half the distance of closest approach in a head-on collision, and ϑ the scattering angle in the frame of reference where the centre-of-mass is at rest.

The terms following the monopole-monopole component of the electromagnetic interaction represent inelastic scattering. The differential cross section for excitation of the scattered nucleus to a certain state n is described by

$$\frac{d\sigma_n}{d\Omega} = P_n \cdot \frac{d\sigma_R}{d\Omega}, \tag{2.4}$$

i.e. P_n, the probability to excite to state n, multiplied by the differential cross section for Rutherford scattering.

2.3 'Safe' Coulomb excitation

During the collision, the two nuclei should not penetrate into each other's surfaces to avoid nuclear interactions, as otherwise the interpretation of the experiment could be difficult. Therefore, in the case of a projectile nucleus colliding with a target at rest, the distance of closest approach $2a$ should be much larger than the de Broglie wavelenght $\bar{\lambda}$ of the projectile:

$$\eta = \frac{2a}{2\bar{\lambda}} = \frac{Z_p Z_t e^2}{\hbar v} >> 1, \tag{2.5}$$

where Z_p and Z_t are the proton numbers of projectile and target, e is the elementary charge, $\hbar$ is the Dirac constant (i.e. the reduced Planck constant) and v is the initial speed of the projectile. Here, the expression for the distance of closest approach $a = \frac{Z_p Z_t e^2}{m_p v^2}$ has been used. η is defined as the Sommerfeld parameter. For a mercury projectile with an initial energy of 2.85 MeV per nucleon incident on a silver target, the Sommerfled parameter can be calculated to be $\eta \approx 350$, well above unity.

In order to ensure that the interaction between the two nuclei is purely electromagnetic, the surfaces of the two nuclei should always be separated by a certain distance. Such a 'safe' distance has been experimentally determined to be approximately 5 fm [Wil80]. When this condition is fulfilled, the Coulomb-excitation process is considered 'safe', as no nuclear interactions can play.

2.4 Excitation amplitudes

After the collision, there is a probability that the scattered nucleus has been left in a certain state $|n\rangle$. The resulting wave function describing the nucleus

in all possible states is the sum of those states multiplied by their excitation amplitudes a_n:

$$|\Psi(t)\rangle = \sum_n a_n(t)|n\rangle. \tag{2.6}$$

In the case where $n = 0$, the nucleus remains in its ground state. The probability to find the nucleus in the state $|n\rangle$ after the collision is found by squaring its excitation amplitude:

$$P_n = |a_n|^2. \tag{2.7}$$

As a result, the sum of the squared excitation amplitudes over all possible final $|n\rangle$ states has to equal 1:

$$\sum_n |a_n|^2 = \sum_n P_n = 1. \tag{2.8}$$

2.5 Transition probabilities

In the case of a nucleus being excited from an initial state $|i\rangle$ to a final state $|f\rangle$, the adiabacity parameter ξ relates the excitation time (i.e. the inverse of the nuclear frequency) $\tau_{nucl.} = \frac{\hbar}{\Delta_{if}}$ to the collision time $\tau_{coll.} = \frac{a}{v}$:

$$\xi_{i\to f} = \frac{\tau_{coll.}}{\tau_{nucl.}} = \frac{a\Delta_{if}}{\hbar v}. \tag{2.9}$$

The probability for exciting a nucleus to a final state $|f\rangle$ can be written as

$$P_f = \sum_\lambda |\chi^{(\lambda)}_{0\to f}|^2 R^2_\lambda(\vartheta, \xi), \tag{2.10}$$

where λ expressed the angular momentum part of the multipolarity of the transition, i.e. the number of exchanged angular momentum units. The $\chi^{(\lambda)}_{0\to f}$ are dimensionless quantities called the strength parameters. The function $R^2_\lambda(\vartheta, \xi)$ is the part of the equation containing the dependence on scattering angle ϑ and adiabacity parameter ξ, the latter depending on the incident particle energy and the nuclear excitation energy. The square of the strength parameter

$|\chi^{(\lambda)}_{0\to f}|^2$ represents the probability for the nucleus to be excited via multipole λ to the final state $|f\rangle$ for $\vartheta = \pi$ and $\xi = 0$. Hence, the function $R^2_\lambda(\vartheta, \xi)$ expresses the λ-pole excitation probability, relative to the $(\vartheta = \pi, \xi = 0)$ case.

The differential cross section for electric excitation into a given state can be written as:

$$d\sigma = \sum_\lambda d\sigma_{E\lambda}, \tag{2.11}$$

with

$$d\sigma_{E\lambda} = \frac{1}{4}a^2|\chi^{(\lambda)}_{0\to f}|^2 R^2_\lambda(\vartheta, \xi)\frac{1}{\sin^4(\frac{\vartheta}{2})}d\Omega. \tag{2.12}$$

The latter may alternatively written as:

$$d\sigma_{E\lambda} = \left(\frac{Z_p e}{\hbar v}\right)a^{-2\lambda+2}B(E\lambda, I_0 \to I_f)df_{E\lambda}(\vartheta, \xi), \tag{2.13}$$

where the $B(E\lambda, I_0 \to I_f)$ is defined as the reduced transition probability of multipole $E\lambda$. It can be related to the nuclear matrix element of the λ-pole electric operator:

$$B(E\lambda, I_0 \to I_f) = \frac{1}{2I_0 + 1}|\langle I_0\|M(E\lambda)\|I_f\rangle|^2. \tag{2.14}$$

Here, I_0 and I_f refer to the spins of the initial and final states. The function $df_{E\lambda}(\vartheta, \xi)$ is then defined by

$$df_{E\lambda}(\vartheta, \xi) = 4\pi\left|\frac{(\lambda-1)!}{(2\lambda+1)!!}\right|^2 R^2_\lambda(\vartheta, \xi)\frac{1}{\sin^4(\frac{\vartheta}{2})}d\Omega, \tag{2.15}$$

and therefore, the strength parameter $\chi^{(\lambda)}_{0\to f}$ can be written as:

$$\chi^{(\lambda)}_{0\to f} = \frac{\sqrt{16\pi}(\lambda-1)!}{(2\lambda+1)!!}\frac{Z_p e}{\hbar v}\frac{\langle I_0\|M(E\lambda)\|I_f\rangle}{a^\lambda\sqrt{2I_0+1}}. \tag{2.16}$$

The equivalent of equation 2.13 for magnetic transitions is the following:

$$d\sigma_{M\lambda} = \left(\frac{Z_p e}{\hbar c}\right) a^{-2\lambda+2} B(M\lambda, I_0 \to I_f) df_{M\lambda}(\vartheta, \xi). \tag{2.17}$$

When comparing to the differential cross section for electric excitation, the speed of light c replaces the initial speed of the projectile v, implying that magnetic excitations are weakened by a factor $\frac{v}{c}$. In the Coulomb-excitation experiments discussed in this work, this results in a factor of ≈ 0.06.

The case of an even-even nucleus being excited from its 0^+ ground state to a single 2^+ state (figure 2.2) can serve as the simplest example of a Coulomb excitation: a one-step process, governed by the $E2$ multipole operator: $d\sigma = d\sigma_{E2}$.

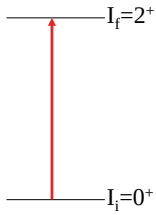

Figure 2.2: A nucleus is excited from its 0^+ ground state to a single 2^+ state involving a one-step process.

2.6 Multiple Coulomb excitations

Excitation probabilities in Coulomb excitation are quadratic expressions of the strength parameters χ and can therefore be written as:

$$P_f = a_2\chi_2 + a_3\chi_3 + a_4\chi_4 + \ldots, \tag{2.18}$$

where the a_i coefficients represent the dependence on scattering angle and adiabacity parameter. The χ parameters connect the initial and the final state through all possible paths, where the first term corresponds to the first order: one-step excitation. The other terms reflect the higher-order effects: multiple-step excitation and possible interference terms.

The process of a double excitation from an initial state I_0 to a final state I_f is visualized in figure 2.3. Here, the direct excitation competes with a double excitation via an intermediate state I_z.

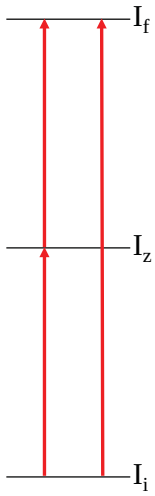

Figure 2.3: The excitation from the ground state I_0 to a state I_f can be a one-step (right) or a two-step process involving an intermediate state I_z (left).

A pure double excitation will be realized when the strength parameter $\chi_{0\to f}$ is small or vanishing in comparison with the product of the strength parameters coupling the initial and final state through the intermediate state:

$$\chi_{0\to f} << \chi_{0\to z}\chi_{z\to f}. \tag{2.19}$$

In many cases, the two possible excitation paths will compete. As an example, a 2^+ state in an even-even nucleus may be excited directly from the 0^+ state, as well as via another $2^{+\prime}$ state. This is shown in figure 2.4.

The probability for the nucleus to get excited to the 2^+ state can then be written in the form:

$$P_2 = a_2|\chi^{(E2)}_{0\to 2}|^2 + a'_2\chi^{(E2)}_{0\to 2}\chi^{(E2)}_{0\to 2'}\chi^{(E2)}_{2'\to 2}, \tag{2.20}$$

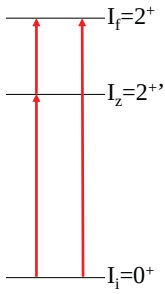

Figure 2.4: In many cases, a 2^+ state in an even-even nucleus may be excited directly or via another $2^{+\prime}$ state.

where the coefficients a_2 and a_2' equal the first two coefficients in formula 2.18, the latter noted accordingly for the sake of clarity. The expression can be derived to be:

$$P_2 = |\chi_{0\to 2}^{(E2)}|^2 R_2^2(\vartheta,\xi)[1 + yc(\vartheta, s, \xi)], \tag{2.21}$$

where

$$y = \frac{\chi_{0\to 2'}^{(E2)}\chi_{2'\to 2}^{(E2)}}{\chi_{0\to 2}^{(E2)}} = \chi_{0\to 2'}\frac{1}{\sqrt{5}}\frac{\langle 2^{+\prime}\|M(E2)\|2^+\rangle}{\langle 0^+\|M(E2)\|2^+\rangle}. \tag{2.22}$$

The function $c(\vartheta, s, \xi)$, like $R_2^2(\vartheta,\xi)$, isolates the dependence on scattering angle and adiabacity parameter, but it also contains $s = \frac{E_{2'}-E_0}{E_2-E_0}$, the ratio of the excitation energies of the $2^{+\prime}$ and 2^+ states.

Since the $E2$ matrix elements involved can have either positive or negative sign, the interference of the two-step and the direct excitation can be either constructive or destructive.

2.7 Influence of the quadrupole moment

An interesting application of formula 2.21 is when the two 2^+ states are the same ($2^+ = 2^{+\prime}$). In this case, the direct $0^+ \to 2^+$ excitation interferes with a two-step process, where the 2^+ state acts as both intermediate and final state

(figure 2.5). Hereby, the intermediate and final states can be interpreted as different magnetic substates of the same 2^+ state. The formula then becomes:

$$P_2 = |\chi_{0\to2}^{(E2)}|^2 R_2^2(\vartheta,\xi)[1 + \chi_{2\to2}^{(E2)} c(\vartheta, s = 1, \xi)]. \tag{2.23}$$

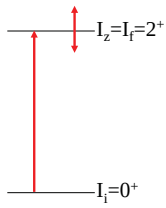

Figure 2.5: The 2^+ state can act as both intermediate and final state.

This can be rewritten as:

$$P_2 = P_2^{(1)}[1 + qK(\vartheta,\xi)], \tag{2.24}$$

with $P_2^{(1)}$ the one-step excitation probability and

$$q = \frac{A_p \Delta E_{MeV} \langle 2^+ \| M(E2) \| 2^+ \rangle}{Z_t(1 + A_p/A_t)}. \tag{2.25}$$

The function $K(\vartheta,\xi)$ expresses the dependence on scattering angle ϑ and adiabacity parameter ξ.

In the nuclear liquid drop model, the static quadrupole moment Q_0 can be written as a function of the deformation parameter β (here to second order) [Cas90]:

$$Q_0 = \frac{3}{\sqrt{5\pi}} Z R_0^2 \beta(1 + 0,16\beta), \tag{2.26}$$

where $R_0 = r_0 A^{\frac{1}{3}}$, r_0 being approximately 1.2 fm. Q_0 is positive for a prolate, and negative for an oblate quadrupole deformation. For a rotational nucleus, the spectroscopic quadrupole moment Q is connected to the static quadrupole moment [Rin80]:

$$Q = \frac{3K^2 - I(I+1)}{(I+1)(2I+3)} Q_0. \tag{2.27}$$

The diagonal matrix element $\langle 2^+ \| M(E2) \| 2^+ \rangle$ in formula 2.25 is directly related to the spectroscopic quadrupole moment of the 2^+ state:

$$\langle 2^+ \| M(E2) \| 2^+ \rangle = \sqrt{\frac{7}{2\pi}} \frac{5}{4} Q \approx \frac{1}{0.7579} Q. \tag{2.28}$$

As an example, figure 2.6 shows the calculated differential cross section for exciting a ^{184}Hg nucleus (incident on a 2 mg/cm^2 ^{112}Cd target) to its first excited 2_1^+ state, and the dependence on the quadrupole moment of that state. The experimental conditions are described further in this work. A B($E2{:}0^+_{g.s.} \rightarrow 2^+_1$) was inferred from [Gaf14]. Influences of other nuclear states have been neglected in the calculation.

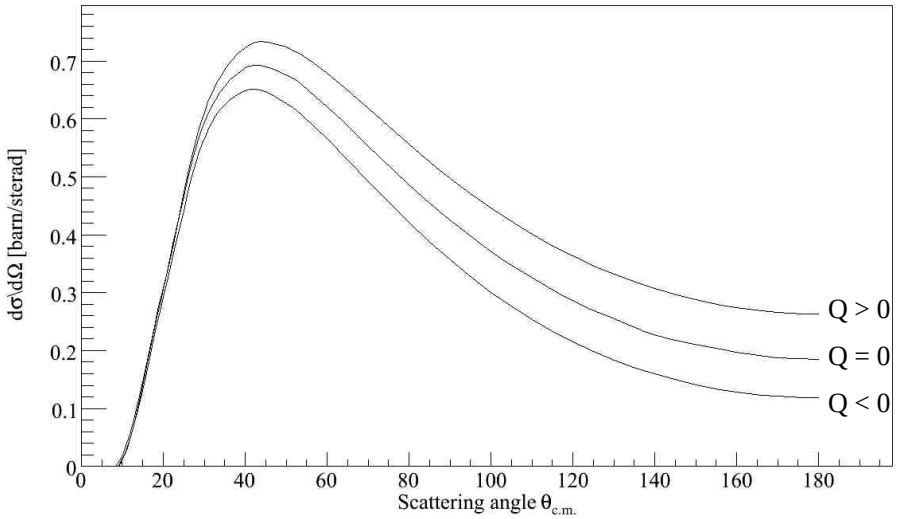

Figure 2.6: The differential cross section for excitation to the 2_1^+ state in ^{184}Hg in function of scattering angle is shown, when assuming different values of Q.

From this figure, it is clear that the presence of a non-zero quadrupole moment of the 2_1^+ state in ^{184}Hg cannot be neglected. The impact on the cross section is shown to be growing with increasing scattering angle.

2.8 Deexcitation rates

The deexcitation rates per second of a nuclear level to a lower-lying level, accompanied by an emitted γ ray, differ per multipole operator. They are directly proportional to the B($E\lambda$) or B($M\lambda$) value and to a power of the difference in energy between the initial and final state [Boh69]:

$$\begin{aligned} T(E1) &= 1.59 \times 10^{15} \mathrm{B}(E1) \\ T(E2) &= 1.22 \times 10^{9}\ \mathrm{B}(E2) \\ T(E3) &= 5.67 \times 10^{2}\ \mathrm{B}(E3) \\ T(E4) &= 1.69 \times 10^{-4} \mathrm{B}(E4) \end{aligned} \tag{2.29}$$

$$\begin{aligned} T(M1) &= 1.76 \times 10^{13} \mathrm{B}(M1) \\ T(M2) &= 1.35 \times 10^{7}\ \mathrm{B}(M2) \\ T(M3) &= 6.28 \times 10^{0}\ \mathrm{B}(M3) \\ T(M4) &= 1.87 \times 10^{-6} \mathrm{B}(M4), \end{aligned}$$

where T equals the number of deexcitations per second, E is expressed in MeV, $B(E\lambda)$ in units of $e^2(\mathrm{fm})^{2\lambda}$, and $B(M\lambda)$ in units of $(e\hbar/2Mc)^2(\mathrm{fm})^{2\lambda-2}$.

The life time of a certain nuclear state can then be calculated:

$$\tau = \frac{1}{\sum_{M\lambda,E\lambda} T}, \tag{2.30}$$

where all possible deexcitation modes including different multipoles have to be included.

Also branching ratios can be calculated when the transition probabilities are known. As an example, when a certain nuclear state I_i can decay to two lower-lying states I_{f1} and I_{f2}, and the two paths are purely of $E2$ character,

the branching ratio of the two γ-ray intensities $I_{I_i \to I_{f1}}$ and $I_{I_i \to I_{f2}}$ will be:

$$\frac{I_{I_i \to I_{f1}}}{I_{I_i \to I_{f2}}} = \left(\frac{\Delta E_{i,f1}}{\Delta E_{i,f2}} \right)^5 \frac{\mathrm{B}(E2 : I_i \to I_{f1})}{\mathrm{B}(E2 : I_i \to I_{f2})}. \tag{2.31}$$

Chapter 3

Experimental setup

In order to perform Coulomb-excitation experiments with exotic nuclei, an acceptable production rate for the isotopes of interest has to be combined with a fast transmission to a post-acceleration system. At the ISOLDE facility at CERN (Geneva, Switzerland), high-quality neutron-deficient mercury isotopes can be produced using the ISOL technique. Afterwards, these nuclei are post-accelerated by REX-ISOLDE to an energy of 2.85 MeV per nucleon (MeV/u) and guided towards a stable target to induce Coulomb excitation. The scattered particles and the γ rays emitted in flight after the inelastic collision are registered respectively by a double-sided silicon strip detector (DSSSD) and the MINIBALL γ-ray spectrometer.

A first experimental campaign was undertaken in the Summer of 2007, where ^{184}Hg, ^{186}Hg and ^{188}Hg were studied. A year later, a second campaign repeated the experiments on these three nuclei, albeit employing different targets, and ^{182}Hg was studied as well.

The next sections aim at describing the experimental set-up that was used: the production and post-acceleration of the isotopes of interest is discussed, followed by a description of the detection system. Furthermore, the Doppler shift of the detected γ-ray energies and the targets employed are addressed. Figure 3.1 shows a lay-out of the ISOLDE facility.

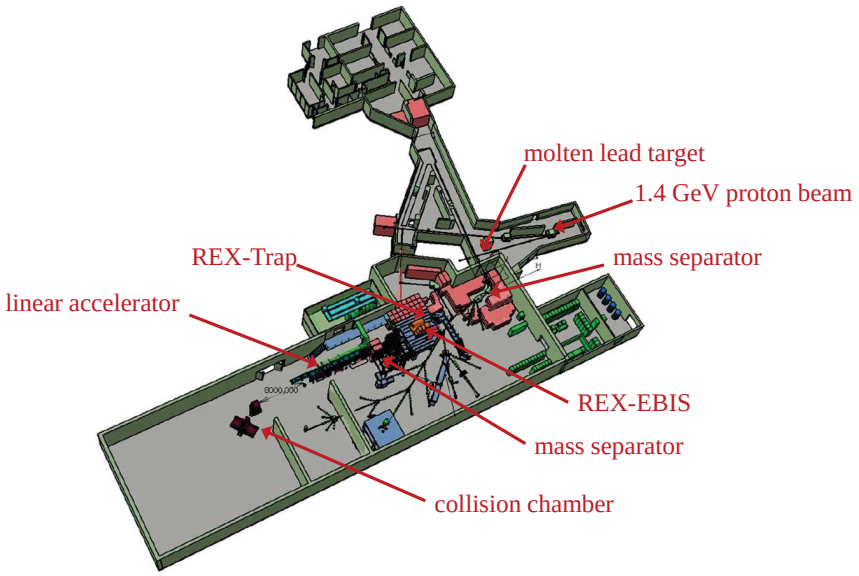

Figure 3.1: The experimental set-up at the radioactive-ion-beam facility ISOLDE at CERN provides the production and post-acceleration of neutron-deficient mercury isotopes, and the detection system for registration of the scattered particles and emitted γ rays.

3.1 Production of exotic isotopes

The isotopes of interest are produced employing the Isotope Separator On Line (ISOL) technique. A molten lead target is bombarded with a proton beam, delivered from the PS (Proton Synchrotron) booster with an energy of 1.4 GeV. By heating up the target to a temperature of approximately 600 °C, the resulting fission, fragmentation and spallation products diffuse and effuse rapidly out of the target container. For this specific reaction, the cross section for spallation is the highest, the other two reaction mechanisms being less probable. Diffusion is the process in which the production fragments move out of the liquid target, whilst effusion occurs in vacuum: in both cases the fragments move outwards like random walkers. The produced nuclei are then ionized using a high-temperature plasma ion source: 1^+ ions are generated by

the electron impact inside the plasma chamber. An electrode at 60 kV is used to extract the ions through the transfer line.

The General Purpose Separator (GPS) consists of an analyzing magnet and is used to select the isotopes with the desired mass. When for example ^{182}Hg needs to be studied, the A/q (mass divided by charge) ratio is set to 182, so only 1^+ ions with 182 nucleons can move through. However, other elements with a total amount of 182 nucleons that are ionized, like lead and gold, will be present as well after mass separation. When the temperature of the target container and the transfer line is kept around 600°C, and not increased by hundreds of degrees, the beam contamination by lead and gold is negligible: the vapor pressure of mercury (i.e. its evaporation rate out of the target container) is four orders of magnitude higher than that of lead, and twelve orders of magnitude higher than that of gold at the typical temperature of the transfer tube between the target container and the ion source.

3.2 Postacceleration of the ions

The REX-ISOLDE set-up [Hab98] ensures an efficient post-acceleration of the produced low-energy beam of mercury ions to an energy of 2.85 MeV/u.

The incident beam of particles with an energy of 60 keV is decelerated to several eV through collisions in the presence of a combination of electric and magnetic fields in REX-Trap. This Penning trap is filled with a buffer gas: a noble gas under low pressure ($\approx 10^{-3}$ mbar) collides with the incident mercury ions and further lowers their energy. By varying the electric field in time while keeping the magnetic field constant, the continuously incoming beam is converted into a bunched beam.

The REX-EBIS (Electron Beam Ion Source) installation provides a charge breeding by electron-impact ionization. Electrons with an energy of several keV are shot by an electron gun on the incoming 1^+ ions, further ionizing them to an n^+ charge state. This leads to a simplification of the acceleration process that follows.

From the distribution of different charge states of the mercury ions, one charge is selected by another analyzing magnet. Table 3.1 shows the charge states used for the 2007 and 2008 experiments on the different mercury isotopes, together with the demanded A/q ratio for the mass separator. In the experiment performed in 2007, the charge breeding time in EBIS amounted to 170 ms. This time is identical to the trapping time in REX-Trap. This means that at a rate of ∼6 Hz, the EBIS bunches the ions into the REX post-accelerator. In 2008, the

EBIS breeding time was set to 200 ms, corresponding to a bunching frequency of 5 Hz.

year	isotope	charge	A/q
2007	^{184}Hg	43^+	4.28
	^{186}Hg	43^+	4.33
	^{188}Hg	44^+	4.27
2008	^{182}Hg	44^+	4.14
	^{184}Hg	44^+	4.18
	^{186}Hg	44^+	4.23
	^{188}Hg	45^+	4.18

Table 3.1: For both experimental campaigns, the selected charge states for the different produced isotopes are shown, together with the A/q ratios imposed on the bending magnet of the mass separator.

Subsequently, the REX linear accelerator (LINAC) accelerates the injected ions to an energy of 2.85 MeV/u. It consists of different elements:

1. A radio-frequency quadrupole (RFQ), accelerating the incident beam to an energy of 0.3 MeV/u,
2. an interdigital H-Structure (IH), boosting the ions to 1.2 MeV/u,
3. three 7-gap resonators increasing the energy of the particles to 2.2 MeV/u,
4. and finally a 9-gap resonator rendering a mercury beam with an energy of 2.85 MeV/u.

A detail of the LINAC system is shown in figure 3.2.

A bending magnet deflects the beam before it impinges on the target in the collision chamber. The final beam intensities and energies after post-acceleration are presented in table 3.2. The stable targets used inducing Coulomb excitation when interacting with the energetic mercury ions are shown as well, together with the total beam-on-target measuring time.

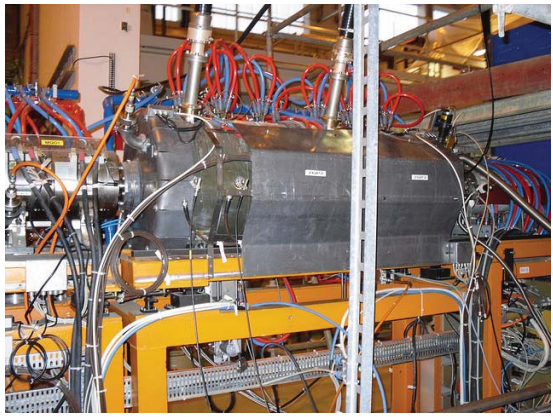

Figure 3.2: The 7-gap resonators are a part of the REX linear accelerator, responsable for the post-acceleration of the mercury beam.

Year	Isotope	I_{beam} [ions/s]	Energy [MeV]	target(s)	thickness [mg/cm^2]	Duration [hours]
2007	^{184}Hg	4.8×10^3	524.4	^{120}Sn	2.3	58.73
				^{107}Ag	1.1	18.3
	^{186}Hg	2.1×10^5	530.1	^{120}Sn	2.3	3.03
				^{107}Ag	1.1	1.42
	^{188}Hg	1.6×10^5	535.8	^{120}Sn	2.3	11.43
				^{107}Ag	1.1	1.62
2008	^{182}Hg	3.5×10^3	518.7	^{112}Cd	2.0	110.53
	^{184}Hg	2.2×10^4	524.4	^{112}Cd	2.0	12.82
	^{186}Hg	3.0×10^4	530.1	^{114}Cd	2.0	5.77
	^{188}Hg	1.0×10^5	535.8	^{114}Cd	2.0	15.95

Table 3.2: The obtained intensities and energies of the mercury beams in the collision chamber are shown here, together with the stable targets employed during the two experimental campaigns and their thicknesses, and the duration of each measurement.

3.3 Detection system

After colliding, the projectile and target particles will be scattered. Their detection is insured by the double-sided silicon strip detector. In the case of an inelastic collision, the emitted γ rays will be registered by the MINIBALL γ-ray spectrometer. A schematic overview of the detection setup is shown in figure 3.3.

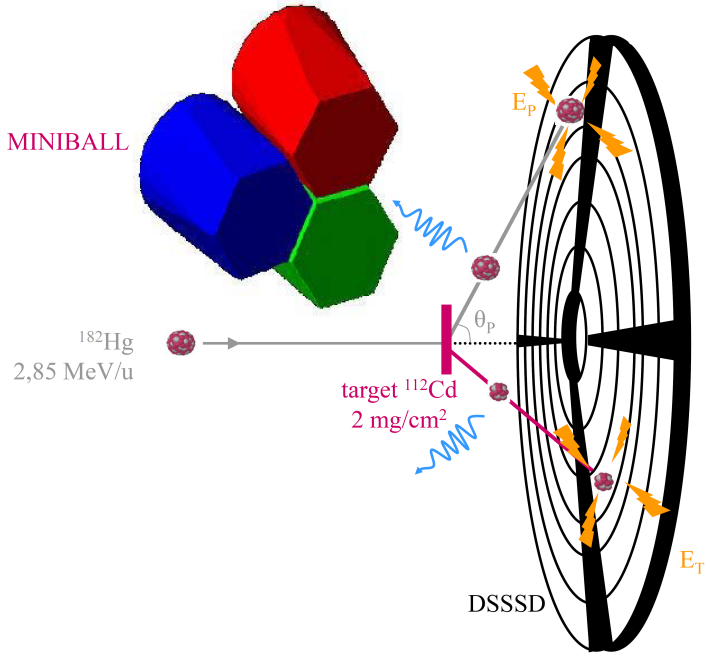

Figure 3.3: Detection set-up for a ^{182}Hg projectile colliding with a ^{112}Cd target. The scattered projectile and recoil ions are detected in the double-sided silicon strip detector. Here E_p and E_t represent the energies of the incident projectile and target respectively. Emitted γ rays will be registered by the MINIBALL γ-ray spectrometer, of which one cluster is shown here, consisting of three crystals.

3.3.1 Double-sided silicon strip detector

The double-sided silicon strip detector [Ost02] is located in the collision chamber for the detection of scattered projectiles and recoils. It was placed at a distance of 32.5 mm behind the cadmium target, and 33.5 mm when the tin or silver target was employed. The detector consists of four quadrants made out of silicon, having an approximate thickness of ≈500 μm. The energy of the incident particle is registered, as well as its exact location, since each quadrant is divided in 16 concentric strips on the front side (called annular strips) and 24 azimuthal strips on the back side (called sector strips). The sector strips are electronically coupled in pairs, so the back side can be regarded as twelvefold segmented. The segmentation of the detector is necessary since γ rays emitted in flight will be Doppler broadened. In order for the measured γ-ray energy to be corrected, the trajectories of the scattered particle and the emitted γ ray need to be known. The annular strips are numbered following the convention that the most outer strip has number 0, and the most inner has number 15. Figure 3.4 shows a picture of the DSSSD, as well as its geometrical features.

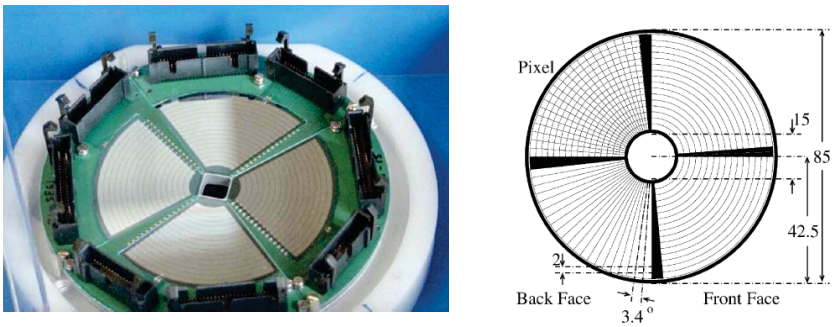

Figure 3.4: The double-sided silicon strip detector. Distances are given in mm.

Since the distance between the DSSSD and the target is known, as well as the exact dimensions of the detector, the angular coverage of each strip can be identified. This will be addressed in the further analysis.

3.3.2 MINIBALL γ-ray spectrometer

The MINIBALL γ-ray spectrometer [War13] is placed in close geometry around the collision chamber to enhance the detection efficiency. It consists of eight clusters, each containing three hyperpure-germanium (HPGe) crystals. A crystal

comprises a central electrode (called the core) and is sixfold segmented, in order to ensure an optimal position sensitivity for the Doppler correction. Since the operational temperature of germanium as a semiconductor is low (around 70°K), the detectors are mounted on cold fingers providing liquid nitrogen (LN_2) for the required cooling. Figure 3.5 shows the different clusters, positioned on aluminium arms, surrounding the collision chamber.

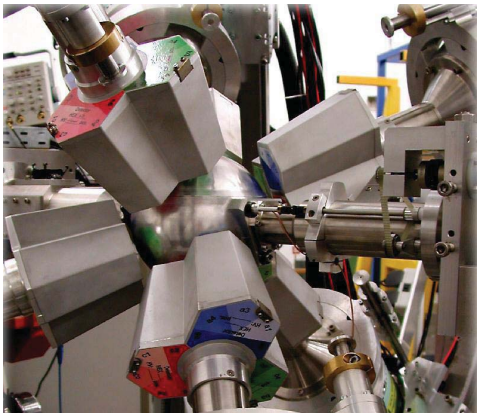

Figure 3.5: The MINIBALL γ-ray spectrometer, surrounding the scattering chamber that hosts the target, the beam diagnostics and the DSSSD detector.

Unfortunately, not all MINIBALL crystals were fully operational. Table 3.3 presents a list of the working crystals during the two experimental campaigns.

This will cause the γ-ray detection efficiency to differ when comparing the two experimental campaigns. Some important consequences for the data analysis can be found in section 4.6.2.

3.3.3 Doppler correction

The life times of the nuclear levels in ^{182,184,186,188}Hg excited by Coulomb excitation typically amount to a few ps. However, the time for a particle to travel from the collision with the target to the DSSSD lies within the range of ns. Hence, a detected γ ray will be emitted in-flight, causing a Doppler shift in its energy, given by the formula:

$$E_{lab} = \frac{\gamma E_0}{1 - \beta \cos(\eta)}, \tag{3.1}$$

cluster number	core number	2007	2008
0	0	> 100 keV	operational
	1	operational	operational
	2	operational	operational
1	3	operational	operational
	4	operational	operational
	5	operational	operational
2	6	operational	operational
	7	operational	not operational
	8	operational	operational
3	9	operational	operational
	10	operational	not operational
	11	operational	operational
4	12	operational	not operational
	13	operational	not operational
	14	operational	not operational
5	15	operational	operational
	16	operational	operational
	17	operational	operational
6	18	operational	not operational
	19	operational	operational
	20	not operational	operational
7	21	> 100 keV	operational
	22	operational	operational
	23	> 100 keV	operational

Table 3.3: The working crystals are presented for both experimental campaigns. In 2007, 23 out of 24 detectors were working, three of them having a threshold of ≈100 keV. In 2008, an entire cluster and 2 crystals were defect, resulting in 18 operational detectors.

where E_{lab} is the detected Doppler-shifted γ-ray energy, E_0 the original energy, $\gamma = \frac{1}{\sqrt{1-\beta^2}}$ the relativistic factor, $\beta = v/c$ the velocity of the particle expressed as a fraction of the speed of light, and η the angle between the scattered particle and the emitted γ ray. This angle can be found by combining the information on the trajectory of the particle (detected in the DSSSD) and the direction of the emitted γ ray (identified by MINIBALL). The angle η can then be calculated according to the formula:

$$\cos(\eta) = \sin(\theta_p)\sin(\theta_\gamma)\cos(\phi_p - \phi_\gamma) + \cos(\theta_p)\cos(\theta_\gamma), \tag{3.2}$$

where θ_p and θ_γ are the angles between the scattered particle or the emitted γ ray and the beam axis and ϕ_p and ϕ_γ the azimuthal angles of particle and γ ray. The detection of the particle energy allows for the speed parameter β to be determined:

$$\beta = \frac{v}{c} = \sqrt{\frac{2E_p}{m_p c^2}} = \sqrt{\frac{2E_p}{A \cdot 931}}, \tag{3.3}$$

where the particle energy E_p is expressed in MeV and the mass A in amount of nucleons. The factor 931 represents the atomic mass unit u expressed in MeV/c^2.

3.3.4 Targets

Several considerations have to be made in the choice for suitable targets. Firstly, the targets should consist of stable or long-living isotopes. Secondly, the overlap of γ deexcitation paths in the target and the projectile should be as small as possible in order for the observed γ rays to be differentiated. The level scheme of the four targets that were employed are shown in figure 3.6. These can be compared with the level schemes of the ^{182,184,186,188}Hg isotopes presented in section 1.4.

The known $E2$ matrix elements in the target nuclei that are necessary for the further analysis are shown in table 3.4.

As an example, the $4_1^+ \rightarrow 2_1^+$ transition in ^{188}Hg with an energy of 592 keV will overlap with the $2_1^+ \rightarrow 0_{g.s.}^+$ transition in the ^{114}Cd target. This case will be addressed in section 6.4.1. A second example is the overlap between the $2_1^+ \rightarrow 0_{g.s.}^+$ transition in ^{182,184}Hg and the $\frac{3}{2}_1^- \rightarrow \frac{1}{2}_{g.s.}^-$ transition in ^{107}Ag, as well as the small energy difference in the $2_1^+ \rightarrow 0_{g.s.}^+$ transition in ^{186,188}Hg and the $\frac{5}{2}_1^- \rightarrow \frac{1}{2}_{g.s.}^-$ transition in ^{107}Ag. For these cases, the other observed transition in ^{107}Ag should be used for the normalization. However, it will be advocated in appendix A that the information on the ^{107}Ag target is not suited for a satisfactory normalization.

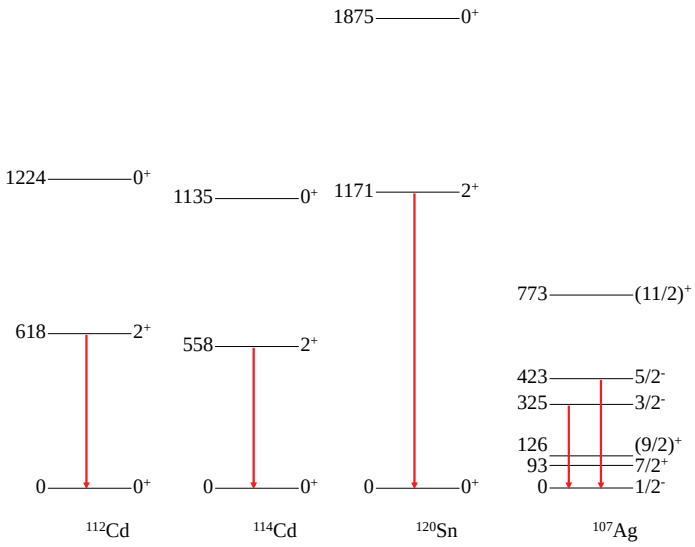

Figure 3.6: During the 2008 campaign, ^{112}Cd was used as the target for the ^{182,184}Hg beams, and ^{114}Cd for the ^{186,188}Hg beams. A year before, a ^{120}Sn as well as a ^{107}Ag target was employed for the ^{184,186,188}Hg beams. The observed transitions are shown in red. Energies are given in keV.

As a third necessary condition, the kinematic signatures of projectile and target detected by the DSSSD have to be distinguishable. This topic will be addressed in section 4.3 for the ^{114}Cd target. The same characteristics apply to the other targets employed, as they do not differ much in mass, giving rise to approximately the same particle trajectories.

Nucleus	$E2$ matrix element [eb]	Known value
^{112}Cd	$\langle 0_1^+ \| E2 \| 2_1^+ \rangle$ $\langle 2_1^+ \| E2 \| 2_1^+ \rangle$	0.714 (14) -0.49 (5)
^{114}Cd	$\langle 0_1^+ \| E2 \| 2_1^+ \rangle$ $\langle 2_1^+ \| E2 \| 2_1^+ \rangle$	0.738 (14) -0.46 (7)
^{120}Sn	$\langle 0_1^+ \| E2 \| 2_1^+ \rangle$	0.449 (4)
^{107}Ag	$\langle \frac{1}{2}_1^- \| E2 \| \frac{3}{2}_1^- \rangle$ $\langle \frac{1}{2}_1^- \| E2 \| \frac{5}{2}_1^- \rangle$	0.651 (31) 0.785 (27)

Table 3.4: Known $E2$ matrix elements connecting low-lying states in the four targets that where used [NND].

Chapter 4

Data analysis

4.1 Sorting of the data

The MINIBALL setup including the DSSSD at REX-ISOLDE aims at registering all quantities necessary to analyze the Coulomb-excitation data. Since this reaction is characterized by emitted γ rays, originating from the deexcitation of the nucleus, as well as the scattered particle(s), emerging from the kinematics of the reaction, the acquired data of MINIBALL and the DSSSD need to be coupled to one another in a specific way. It is important that a good format for the definition of an 'event' is found for the further analysis of the Coulomb-excitation data. Therefore, an event in this work has been defined by:

1. One γ ray.
2. At least one particle coincident with the γ ray in a window of 4 μs, with the condition that there is only one particle per quadrant in the DSSSD at the same time.

Hence, γ rays without any coincident particles within the 4 μs time window, and particles with no coincident γ ray, are not present in the data to be analyzed. A certain part of the 4 μs can be downscaled, meaning that only one out of a certain amount of events is stored by the data acquisition system (DAQ). This will be explained in section 4.2.

The necessary information on the γ ray and the coincident particle(s) is the following:

1. The γ-ray energy: the intensities of photo peaks originating from the deexcitation after Coulomb excitation need to be known. The γ-ray energy is measured by the MINIBALL crystal cores. An add-back procedure is applied here: this means that the energies of two γ rays detected by different cores in the same cluster are summed.

2. γ-ray direction: the difference in direction of the γ ray and the particle(s) is known to perform the Doppler correction. The direction is deduced from the energy distribution in the MINIBALL segments.

3. The particle energy: the energy and direction of the incident particle are used to identify the particle, as the kinematics are known. The energy is also needed for the Doppler correction. It is measured by the annular strip of the DSSSD in which it is detected.

4. The particle direction: this is needed for the Doppler correction and the identification of the particle. It is found by the annular and sector strip of the DSSSD in which it is detected.

5. The particle-γ time difference: this is needed to know if the particle and the γ ray are in prompt or random coincidence. Section 4.2 will elaborate on this. The particle-γ time difference is measured using the timing information of the annular strips in the DSSSD and the timing information in the MINIBALL segments.

4.2 Prompt and random radiation

The structure of the acquired data can be modified according to the experimental quantities that need to be extracted. The output of the data acquisition described in the previous section consists of individual particles in one of the four quadrants of the particle detector, coincident with one or more detected γ rays within a time window of 4 μs. When a γ ray is coincident with more than one particle (in different quadrants), the data acquisition stores this as two different events. For the analysis of the Coulomb-excitation data, it is necessary to correlate each detected γ ray with the particle or particles that coincide with it, being projectile or target or both.

After resorting the data, the output consists thus of individual γ rays with their coincident particles. Since the nuclei under investigation are radioactive, there will be a constant flow of γ rays originating from this decay, together with the natural background radiation and the X-ray radiation from the accelerator cavities, which all can be defined as 'random' γ rays. Since the interest of

the Coulomb-excitation experiment lies in the γ rays arising directly from the collision, a difference has to be made between these γ rays, defined as 'prompt', and the random ones. Figure 4.1 shows the time difference between the γ rays and a coincident particle for each individual collision in the experiment of ^{188}Hg on ^{114}Cd. The peak around -800 ns shows the prompt events. However, it is not situated around zero due to electronic settings. Under the peak, a semi-constant background of the γ rays in random coincidence with a particle is present. The gate for prompt coincidences between γ ray and particle can be put between -900 ns and -600 ns, while the purely random window can be defined from -1350 ns to -900 ns. The rest of the events coincident within the 4 μs range has been downscaled. This means that only one out of a certain number of events (in this case 64) is stored in the data files by the electronics.

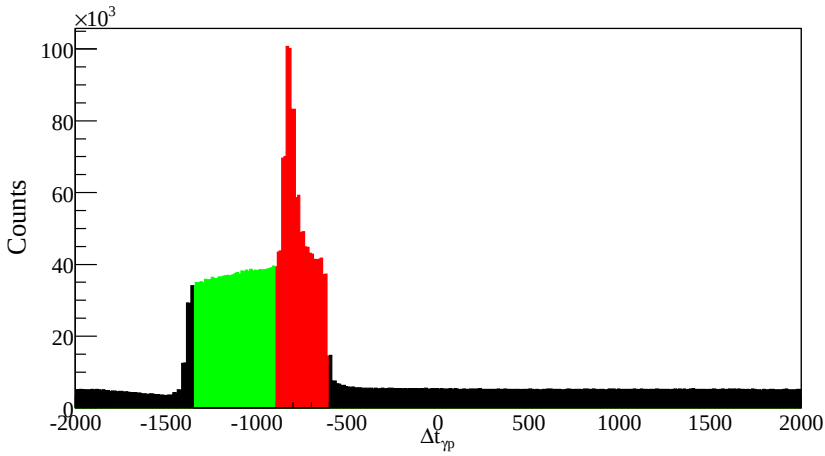

Figure 4.1: Time difference in ns between the detected γ and particle for the ^{188}Hg-on-^{114}Cd experiment. The prompt coincidence window is indicated in red, the random one in green. Random events are also present underneath the prompt peak.

In order to subtract the random events within the prompt window of 300 ns in the γ-ray spectrum, the events in the random window of 450 ns can be rescaled with a factor of $\frac{300}{450} = \frac{2}{3}$ and then subtracted from the prompt ones. In figure 4.2, both γ-ray spectra within prompt and random coincidence are shown for the experiment of ^{184}Hg on ^{112}Cd, the latter being rescaled by a factor of $\frac{2}{3} \approx 0.667$. The same scaling factors were used for all experiments employing the ^{112}Cd or ^{114}Cd target. For the experiments in which a ^{186}Hg or ^{188}Hg was incident on the ^{107}Ag or ^{120}Sn target, the prompt window was defined from -900 ns to -625

ns, due to downscaling effects. This yields a rescaling factor of ≈ 0.611. In the ^{184}Hg experiments on the ^{107}Ag and ^{120}Sn target, no downscaling was applied. The random window was chosen to be the full time range of 4 μs, the prompt window being left out, leading to a scaling factor of ≈ 0.095.

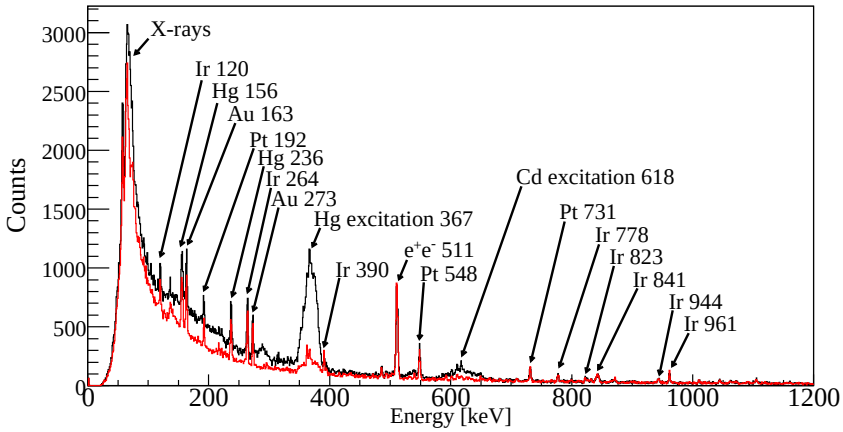

Figure 4.2: γ-ray spectra within prompt (black) and random (red) coincidence, the latter having been rescaled. These data were obtained from the ^{184}Hg-on-^{112}Cd experiment. β decay and electron capture of ^{184}Hg and isobaric daughter nuclei result in the presence of γ transitions at specific energies. These are presented with the chemical element of the mother nucleus, and the energy in keV. The decay chain also leads to the observation of X-rays. However, X-rays can also be produced by the accelerator cavities, or can originate from the deexcitation of ^{184}Hg after Coulomb excitation. The photo peak at 511 keV is caused by positron-electron pair annihilation. Coulomb excitation of the ^{184}Hg projectile and the ^{112}Cd target leads to the observation of the peaks at 367 keV and 618 keV.

After subtracting the rescaled random from the prompt γ-ray spectrum, only the transitions directly caused by the projectile-target collision are remaining, as shown in figure 4.3. The Doppler broadened photo peaks of the $2_1^+ \rightarrow 0_1^+$, $4_1^+ \rightarrow 2_1^+$ and $2_2^+ \rightarrow 0_1^+$ transitions in ^{184}Hg can be observed. Also a peak around 69 keV remains present, suggesting a production of X-rays directly related to the collision. Note that in the non-random-subtracted spectrum a clear peak around 65 keV was present, arising mainly from the β-decay and electron capture of ^{184}Ir, on top of the X-ray radiation from the accelerator cavities. Subtracting the spectra causes these X-rays to vanish, resulting in the

observation of the beam-related X-rays with a slightly different energy. Also the Doppler-broadened photo peak of the $2_1^+ \rightarrow 0_1^+$ transition in ^{114}Cd is observed.

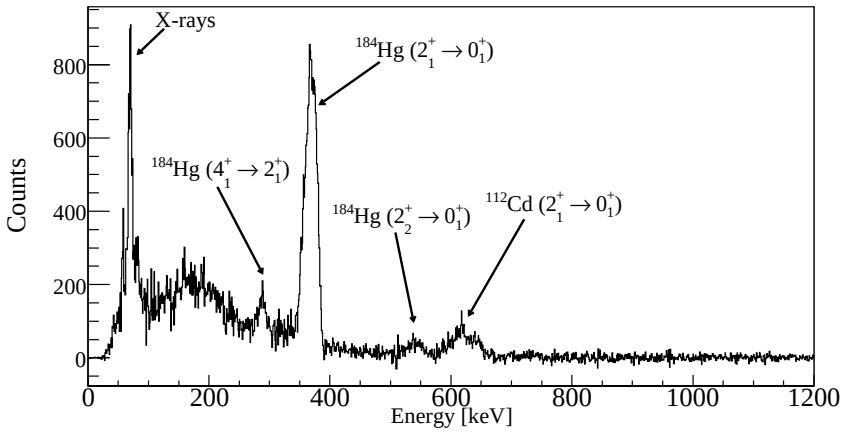

Figure 4.3: Prompt minus rescaled random γ-ray spectrum of the ^{184}Hg experiment on the ^{112}Cd target.

4.3 Reaction kinematics

When the mercury projectile interacts with a target atom, both particles undergo Rutherford scattering. In the experiments employing the ^{112,114}Cd targets, the DSSSD particle detector covers an angular range from 15.5° to 51.6° in the laboratory frame, corresponding to different c.m. angular ranges for projectile and target. Figure 4.4 shows the relation between the laboratory and the c.m. angles for the elastic scattering of a ^{182}Hg projectile incident on a ^{112}Cd target.

Figure 4.5 shows the energy of projectile and target as a function of the scattering angle in the laboratory frame. When a particle with an energy around 400 Mev is detected under a small scattering angle, it is unclear whether it is a projectile or a target ion.

These relations have been calculated assuming conservation of energy during the interaction. However, the mercury projectile will loose energy when traveling through the target. Using the programme SRIM [SRI], the energy loss of mercury in the cadmium target can be calculated to be $\approx 55 \frac{\text{MeV}}{\text{mg/cm}^2}$ when the

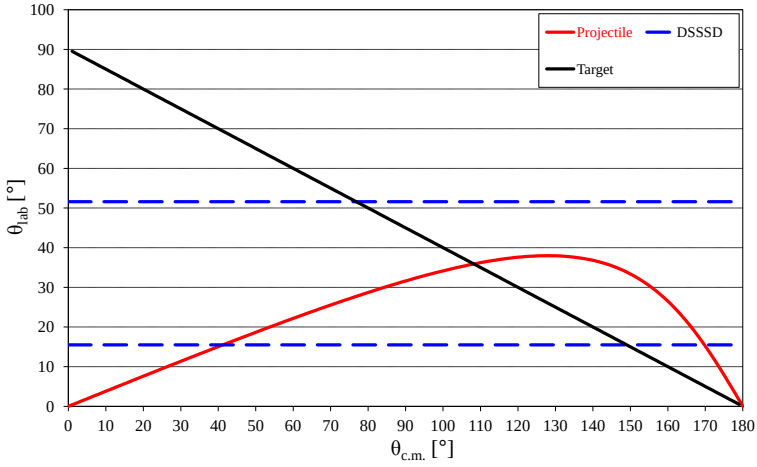

Figure 4.4: Scattering angle in the laboratory frame versus scattering angle in the c.m. frame for a ^{182}Hg projectile colliding with a ^{112}Cd target ion, given for both projectile (red) and target (black). The angular coverage of the DSSSD particle detector is indicated in blue.

mercury has an incident energy of 518.7 MeV (corresponding to 2.85 MeV/u). Since the cadmium foil has a thickness of 2.0 mg/cm^2, the mercury will lose ≈110 MeV in the target. As the two ions can interact at any place in the target, a certain distribution of energy losses is expected.

Due to the similarity in mass between the employed targets (^{112,114}Cd, ^{120}Sn and ^{107}Ag) and the fact that the projectile mass does not alter substantially (^{182,184,186,188}Hg), the kinematics in the different experiments will be very comparable.

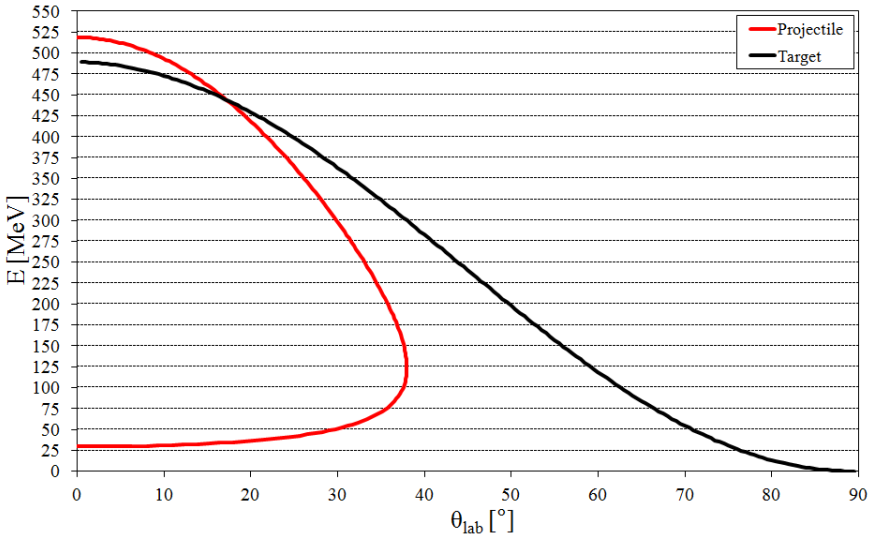

Figure 4.5: Energy of the scattered projectile (red) and target (black) versus the scattering angle in the laboratory frame for a ^{182}Hg projectile colliding with a ^{112}Cd target ion.

4.4 Two-particle events

When a particle is detected in the DSSSD under a small laboratory scattering angle (and thus high annular strip number) and high energy, it can not be directly identified as a projectile or a target particle. This overlap can be coped with by demanding the detection of exactly two particles in opposite quadrants. As indicated in figure 4.4, there is a considerable c.m. angular range where two particles are incident on the DSSSD, i.e. from 77° to 149°. When a detected particle under a small laboratory scattering angle with high energy is in coincidence with a particle with low energy scattered under a large laboratory angle in the opposite quadrant of the DSSSD, the first can be assumed to be mercury, and the latter to be cadmium. However, when the coincident particle has a low energy but is also scattered under a small laboratory angle, the first particle is supposed to be cadmium and the second mercury. Ideally, when demanding the detection of two particles, no mercury will be present in annular strips 13 to 15 of the DSSSD, since the corresponding cadmium particle will not be detected.

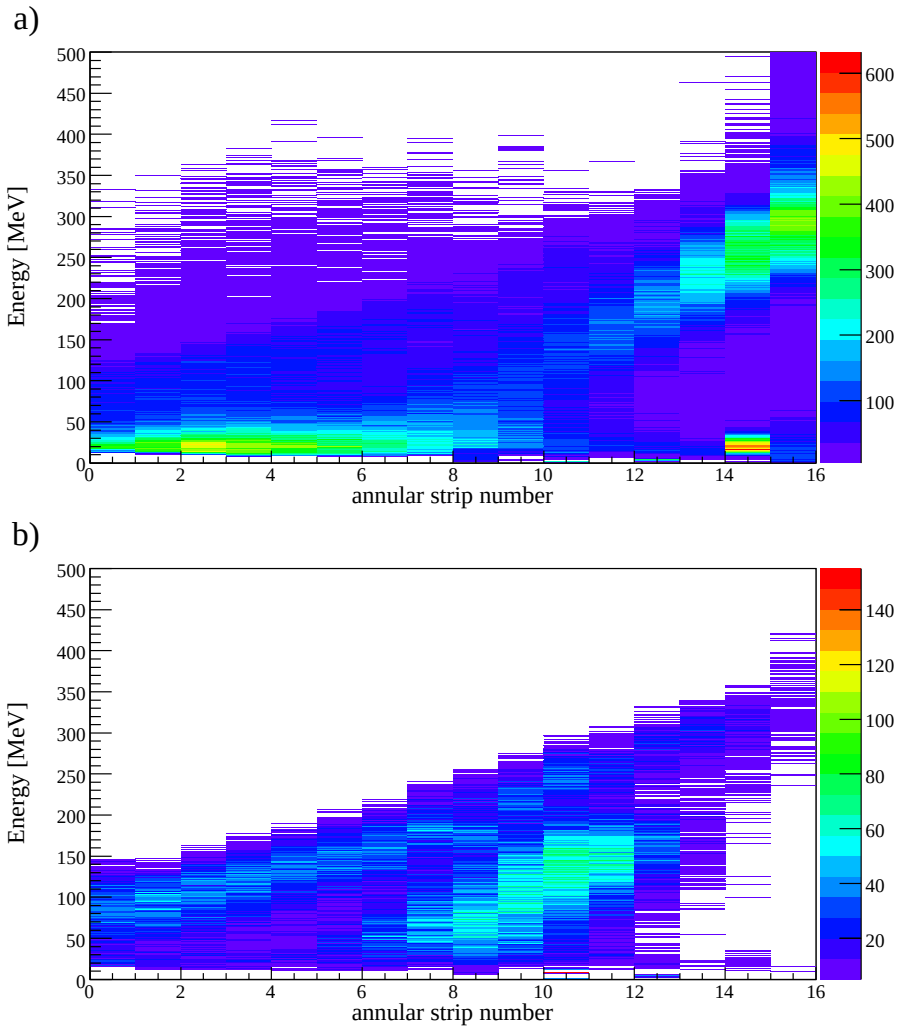

Figure 4.6: a) Intensity of the particles plotted as a function of their energy and annular strip number in the DSSSD for a ^{182}Hg projectile colliding with a ^{112}Cd target ion. Here no specific amount of detected particles was requested. b) Idem, but with with the demand of detecting exactly two particles in opposite quadrants of the DSSSD.

Figure 4.6 shows the energy of the detected particles related to the annular strip number for the ^{182}Hg experiment on the ^{112}Cd target, with the request of any amount of detected particles, and with the extra condition of exactly detecting two particles in opposite quadrants. In the first one, low-energy noise is present in the lower strip numbers, and an electronic problem seems to occur in strip 14 in one of the four quadrants. However, the latter spectrum seems to be very selective, although the mercury ions incident in the higher strip numbers at high energy will not contribute anymore to the further analysis. The importance of omitting these data will be discussed in section 6.1.5.

The condition that the two particles must be incident on opposite quadrants of the DSSSD will be implicitly assumed in the further analysis.

When demanding the detection of exactly two particles coincident with a γ ray, it is important that the particles themselves are in coincidence with each other. Figure 4.7 shows the correlation of the γ-particle time difference for the two detected particles, as well as the time difference between the two particles, this time for the ^{188}Hg projectile incident on the ^{114}Cd target. In figure 4.7.a, the events around the $y = x$ line are the ones of interest. Therefore, a coincidence window of $\Delta t_{p_1p_2} \leq 50$ ns is defined (figure 4.7.b). A common $\Delta t_{\gamma p}$ time difference can then be defined by projecting the events in the first figure on the $y = x$ axis by the formula

$$\Delta t_{\gamma p} = \frac{\Delta t_{\gamma p_1} + \Delta t_{\gamma p_2}}{2}. \tag{4.1}$$

Indeed, when assuming the two particles to have the same time difference with the coincident γ ray, it can be calculated by taking the average of the individual γ-particle time differences. This definition of the γ-particle time difference for a two-particle event will be employed in the prompt and random windows in the further analysis.

The selectivity of the two-particles events can be further improved by gating strip by strip on the expected energy range of the cadmium recoil. The other particle should then be mercury, incident in the corresponding angular scope and energy range. Gating on the mercury projectile and subsequently investigating were the cadmium recoil is detected is much more complicated, as with decreasing energy, the scattering angle in the laboratory frame of mercury increases first to bend back later to lower values. This causes annular strips 7, 8 and 9 to cover a very large c.m. angular range, without the ability of further gating. Therefore, gating was performed on the cadmium particles, which serves as a magnifying glass in the kinematics of the reaction.

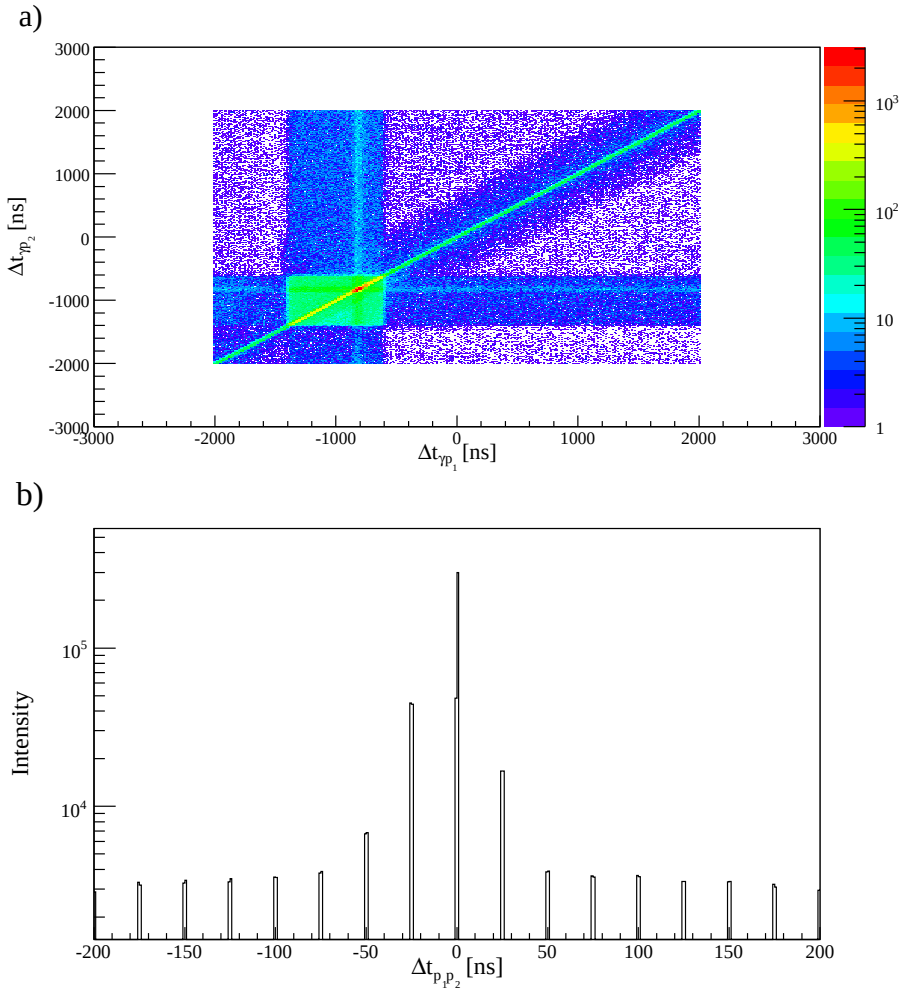

Figure 4.7: a) Intensity of the particles plotted as a function of the γ-p_1 time difference (i.e. the time difference between the detected γ ray and the first particle) and the γ-p_2 time difference (idem, but with the second particle), when exactly two particles were registered in the DSSSD. The z axis (in colour code) is in logarithmic scale. b) Time difference between the two detected particles, with the y axis in logarithmic scale.

Figure 4.8 shows the selected cadmium particles for six annular strips, the corresponding second particles, which are supposed to be mercury, and a gate that was put on the latter to ensure that they are only mercury. Again this is done for the ^{188}Hg projectile incident on the ^{114}Cd target. When the cadmium gate is put on strips 8 to 12, it can also contain mercury particles. This is observed in column b of the figure, where a part of the corresponding detected particles are clearly cadmium, and not mercury. With increasing strip number in column a, these corresponding particles decrease in strip number and energy, as predicted by the kinematics. These events are omitted in column c, so the true cadmium recoil and mercury ejectile are identified.

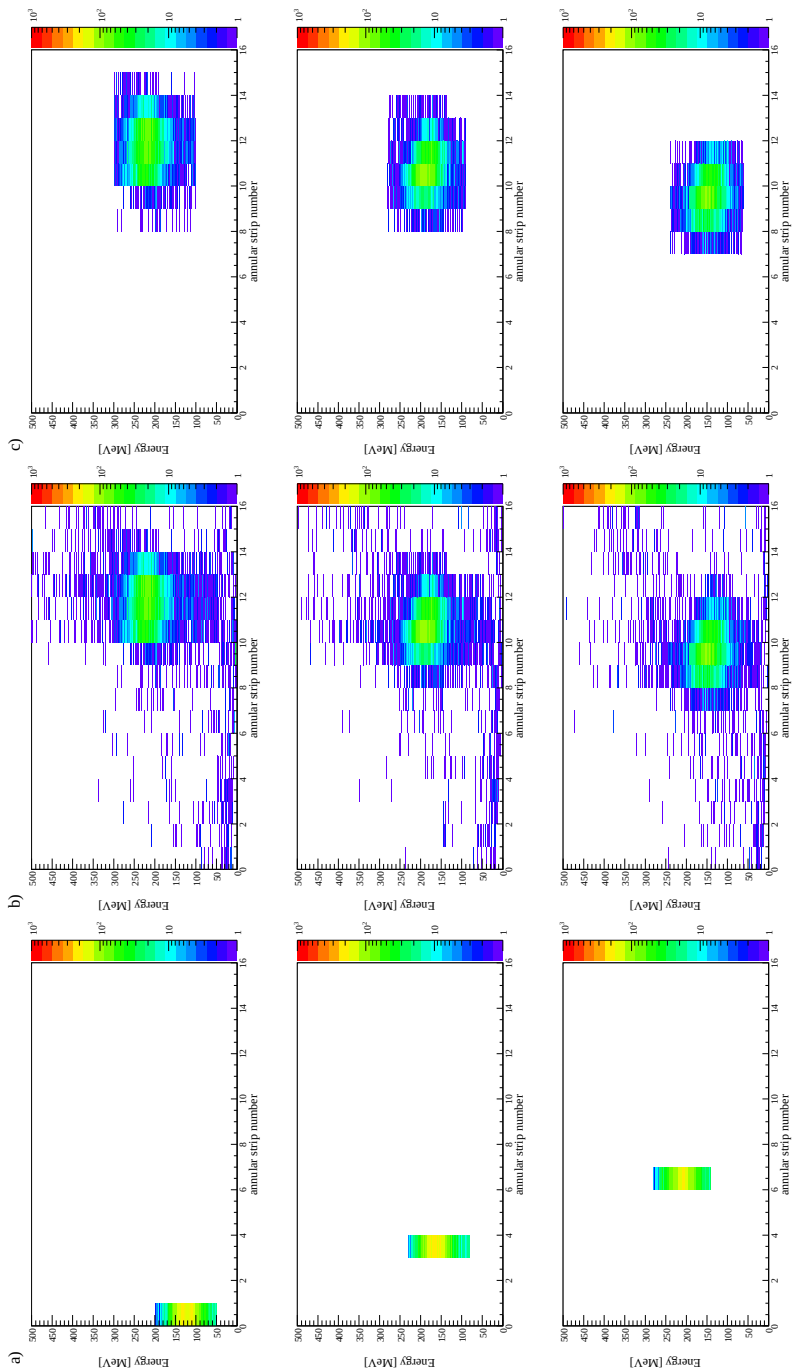

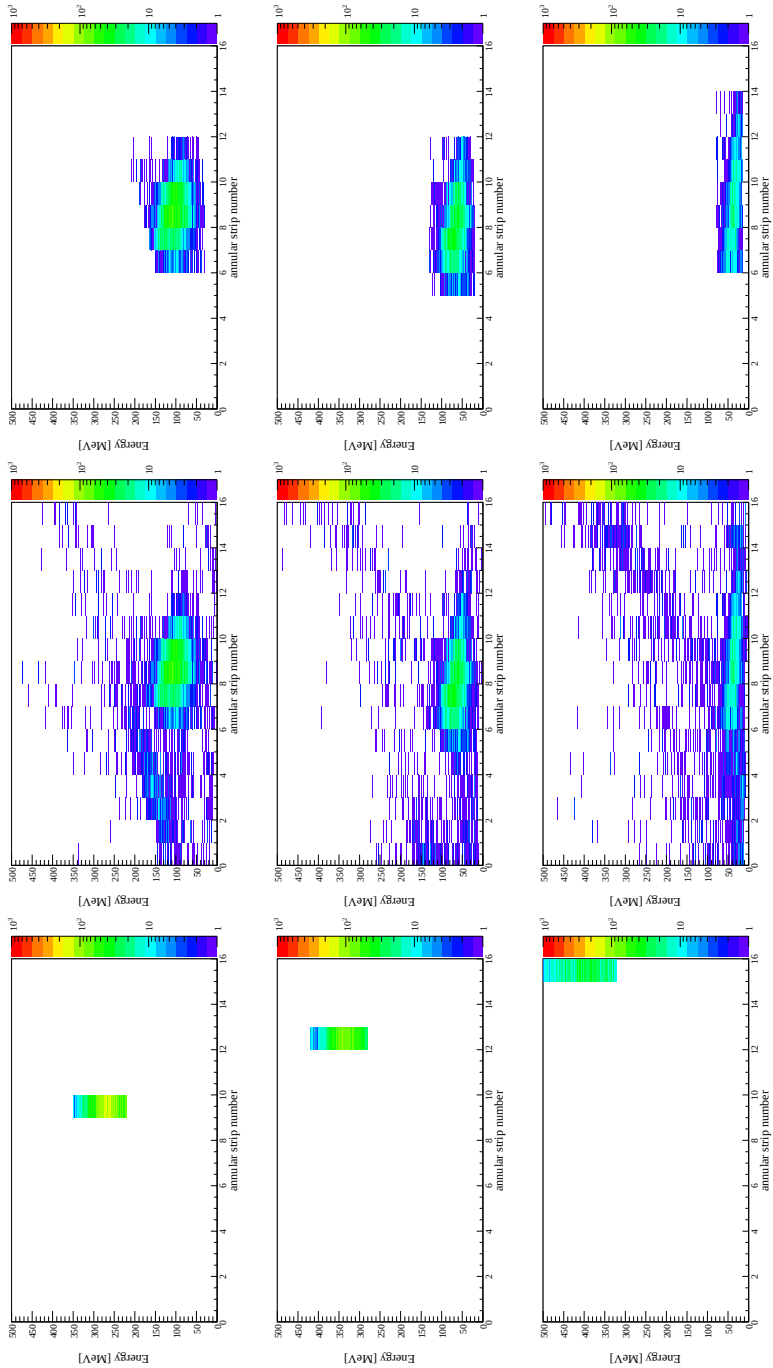

Figure 4.8: a) The selected energy range of particles presumed to be cadmium in the ^{188}Hg-on-^{114}Cd experiment. b) The corresponding secondly detected particles, assumed to be mercury. c) The corresponding secondly detected particles, with a gate on where the mercury is expected according to the kinematics.

4.5 Extraction of the integrals

The observed two-particle events can now be Doppler corrected according to formula 3.1 on an event-per-event basis. Since both projectile and target are detected in the DSSSD, the observed γ ray in an event will be Doppler corrected for mercury and added to the spectrum serving for the integration of the photo peaks originating from mercury, and it will be Doppler corrected for cadmium and included in the spectrum used for integrating the photo peaks from deexcitation in cadmium. Hence, the two produced spectra have the same amount of counts. As an example, figure 4.9 shows the random-subtracted γ-ray spectra coincident with two identified particles Doppler corrected for ^{188}Hg and ^{114}Cd when the cadmium was detected in annular strip 4 of the DSSSD.

The integration of a peak is not performed by fitting its shape, but by exactly counting its intensity. For this procedure, the background in the random-subtracted spectrum needs to be estimated. This can be done by interpolating the observed background on the left and right of the photo peak that needs to be integrated. Figure 4.10 shows how this procedure works for the integration of the $2_1^+ \rightarrow 0_1^+$ transition of ^{188}Hg range when it is incident on the ^{114}Cd target. The figure presents the random-subtracted γ ray spectrum coincident with two identified particles Doppler corrected for the projectile. Here, the 15 spectra, where a gate was placed on the cadmium per annular strip of the DSSSD and the corresponding mercury particles were selected, have been added. The target gate on strip 15 has not been included, since this strip was not operational in one of the four quadrants. Moreover, cross sections for both projectile and target are low in this strip's angular range.

The background is supposed here to have a linear behavior and the interpolation is determined by the line going through the two points $(\frac{b_1+b_2}{2}, \frac{\int_{b_1}^{b_2} I_\gamma dE_\gamma}{b_2-b_1})$ and $(\frac{b_3+b_4}{2}, \frac{\int_{b_3}^{b_4} I_\gamma dE_\gamma}{b_4-b_3})$, where E_γ is the γ-ray energy and I_γ the γ-ray intensity per energy. The counts which are present under this line between the integration limits a_1 and a_2 are then subtracted from the total integral $\int_{a_1}^{a_2} I_\gamma dE_\gamma$. The resulting error is then

$$\sigma_{res} = \sqrt{\sigma_{p-r}^2 + \sigma_{bg}^2}, \tag{4.2}$$

where σ_{p-r} is the error on the total integral $\int_{a_1}^{a_2} I_\gamma dE_\gamma$ in the random-subtracted prompt spectrum (which includes the background counts) and σ_{bg} is the error on the background, estimated under the true photo peak. Since the error on

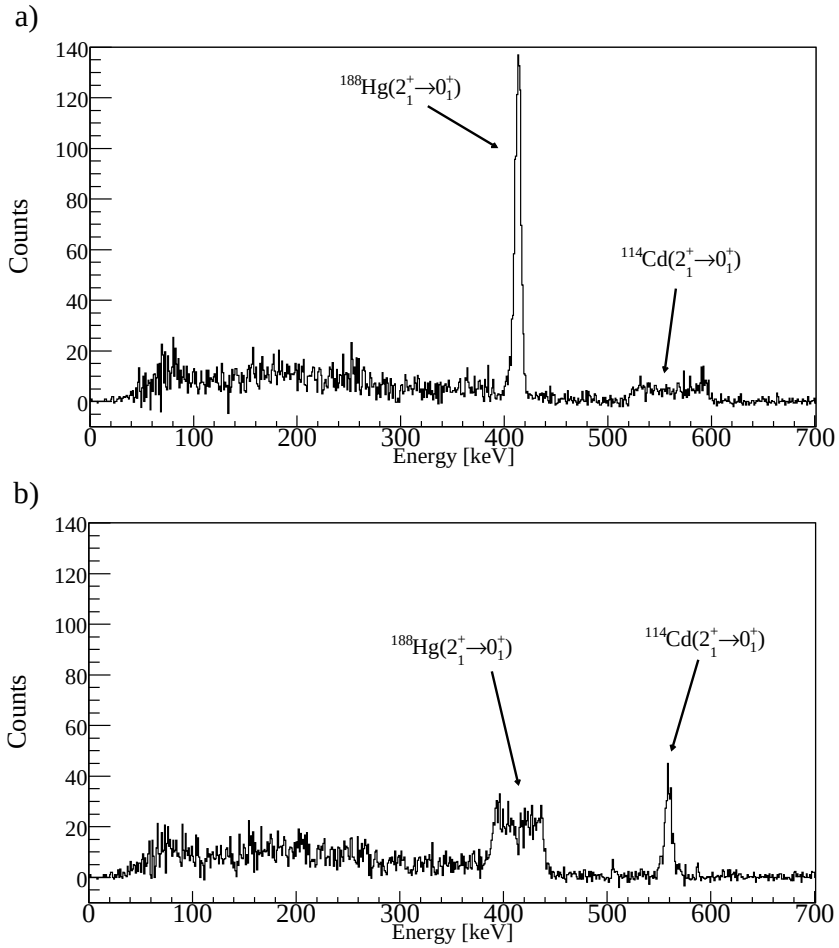

Figure 4.9: Random-subtracted γ-ray spectra coincident with two identified particles Doppler corrected for ^{188}Hg (a) and ^{114}Cd (b) when the cadmium was detected in annular strip 4 of the DSSSD. A gate was placed on the detected corresponding particles to ensure they were in the expected projectile range of the kinematics.

an observed amount of counts is the square root of the amount of counts itself, formula 4.2 reduces to

$$\sigma_{res} = \sqrt{I_{\gamma,p-r} + I_{\gamma,bg}}. \tag{4.3}$$

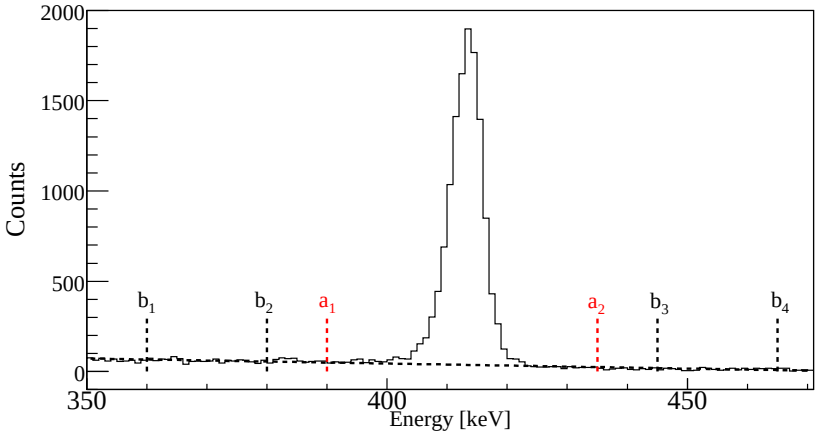

Figure 4.10: Random-subtracted γ-ray spectra coincident with two identified particles Doppler corrected for ^{188}Hg when the cadmium was detected in annular strips 0 to 14 of the DSSSD. The background on the left is estimated in the region [b_1,b_2], the right one in the region [b_3,b_4]. An interpolation line is drawn between the two background regions, estimating the total backround under the integrated photo peak, present in the interval [a_1,a_2]. In this particular case b_1=360 keV, b_2=380 keV, b_3=454 keV, b_4=465 keV, a_1=390 keV and a_2=435 keV. The integration window is quite wide, since at high particle centre-of-mass angles, the peak is less sharp, and the window is chosen to be the same throughout the whole c.m. range.

In this formula, the error on the random counts is not taken into account. However, sometimes the count rate in certain energy regions in the random spectrum cannot be neglected. This is for example the case when integrating the peak of K X-rays originating from mercury at an energy of 69 keV. Section 4.2 already discussed the presence of X-rays from the β-decay (or electron-capture) products of the produced mercury (and X-rays originating from the accelerator), which are very similar in energy, but are equally present in the prompt as in the random spectrum. As a consequence, these X-rays vanish when subtracting the (rescaled) random from the prompt spectrum. When a certain intensity $I_{\gamma,r}$ is observed in the random spectrum, its error amounts to $\sqrt{I_{\gamma,r}}$. If the scaling factor for subtracting the random spectrum from the prompt spectrum equals s, the observed intensity with its error becomes $sI_{\gamma,r} \pm s\sqrt{I_{\gamma,r}}$. For the ^{188}Hg-on-^{114}Cd experiment, the scaling factor s was defined to be $\frac{2}{3} \approx 0.667$.

Also including this error on the random counts adds a term in formula 4.3:

$$\sigma_{res} = \sqrt{I_{\gamma,p} + s^2 \cdot I_{\gamma,r} + I_{\gamma,bg}}. \tag{4.4}$$

When gating on the cadmium particles in the higher annular strips, the corresponding mercury particle is expected to have a low energy, and its detection can not always be guaranteed. However, when only the cadmium particle is detected, the event is omitted, so it will not contribute to the target deexcitation photo peak, nor to the one(s) observed in mercury. As a consequence, demanding the detection of two particles solves the problem of lower particle detection efficiencies at lower energies, since this effect is seen in the spectra Doppler corrected for the target as well as in the spectra Doppler corrected for the projectile. Normalizing a projectile photo peak to the photo peak from target excitation means dividing the intensity of the first one by the intensity of the latter one, canceling out this effect.

4.6 $\gamma - \gamma$ coincidences

4.6.1 Construction of the γ-ray spectra

It is useful in the analysis of the Coulomb-excitation experiments to have knowledge about coincident deexcitations. A simple case is that of an even-even nucleus with an evident 0^+ ground state, an excited 2^+ state, and a 4^+ state, higher in energy. The nucleus can only get excited to the 4^+ state via two subsequent $E2$ excitations: one from the 0^+ ground state to the excited 2^+ state, and a further excitation to the 4^+ state. The deexcitation will happen mainly via the subsequent E2($4^+ \rightarrow 2^+$) and E2($2^+ \rightarrow 0^+$) γ-ray transitions. Other paths, like the slow E4($4^+ \rightarrow 0^+$) and possible electron conversion are neglected here. Apart from the known electron conversion path, the $4^+ \rightarrow 2^+$ deexcitation will hence be always coincident with the $2^+ \rightarrow 0^+$ transition. However, the γ-ray detection efficiency needs to be taken into account, since only a limited amount of emitted γ rays will be detected by the MINIBALL γ-ray spectrometer. The γ-ray detection efficiency will be addressed in section 5.3.

Due to statistical limitations, only coincidences with the $2_1^+ \rightarrow 0_{g.s.}^+$ transition in ^{182,184,186,188}Hg will be used in the analysis, since this is the most intense transition. A particle gate is placed on the region where mercury is expected. Also events with only one particle are included, since the $\gamma - \gamma$ coincidence data are scarce. The spectra are created by investigating the neighbouring events in

the raw data, i.e. the γ rays that are in the same electronic read-out, which has a length of ≈ 10 μs.

A gate is placed on the energy of the $2_1^+ \rightarrow 0_{g.s.}^+$ transition, Doppler corrected for the particle in the mercury gate of the DSSSD. The coincident γ rays are then Doppler corrected for the same particle and added to the coincidence spectrum. A prompt-prompt event is defined by the first γ ray being in prompt coincidence with a particle (the timing conditions are discussed in section 4.2) and the two γ rays are in coincidence with each other, meaning that the time difference between them is less than 300 ns. A random-prompt event means that the first γ ray is in random coincidence with a particle, and the two γ rays are in coincidence with each other. The spectrum consisting of these events should be rescaled and subtracted from the prompt-prompt spectrum. The prompt-random spectrum consists of the events of which the first γ ray is in prompt coincidence with a particle, but the two γ rays mutually are not: the time difference between them has a value between 400 ns and 700 ns. This spectrum should also be subtracted from the prompt-prompt spectrum. Random-random events do not have to be subtracted, since they are obviously not present in the prompt-prompt spectrum. Section 6.1.2.1 elaborates on the coincidence spectra of ^{182}Hg.

The integral of the photo peaks observed in the γ-ray spectrum coincident with the $2_1^+ \rightarrow 0_{g.s.}^+$ transition, is taken in the same way as shown in figure 4.10, and the error on the background intensity, as well the errors in the prompt-prompt, prompt-random and random-prompt spectra contribute to the resulting error.

In order to estimate random coincidences, a gate is placed on an energy range lower than the $2_1^+ \rightarrow 0_{g.s.}^+$ transition, and also a gate with higher energy. The intensities and the errors of the possible coincident transitions are taken in the same way as described above. A line is constructed connecting these two intensities, and its interpolated intensity under the integral of the transitions in coincidence with the $2_1^+ \rightarrow 0_{g.s.}^+$ transition is subtracted. Also the errors on the intensities coincident with lower and higher energies than the $2_1^+ \rightarrow 0_{g.s.}^+$ transition contribute to the resulting error. A clarifying example for the ^{182}Hg case is given in section 6.1.2.1.

4.6.2 Extraction of the singles integrals from the coincident γ-ray spectra

The intensities of the transitions observed in the γ-ray spectrum coincident with the $2_1^+ \rightarrow 0_{g.s.}^+$ transition can be converted to intensities in the total-range

two-particle spectrum, being the spectrum with two identified particles adding the spectra where cadmium was detected in strips 0 to 14.

When a certain transition is seen in both spectra, the ratio of its intensities can be used to convert the intensities of other transitions which are only observed in the coincidence spectrum to the total-range two-particle spectrum. For example, in all experiments on ^{182}Hg and ^{184}Hg, the $4^+ \rightarrow 2^+$ is observed in both spectra. This ratio, defined per experiment as

$$R_{4_1^+ \rightarrow 2_1^+} = I_{4_1^+ \rightarrow 2_1^+, coin} / I_{4_1^+ \rightarrow 2_1^+, singles}, \tag{4.5}$$

can be used to convert the observed intensity of the $2_2^+ \rightarrow 2_1^+$ transition in the ^{182}Hg-on-^{112}Cd experiment to the total-range two-particle γ-ray spectrum. However, since the population of the 4_1^+ state is always a two-step Coulomb-excitation process, employing the ratio $R_{4_1^+ \rightarrow 2_1^+}$ implicitly assumes that the 2_2^+ state is also populated this way. This is due to the difference in the covered angular particle range when comparing two-particle events and events with any amount of particles. Since in the latter one, also mercury particles are present in the high energy projectile branch of strips 13 to 15, the intensity ratio will differ for one-step and two-step Coulomb excitations, where the maximum of the angle-dependent cross-section curve shifts to higher angles in the latter case. Still, the population of the 2_2^+ state can also have a one-step nature. Nevertheless, the errors on the observed intensities in the coincidence spectra for the different experiments are so large this assumption should not affect the analysis in a thorough way.

When such a transition is not observed, the conversion from an intensity in the coincidence spectrum to the singles intensity can be calculated by:

$$I_{singles} = \frac{I_{coin}}{\frac{7}{8} \cdot \epsilon_{\gamma, 2_1^+ \rightarrow 0_{g.s.}^+}}, \tag{4.6}$$

where $I_{singles}$ is the calculated intensity of the transition coincident with the $2_1^+ \rightarrow 0_{g.s.}^+$ transition in the total two-particle γ-ray spectrum, I_{coin} is its observed intensity in the $\gamma - \gamma$ coincidence spectrum, and $\epsilon_{\gamma, 2_1^+ \rightarrow 0_{g.s.}^+}$ is the γ-ray detection efficiency of the $2_1^+ \rightarrow 0_{g.s.}^+$ transition in the MINIBALL spectrometer. The factor $\frac{7}{8} = 0.875$ accounts for the add-back: if a γ ray is detected in one of the eight MINIBALL clusters, a coincident γ ray can not be detected by the same cluster, since their energies would be summed. During the 2007 campaign, two cores in different clusters were not operational, causing the factor to change to 0.877. For the experiments performed in 2008, a whole MINIBALL cluster

was missing, and three other cores in different clusters were not operational, rendering a factor of 0.852.

When comparing calculated singles intensities from the coincidence spectra with observed intensities in the total γ ray spectrum (e.g. for the $4_1^+ \rightarrow 2_1^+$ state in ^{182,184}Hg), it is clear that the calculated ones are highly overestimated. This is due to the fact that the singles spectrum demands the detection of two identified particles, and the coincidence spectrum does not. This also means that in the singles spectrum, no mercury is present in the high energy kinematic branch in strips 13, 14 and 15, whilst these events do appear in the coincidence spectrum. A correction factor can be found when taking the ratio between the $2_1^+ \rightarrow 0_{g.s.}^+$ intensity in the two-particle singles spectrum, and its intensity in the singles spectrum with any amount of coincident particles. Formula 4.6 then becomes:

$$I_{singles} = \frac{I_{coin}}{\frac{7}{8} \cdot \epsilon_{\gamma, 2_1^+ \rightarrow 0_{g.s.}^+}} \cdot \frac{I_{2_1^+ \rightarrow 0_{g.s.}^+ 2p}}{I_{2_1^+ \rightarrow 0_{g.s.}^+ np}}, \tag{4.7}$$

where "2p" means the detection of exactly two identified particles, and "np" the detection of any (n=1,2,3,...) amount of particles.

4.7 GOSIA analysis

In order to determine matrix elements in the isotopes of interest, the coupled-channels code GOSIA [Cli12] is used. The following list serves as an input for the GOSIA code:

1. The nuclear level scheme, limited to the relevant energy levels.
2. The matrix elements connecting the different levels.
3. A list of performed experiments, including information on the kinematics (beam energy, mass and proton number of projectile and target), energy loss in the target, the detector geometry of the DSSSD and the MINIBALL γ-ray spectrometer (and the detection efficiency of the latter), the observed count rates for the deexcitation paths. A single experiment can also be divided in different particle scattering angles, all covered by the DSSSD; these particle cuts can be declared as different experiments.
4. Nuclear-structure information like known branching ratios, conversion coefficients, mixing ratios, life times and matrix elements.

When a normalization to a certain target is necessary, this information is also given for the particular target employed.

The nuclear matrix elements are allowed to vary between declared limits. Based on the initial matrix elements, the excitation cross sections of the different nuclear levels are calculated. Moreover, the deexcitation count rates and the nuclear-structure information can be derived. A comparison is made between the obtained and the experimentally observed values for these quantities, and the total χ^2 is calculated. Then, the matrix elements are modified in order for the total χ^2 to decrease. This procedure is constantly repeated until the matrix elements reproduce the experimental count rates and nuclear quantities with the smallest possible total χ^2 value.

Chapter 5

X-ray production

5.1 Introduction

During last years, Coulomb-excitation experiments in inverse kinematics using heavy post-accelerated radioactive-ion beams have been initiated at the REX-ISOLDE facility, located at CERN. Beams of neutron-deficient mercury, lead, polonium and radon and neutron-rich radium and radon isotopes at energies around ~ 3 MeV/u were sent onto different targets like tin, silver, cadmium and palladium. As a result, low-lying excited states of the beam and/or the target are populated in multiple-step Coulomb excitation. The MINIBALL γ-ray spectrometer was used for the detection of γ rays originating from electromagnetic transitions in the investigated nuclei. The nuclear levels populated by Coulomb excitation do not only decay to a lower-lying energy level by emitting a γ ray, but also by conversion electrons. Especially $0_2^+ \rightarrow 0_1^+$ $E0$ deexcitations and $E0$ components of mixed multipolarity transitions are important in this region of the nuclear chart, due to the high proton number Z and nuclear-structure arguments. Different coexisting nuclear shapes are present in the nuclei under investigation. The quantum-mechanical wave functions of nuclear energy levels with the same spin and parity and corresponding to dissimilar shapes can mix, giving rise to an enhanced $E0$ transition rate between the levels [Woo92]. Moreover, in even-even nuclei featuring shape coexistence, the excited 0_2^+ state can have a very low excitation energy or even become the first excited state in the nucleus, decaying to the 0_1^+ ground state via an $E0$ transition.

a)

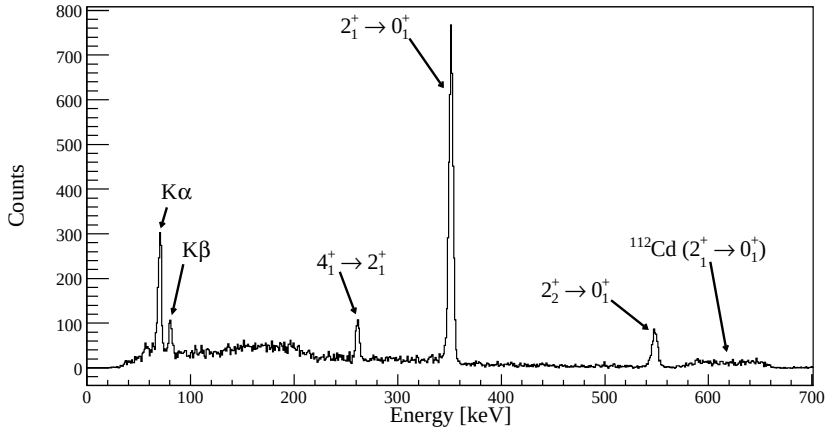

c)

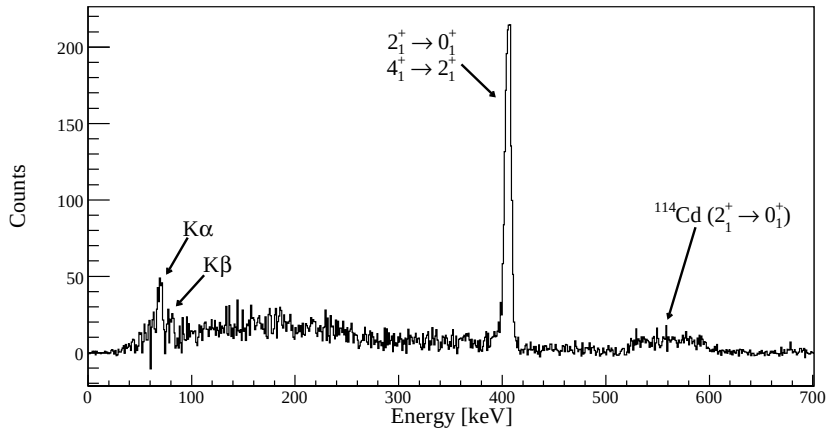

b)

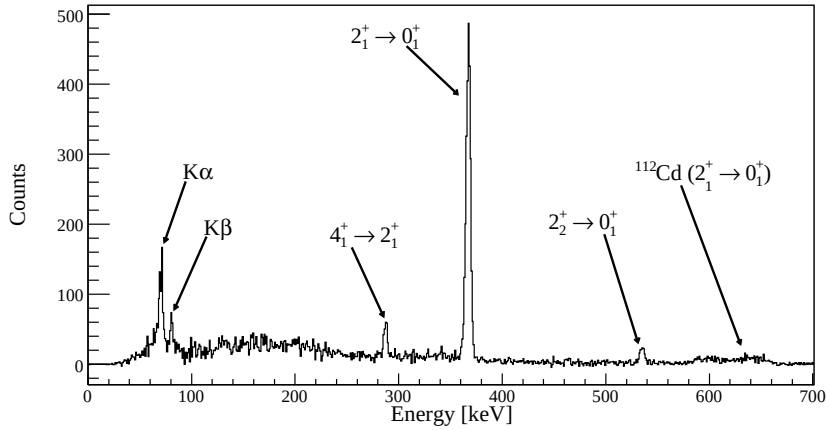

d)

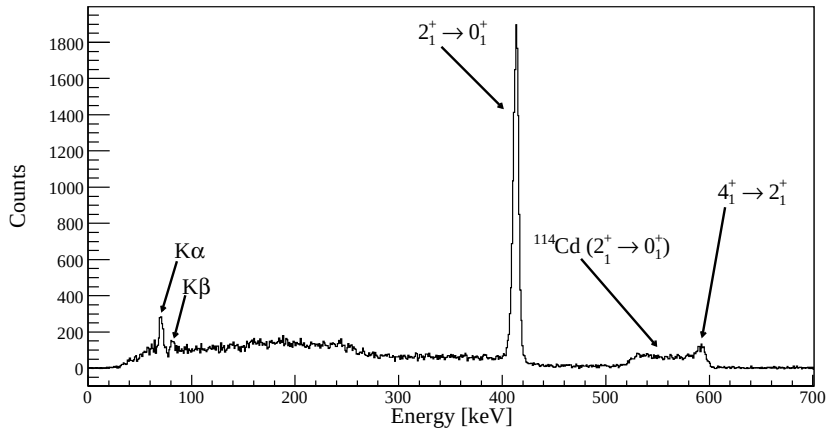

Figure 5.1: Random-subtracted photon spectra of ^{182}Hg (a), ^{184}Hg (b), ^{186}Hg (c), and ^{188}Hg (d), Doppler corrected for the mercury projectile excitation. Both collision partners were detected in coincidence in the DSSSD. The detector hereby covers the angular range {76.8°,142.6°}, expressed for the projectile in the centre-of-mass frame.

Hence, observed γ-ray intensities do not suffice to analyze Coulomb-excitation data in a proper way: the decay from populated levels involving electrons is crucial to be included in order to determine the correct population of these levels. Electron conversion is accompanied by the emission of characteristic X-rays. The MINIBALL γ-ray spectrometer can be used to detect the more energetic K X-rays, and after correction for the K-to-total ratio ($\approx 74\%$) and the fluorescence ($\approx 96\%$) of the transition, the total amount of decays via electrons can be estimated. However, also other atomic processes give rise to K-vacancy creation and thus to the production of X-rays. Moreover, the determination of the X-ray detection efficiency with MINIBALL has been investigated.

Random-subtracted photon spectra collected in coincidence with scattered mercury-beam and cadmium-target ions are shown in figure 6.14. These spectra have been corrected for the Doppler shift of the mercury projectile. The X-rays originating from the accelerator cavities, as well as those arising from β decay (or electron capture) are present in both prompt and random spectra, so they disappear in the random-subtracted spectrum. In these four spectra, mercury X-rays are clearly present. They are in prompt coincidence with two scattered particles, and a Doppler correction for the projectile needs to be applied, meaning that they come from the projectile in flight interacting with the target. The amount of X-rays compared to the $2_1^+ \rightarrow 0_1^+$ is significantly higher in ^{182,184}Hg than in ^{186,188}Hg. Note that the observed X-rays come from holes created in the K shell of the atom, which give rise to X-rays at 69 keV (K_α line) and 80 keV (K_β line) [Fir96]. The X-rays originating from electron vacancies created in higher-lying orbitals are too low in energy to be detected by the MINIBALL γ-ray spectrometer. After correction for the K_α intensity ratio and the fluorescence of the transition, the total amount of electronic decays can be gauged.

5.2 Heavy-ion induced K-vacancy creation

The number of observed X-rays in ^{188}Hg can be attributed to K-vacancy creation and the only X-rays originating from nuclear effects are those from the conversion of observed γ-ray transitions. The conversion of the observed $2_1^+ \rightarrow 0_1^+$ and $4_1^+ \rightarrow 0_2^+$ $E2$ transitions amounts to 43 (5) % of the total number of detected K X-rays when the ^{114}Cd target is used and decreases to 16 (1) % when a ^{182}Hg beam impinges on a ^{112}Cd target. The fraction of conversion-induced K X-rays originating from observed transitions to the total amount of detected K X-rays is presented in table 5.1 for the different mercury isotopes on the used targets.

Target	Isotope	Observed	Conversion	Ratio [%]
^{114}Cd	^{188}Hg	803 (83)	344 (24)	43 (5)
^{107}Ag	^{188}Hg	98 (25)	49 (4)	50 (13)
^{120}Sn	^{188}Hg	916 (87)	381 (26)	42 (5)
^{114}Cd	^{186}Hg	122 (34)	46 (3)	38 (11)
^{107}Ag	^{186}Hg	253 (38)	82 (6)	33 (5)
^{120}Sn	^{186}Hg	423 (59)	159 (11)	38 (6)
^{112}Cd	^{184}Hg	529 (45)	97 (6)	18 (2)
^{107}Ag	^{184}Hg	79 (16)	14 (1)	18 (4)
^{120}Sn	^{184}Hg	517 (42)	121 (7)	23 (2)
^{112}Cd	^{182}Hg	1017 (51)	167 (10)	16 (1)

Table 5.1: Total number of detected K X-rays with an energy of 69 keV and amount of conversion-induced K X-rays originating from observed $E2$ transitions.

The total cross section for K-shell ionization of a target atom by a colliding incident ion can be described by a universal form [Gar73], given by

$$\sigma = \frac{Z_p^2}{I_K^2} f(E_p/I_K), \tag{5.1}$$

where E_p and Z_p are respectively the energy and proton number of the incoming ion, I_K the binding energy of the K electron in the target and f the universal curve.

Romo-Kröger et al. deduced a phenomenological curve from this theoretical approach, based on the proton-induced K-vacancy created in any target atom [Rom05]. The cross section σ for K ionization by an incident proton is estimated by a fifth-order polynomial:

$$\ln(\sigma I_K^2) = \sum_{i=0}^{5} b_i (\ln(E_p/I_K))^i, \tag{5.2}$$

where $\{b_i\} = \{11.122, 0.6564, -0.5981, 0.0091, 0.0285, 0.006\}$. Here, E_p is given in MeV, I_K in keV, and the cross section σ in barn. The cross section for K-vacancy creation of a target atom irradiated by a heavy projectile with

proton number Z_p and atomic number A_p is derived from the proton-induced cross section by a scaling factor Z_p^2, as proposed in the theoretical formula:

$$\sigma_{\text{proj}}(E_p) = Z_p^2 \sigma_{\text{proton}}(E_p/A_p). \tag{5.3}$$

Thus, only the energy per nucleon of the beam appears in the calculation of the cross section for creating a K vacancy in the target atom. Also a correction of replacing I_K by$I_K^{0.95}$ on both sides of equation (5.2) is suggested, corresponding to an effective charge for the target being lower for heavier targets [Rom00].

In order to infer the cross section for K-vacancy production in the mercury projectile of interest in the Coulomb-excitation experiment, a change of frame of reference is needed. An incoming cadmium projectile should be considered, incident on a mercury target at rest, inducing a K vacancy. In both frames of reference the total energy in the centre-of-mass frame should be equal. In all systems with any projectile colliding with a target at rest, the total energy in the centre-of-mass frame is calculated to be [Ald75]:

$$E_{c.m.} = E_{lab,p} \frac{m_t}{m_p + m_t}, \tag{5.4}$$

where $E_{lab,p}$ is the energy of the incoming projectile, and m_p and m_t are the atomic masses of the incoming projectile and target respectively. When the reference frame the projectile and target are interchanged, and the calculated energy in the centre-of-mass frame should be equal, and this gives:

$$\frac{E_{lab,Cd}}{m_{Cd}} = \frac{E_{lab,Hg}}{m_{Hg}}, \tag{5.5}$$

implying that when going from the frame of reference where the cadmium is the target at rest to the one where the mercury is the target at rest, the energy of the incoming projectile per unit mass remains unaltered. Since in the experiments discussed in this paper, the mercury is incident on the cadmium with an energy of 2.85 MeV per nucleon, it is correct to calculate the cross sections for K-vacancy production in the mercury considering a cadmium projectile with an energy of 2.85 MeV per nucleon incident on a mercury atom at rest.

Considering experimentally inferred cross sections, it has been suggested by Foster et al. that when $E_p/I_K \leq 10^{-1}$ the measured values are lower than those predicted by theory [Fos76]. H.-H. Bencke et al. published experimentally determined K-vacancy production cross sections in projectile and target using ^{132}Xe and ^{208}Pb beams at energies of ∼3.6, ∼4.7 and ∼5.9 MeV per nucleon on

a broad scope of different targets [Beh79]. Projectile K-ionization cross sections for a ^{208}Pb beam with an energy of ∼2.4 MeV/u on some target atoms have been published by Anholt et al. [Anh76]. However, experimental values for the cross section of mercury K ionization are not reported, therefore they should be estimated.

The ratio between experimentally obtained cross sections for K-vacancy creation [Beh79, Anh76] and those theoretically predicted are shown in figure 5.2. The proton numbers of xenon (54) and cadmium (48) are similar, the latter being the atom of interest in this study. It is clear that around $Z = 80$, the ratios are considerably constant at a value of 0.06-0.08, slightly increasing with decreasing beam energy. Also the ratio between the experimentally obtained cross sections of the ^{208}Pb ($Z = 82$) atom undergoing K ionization on different atoms at the four mentioned energies and the theoretically predicted ones are shown. Again, around target proton number 48, the ratios are stable around 0.06-0.08, increasing with decreasing beam energy. For the particular Coulomb-excitation measurement of interest, a mercury beam energy of 2.85 MeV per nucleon was employed, so the presence of some data points at an energy of 2.4 MeV per nucleon is crucial to give an estimate. We adopt the value of 0.070±0.015 which the theoretical predicted calculation should be corrected for when estimating the cross section for K ionization in mercury when colliding with the cadmium target.

As only detected γ and X-rays are registered when coincident with a detected particle in the DSSSD, only a part of the total K ionization cross sections is measured, since the ions scattered outside the angular range covered by the DSSSD will not be present in the obtained γ-ray spectra. For this experiment, the detection range of the DSSSD in the laboratory frame extended from 18.7° to 51.6°, equivalent to 76.8° to 142.6° in the centre-of-mass frame. Differential cross sections for K-vacancy creation in ^{208}Pb by an incident ^{136}Xe beam at ∼4.7 MeV per nucleon have been obtained as a function of the impact parameter [Gre77]. Comparison with xenon beams at higher energies (∼4.6, ∼5.9, ∼7.2 and ∼8.5 MeV per nucleon) indicates that only the magnitude of the differential cross section is increasing when more energy is present, not affecting substantially its shape [Anh82]. Converting the differential cross sections as a function of the scattering angle in the centre-of-mass frame, one obtains the curve shown in figure 5.3. Integrating the differential cross section curve for K-vacancy production, a fraction of $\frac{\sigma_{76.8°-142.6°}}{\sigma_{0°-180°}}$ =0.13±0.01 can be inferred.

The predicted number of K vacancies induced by the colliding heavy ions, corrected for fluorescence and relative intensity of the K_α line, should be compared with the K_α X-ray count rate observed. Since the total number of particles incident on the target is inferred from the known B(E2:$0_1^+ \rightarrow 2_1^+$) value

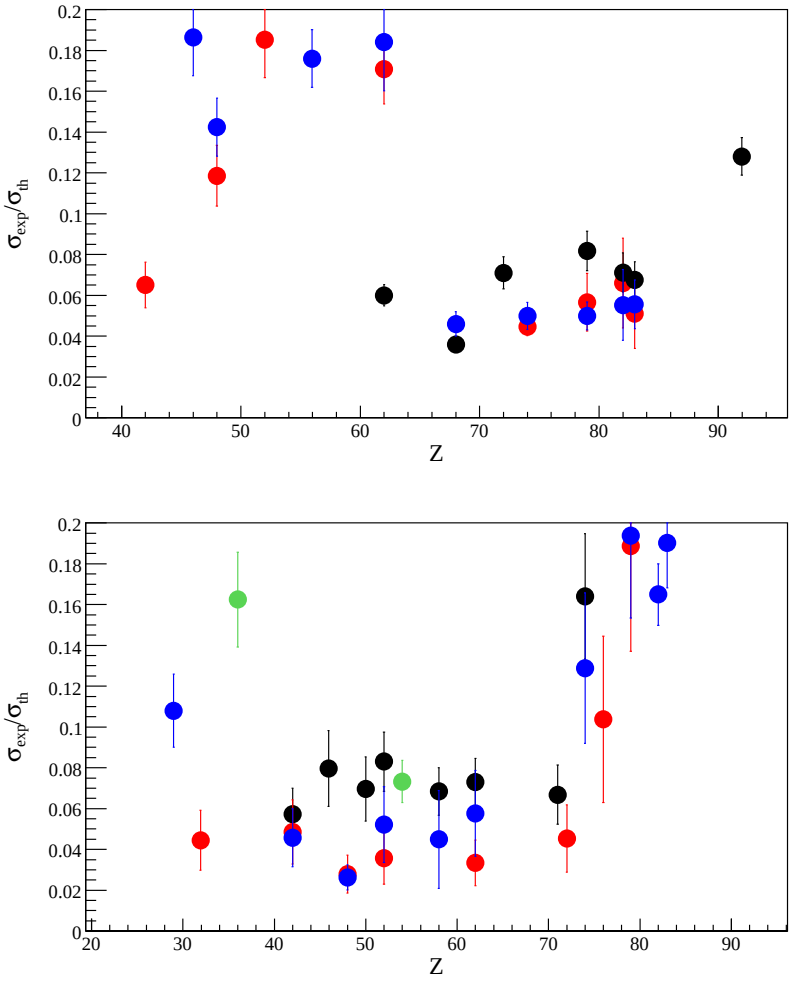

Figure 5.2: Ratios between experimental and theoretically predicted K-vacancy creation cross sections. Above: A ^{132}Xe projectile with an incident energy of ∼3.6 MeV/u (black), ∼4.7 MeV/u (red) and ∼5.9 MeV/u (blue) inducing a K vacancy in a target with proton number Z. Below: A ^{208}Pb projectile with an energy of ∼3.6 MeV/u (black), ∼4.7 MeV/u (red), ∼5.9 MeV/u (blue) and ∼2.4 MeV/u (green) in which a K vacancy is created when colliding with a target with proton number Z.

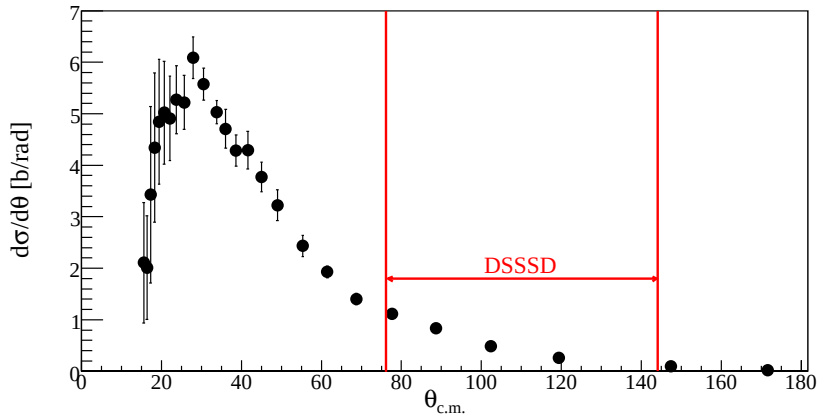

Figure 5.3: Differential cross section as function of the scattering angle in the centre-of-mass frame. The angular range covered by the DSSSD is indicated for the specific case of a ^{188}Hg projectile on a ^{114}Cd target.

in the cadmium target and the observed excitation to its first 2^+ state gives rise to a γ ray of 619 keV (^{112}Cd) or 558 keV (^{114}Cd), the energy-dependent γ-ray detection efficiency of the MINIBALL γ-ray spectrometer should be characterized.

5.3 The energy-dependent detection efficiency of MINIBALL

The MINIBALL γ-ray spectrometer is a detector array of eight clusters consisting each of three sixfold-segmented hyperpure-germanium (HPGe) crystals. In order to determine the full-energy γ-ray efficiency down to the K_α X-ray region, two calibration sources have been placed separately at the centre of the collision chamber inside the MINIBALL γ-ray spectrometer. The experimental intensities of the most intense γ rays originating from the decay of the ^{152}Eu and ^{133}Ba sources were compared to the ones predicted by the well-known decay patterns of these two sources, providing two relative efficiency curves for the two data sets as a function of the γ-ray energy. The γ rays with approximately the same energy as natural background radiation lines or those originating from contaminations were omitted. For ^{152}Eu, fourteen data points were taken into account with energies $E_i = \{122, 245, 296, 344, 368, 411, 444, 689, 779, 867,$

964, 1112, 1299, 1408} keV, and for ^{133}Ba, seven data point with energies E_i = {53, 80, 161, 223, 276, 303, 356} keV were considered [NND].

A coincidence method has been employed that enables the absolute efficiency curves to be inferred. When a certain path in the decay of the source contains a cascade of different γ rays, a gate was put on one of the γ rays, looking at the number of observed coincident γ rays to deduce their absolute detection efficiency, correcting for relative branchings and conversion coefficients.

For example, if a particular γ ray γ_1 can be followed by another γ ray γ_2, the absolute detection efficiency for γ_2 is expressed as

$$\epsilon_{\gamma_2} = \frac{N_{\gamma_2 \circ \gamma_1}}{N_{\gamma_1}} \cdot \frac{\sum_i^{\#paths} I_{\gamma_i}(1+\alpha_i)}{I_{\gamma_2}(1+\alpha_2)} \cdot (1+\alpha_2), \tag{5.6}$$

which reduces to

$$\epsilon_{\gamma_2} = \frac{N_{\gamma_2 \circ \gamma_1}}{N_{\gamma_1}} \cdot \frac{\sum_i^{\#paths} I_{\gamma_i}(1+\alpha_i)}{I_{\gamma_2}}, \tag{5.7}$$

where $N_{\gamma_2 \circ \gamma_1}$ is the number of detected γ_2's coincident with a detected γ_1, and N_{γ_1} the number of detected γ_1's without any coincidence condition. I_{γ_i} represents a the γ intensity of a possible decay channel from the level fed by γ_1. The sum loops over all possible absolute intensities depopulating that particular level. The factors $(1+\alpha)$, with α the total conversion coefficient for the transition, correct the γ intensities to become absolute decay intensities. By interchanging γ_1 and γ_2 in equation (5.7), the absolute detection efficiency for γ_1 can be deduced. The sum now loops over all the absolute intensities feeding the level that decays via γ_2.

Applying this method gives the absolute full-energy γ-detection efficiency at one particular energy point. Dividing the absolute by the relative efficiency at this energy yields a scaling factor with which the complete relative efficiency curve can be made absolute. The following cascades have been used to derive four scaling factors for ^{152}Eu.

An add-back procedure is applied at the cluster level, meaning that the energies of two γ rays incident in two germanium crystals of the same cluster are summed, supposing that they come from one single γ ray undergoing Compton scattering. This is only done if both signals have an energy above 100 keV. Hence, it is impossible to detect two coincident γ rays in one cluster. This effect of decreased efficiency when requiring coincidences is taken into account when calculating the scaling factor.

γ_2 [keV]	γ_1 [keV]	Scaling factor [a.u.]
122	245	6.84 (22)
245	122	6.84 (22)
344	789	7.40 (29)
789	344	6.94 (15)

Table 5.2: Scaling factors for four γ energies in ^{152}Eu. The absolute efficiency of γ_2 is calculated, demanding a coincidence with γ_1.

The cascades in ^{133}Ba used to infer the scaling factor for converting the relative efficiency curve into the absolute one are calculated the same way as for ^{152}Eu.

γ_2 [keV]	γ_1 [keV]	Scaling factor [a.u.]
81	303	2.86 (16)
303	81	2.63 (11)
81	356	2.81 (13)
356	81	2.81 (7)
53	303	2.21 (41)
303	53	3.27 (58)

Table 5.3: Scaling factors for four γ energies in ^{133}Ba. The absolute efficiency of γ_2 is calculated, demanding a coincidence with γ_1.

In ^{133}Ba, also a weaker γ transition at 80 keV is present, and in the calculations the intensities for the 81 keV γ line has been corrected for this. The add-back effect discussed previously does not need to be taken into account when studying coincidences with a 53 keV or 81 keV γ ray, since the condition for add-back implies that both γ rays have an energy above 100 keV. A weighted scaling factor of 2.77 (5) is found to obtain the ^{133}Ba absolute efficiency curve.

The absolute efficiencies for ^{133}Ba and ^{152}Eu obtained separately using the coincidence method are shown in figure 5.4, together with a fit expressing the

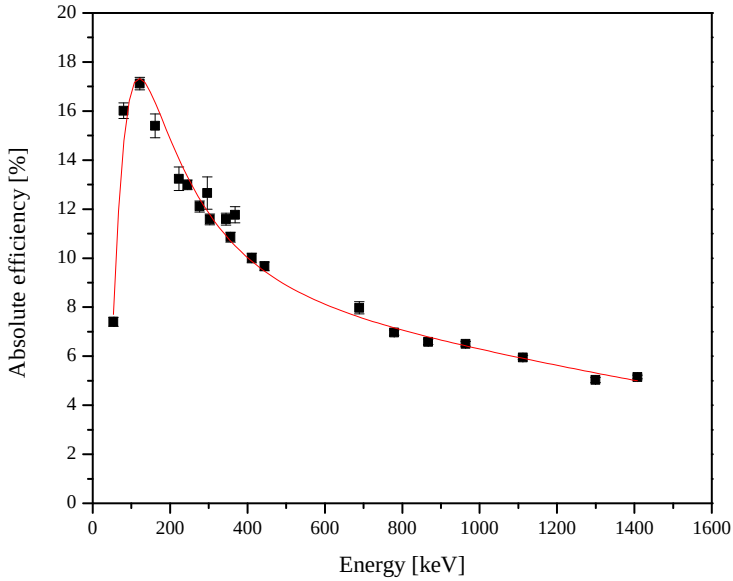

Figure 5.4: Fit combining the absolute efficiencies of ^{133}Ba and ^{152}Eu sources.

logarithm of the absolute efficiency as a function of the logarithm of the energy using a fourth grade polynomial, like in the following formula [Deb88].

$$\ln(\epsilon_\gamma) = \sum_{i=0}^{4} a_i \cdot \left[\ln(\frac{E_\gamma}{200})\right]^i. \tag{5.8}$$

By dividing the energy by 200, a reasonable error is insured for the whole energy range of interest. The obtained fit is shown in figure 5.4.

An alternative method for the determination of the absolute efficiency taking into account both data sets (on the two sources) curve is based on the suggestion that the absolute γ-detection efficiency at intermediate energies (200-1500 keV) can be parameterized using a linear relation between the logarithms of the efficiency and the energy:

$$\ln(\epsilon_\gamma) = a + b \cdot \ln(\frac{E_\gamma}{500}). \tag{5.9}$$

Here a = 2.204±0.011 and b = -0.550±0.017 for the ^{152}Eu data set. Dividing the energy by 500, a reasonable error is insured for this energy range.

The determination of the absolute efficiency curve can now be achieved by considering the absolute efficiency of the intermediate energy part of the ^{152}Eu data and then scaling the relative ^{133}Ba efficiency curve into the absolute ^{152}Eu efficiency curve. In order to obtain the latter, the data points of the relative ^{152}Eu efficiency curve are scaled with the weighted average of the four obtained scaling factors in table 5.2 (which equals 6.95 (10)), and then the point at 122 keV is omitted. The rescaled ^{152}Eu data points now represent absolute efficiencies.

The relative efficiency curve of the intermediate energy part of the ^{133}Ba data (223, 276, 303 and 356 keV) can then be fitted into the absolute ^{152}Eu efficiency curve using the formula

$$\ln(\epsilon_\gamma) = a' + b \cdot \ln(\frac{E_\gamma}{500}). \tag{5.10}$$

The slope of the curve b is demanded to be the same in the relative efficiency data on ^{133}Ba as in the absolute efficiency data on ^{152}Eu, the reason for this being that the relative ^{133}Ba data points should only be shifted by a constant to become absolute. The relative ^{133}Ba points are then scaled into the absolute ^{152}Eu efficiency curve. The linear function fit combining the intermediate energy part of the two sources is shown in figure 5.5. The remaining ^{152}Eu point at 122 keV can then be added, as well as the remaining low-energy points of ^{133}Ba. Hence, these obtained data points represent absolute efficiencies. Then a new fit is performed using the same parametrization as in expression (5.8) which is shown in figure 5.6.

The absolute efficiency curves inferred from the two methods are in agreement within the error bars. As an example efficiency values with errors are given in table 5.4 for different energies that are important in the performed Coulomb-excitation experiment.

For the analysis in this particular experiment the method of scaling the relative ^{133}Ba efficiency curve scaled to the absolute ^{152}Eu curve has been selected for the estimation of the analysis.

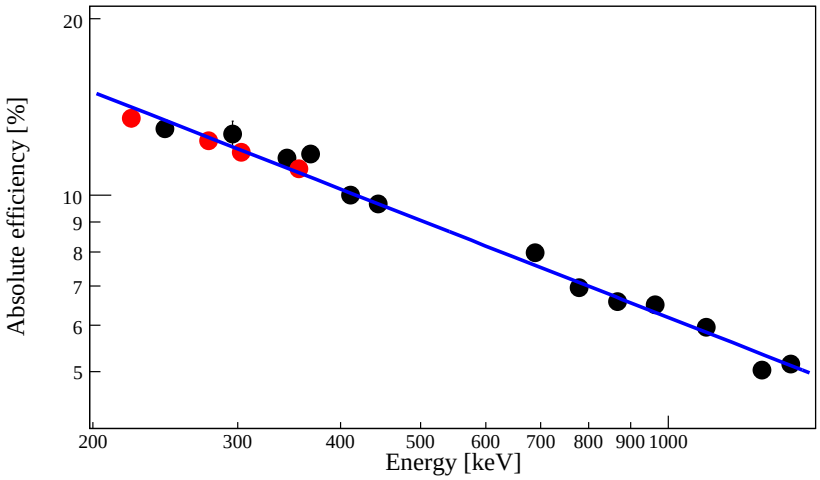

Figure 5.5: Linear fit for the intermediate energy part of the two sources with logarithmic scale for both axes. The ^{152}Eu data points are shown in black, those of ^{133}Ba in red.

E_γ [keV]	$\epsilon_{\gamma,scaled}$ [%]	$\epsilon_{\gamma,indep}$ [%]	Ratio
69	12.81 (81)	12.47 (80)	1.03 (9)
413	9.91 (35)	9.85 (36)	1.01 (5)
558	8.45 (50)	8.41 (50)	1.00 (8)

Table 5.4: Absolute efficiencies using the method of the relative ^{133}Ba curve scaled to the absolute ^{152}Eu curve and the method of the two independent efficiency curves. The mercury X-rays have an energy of 69 keV, the 2_1^+ state in ^{188}Hg lies at 413 keV and the 2_1^+ state in ^{114}Cd at 558 keV.

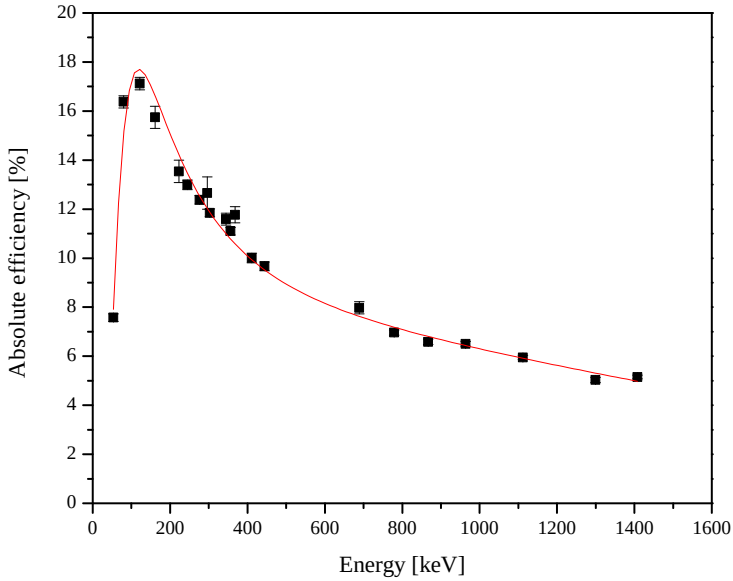

Figure 5.6: Fit combining the absolute efficiencies of ^{152}Eu and the scaled ^{133}Ba efficiencies.

One footnote has to be made however. The fitting procedure gives values for the parameters a_i with errors $\sigma(a_i)$. When calculating the efficiency at a certain energy E_γ, formula (5.8) is applied with the a_i's obtained from the fitting procedure. The error on the calculated efficiency is then given by:

$$\sigma(\epsilon_\gamma) = \epsilon_\gamma \cdot \sqrt{\sum_{i=0}^{4} \sigma^2(a_i) \cdot \left[\left[\ln(\frac{E_\gamma}{200})\right]^i\right]^2}. \tag{5.11}$$

However, when in the analysis of the performed experiment the integrals for two γ peaks need to be compared to obtain a ratio of intensities, only the relative efficiency is needed, and the error on a_0 can be omitted, since in both the numerator as in the denominator the factor e^{a_0} is canceled out due to the independence of the γ-ray energy.

5.4 X-rays detected by the MINIBALL γ-ray spectrometer

The cross sections for heavy-ion induced K-vacancy production in ^{188}Hg have been calculated taking into account the energy losses in the target, adjusted for the ratio between calculated and observed values and the limited detection range of the DSSSD. The results are summarized in table 5.5.

Target	Isotope	σ [barn]
^{114}Cd	^{188}Hg	0.139 (33)
^{107}Ag	^{188}Hg	0.144 (34)
^{120}Sn	^{188}Hg	0.155 (37)

Table 5.5: Estimated cross sections for K-vacancy production in ^{188}Hg for the three targets employed. The cross sections for the other mercury isotopes are very similar when the same target is used. Note that the cross sections for exciting one of the mercury isotopes to its 2_1^+ state using these targets amounts to a couple of barns.

These cross sections have to be corrected for the fluorescence and the relative branching for K_α emission at 69 keV.

The beam intensity is determined from the γ-ray intensities coming from the deexcitation of the ^{112,114}Cd and ^{107}Ag targets, which have been Coulomb excited. In the experiments with the ^{120}Sn target, no satisfactory target excitation was observed, therefore the beam intensity needed to be extracted from the number of observed $2_1^+ \rightarrow 0_1^+$ transitions in mercury, estimating its $\langle 0_1^+ \| E2 \| 2_1^+ \rangle$ matrix element from the experiments on cadmium. Table 5.6 shows the ratio of predicted and observed heavy-ion induced K X-rays at the energy of 69 keV per projectile-target combination. The number of observed K X-rays have been corrected for contributions from electron conversion of detected $E2$ γ-ray transitions. Also the efficiencies are taken into account.

Isotope	Target	Expected	Observed	Ratio [%]
^{188}Hg	^{114}Cd	709 (180)	459 (86)	65 (20)
^{188}Hg	^{107}Ag	98 (25)	49 (25)	50 (28)
^{188}Hg	^{120}Sn	1062 (264)	535 (91)	50 (15)
^{186}Hg	^{114}Cd	86 (22)	76 (34)	89 (46)
^{186}Hg	^{107}Ag	141 (35)	171 (41)	121 (42)
^{186}Hg	^{120}Sn	400 (100)	264 (60)	66 (22)
^{184}Hg	^{112}Cd	111 (29)	432 (45)	387 (109)
^{184}Hg	^{107}Ag	24 (6)	65 (16)	272 (97)
^{184}Hg	^{120}Sn	133 (33)	396 (43)	297 (80)
^{182}Hg	^{112}Cd	203 (53)	850 (52)	418 (111)

Table 5.6: Expected intensities of the 69 keV X-ray due to K-vacancy creation and observed intensities.

The agreement between calculated and observed X-rays is reasonable in the two heaviest isotopes where no $E0$ $0_2^+ \rightarrow 0_1^+$ or strongly converted $2_2^+ \rightarrow 2_1^+$ transition are expected. For the two lightest isotopes an excess of X-rays is observed and this can be attributed to the $E0$ component of the $2_2^+ \rightarrow 2_1^+$ transition and the $E0$ $0_2^+ \rightarrow 0_1^+$ deexcitation. The ratio of detected and expected K X-rays per projectile-target combination is presented in figure 5.7.

As cross sections in table 5.5 do not deviate significantly per target, the number of X-rays in ^{188}Hg corrected for the conversion of the observed γ transitions can be used to extract the experimental cross section for K-vacancy production. Since the reaction kinematics are dependent on the target used, three experimental cross sections are extracted for K-vacancy production in ^{188}Hg, which is then used to calculate the number of X-rays originating from K ionization in the lighter isotopes. Table 5.7 gives these experimental values.

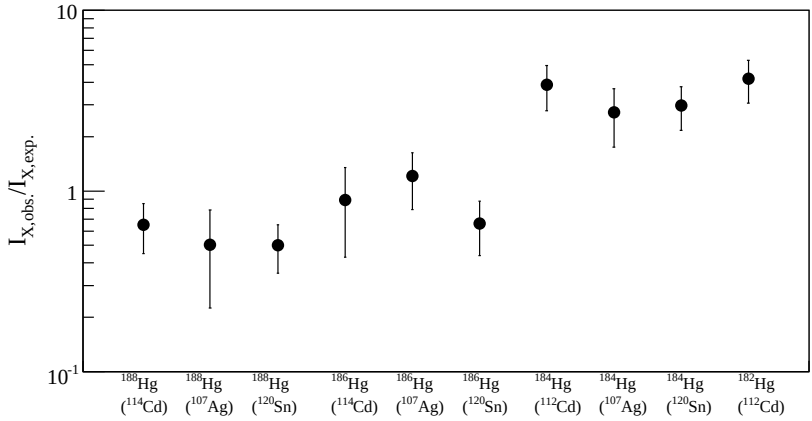

Figure 5.7: Ratio of observed and expected heavy-ion induced K X-rays are shown for the four mercury isotopes when incident on the different targets. In the lighter isotopes, the excess of K X-rays is significantly larger.

Target	σ_{exp} [barn]
^{112,114}Cd	0.090 (19)
^{107}Ag	0.077 (40)
^{120}Sn	0.073 (15)

Table 5.7: Experimental cross sections for heavy-ion induced K-vacancy creation deduced from the amount of X-rays presence in the data taken on ^{188}Hg per target.

The calculated amount of X-rays for all projectile-target combinations using the empirical cross section for ^{188}Hg are shown in table 5.8, together with the remaining X-rays (from which also the conversion from the known $E2$ transitions has been subtracted). The latter X-ray amount can then be attributed to the $E0$ component of the $2_2^+ \rightarrow 2_1^+$ transition and the $E0(0_2^+ \rightarrow 0_1^+)$ deexcitation.

Target	Isotope	K-vacancy X-rays	Remaining X-rays
^{114}Cd	^{188}Hg	459 (86)	none
^{107}Ag	^{188}Hg	98 (25)	none
^{120}Sn	^{188}Hg	535 (91)	none
^{114}Cd	^{186}Hg	55 (13)	21 (36)
^{107}Ag	^{186}Hg	70 (37)	100 (55)
^{120}Sn	^{186}Hg	202 (44)	62 (74)
^{112}Cd	^{184}Hg	72 (20)	360 (49)
^{107}Ag	^{184}Hg	12 (6)	53 (17)
^{120}Sn	^{184}Hg	67 (15)	328 (45)
^{112}Cd	^{182}Hg	129 (30)	721 (60)

Table 5.8: Calculated K-vacancy X-ray intensities employing the observed amount of X-rays in the data taken on ^{188}Hg for the determination of the K-vacancy cross section. This value is extrapolated per target to the lighter isotopes. The remaining X-rays in the last column can be attributed to the $E0$ component of the $2_2^+ \rightarrow 2_1^+$ transition and the $E0(0_2^+ \rightarrow 0_1^+)$ deexcitation.

Figure 5.8 shows the ratio between the amount of X-rays originating from heavy-ion induced K-vacancy creation and the number of X-rays observed in the different experiments, the latter corrected for conversion of observed $E2$ transitions.

Also spectra of X-rays coincident with the $2_1^+ \rightarrow 0_1^+$ transition in the different mercury isotopes have been investigated, and in case a Coulomb excitation to the 2_1^+ state takes place together with the creation of a K vacancy, the cross section can be calculated by combining the two cross sections with the formula

$$\sigma_{2_1^+ and K} = P_{2_1^+} \cdot P_K \cdot \sigma_{Ruth}, \tag{5.12}$$

where $\sigma_{2_1^+} = P_{2_1^+} \cdot \sigma_{Ruth}$ is the Coulomb-excitation cross section for the 2_1^+ state and $\sigma_K = P_K \cdot \sigma_{Ruth}$ is the cross section for K-vacancy creation. After subtraction of this predicted amount of K ionizations from the total mount of X-rays observed in the coincidence spectra, only X-rays originating from nuclear processes remain.

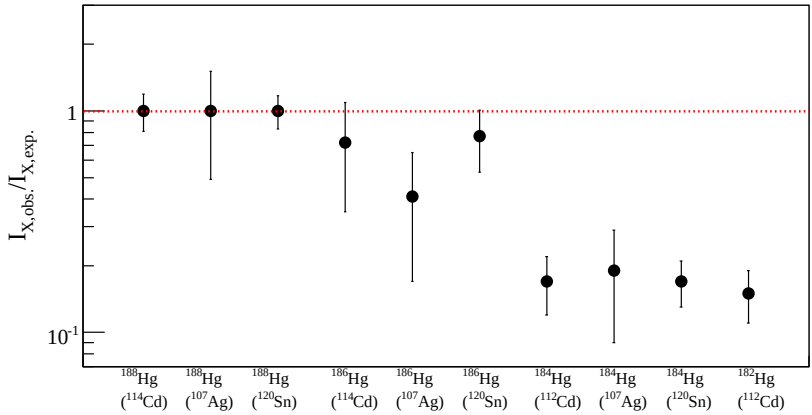

Figure 5.8: Ratio of X-rays originating from heavy-ion induced K-vacancy creation to the observed ones per projectile-target combination.

In ^{184}Hg, the spectra of γ rays coincident with the $2_1^+ \rightarrow 0_1^+$ indicate a surplus of X-rays that cannot be attributed to conversion from the $4_2^+ \rightarrow 2_1^+$ or other $E2$ transitions, suggesting that they originate from the $2_2^+ \rightarrow 2_1^+$ transition. However, a certain amount of X-rays still remains and can be interpreted as the $E0$ deexcitation of the 0_2^+ state. In ^{182}Hg, this effect is even more clearly present.

5.5 Conclusions

The atomic process of K-vacancy creation has been used to determine the origin of X-rays in the Coulomb-excitation experiments on ^{182,184,186,188}Hg. Comparing theoretical predictions with experimental evidence and correcting for the limited detection range of the employed particle detector gives the following estimation for the amount of detected K_α X-rays originating from K-vacancy production in the collision:

$$N_{K_\alpha,estim} = \epsilon_X S_{det} S_{exp} F I_{K_\alpha} Z_t^2 \frac{1}{(I_K^{0.95})^2} \exp\left[\sum_{i=0}^{5} b_i (\ln(E_p/I_K^{0.95}))^i\right] \frac{\rho d N_A}{A_t} \cdot I_b, \tag{5.13}$$

where ϵ_X is the absolute detection efficiency at 69 keV, S_{det} the angular fraction of the total cross section covered by the DSSSD (i.e. 0.13±0.01 for a ^{188}Hg projectile on a ^{114}Cd target), S_{exp} the accepted factor for decreasing theoretically calculated cross sections to empirical values (i.e. 0.070±0.015), F the fluorescence of mercury, I_{K_α} the relative intensity for K_α X-rays, Z_t the proton number of the target, I_K the binding energy of the K electron (in keV), b_i the parameters used in the phenomenological curve described in section 5.2, E_p the projectile energy per nucleon in the middle of the target (in MeV), ρ the target density, d the target thickness, N_A the Avogadro number, A_t the atomic mass of the target and I_b the total dose of incident projectile ions on the target. When assuming that there are no X-rays present in the experiments on ^{188}Hg that originate from nuclear effects (after subtraction of the conversion of known $E2$ transitions), all observed X-rays can be attributed to K-vacancy creation. The experimental K-vacancy intensities in the three experiments on ^{188}Hg relate to the estimated intensities in formula 5.13 as:

$$N_{K_\alpha,exp} = A \cdot N_{K_\alpha,estim}, \tag{5.14}$$

where $A = 0.65$ (20) for the experiment on ^{114}Cd, $A = 0.50$ (28) for the experiment on ^{107}Ag, and $A = 0.50$ (15) for the experiment on ^{120}Sn.

Chapter 6

Results

6.1 The ^{182}Hg case

6.1.1 Intensity of the observed transitions

As described in chapter 3, only one experiment was carried out to investigate the ^{182}Hg isotope, whereby a 2.0 mg/cm^2 ^{112}Cd foil was employed as a target to induce Coulomb excitation. The detected particle scattering range can be divided into different angular ranges by gating on the individual annular strips of the DSSSD. As explained in section 4.4, the gate is always put on the ^{112}Cd target, and a second particle is demanded to lie in the corresponding ^{182}Hg scattering range. Since γ-ray statistics are too low when gating on individual strips, broader scattering ranges have been employed by adding the γ-ray spectra of neighbouring strips. A satisfying compromize between statistics and the need for angular sensitivity is found when three scattering ranges are used, i.e. a low angle c.m. range summing the γ-ray spectra gating on annular strips 0 to 4, an intermediate angle range combining strips 5 to 9, and a high angle range covering strips 10 to 14. Strip 15 of the DSSSD is omitted due to a malfunction in one of the quadrants. This does not imply a big loss of statistics, since strip 15 is located at high c.m. range, where the excitation cross section for both projectile and target is low. Figure 6.1 shows the random-subtracted γ-ray spectrum Doppler corrected for the mercury projectile coincident with two identified particles, for the three angular particle ranges. Their sum gives the full statistics spectrum.

a)

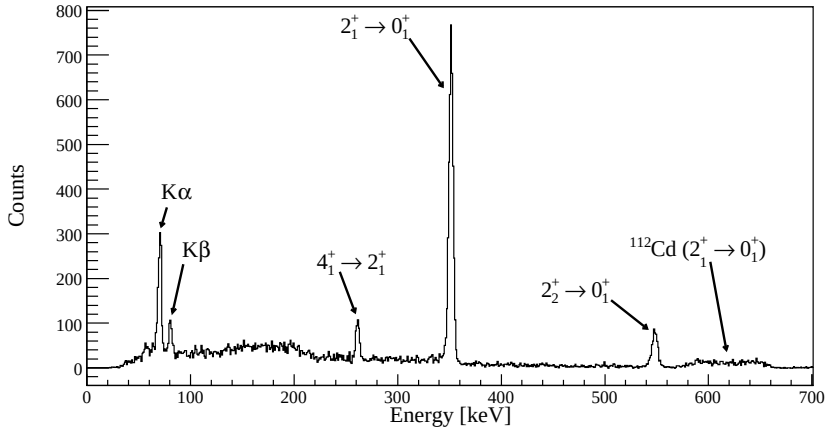

c)

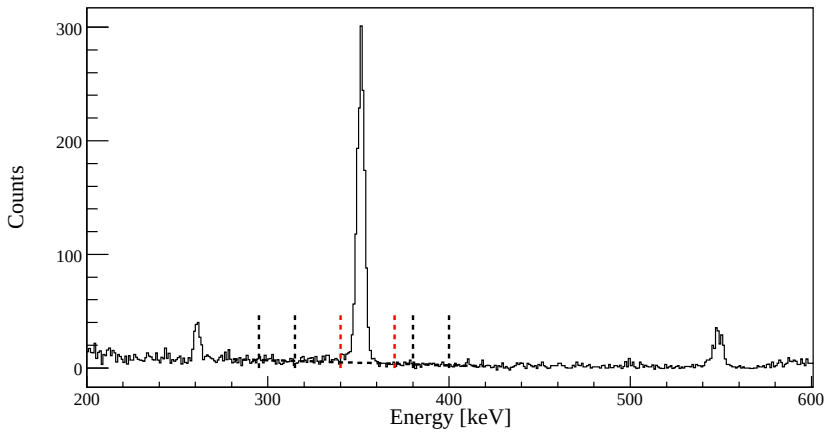

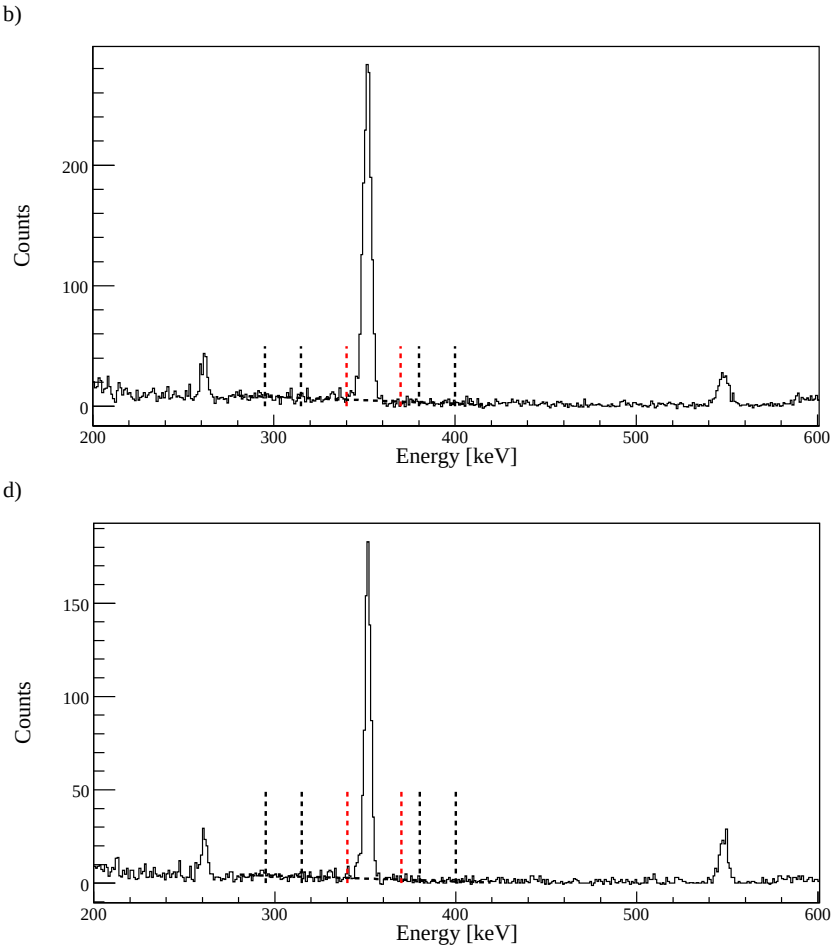

Figure 6.1: a) Random-subtracted γ-ray spectrum Doppler corrected for the mercury projectile coincident with two identified particles. The observed photo peaks are identified as the $2_1^+ \rightarrow 0_1^+$, the $4_1^+ \rightarrow 2_1^+$ and the $2_2^+ \rightarrow 0_1^+$ deexcitations. Also prompt X-rays are detected with an energy around 69 keV. The γ-rays around 619 keV originating from the $2_1^+ \rightarrow 0_1^+$ deexcitation in ^{112}Cd are Doppler broadened. b) c) and d) Idem, but the particles are in one of the three scattering ranges: low (b), intermediate (c) and high (d) c.m. angles. The way of taking the integrals is shown in these three spectra.

Figure 6.2 shows the same spectrum, but Doppler corrected for the ^{112}Cd target particle. An important remark is that this is exactly the same spectrum as the one shown in figure 6.1(a). Only this time, the γ rays are Doppler corrected for the other coincident particle, which is assumed to be the ^{112}Cd target. The integrated photo peak intensities are summarized in table 6.1. Also the amount of K_α and K_β X-rays can be estimated: they are presented in table 6.2.

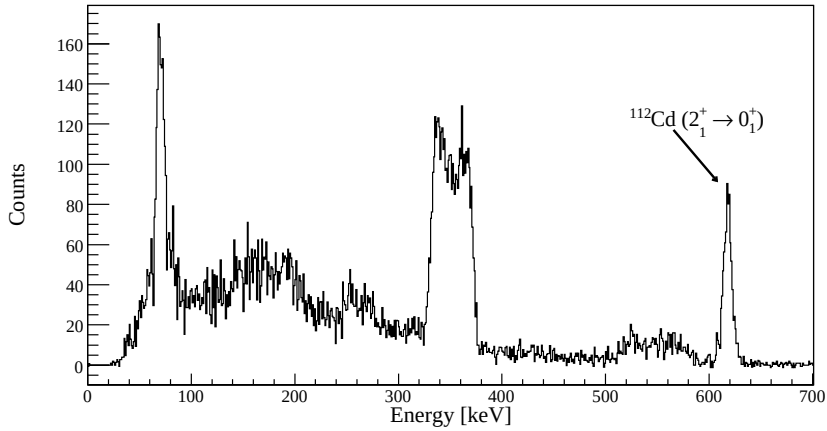

Figure 6.2: Idem as figure 6.1(a), but with a Doppler correction for the ^{112}Cd target particle. Now the deexcitations in ^{182}Hg are Doppler broadened.

The ratio of K_α to K_β X-rays is known to equal 3.6 in the mercury isotopes [Fir96], independent of how the K vacancy has been produced. Considering the total angular detection range, table 6.2 gives a ratio of 4.2 (7), which is in good agreement with the expected value.

The integrated photo peak intensities for transitions observed in ^{112}Cd are given in table 6.3.

$I_i \to I_f$	E_γ [keV]	$\theta_{lab,t}[^\circ]$	$\theta_{c.m.}[^\circ]$	I_γ	$\epsilon_{\gamma,abs}[\%]$	$I_{\gamma,tot}$
$2_1^+ \to 0_1^+$	352	18.7 - 51.6	76.8 - 142.6	3812 (68)	10.85 (24)	35120 (1004)
		43.6 - 51.6	76.8 - 92.8	1552 (43)		14298 (512)
		32.9 - 43.6	92.8 - 114.2	1482 (42)		13654 (494)
		18.7 - 32.8	114.4 - 142.6	778 (31)		7168 (325)
$2_2^+ \to 0_1^+$	549	18.7 - 51.6	76.8 - 142.6	556 (27)	8.52 (47)	6522 (481)
		43.6 - 51.6	76.8 - 92.8	182 (17)		2158 (231)
		32.9 - 43.6	92.8 - 114.2	232 (16)		2722 (243)
		18.7 - 32.8	114.4 - 142.6	140 (14)		1642 (186)
$4_1^+ \to 2_1^+$	261	18.7 - 51.6	76.8 - 142.6	319 (42)	12.97 (12)	2460 (323)
		43.6 - 51.6	76.8 - 92.8	116 (27)		895 (206)
		32.9 - 43.6	92.8 - 114.2	119 (26)		918 (198)
		18.7 - 32.8	114.4 - 142.6	84 (19)		648 (147)

Table 6.1: The integrated photo peak intensities I_γ are given for the three observed transitions in ^{182}Hg for the total angular range and the three particle gates. Using the absolute photo peak γ efficiencies $\epsilon_{\gamma,abs}$, the total amount of γ rays $I_{\gamma,tot}$ can be estimated, its error being the combination of errors on I_γ and on $\epsilon_{\gamma,abs}$. The relation between the angles in the laboratory frame and the centre-of-mass system is discussed in section 4.3.

X-rays	E_X [keV]	$\theta_{lab,t}[^\circ]$	$\theta_{c.m.}[^\circ]$	I_X	$\epsilon_{\gamma,abs}[\%]$	$I_{X,tot}$
K_α	≈ 69	18.7 - 51.6	76.8 - 142.6	1017 (51)	12.81 (78)	7941 (630)
		43.6 - 51.6	76.8 - 92.8	323 (33)		2522 (299)
		32.9 - 43.6	92.8 - 114.2	401 (31)		3131 (309)
		18.7 - 32.8	114.4 - 142.6	293 (24)		2288 (236)
K_β	≈ 80	18.7 - 51.6	76.8 - 142.6	285 (39)	8.03 (56)	1888 (271)
		43.6 - 51.6	76.8 - 92.8	85 (25)		563 (171)
		32.9 - 43.6	92.8 - 114.2	107 (24)		709 (163)
		18.7 - 32.8	114.4 - 142.6	86 (17)		570 (114)

Table 6.2: The integrated X-ray intensities I_X are given for the total angular range and the three particle gates. I_X represents the intensity observed in the random-subtracted photon spectrum, not corrected for efficiency, nor for X-rays originating from conversion or heavy-ion induced K-vacancy creation, nor for $E0$ transitions. $I_{X,tot}$ equals I_X divided by the efficiency.

$I_i \rightarrow I_f$	E_γ [keV]	$\theta_{lab,t}[^\circ]$	$\theta_{c.m.}[^\circ]$	I_γ	$\epsilon_{\gamma,abs}[\%]$	$I_{\gamma,tot}$
$2_1^+ \rightarrow 0_1^+$	619	18.7 - 51.6	76.8 - 142.6	858 (31)	8.03 (56)	10682 (829)
		43.6 - 51.6	76.8 - 92.8	375 (20)		4669 (408)
		32.9 - 43.6	92.8 - 114.2	325 (19)		4046 (359)
		18.7 - 32.8	114.4 - 142.6	158 (13)		1967 (212)

Table 6.3: The integrated photo peak intensities I_γ are given for the observed $2_1^+ \rightarrow 0_1^+$ transition in ^{112}Cd for the total angular range and the three particle gates. $I_{\gamma,tot}$ equals I_γ divided by the efficiency.

6.1.2 Intensity of the $\gamma - \gamma$ coincidences

6.1.2.1 Construction of the γ-ray spectra

According to the procedure described in section 4.6, the amount of γ rays coincident with the $2_1^+ \rightarrow 0_1^+$ transition can be estimated when gating on the γ rays around an energy of 352 keV, i.e. the energy region between 335 keV and 365 keV. An estimation of the coincidences with γ rays having an energy slightly lower or higher than this energy region is also needed. Therefore two energy windows were selected: the range between 300 keV to 330 keV and the range between 370 keV and 400 keV. Following the procedure in section 4.6.1, we can construct three different γ_2-ray spectra, dependent on the γ_1-ray energy range. Note that we define γ_1 as the γ ray on which was gated: it is the γ ray around 352 keV. γ_2 is the γ ray in coincidence with it.

If the time difference between γ_1 and its coincident particle lies between -900 ns and -600 ns (i.e. a prompt coincidence between γ_1 and the particle) and the time difference between γ_1 and γ_2 is less that 300 ns, the event is considered a prompt-prompt $\gamma_1 - \gamma_2$ coincidence.

However, if γ_1 is in random coincidence with a particle (the time difference lies between -1350 ns and -900 ns), and the time difference between γ_1 and γ_2 is less than 300 ns, the event is defined as a random-prompt event, due to the fact that the γ_1 is in random coincidence with a particle, but γ_2 is in prompt coincidence with γ_1. These events should be rescaled by a factor $\frac{2}{3}$ (the particle random window is larger than the particle prompt) and subtracted from the prompt-prompt events.

In the case that γ_1 is in prompt coincidence with a particle (their time difference lies between -900 ns and -600 ns), but γ_2 is found to be outside of the 300 ns $\gamma - \gamma_2$ coincidence window (but between 400 ns and 700 ns), the event is called prompt-random, due to the particle-γ_1 prompt coincidence but the random coincidence between the γ's. These events should also be subtracted from the prompt-prompt events. A rescaling is not necessary, since both $\gamma_1 - \gamma_2$ time windows have a width of 300 ns.

The $\gamma_1 - \gamma_2$ events which are defined as random-random have both a random coincidence with a particle (the time difference lies between -1350 ns and -900 ns) and a random coincidence between the γ rays (there is a time separation of more than 300 ns between them). They do not have to be subtracted from the prompt-prompt events, since none of these events are possibly present in the prompt-prompt spectrum.

6.1.2.2 Extraction of the singles integrals

Applying the construction of the $\gamma - \gamma$ ray spectrum described above, figure 6.3 shows the γ rays coincident with the $2_1^+ \rightarrow 0_{g.s.}^+$ γ transition at 352 keV. The first spectrum shows the coincident γ_2 rays of the prompt-prompt events minus the (rescaled) random-prompt events minus the prompt-random events when the gate on γ_1 is put around 352 keV (335 - 365 keV). The two other spectra show the same spectrum but here the γ_1 gate is placed at slightly lower (300 - 330 keV) and slightly higher energies (370 - 400 keV).

Three transitions are observed in the first spectrum: the $4_1^+ \rightarrow 2_1^+$ transition with an energy of 261 keV, a trace of the $2_2^+ \rightarrow 2_1^+$ transition at 197 keV and the K X-rays. Table 6.4 shows the integrals of the transitions in the three spectra above, together with the final integral. The calculation of the latter is described in section 4.6.1.

Following the procedure discussed in section 4.6.2, the integral of the $4_1^+ \rightarrow 2_1^+$ γ transition is compared to its integral in the full γ-ray spectrum, the latter being the random subtracted γ-ray spectrum Doppler-corrected for ^{182}Hg, gating on any cadmium particle with the ^{182}Hg particle incident in the corresponding angular range. This ratio for the $4_1^+ \rightarrow 2_1^+$ γ transition,

$$R_{4_1^+ \rightarrow 2_1^+} = I_{4_1^+ \rightarrow 2_1^+, coin} / I_{4_1^+ \rightarrow 2_1^+, singles} = 0.26(5), \tag{6.1}$$

is then used to convert the intensities of the transitions observed in the coincidence spectrum to the total two-particle γ-ray spectrum. The converted integrals are presented in table 6.5. One has to note here that, since the ratio $R_{4_1^+ \rightarrow 2_1^+}$ has been defined using the $4_1^+ \rightarrow 2_1^+$ transition, the full integral of this transition has been directly taken from the full γ-ray spectrum. For the other two transitions, the ratio $R_{4_1^+ \rightarrow 2_1^+}$ has been used to make the conversion.

The amount of 139 (60) counts originating from the $2_2^+ \rightarrow 2_1^+$ transition has not been observed in the full γ-ray spectrum, due to the presence of the Compton edge of the $2_1^+ \rightarrow 0_{g.s.}^+$ γ transition, lying at an energy of 204 keV.

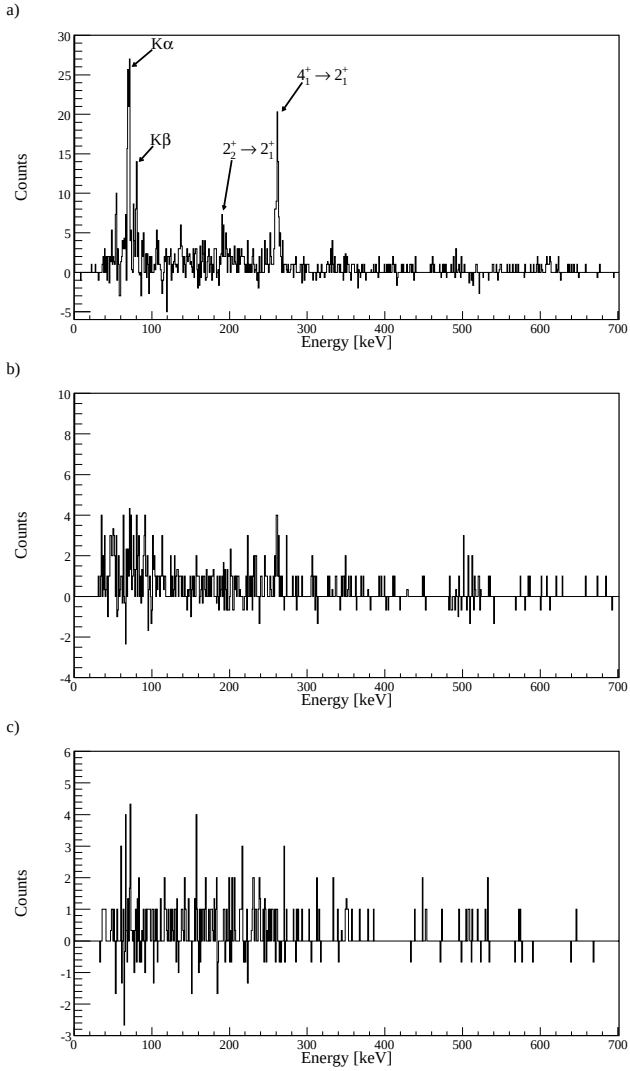

Figure 6.3: a) Spectrum of the γ rays coincident with a γ_1 ray around 352 keV (within the range 335 - 365 keV). b) and c) Idem, but the γ_1 ray energy window is slightly lower (within a range of 300 - 330 keV) or higher (within a range of 370 - 400 keV). The γ rays in these three spectra are Doppler corrected for the ^{182}Hg projectile.

Transition	E_γ [keV]	Integral centre	Integral left	Integral right	Total integral
$4_1^+ \rightarrow 2_1^+$	261	90 (11)	17 (5)	-2 (4)	83 (12)
$2_2^+ \rightarrow 2_1^+$	197	30 (12)	-9 (8)	-3 (6)	36 (14)
K_α	69	79 (14)	0 (6)	11 (5)	74 (15)

Table 6.4: Integrals of the three observed transitions in the constructed coincidence spectra, together with the calculated total integral.

Transition	E_γ [keV]	Integral in coincidence	Integral in full spectrum
$4_1^+ \rightarrow 2_1^+$	261	83 (12)	319 (42)
$2_2^+ \rightarrow 2_1^+$	197	36 (14)	139 (60)
K_α	69	74 (15)	284 (80)

Table 6.5: Calculation of the photo peak intensity in the full γ-ray spectrum from the observed integral in the spectrum of γ rays coincident with the $2_1^+ \rightarrow 0_{g.s.}^+$ γ transition at 352 keV.

Concerning the amount of K_α X-rays, a short recapitulation of section 5.4 might be useful. The amount of observed K_α X-rays in the full spectrum amounts to 1017 (51). The section also explains the creation of K_α vacancies due to a heavy-ion collision, which is responsible for 129 (30) counts. Also electron conversion from other observed transitions are present in the full K_α X-ray photo peak: 138 (9) counts originate from the $2_1^+ \rightarrow 0_{g.s.}^+$ transition, 20 (3) counts from the $4_1^+ \rightarrow 2_1^+$ transition and 9 (1) from the $2_2^+ \rightarrow 0_{g.s.}^+$ transition. Subtracting the electrons due to the heavy-ion vacancy creation and to conversion from known transitions, the remaining amount of K_α X-rays is 721 (60). This amount can be attributed purely to $E0$ transitions. In the coincidence spectrum, X-rays originating from heavy-ion K_α vacancy creation are present as well, estimated by the formula

$$\sigma_{2_1^+ and K} = P_{2_1^+} \cdot P_K \cdot \sigma_{Ruth}, \tag{6.2}$$

where $\sigma_{2_1^+} = P_{2_1^+} \cdot \sigma_{Ruth}$ is the Coulomb-excitation cross section for the 2_1^+ state and $\sigma_K = P_K \cdot \sigma_{Ruth}$ is the cross section for K-vacancy creation. From the 74 (15) K_α X-rays observed in the coincidence spectrum, 9 (2) can be attributed to this atomic process. The electron conversion from the 83 (12) observed $4_1^+ \rightarrow 2_1^+$ in the coincidence spectrum amounts to 5 (1) K_α's. After subtraction of these two sources of electrons, an amount of 60 (15) K_α X-rays remain in the coincidence spectrum, which are due to a purely nuclear process in coincidence with the $2_1^+ \rightarrow 0_{g.s.}^+$ transition. Using the ratio $R_{4_1^+ \rightarrow 2_1^+}$, its integral in the full γ-ray spectrum can be estimated to be 231 (74). This count rate is suggested to arise from the $E0$ component of the $2_2^+ \rightarrow 2_1^+$ transition. When subtracting these 231 (74) counts from the total amount of 721 (60) K_α X-rays emerging from $E0$ transitions, 490 (95) counts remain which are attributed to the $E0$ deexcitation of the 0_2^+ state.

Since, in the further analysis, the total count rate of these two deexcitation paths is needed, these values need to be corrected for the K_α branching and the fluorescence. These values can be found in section 5.2.

Table 6.6 summarizes the photo peak intensities in the full γ-ray spectrum, derived from the observed count rates in the coincidence spectra. All conversions and corrections mentioned above have been applied here.

Transition	Corrected integral in full spectrum
$\gamma(2_2^+ \rightarrow 2_1^+)$	139 (60)
$E0(2_2^+ \rightarrow 2_1^+)$	325 (104)
$E0(0_2^+ \rightarrow 0_1^+)$	690 (134)

Table 6.6: Full γ-ray spectrum photo peak intensities derived from the coincidence spectra, after corrections.

It is important to emphasize that the $E0$ count rates give the total intensities, including non-fluorescent deexcitation and other electron paths than the K_α channel.

6.1.3 Combined information on ^{182}Hg

6.1.3.1 Life times

In two articles, Grahn et al. [Gra09] and Scheck et al. [Sch10] have published life times of the yrast states with positive parity and even spin up to spin 10^+. Table 6.7 summarizes the life times of the states relevant for the analysis of the Coulomb-excitation data.

Nuclear state I^π	Life time τ [ps]
2_1^+	42.1 (23)
4_1^+	37.1 (11)
6_1^+	9.1 (9)

Table 6.7: Measured life times of the 2_1^+, 4_1^+ and 6_1^+ yrast states in ^{182}Hg from.

6.1.3.2 Branching ratios and conversion coefficients

From a ^{182}Tl β decay experiment, Rapisarda et al. [Rap] have determined branching ratios and a conversion coefficient in ^{182}Hg that can be used in the analysis of the Coulomb-excitation data. Table 6.8 presents the extracted values. The last column of the table represents the information from the Coulomb-excitation data. These are taken from the total spectrum of γ rays coincident with two identified particles, and thus without any particle cuts. In order to estimate the $\frac{\gamma(2_2^+ \to 2_1^+)}{\gamma(2_2^+ \to 0_1^+)}$ branching ratio and the $\frac{e^-(2_2^+ \to 2_1^+)}{\gamma(2_2^+ \to 2_1^+)}$ conversion coefficient,the information originating from the spectrum of γ rays coincident with the $2_1^+ \to 0_{g.s.}^+$ γ transition has been converted to the total γ-ray spectrum, as described in section 6.1.2.2.

It is clear that the measured values from the ^{182}Tl β decay experiment are in good agreement with the values extracted from the Coulomb-excitation γ-ray spectrum. Moreover, including the measured branching ratios and the conversion coefficient will refine the further analysis substantially, due to smaller uncertainties. Also the unobserved $2_2^+ \to 0_2^+$ transition can now be estimated since the $\frac{\gamma(2_2^+ \to 0_2^+)}{\gamma(2_2^+ \to 0_1^+)}$ branching ratio is known.

$\frac{I_i \to I_{f_1}}{I_i \to I_{f_2}}$	Ratio from ^{182}Tl β decay [Rap]	Ratio from Coulomb excitation
$\frac{\gamma(2_2^+ \to 2_1^+)}{\gamma(2_2^+ \to 0_1^+)}$	0.088 (32)	0.14 (6)
$\frac{\gamma(2_2^+ \to 0_2^+)}{\gamma(2_2^+ \to 0_1^+)}$	0.065 (23)	<0.09
$\frac{\gamma(2_3^+ \to 2_1^+)}{\gamma(2_3^+ \to 0_2^+)}$	0.70 (22)	unknown
$\frac{e^-(2_2^+ \to 2_1^+)}{\gamma(2_2^+ \to 2_1^+)}$	4.7 (13)	3.2 (17)

Table 6.8: Information on the branching ratios and the conversion coefficient in ^{182}Hg. The last column shows these values extracted from the total Coulomb-excitation γ-ray spectrum.

6.1.3.3 Summary

For the analysis of the Coulomb-excitation experiment on ^{182}Hg the following information will be used:

1. The extracted integrals from the Coulomb-excitation γ-ray spectra. The photo peak intensities can be found in table 6.1, including the integrals when gating on three different angular particle cuts.
2. The extracted integrals of the $2_2^+ \to 2_1^+$ γ transition, and the calculated intensities of the $E0(2_2^+ \to 2_1^+)$ and $E0(0_2^+ \to 0_1^+)$ transitions in the total γ-ray spectrum. These can be found in table 6.6.
3. The life times of the 2_1^+, 4_1^+ and 6_1^+ states, presented in table 6.7.
4. The measured branching ratios relevant for the further analysis and the conversion coefficient of the $2_2^+ \to 2_1^+$ transition, given in table 6.8.

6.1.4 GOSIA analysis

The program GOSIA will be employed in order to acquire information on the $E2$ matrix elements connecting the nuclear low-energy states in ^{182}Hg. Section 6.1.3.2 emphasized the agreement between known measured branching ratios

and the ones observed in the Coulomb-excitation data. However, in order to verify whether the known life times mentioned in section 6.1.3.1 are compatible with the data obtained from the Coulomb-excitation experiment, GOSIA can be used first without the information on the life times in order to estimate preliminary matrix elements. These matrix elements can be converted into life times, according to formula 2.30. It is therefore appropriate to first perform a GOSIA calculation without inclusion of the known life times.

GOSIA1 has to be used when treating a set of data where more than two nuclear states are involved. It treats all matrix elements relatively to one another: there is no absolute normalization to the target. In the case of an even-even nucleus, the matrix elements calculated in a GOSIA1 minimization are all normalized to one specific matrix element, i.e. $\langle 0_1^+ \| E2 \| 2_1^+ \rangle$. Due to the absence of absolute normalization to the target, this matrix element served as an input for the GOSIA1 analysis.

As a consequence, the $\langle 0_1^+ \| E2 \| 2_1^+ \rangle$ matrix element needs to be known in order to obtain correct results for the other matrix elements involved in the analysis. Since a comparison to the known life times is aimed at, the $\langle 0_1^+ \| E2 \| 2_1^+ \rangle$ has to be extracted from the Coulomb-excitation experiment itself. For this purpose, a simplified level scheme of ^{182}Hg only containing the 0_1^+ ground state and the first excited 2_1^+ state can be used to perform a direct calculation of the $\langle 0_1^+ \| E2 \| 2_1^+ \rangle$ matrix element. No branching ratios or additional data are included here.

6.1.4.1 First approximation of $\langle 0_1^+ \| E2 \| 2_1^+ \rangle$

When demanding the detection of two coincident particles, a gate is placed on the detected cadmium ion and the angular range is divided in three ranges: a low c.m. angular range (cadmium detected in strips 0 to 4), an intermediate range (cadmium detected in strips 5 to 9) and a high c.m. range (cadmium detected in strips 10 to 14). Strip 15 is not included, since this strip was only working for three of the four quadrants, and excitation for both projectile and target is scarce. Figure 4.6.b showed the two-particle events in the ^{182}Hg experiment.

It is clear that the mercury incident in strips 13 to 15 is not present, since the trajectory of the coincident cadmium particle lies outside the detection coverage of the particle detector. The observed $2_1^+ \rightarrow 0_1^+$ γ intensities for the ^{182}Hg projectile and for the ^{112}Cd target are given in table 6.9.

Since GOSIA includes the correction for the γ ray detection efficiency, the errors of the efficiency have to be taken into account. This is the reason why the errors on the integrals of the observed transitions in table 6.9 differ from those in tables 6.1 and 6.3.

$\theta_{lab,t}[^\circ]$	$I_\gamma(2_1^+ \to 0_1^+)$ in ^{182}Hg	$I_\gamma(2_1^+ \to 0_1^+)$ in ^{112}Cd
43.6 - 51.6	1552 (56)	375 (33)
32.9 - 43.6	1482 (54)	325 (29)
18.7 - 32.8	778 (35)	158 (17)

Table 6.9: The integrated photo peak intensities I_γ are given for the observed $2_1^+ \to 0_1^+$ transition in ^{182}Hg and in ^{112}Cd for the three angular particle gates.

The cadmium energy rises with its strip number, and the corresponding mercury energy decreases, going from strip 12 to strip 7 bending back to higher strip number at lower mercury energies. When following this path, the c.m. angle for both cadmium and mercury increases.

Now the $\langle 0_{g.s.}^+ \| E2 \| 2_1^+ \rangle$ and $\langle 2_1^+ \| E2 \| 2_1^+ \rangle$ matrix elements in ^{182}Hg need to be estimated. This has been accomplished using GOSIA1 for the calculation of cross sections in both projectile and target nucleus. No minimizations were performed here. Assuming a certain $\langle 2_1^+ \| E2 \| 2_1^+ \rangle$ in ^{182}Hg, the $\langle 0_{g.s.}^+ \| E2 \| 2_1^+ \rangle$ in ^{182}Hg can be calculated according to formula 2.24 and it should be constant over the three angular ranges. Figure 6.4 shows this procedure.

A value between 0 and 1 for the $\langle 2_1^+ \| E2 \| 2_1^+ \rangle$ matrix element can be assumed, yielding a $\langle 0_{g.s.}^+ \| E2 \| 2_1^+ \rangle$ value of approximately 1.2.

Also the program GOSIA2 can be used to perform a direct calculation. GOSIA2 extracts the three excitation cross sections for the first 2_1^+ state in the target nucleus, one per angular particle range. These three values are compared to the three deexcitation yields of the 2_1^+ state in ^{112}Cd, yielding three absolute normalization constants. In the minimization, the $\langle 0_{g.s.}^+ \| E2 \| 2_1^+ \rangle$ and $\langle 2_1^+ \| E2 \| 2_1^+ \rangle$ in ^{182}Hg are then varied until they reproduce the three deexcitation yields of the 2_1^+ state in ^{182}Hg. However, in order to estimate the errors on the matrix elements correctly, it is better to do a GOSIA2 calculation of the reduced χ_ν^2 per combination of $\langle 0_{g.s.}^+ \| E2 \| 2_1^+ \rangle$ and $\langle 2_1^+ \| E2 \| 2_1^+ \rangle$ in ^{182}Hg and plot this in a two-dimensional graph, as shown in figure 6.5.

These reduced χ_ν^2's are the sum of the reduced χ_ν^2's calculated in the projectile and in the target.

A minimum of the reduced χ_ν^2 is found when $\langle 0_{g.s.}^+ \| E2 \| 2_1^+ \rangle = 1.24$ and

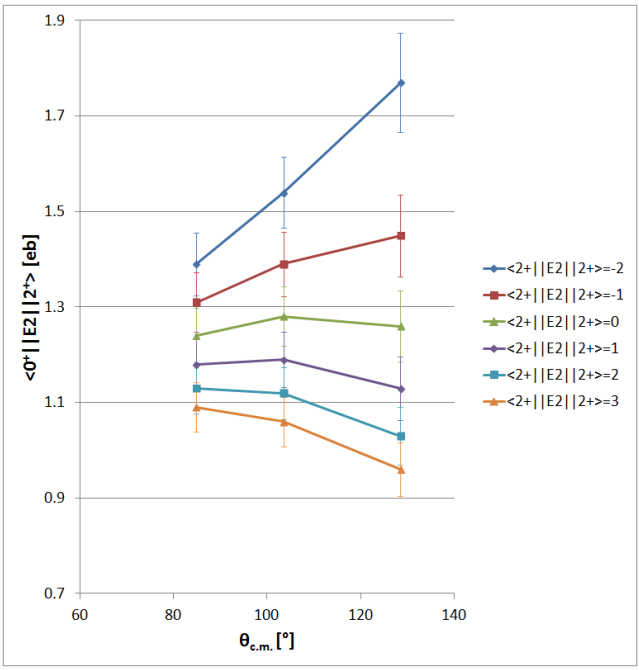

Figure 6.4: The $\langle 0^+_{g.s.} \| E2 \| 2^+_1 \rangle$ matrix element in ^{182}Hg for the three angular ranges, assuming different integer values of the $\langle 2^+_1 \| E2 \| 2^+_1 \rangle$ matrix element in this nucleus.

$\langle 2^+_1 \| E2 \| 2^+_1 \rangle = 0.2$. By increasing the minimal χ^2 (not the reduced χ^2_ν) by 1, 1σ statistical uncertainties on both matrix elements can be found. For the statistic used in GOSIA, the following formula can be found:

$$\chi^2_\nu = \frac{\chi^2}{\#\text{ degrees of freedom}}, \tag{6.3}$$

where the amount of degrees of freedom equals the amount of angular cuts [Cli12].

The reduced χ^2_ν two-dimensional plot with only values of χ^2_ν where $\chi^2 < \chi^2_{\text{min}} + 1$ is shown in figure 6.6.

By consequence the obtained values from this first analysis are $\langle 0^+_{g.s.} \| E2 \| 2^+_1 \rangle = 1.24\ (10)$ and $\langle 2^+_1 \| E2 \| 2^+_1 \rangle = 0.2\ (10)$.

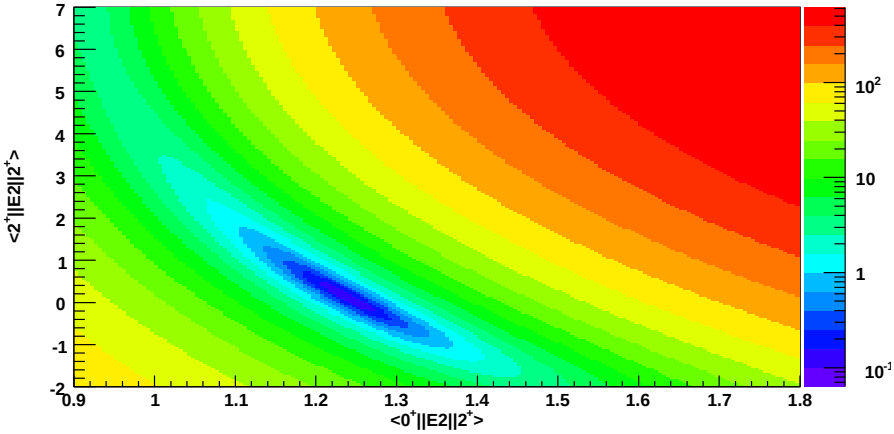

Figure 6.5: Reduced χ^2_ν surface assuming different values of the $\langle 0^+_{g.s.}\|E2\|2^+_1\rangle$ and $\langle 2^+_1\|E2\|2^+_1\rangle$ in ^{182}Hg.

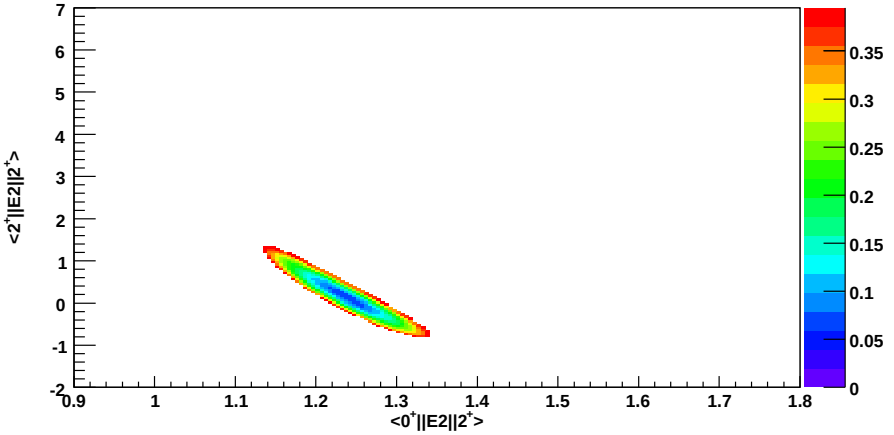

Figure 6.6: Reduced χ^2_ν surface with the condition $\chi^2 < \chi^2_{\min} + 1$, enabling error bars for $\langle 0^+_{g.s.}\|E2\|2^+_1\rangle$ and $\langle 2^+_1\|E2\|2^+_1\rangle$ to be estimated.

6.1.4.2 Further analysis in GOSIA1

The specific input in the GOSIA1 analysis without inclusion of the life times, is discussed in this section.

6.1.4.2.1 The energy level scheme

Table 6.10 presents the included nuclear levels, together with their spins, parities and energies. Figure 6.7 visualizes the level scheme of ^{182}Hg.

I^π	Energy [keV]
0_1^+	0
0_2^+	335
2_1^+	352
2_2^+	548
4_1^+	613
6_1^+	946
2_3^+	974
4_2^+	1125

Table 6.10: Nuclear levels included in the analysis.

Also two non-existing nuclear states with spin and parity 1^+ have been included at energies of 266 keV and 479 keV. This is necessary for the treatment of the observed $E0$ transitions between the 2_2^+ and 2_1^+ states and the 0_2^+ and 0_1^+ states. The next paragraph will elaborate on this issue.

6.1.4.2.2 The matrix elements

The declaration of matrix elements allows GOSIA1 to vary them in order to reproduce the observed data. Table 6.11 shows which matrix elements are used in the calculations.

The $E2$ matrix elements will always be expressed in units of eb, the $M1$ matrix elements in units of the nuclear magneton μ_N. Since no deexcitation of the 6_1^+, 2_3^+ and 4_2^+ states has been observed in the Coulomb-excitation data, these states serve here as buffer states. This means that GOSIA1 can allow them to be populated, not giving rise to a deexcitation that is strong enough to be observed in the Coulomb-excitation spectra. In this analysis, the 2_3^+ state is only interacting with the 0_2^+ and 2_1^+ state, since only this branching is known and the 2_3^+ state is not observed in the Coulomb-excitation experiment. This means also that excitations to that state can only happen via the two states

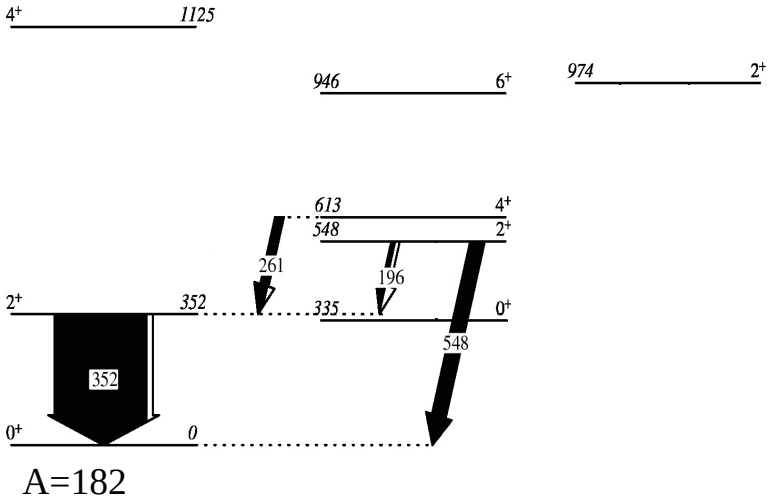

Figure 6.7: Scheme of the nuclear levels at low energy in ^{182}Hg. Black arrows indicate observed transitions in the total γ-ray spectrum of the Coulomb-excitation experiment, their relative thicknesses being related to their observed intensities.

to which it is connected. This has to be done in order not to create too many degrees of freedom combined with insufficient information.

Since GOSIA1 does not include $E0$ transitions, a way to get round the observed electron decay paths has to be found. A possibility has been advocated to deviate the electrons via non-existing $M1$ transitions. The two 1^+ states mentioned in the previous paragraph can be used for this. Four extra matrix elements need to be declared, which are presented in table 6.12

These $M1$ matrix elements allow for the deexcitation of the 0_2^+ and 2_2^+ states to occur via another path than the $E2$ connections given in table 6.11. The excitation process via $M1$ is very unlikely compared with $E2$ excitation, so the $M1$ connection between the states is a good alternative for $E0$. It is however important to notice that table 6.11 also includes a real $M1$ matrix element between the two 2^+ states. Indeed, the deexcitation via γ-ray emission can be either $M1$ or $E2$ (or $M3$ or $E4$). That way, the $M1$ deexcitation path from the 2_2^+ state to the 2_1^+ state can be distinguished from the $E0$ path, represented by two subsequent $M1$ transitions in GOSIA.

ME
$\langle 0_1^+ \| E2 \| 2_1^+ \rangle$
$\langle 0_1^+ \| E2 \| 2_2^+ \rangle$
$\langle 0_2^+ \| E2 \| 2_1^+ \rangle$
$\langle 0_2^+ \| E2 \| 2_2^+ \rangle$
$\langle 0_2^+ \| E2 \| 2_3^+ \rangle$
$\langle 2_1^+ \| E2 \| 2_1^+ \rangle$
$\langle 2_1^+ \| E2 \| 2_2^+ \rangle$
$\langle 2_1^+ \| E2 \| 4_1^+ \rangle$
$\langle 2_1^+ \| E2 \| 2_3^+ \rangle$
$\langle 2_1^+ \| E2 \| 4_2^+ \rangle$
$\langle 2_2^+ \| E2 \| 2_2^+ \rangle$
$\langle 2_2^+ \| E2 \| 4_1^+ \rangle$
$\langle 4_1^+ \| E2 \| 4_1^+ \rangle$
$\langle 4_1^+ \| E2 \| 6_1^+ \rangle$
$\langle 2_1^+ \| M1 \| 2_2^+ \rangle$

Table 6.11: Matrix elements that can be varied by GOSIA1 to reproduce the observed data.

ME
$\langle 0_1^+ \| M1 \| 1_1^+ \rangle$
$\langle 1_1^+ \| M1 \| 0_2^+ \rangle$
$\langle 2_1^+ \| M1 \| 1_2^+ \rangle$
$\langle 1_2^+ \| M1 \| 2_2^+ \rangle$

Table 6.12: Non-existing $M1$ matrix elements that are used to replace the $E0$ deexcitations.

The two 1^+ states have been defined in a way that the energy difference between the 1_1^+ state and 0_2^+ state and the energy difference between the 1_2^+ state and 2_2^+ state exactly equal 69 keV, the energy of the K_α X-ray. This simplifies the

GOSIA input since no corrections for efficiency are needed. The fluorescence and K_α branching had to be corrected for.

The known branching ratios and the conversion coefficient mentioned in section 6.1.3.2 will also be included in the GOSIA1 analysis.

6.1.4.2.3 Coulomb-excitation data

The input for the GOSIA1 from the Coulomb-excitation experiment consists of four different experiments: the first three are the particle angular cuts in which the data have been subdivided, the fourth one is the total angular range. In each experiment certain γ-ray (or X-ray) intensities are given.

The first three experiments are normalized to each other. This means that GOSIA1 is first used to compare the three calculated deexcitation rates from the $2_1^+ \rightarrow 0_{g.s.}^+$ γ transition in ^{112}Cd in the three angular particle cuts to the observed integrals. GOSIA1 then gives three normalization constants as an output, linking these three experiments to one another. It is important to notice that this does not give an absolute normalization to the target, only a relative normalization between the three angular particle cuts. Dividing for example the three normalization constants by the same factor, would not influence the further analysis. The comparison with the observed transitions in ^{112}Cd in order to perform a correct normalization is necessary, due to differences in particle detection efficiency in these three particle cuts.

In order to calculate the normalization constants, the integrals of the $2_1^+ \rightarrow 0_{g.s.}^+$ γ transition in ^{112}Cd need to be given as an input to GOSIA1, as presented in the last column of table 6.9. The error on the efficiency has been calculated and then included in the error of the observed transition. Here, this is done merely for clarity, since the output consists of the three normalization constants without an error. These can be used as an input in the GOSIA1 minimization on ^{182}Hg. The observed transitions in ^{182}Hg are summarized in table 6.13.

Again, the error bars on the integrals are larger compared to the ones prestented in table 6.1. This is because not only the error on the γ-ray detection efficiency needs to be included, but also the statistical error on the $2_1^+ \rightarrow 0_{g.s.}^+$ γ transition in ^{112}Cd (and the error on its γ-ray detection efficiency as well), due to the absence of error bars on the normalization constants.

Due to the absence of an absolute normalization to the target, the value of the $\langle 0_1^+ \| E2 \| 2_1^+ \rangle$ matrix element derived in section 6.1.4.1 will be included in the analysis. The $\langle 2_1^+ \| E2 \| 2_1^+ \rangle$ will not be included, since it is implicitly present in the relative normalization constants. After further analysis including other nuclear states, the $\langle 0_1^+ \| E2 \| 2_1^+ \rangle$ and $\langle 2_1^+ \| E2 \| 2_1^+ \rangle$ matrix elements can differ

$I_i \rightarrow I_f$	E_γ [keV]	$\theta_{lab,t}[^\circ]$	I_γ
$2_1^+ \rightarrow 0_1^+$	352	43.6 - 51.6	1552 (147)
$2_2^+ \rightarrow 0_1^+$	549		184 (26)
$4_1^+ \rightarrow 2_1^+$	261		116 (29)
$2_1^+ \rightarrow 0_1^+$	352	32.9 - 43.6	1482 (144)
$2_2^+ \rightarrow 0_1^+$	549		232 (29)
$4_1^+ \rightarrow 2_1^+$	261		119 (28)
$2_1^+ \rightarrow 0_1^+$	352	18.7 - 32.8	778 (92)
$2_2^+ \rightarrow 0_1^+$	549		140 (22)
$4_1^+ \rightarrow 2_1^+$	261		84 (21)

Table 6.13: The integrated photo peak intensities I_γ are given for observed transitions in ^{182}Hg for the three angular particle gates.

from those obtained in section 6.1.4.1, due to the presence of other excitation and deexcitation paths.

The $2_2^+ \rightarrow 2_1^+$ γ transition is not observed in the three angular particle cuts due to its low statistics. Furthermore, no angular particle cuts can be made for the $E0(2_2^+ \rightarrow 2_1^+)$ transition, since its intensity needs to be extracted from the spectrum coincident with the $2_1^+ \rightarrow 0_{g.s.}^+$ γ transition. Also, the $E0(0_2^+ \rightarrow 0_1^+)$ transition depends on the intensity of the $E0(2_2^+ \rightarrow 2_1^+)$ transition, as discussed in section 6.1.2.2. As a consequence, the intensities of these three transitions should be given in the fourth experiment, covering the total angular range. These are given in table 6.14.

However, a remark on the $E0(2_2^+ \rightarrow 2_1^+)$ and $E0(0_2^+ \rightarrow 0_1^+)$ transitions has to be made. The $E0(2_2^+ \rightarrow 2_1^+)$ is characterized in GOSIA1 by two data points: firstly, the measured intensity in the Coulomb-excitation spectrum, which is derived from the γ ray spectrum coincident with the $2_1^+ \rightarrow 0_{g.s.}^+$ transition, and secondly the intensity calculated from the observed $2_2^+ \rightarrow 0_{g.s.}^+$ intensity combined with the $\frac{\gamma(2_2^+ \rightarrow 2_1^+)}{\gamma(2_2^+ \rightarrow 0_1^+)}$ branching ratio and the $\frac{e^-(2_2^+ \rightarrow 2_1^+)}{\gamma(2_2^+ \rightarrow 2_1^+)}$ conversion coefficient. On the other hand, the $E0(0_2^+ \rightarrow 0_1^+)$ transition is only characterized by one data point, being the difference between the total number of $E0$ transitions and those originating from the $E0(2_2^+ \rightarrow 2_1^+)$ transition, the latter taken from

the Coulomb-excitation spectra. As a consequence, a new data point for the $E0(0_2^+ \rightarrow 0_1^+)$ transition can be added by subtracting the calculated number of $E0(2_2^+ \rightarrow 2_1^+)$ transitions (from the branchings and the conversion coefficient) from the total amount of $E0$ transitions. This yields an intensity of 555 (138). Calculating the weighted average with the already mentioned number of 690 (134) counts from table 6.6 gives an intensity of 624 (96).

$I_i \rightarrow I_f$	E_γ [keV]	$\theta_{lab,t}[^\circ]$	I_γ
$2_1^+ \rightarrow 0_1^+$	352	18.7 - 51.6	3812 (68)
$2_2^+ \rightarrow 2_1^+$	196		139 (60)
$2_2^+ \rightarrow 1_2^+$	69		325 (104)
$0_2^+ \rightarrow 1_1^+$	69		624 (96)

Table 6.14: The integrated photo peak intensities I_γ and I_X are given for observed transitions in ^{182}Hg for the total angular particle range.

This last experiment is not normalized to any other. Therefore no additional error due to the statistical uncertainties in the $2_1^+ \rightarrow 0_{g.s.}^+$ γ transition in ^{112}Cd has to be added. This can be interpreted as if the $2_1^+ \rightarrow 0_{g.s.}^+$ γ transition in ^{182}Hg were characterized by the first three experiments, and the fourth experiment serves to normalize additional observed transitions to the known $2_1^+ \rightarrow 0_{g.s.}^+$ γ transition in ^{182}Hg. This is also the reason why the intensity of the $2_1^+ \rightarrow 0_{g.s.}^+$ γ transition should be given in the fourth experiment. Moreover, the uncertainty on the γ detection efficiency of the $2_1^+ \rightarrow 0_{g.s.}^+$ γ transition in ^{182}Hg can be omitted, since the other transitions already include that efficiency error by the way the coincidence spectrum has been constructed and the integrals in it have been extracted.

The total angular range of the fourth experiments covers in fact the three angular particle cuts of the three first experiments. Since due to the condition of always having two coincident particles, the particle detection efficiency can alter with changing particle angle. This can cause small incorrectnesses, since GOSIA1 treats the angular range of the fourth experiment as if it would maintain the same particle detection effiency throughout its entire angular range. If the particle detection efficiency were constant, dividing the $2_1^+ \rightarrow 0_{g.s.}^+$ γ transitions in ^{112}Cd in the three angular cuts by calculated deexcitations, should yield a constant factor. However this is not the case here. A way to cope with this

is to define a limited azimuthal detection range for two of the three angular ranges within the total angular range of the fourth experiment. The angular range with the highest particle detection efficiency is then defined to have a fully working particle detector with an azimuthal coverage of 360°, the other two angular ranges working with an azimuthal coverage that is lower. Figure 6.8 shows this correction for this experiment.

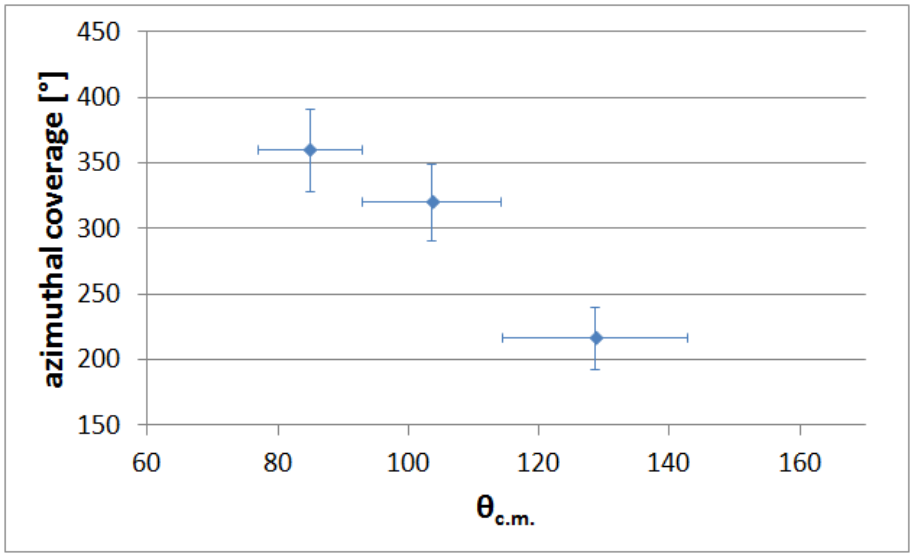

Figure 6.8: The three particle ranges have different efficiencies for simultaneously detecting a mercury projectile and a cadmium target. This can be coped with by declaring in GOSIA1 that for certain angular ranges no full azimuthal coverage of 360° was achieved. Here the low c.m. range (i.e. where the cadmium is detected under a large laboratory scattering angle) has the highest detection efficiency.

A detection limit of 30 counts has been included in the fourth experiment, meaning that GOSIA1 can never calculate matrix elements in such a way that they would give rise to transitions with a higher count rate than 30 counts which are not declared as observed transitions in the analysis. To make sure that observed transitions which are only declared in the first three experiments are not blocked by the detection limit in experiment four, they are also declared in the latter, but with a large error bar so they do not contribute to the minimization. The integral of the $2_2^+ \rightarrow 0_{g.s.}^+$ γ transition will therefore be declared as being 556 (10000), the one of the $4_1^+ \rightarrow 2_1^+$ γ transition being 319 (10000). Also the deexcitation of the 1_2^+ state to the 2_1^+ and of the 1_1^+ state to

the 0_1^+, which are the only possible deexcitations of these states, will be declared with the same intensities as their feeding transitions, but with a large error bar. This is done for reasons of minimization speed. The $2_2^+ \rightarrow 0_2^+$ γ transition will also be declared with an error bar that makes the integral statistically insignificant. This is done since the detection limit around that energy will be approximately three times higher than 30, due to the presence of the Compton edge of the $2_1^+ \rightarrow 0_{g.s.}^+$ γ transition. This is also reflected in the upper limit for the branching ratio in table 6.8.

6.1.4.2.4 Results

The resulting values for the matrix elements in ^{182}Hg are found in table 6.15.

ME	Obtained value [eb or μ_N]
$\langle 0_1^+ \| E2 \| 2_1^+ \rangle$	$1.24^{0.09}_{0.08}$
$\langle 0_1^+ \| E2 \| 2_2^+ \rangle$	$0.40^{0.02}_{0.03}$
$\langle 0_2^+ \| E2 \| 2_1^+ \rangle$	$-1.87^{0.14}_{0.12}$
$\langle 0_2^+ \| E2 \| 2_2^+ \rangle$	$1.08^{0.17}_{0.20}$
$\langle 0_2^+ \| E2 \| 2_3^+ \rangle$	$-0.67^{0.61}_{0.44}$
$\langle 2_1^+ \| E2 \| 2_1^+ \rangle$	$0.81^{1.14}_{0.83}$
$\langle 2_1^+ \| E2 \| 2_2^+ \rangle$	$1.43^{0.24}_{0.55}$
$\langle 2_1^+ \| E2 \| 4_1^+ \rangle$	$-3.83^{0.33}_{0.34}$
$\langle 2_1^+ \| E2 \| 2_3^+ \rangle$	$-0.60^{1.78}_{0.85}$
$\langle 2_1^+ \| E2 \| 4_2^+ \rangle$	$0.00^{1.60}_{1.60}$
$\langle 2_2^+ \| E2 \| 2_2^+ \rangle$	$8.39^{0.70}_{1.05}$
$\langle 2_2^+ \| E2 \| 4_1^+ \rangle$	$3.33^{0.56}_{0.52}$
$\langle 4_1^+ \| E2 \| 4_1^+ \rangle$	$2.65^{1.68}_{1.69}$
$\langle 4_1^+ \| E2 \| 6_1^+ \rangle$	$3.01^{1.27}_{9.61}$
$\langle 2_1^+ \| M1 \| 2_2^+ \rangle$	$0.19^{0.03}_{0.29}$
$\langle 0_1^+ \| M1 \| 1_1^+ \rangle$	$0.10^{9.42}_{9.60}$
$\langle 1_1^+ \| M1 \| 0_2^+ \rangle$	$0.10^{9.42}_{9.60}$
$\langle 2_1^+ \| M1 \| 1_2^+ \rangle$	$0.10^{9.42}_{9.09}$
$\langle 1_2^+ \| M1 \| 2_2^+ \rangle$	$2.86^{0.38}_{0.31}$

Table 6.15: Matrix elements obtained from the GOSIA1 analysis without inclusion of the known life times.

So-called buffer states, which are only connected to one particular state lower in energy, give rise to large error bars, since no deexcitation from it has been observed: e.g. the $\langle 2_1^+ \| E2 \| 4_2^+ \rangle$ and $\langle 4_1^+ \| E2 \| 6_1^+ \rangle$ matrix elements have huge uncertainties. The $M1$ matrix elements $\langle 0_1^+ \| M1 \| 1_1^+ \rangle$, $\langle 1_1^+ \| M1 \| 0_2^+ \rangle$ and $\langle 2_1^+ \| M1 \| 1_2^+ \rangle$ are characterized by large error bars as well, since the 1_1^+ and 1_2^+ non-existing auxiliary states and the existing 0_2^+ state have only one way of deexcitation. Moreover, $M1$ matrix elements only produce very weak excitation. Therefore the matrix element connecting such a state to the lower-lying state to which it uniquely decays, cannot be estimated. It is also important to state that the obtained solution is independent of the sign of the $M1$ matrix elements, including the $\langle 2_1^+ \| M1 \| 2_2^+ \rangle$ matrix element.

6.1.4.2.5 Comparison with known life times

Life times for the 2_1^+ and 4_1^+ yrast states in ^{182}Hg can be calculated from the obtained matrix elements. A comparison to the known life times (from table 6.7) is given in table 6.16.

Nuclear state I^π	Life time τ [ps] from matrix elements	Known life time τ [ps]
2_1^+	45.9 (67)	42.1 (23)
4_1^+	34.8 (62)	37.1 (11)

Table 6.16: Comparison of the life times of the 2_1^+ and 4_1^+ yrast states in ^{182}Hg deduced from the matrix elements obtained from the Coulomb-excitation experiment to the known life times.

These values are clearly in agreement. As a next step, we include the known life times in the further GOSIA1 analysis in order to refine the results.

6.1.4.3 Including the life times in GOSIA1

6.1.4.3.1 Obtained matrix elements

After including the known life times in GOSIA1, the reduced χ_ν^2 reaches a minimum at a value of 0.674. Table 6.17 presents the physically relevant matrix elements determined by the GOSIA1 minimization.

ME	Obtained value [eb or μ_N]
$\langle 0_1^+ \| E2 \| 2_1^+ \rangle$	$1.29^{0.04}_{0.03}$
$\langle 0_1^+ \| E2 \| 2_2^+ \rangle$	$0.42^{0.02}_{0.02}$
$\langle 0_2^+ \| E2 \| 2_1^+ \rangle$	$-1.95^{0.15}_{0.14}$
$\langle 0_2^+ \| E2 \| 2_2^+ \rangle$	$1.13^{0.18}_{0.21}$
$\langle 2_1^+ \| E2 \| 2_1^+ \rangle$	$0.69^{1.04}_{0.83}$
$\langle 2_1^+ \| E2 \| 2_2^+ \rangle$	$1.90^{0.12}_{0.35}$
$\langle 2_1^+ \| E2 \| 4_1^+ \rangle$	$-3.72^{0.06}_{0.06}$
$\langle 2_2^+ \| E2 \| 2_2^+ \rangle$	$8.13^{0.74}_{1.09}$
$\langle 2_2^+ \| E2 \| 4_1^+ \rangle$	$2.82^{0.58}_{0.52}$
$\langle 4_1^+ \| E2 \| 4_1^+ \rangle$	$0.57^{1.84}_{1.93}$
$\langle 4_1^+ \| E2 \| 6_1^+ \rangle$	$5.14^{0.32}_{0.22}$
$\langle 2_1^+ \| M1 \| 2_2^+ \rangle$	$-0.05^{0.2}_{0.07}$

Table 6.17: Physically relevant matrix elements obtained from the GOSIA1 analysis with inclusion of the known life times.

In order to reproduce the 6_1^+ life time, an additional $6_1^+ \rightarrow 4_1^+$ with large error bar had to be included in experiment four, since the calculated intensity would exceed the detection limit of 30 counts. This is due to the presence of the $2_1^+ \rightarrow 0_{g.s.}^+$ γ transition at 352 keV, close to the $6_1^+ \rightarrow 4_1^+$ γ transition at 333 keV.

It is clear from table 6.17 that the presence of the life times drastically decrease the error bars on the $\langle 0_1^+ \| E2 \| 2_1^+ \rangle$, $\langle 2_1^+ \| E2 \| 4_1^+ \rangle$ and $\langle 4_1^+ \| E2 \| 6_1^+ \rangle$ matrix elements. Also the sign of the $\langle 2_1^+ \| M1 \| 2_2^+ \rangle$ has changed, but it has already been advocated in section 6.1.4.2 that the obtained set of matrix elements is independent of the signs of the $M1$ matrix elements.

6.1.4.3.2 Validity of the found matrix elements

The high value of $8.13^{0.74}_{1.09}$ obtained for the diagonal $\langle 2_2^+ \| E2 \| 2_2^+ \rangle$ matrix element can be considered unphysical. Applying the rotational model to the excited band consisting of the 0_2^+, 2_2^+, 4_1^+ and 6_1^+, based on the $\langle 4_1^+ \| E2 \| 6_1^+ \rangle$ matrix element, derived from the known 6_1^+ state life time, is presented in table 6.18.

ME	Rotational model value (absolute value) [eb or μ_N]
$\langle 0_2^+ \| E2 \| 2_2^+ \rangle$	2.54
$\langle 2_2^+ \| E2 \| 2_2^+ \rangle$	3.04
$\langle 2_2^+ \| E2 \| 4_1^+ \rangle$	4.08
$\langle 4_1^+ \| E2 \| 4_1^+ \rangle$	3.89
$\langle 4_1^+ \| E2 \| 6_1^+ \rangle$	5.14

Table 6.18: Values for the matrix elements in ^{182}Hg connecting states in the excited band inferred from the rotational model, taking $\langle 4_1^+ \| E2 \| 6_1^+ \rangle$ as a reference matrix element.

It can thus be concluded that the value for the diagonal matrix element is incompatible with the proposed value from the rotational model, which is almost three times lower.

6.1.4.3.3 An alternative set of matrix elements

An alternative solution during the minimization with GOSIA1 has been found at a slightly higher reduced χ^2_ν of 0.715. In spite of this higher χ^2_ν value, the set of matrix elements shows sufficient stability. This means that when changing one or two matrix elements to much decreased or increased numbers, the same solution is found after a new minimization. This set of matrix elements is presented in table 6.19.

When comparing these matrix elements with the values from the rotational model, it is clear that they are more physically reasonable than the matrix elements from the solution with slightly lower reduced χ^2_ν presented in table 6.17. Two other issues that need to be addressed here are the E2/M1 mixing ratio of the $2_2^+ \rightarrow 2_1^+$ transition and a consistency check concerning the normalization to the ^{112}Cd target.

6.1.4.3.4 E2/M1 mixing ratio of the $2_2^+ \rightarrow 2_1^+$ γ transition

In this analysis, a number of X-rays has been attributed to the $E0(2_2^+ \rightarrow 2_1^+)$ deexcitation. Since the $E2$ and $M1$ channels of the deexcitation are also partially converted, the amount of electrons coming from the $E2$ and $M1$ paths

ME	Obtained value [eb or μ_N]
$\langle 0_1^+ \| E2 \| 2_1^+ \rangle$	$1.29^{0.04}_{0.03}$
$\langle 0_1^+ \| E2 \| 2_2^+ \rangle$	$0.61^{0.03}_{0.03}$
$\langle 0_2^+ \| E2 \| 2_1^+ \rangle$	$-2.68^{0.15}_{0.13}$
$\langle 0_2^+ \| E2 \| 2_2^+ \rangle$	$1.66^{0.22}_{0.21}$
$\langle 2_1^+ \| E2 \| 2_1^+ \rangle$	$-0.04^{1.30}_{1.40}$
$\langle 2_1^+ \| E2 \| 2_2^+ \rangle$	$2.17^{0.12}_{0.22}$
$\langle 2_1^+ \| E2 \| 4_1^+ \rangle$	$-3.71^{0.06}_{0.06}$
$\langle 2_2^+ \| E2 \| 2_2^+ \rangle$	$0.78^{1.05}_{0.65}$
$\langle 2_2^+ \| E2 \| 4_1^+ \rangle$	$3.10^{0.31}_{0.27}$
$\langle 4_1^+ \| E2 \| 4_1^+ \rangle$	$4.39^{2.77}_{2.15}$
$\langle 4_1^+ \| E2 \| 6_1^+ \rangle$	$5.14^{0.32}_{0.23}$
$\langle 2_1^+ \| M1 \| 2_2^+ \rangle$	$0.19^{0.02}_{0.02}$

Table 6.19: Physically relevant matrix elements of the alternative solution obtained from the GOSIA1 analysis with inclusion of the known life times.

have been incorrectly assigned to the $E0(2_2^+ \rightarrow 2_1^+)$ deexcitation. Moreover, the conversion coefficients for $M1$ and $E2$ differ, so the influence of the E2/M1 mixing must be investigated using GOSIA.

The mixing ratio δ is defined as:

$$\delta = 0.835 \cdot E_\gamma \cdot \frac{\langle 2_1^+ \| E2 \| 2_2^+ \rangle}{\langle 2_1^+ \| M1 \| 2_2^+ \rangle}, \tag{6.4}$$

where E_γ is expressed in MeV, $\langle 2_1^+ \| E2 \| 2_2^+ \rangle$ in units of eb and $\langle 2_1^+ \| M1 \| 2_2^+ \rangle$ in units of μ_N. In the beginning of the analysis, a starting value of $\delta = 1.85$ was introduced in GOSIA. This value has been extracted from known values in even-even nuclei in this region of the nuclear chart [Wrz]. The values for the matrix elements presented in table 6.19 yield a mixing ratio of $\delta = 1.87(27)$, meaning that it hardly changed during the GOSIA analysis.

Changing the mixing ratio, and using GOSIA to run a new minimization, hardly affects the χ^2_ν value in GOSIA, and results in no considerable change in the matrix elements, indicating that the influence is rather small. This is probably

due to the large uncertainty on the total amount of X-rays coming from the deexcitation from the 2_2^+ to the 2_1^+ state.

6.1.4.4 Absolute normalization to the ^{112}Cd target using GOSIA2

The procedure of approximating the $\langle 0_1^+ \| E2 \| 2_1^+ \rangle$ matrix element in ^{182}Hg by the normalization to the observed $2_1^+ \rightarrow 0_{g.s.}^+$ γ transition in the ^{112}Cd target has been addressed in section 6.1.4.1. Hereby only a limited nuclear level scheme of ^{182}Hg was assumed, only consisting of the $0_{g.s.}^+$ and 2_1^+ states. It is possible to extend this level scheme to the one introduced in the GOSIA1 analysis. A new reduced χ_ν^2 surface can be calculated in GOSIA2, where all matrix elements are fixed to their values obtained in table 6.19, with exception of the transitional $\langle 0_1^+ \| E2 \| 2_1^+ \rangle$ and diagonal $\langle 2_1^+ \| E2 \| 2_1^+ \rangle$ matrix elements, which are allowed to vary. Like in the minimization with the limited level scheme of ^{182}Hg, only the $2_1^+ \rightarrow 0_{g.s.}^+$ γ transitions in the three angular cuts are included in the analysis, since the fixed matrix elements connecting the other added states will reproduce the other observed transitions in the Coulomb-excitation spectra. The reduced χ_ν^2 surface with the condition $\chi^2 < \chi^2_{\text{min}} + 1$ is shown in figure 6.9.

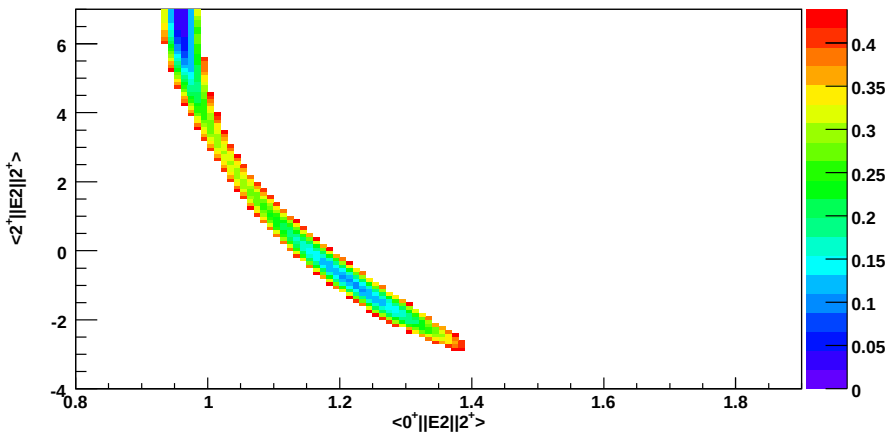

Figure 6.9: Reduced χ_ν^2 surface for the ^{182}Hg-on-^{112}Cd experiment with the condition $\chi^2 < \chi^2_{\text{min}} + 1$, enabling error bars for $\langle 0_{g.s.}^+ \| E2 \| 2_1^+ \rangle$ and $\langle 2_1^+ \| E2 \| 2_1^+ \rangle$ to be estimated. The matrix elements connecting the added states reproduce the observed transitions other than the $2_1^+ \rightarrow 0_{g.s.}^+$ transition.

Two minima are present in the reduced χ^2_ν surface. The minimum found at matrix element values of approximately $\langle 0^+_1 \| E2 \| 2^+_1 \rangle \approx 0.97$ and $\langle 2^+_1 \| E2 \| 2^+_1 \rangle \approx 6.8$ can be excluded, due to the unphysically high diagonal matrix element of the first 2^+_1 state. The other minimum suggests a diagonal matrix element $\langle 2^+_1 \| E2 \| 2^+_1 \rangle$ of approximately -0.8, and the corresponding transitional matrix element $\langle 0^+_1 \| E2 \| 2^+_1 \rangle$ amounts to 1.22 with an error bar to the positive side of 0.17. This number is clearly in agreement with the value of $1.29^{0.04}_{0.03}$ obtained from the GOSIA1 analysis (table 6.19).

6.1.5 Two-particle analysis versus one-particle analysis

6.1.5.1 Two-particle analysis

Section 6.1.4.1 treated the first approach to determine the $\langle 0^+_{g.s.} \| E2 \| 2^+_1 \rangle$ matrix element by employing a direct calculation in GOSIA1 and a reduced χ^2_ν approximation in GOSIA2. This and the whole further analysis were performed by only taking into account nuclear transitions in coincidence with the detection of two particles: the projectile as well as the target were demanded to be registered in the DSSSD. This method of stringent γ-ray selection serves as a basis for the considerations further on in this section.

6.1.5.2 One-particle analysis

A larger angular range for the detection of particles can be achieved by also including the events where the mercury projectile is incident in strips 12, 13, 14 and 15. In these strips mercury can have a high energy or a low energy, due to the back-bending in these kinematics. The higher-energy kinematic branch is meant here, and this will be implicitly presumed in the rest of this section. In these events, the cadmium target ion is not detected in the particle detector. The angular relations are given in table 6.20.

It is important to notice that in these strips, not only mercury, but also cadmium is present at the same energy. A way to select only the mercury is to demand that only one particle should be detected in the particle detector. Indeed, ideally, when assuming the particle in stips 12 to 15 to be cadmium, there should be a second particle (mercury) detected. However, due to the low energy of the corresponding mercury projectile, the detection cannot be absolutely guaranteed.

Figure 4.6.a showed the detection pattern in the particle detector when only assuming one incident particle.

Strips	$\theta_{lab}[^\circ]$	$\theta_{c.m.}[^\circ]$
15	15.5 - 18.6	41 - 50
14	18.7 - 21.7	50 - 59
13	21.8 - 24.7	59 - 67
12	24.8 - 27.5	68 - 77

Table 6.20: Angular relations gating on the mercury particle.

Figure 6.10 shows the random-subtracted γ-ray spectrum, Doppler-corrected for mercury when gating on strips 12 to 14, in coincidence with exactly one particle, and in coincidence with any amount of particles. Again, we do not consider strip 15 here, since only three of the four quadrants were functioning, so adding this gate to the total spectrum would not be desirable.

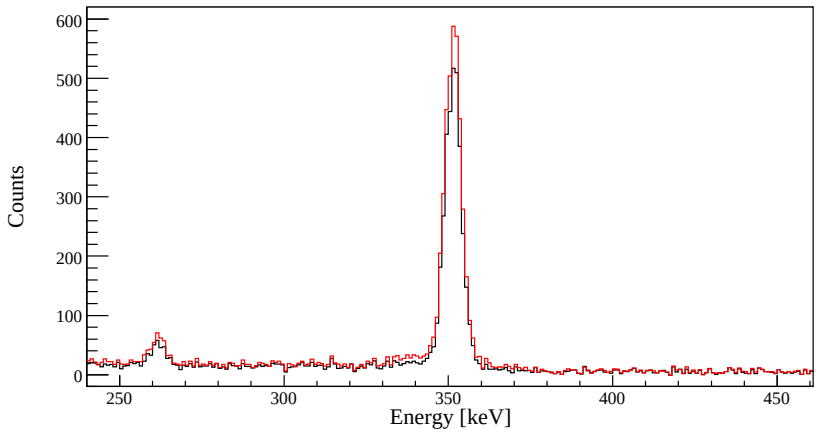

Figure 6.10: γ-ray spectrum around 352 keV coincident with exactly one particle (black) and any amount of particles (red), assuming the detection of a mercury particle in strips 12 to 14 and Doppler-corrected for mercury.

In case of coincidence with any amount of particles, there is a larger bump of wrongly Doppler-corrected particles present underneath the photo peak of the

$2_1^+ \rightarrow 0_{g.s.}^+$ γ transition, indicating the presence of cadmium particles in the gate that has been imposed.

A kinematic simulation can be used to estimate the effect of the one-particle requirement. Figure 6.11 shows the characteristics of the mercury projectile kinematics when gating on strips 12 to 15.

It is clear that the c.m. angular range is broader than predicted by the kinematics (table 6.20). This is due to the fact that a beam with a certain width has been assumed for the simulation. A comparison between demanding exactly one particle and any amount of particle is made in figure 6.12 for strips 12 and 11.

Events at the higher c.m. are lost, since there the corresponding cadmium target should be detected in the particle detector as well. It is clear that for strip 11, this effect is even more dramatic. When gating on strip 11, 74 % of the events are lost when demanding only one particle. For strip 12 and higher, the lost events amount to less than 10 %, so this effect can be neglected in the analysis.

a)

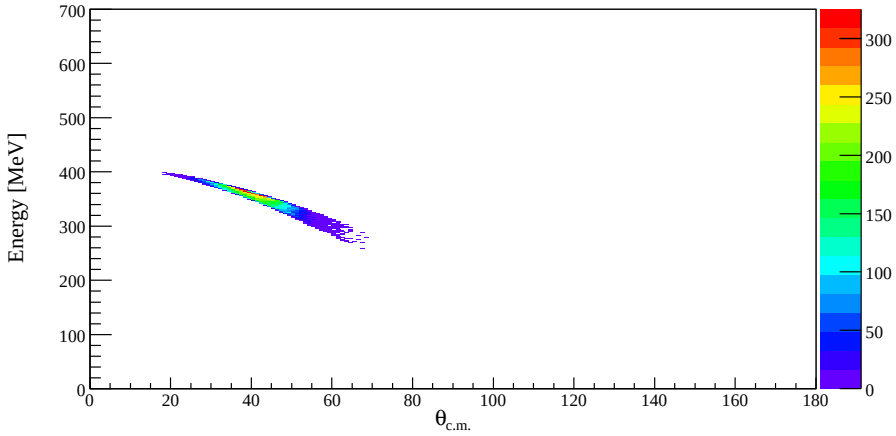

c)

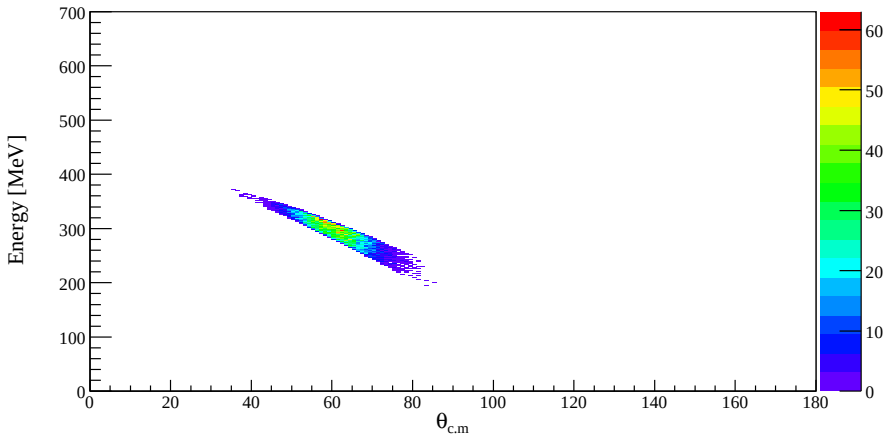

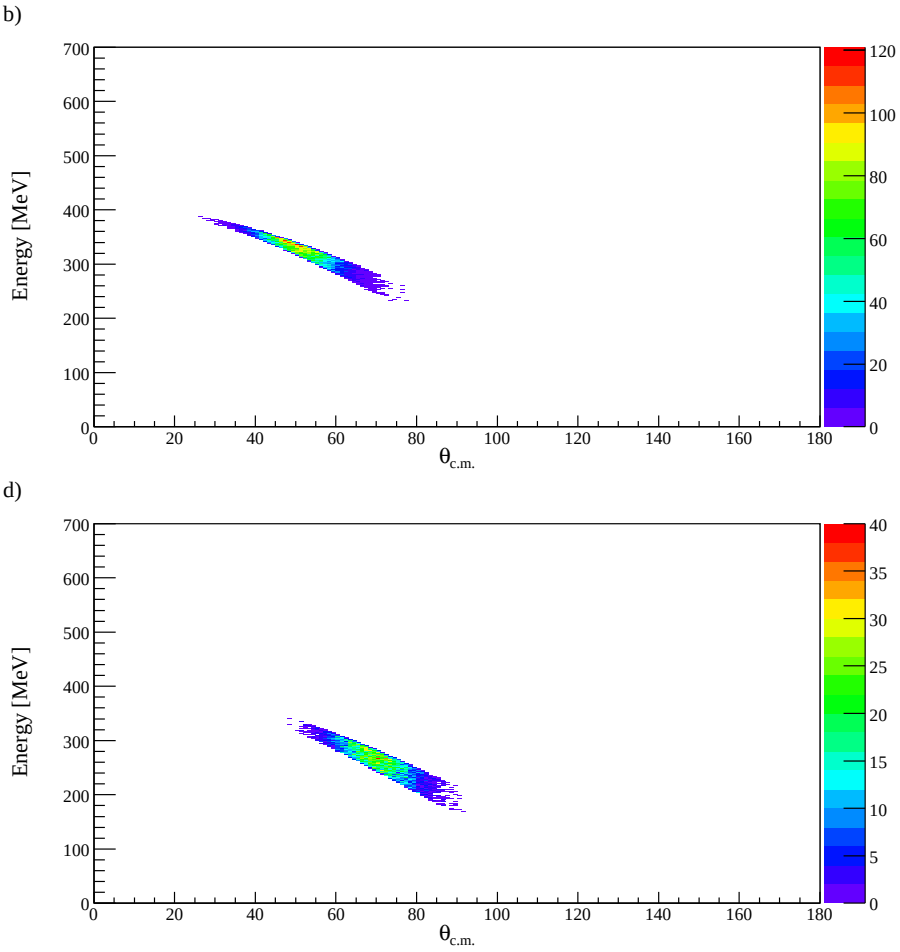

Figure 6.11: Energy of the mercury projectile versus c.m. angle gating on strips 15 (a), 14 (b), 13 (c) and 12 (d).

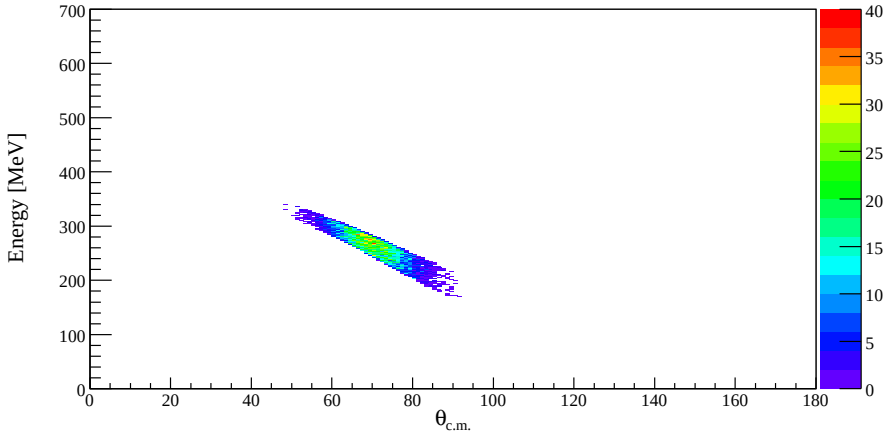

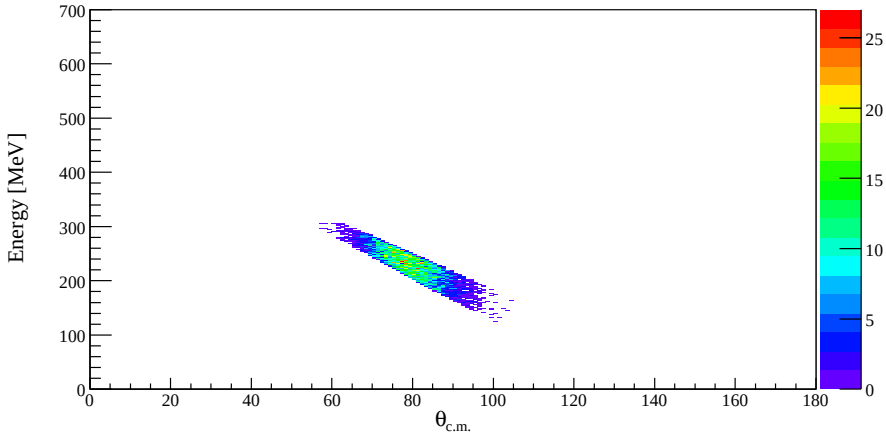

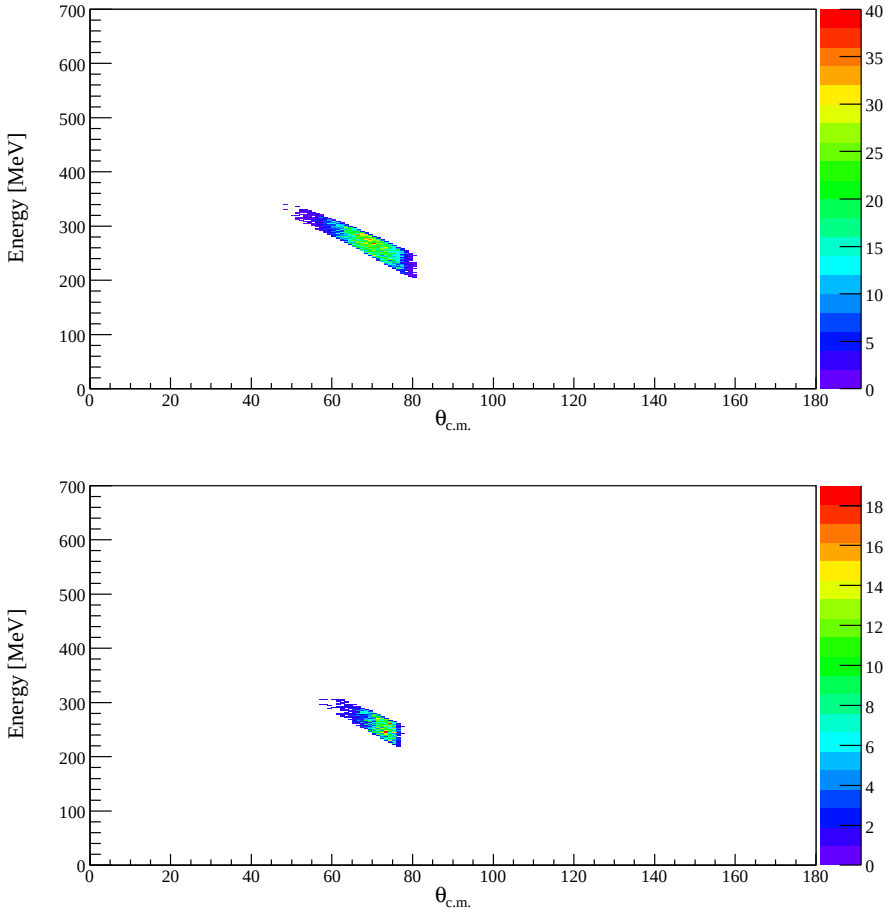

Figure 6.12: Energy of the mercury projectile versus c.m. angle gating for strips 12 (above) and 11 (below) assuming any amount of particles (left) and exactly one particle (right).

6.1.5.3 Construction of the γ-ray spectra

When gating on strips 12 to 15, the corresponding γ-ray spectra can be constructed. With the requirement of only one detected particle, it can be assumed to be mercury. Since the mercury γ rays are emitted in flight at an energy of approximately 300 MeV, they need to be Doppler corrected. The corresponding target particle flies outside the angular range of the particle detector, and in case of cadmium excitation, the γ ray will be almost non-Doppler broadened. This can be seen in figure 6.13, where the particle energy of the cadmium target is shown when a mercury projectile is detected in strip 15.

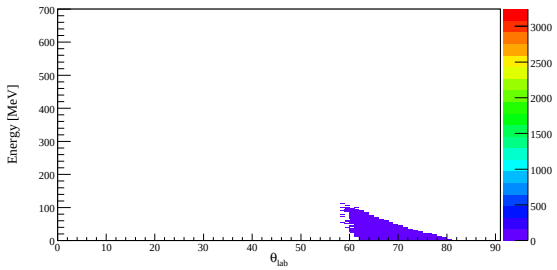

Figure 6.13: Energy of the cadmium target projectile versus laboratory angle when a mercury projectile is detected in strip 15.

Indeed, the cadmium particles are either stopped in the target or only a very low energy remains. For strips with a lower number the energy increases.

Four spectra can now be constructed.

1. The non-Doppler corrected γ-ray spectrum.
2. The γ-ray spectrum Doppler-corrected for mercury.
3. The γ-ray spectrum Doppler-corrected for cadmium, assuming the detected particle is not mercury but cadmium.
4. The γ-ray spectrum Doppler-corrected for cadmium, assuming the detected particle is mercury and the cadmium falls outside the reach of the particle detector, at low energy. In this case the trajectory of the cadmium needs to be reconstructed in order to perform the Doppler correction.

These γ-ray spectra are plotted in figure 6.14, with a zoom on the cadmium transition. The included strips are 12, 13 and 14.

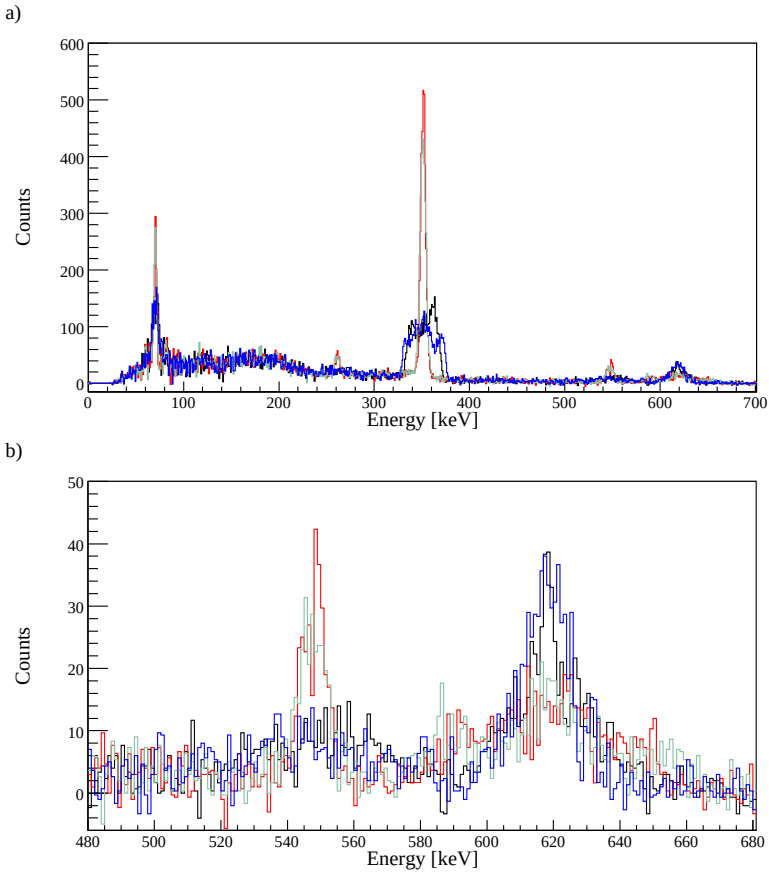

Figure 6.14: a) The four spectra are plotted in a colour referring to their number in the list in the text: black (1), red (2), green (3) and blue (4). b) A focus around the energy region of the $2_1^+ \rightarrow 0_{g.s.}^+$ γ transition in ^{112}Cd.

It is clear that for the integration of the photo peaks originating from mercury excitation, the red spectrum should be used. The green spectrum also performs a good Doppler correction for mercury, since only the mass number changes in the Doppler correction formula. However, the green spectrum apparently does not seem to perform a good correction for the cadmium photo peak, suggesting there are not many cadmium particles underneath the mercury particle gates. The choice between the black or blue spectrum for the integration of the cadmium photo peak is ambiguous. In figure 6.15, the γ-ray spectra for integration of the photo peak originating from cadmium are shown for the individual strips.

a)

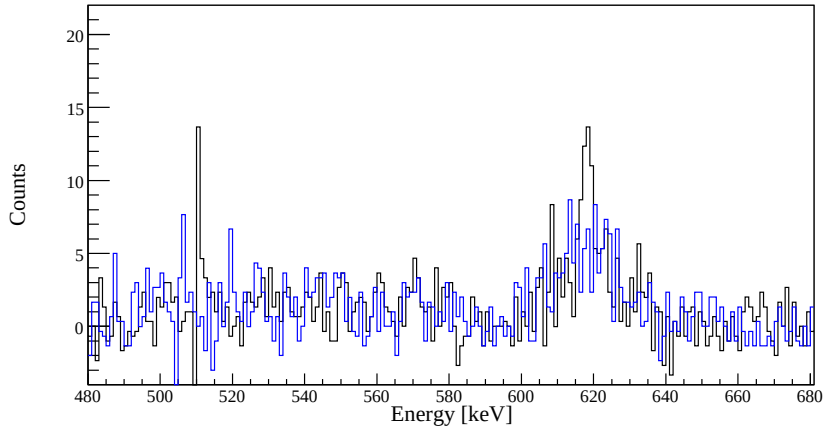

c)

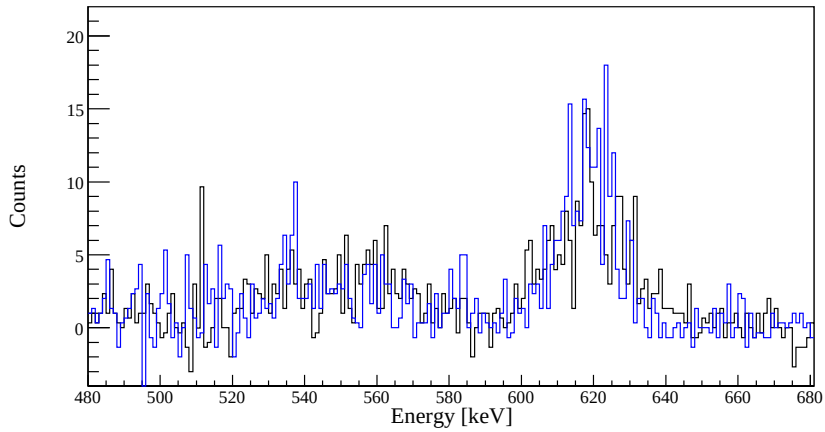

b)

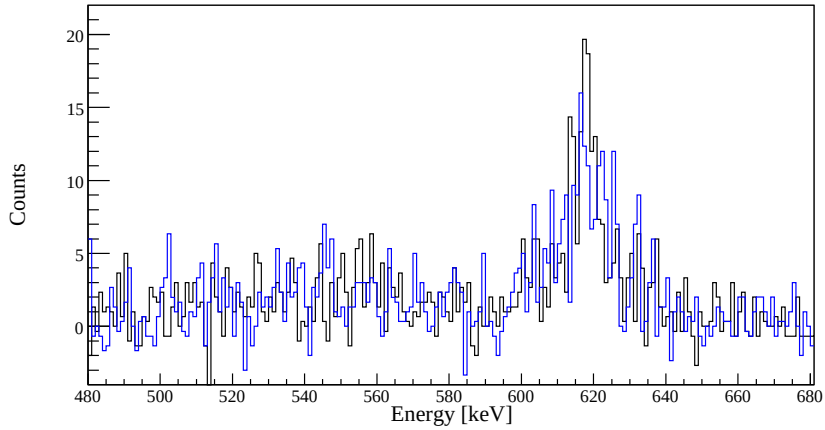

d)

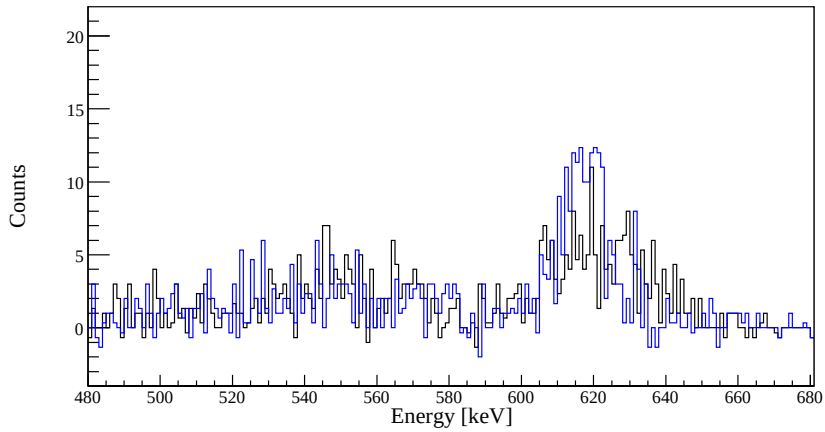

Figure 6.15: γ-ray spectra used for the integration of the photo peak originating from cadmium for strips 15 (a), 14 (b), 13 (c) and 12 (d). The black spectra are non-Doppler corrected, the blue spectra are Doppler corrected for cadmium, assuming cadmium falls out of the particle detector.

These spectra indicated that a careful Doppler correction is more and more essential when gating on decreasing strip number. However, when integrating the photo peak originating from the $2_1^+ \rightarrow 0_{g.s.}^+$ transition in cadmium, both spectra yield a similar integral.

6.1.5.4 Extracting the matrix elements

Figure 6.4 can now be expanded by four new data points, which are shown in figure 6.16.

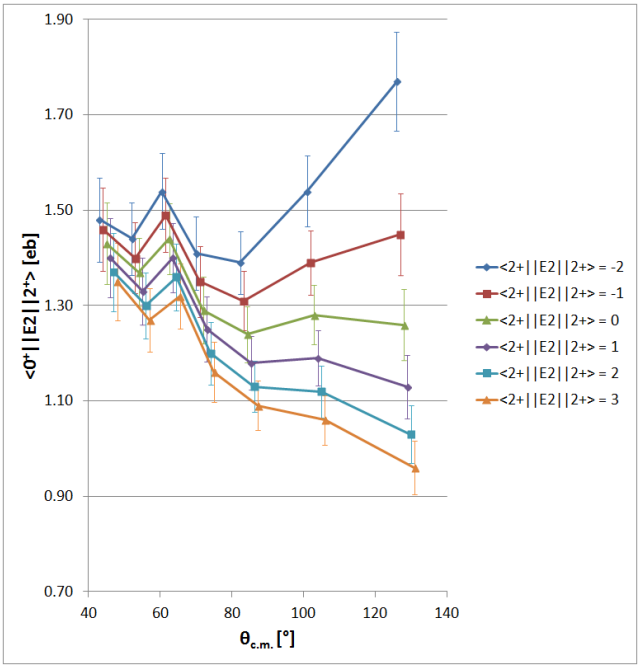

Figure 6.16: $\langle 0_{g.s.}^+ \| E2 \| 2_1^+ \rangle$ for the seven angular ranges, assuming different integer values of $\langle 2_1^+ \| E2 \| 2_1^+ \rangle$.

However, these calculations can also be performed when assuming that all cadmium particles are still present in the mercury gate. This would yield an extra count rate of wrongly Doppler-corrected events in the photo peak of the $2_1^+ \rightarrow 0_{g.s.}^+$ transition in mercury, still present in the integral. Also the integral of the photo peak of the $2_1^+ \rightarrow 0_{g.s.}^+$ transition in cadmium would be overestimated, but to another extent. Since the $\langle 0_{g.s.}^+ \| E2 \| 2_1^+ \rangle$ and $\langle 2_1^+ \| E2 \| 2_1^+ \rangle$ are known

in ^{112}Cd, the contribution to the total $0^+_{g.s.} \rightarrow 2^+_1$ excitation cross section in cadmium due to cadmium particles in the mercury gate in the individual strips 12 to 15 can be calculated to be {18.5 %, 16.1 %, 14.8 %, 14.5 % }. For the estimation of the contribution of cadmium particles to the total $0^+_{g.s.} \rightarrow 2^+_1$ excitation cross section in ^{182}Hg, the $\langle 0^+_{g.s.} \| E2 \| 2^+_1 \rangle$ and $\langle 2^+_1 \| E2 \| 2^+_1 \rangle$ matrix elements in ^{182}Hg are taken from the two-particle analysis in the lower strip numbers (cfr. section 6.1.4.3.3), yielding a contribution to the excitation cross section in ^{182}Hg of {24.8 %, 23 %, 21.3 %, 20 % }. However, the Doppler shift at 619 keV (cadmium photo peak) would be higher than at 352 keV (mercury photo peak), suggesting that perhaps the overestimation of the photo peak integral would be higher at low energies.

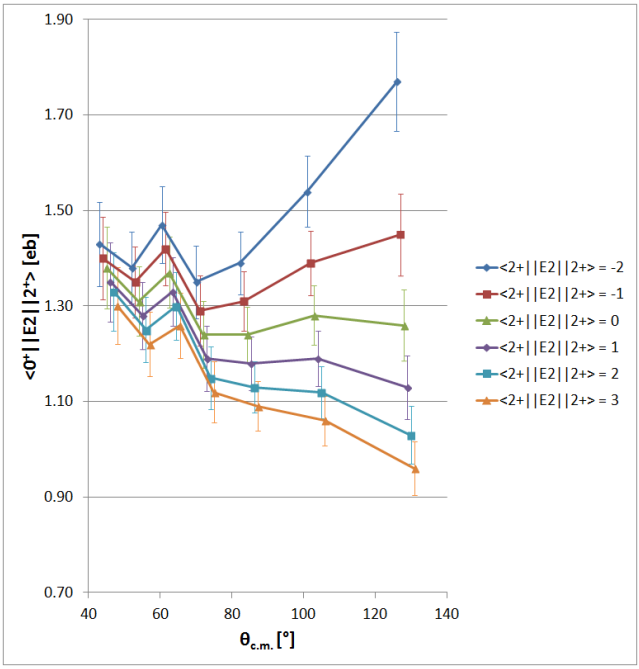

Figure 6.17: $\langle 0^+_{g.s.} \| E2 \| 2^+_1 \rangle$ for the seven angular ranges, assuming different integer values of $\langle 2^+_1 \| E2 \| 2^+_1 \rangle$. Both photo peaks originating from mercury and cadmium are supposed to be overestimated.

Figure 6.17 is a copy of figure 6.16 assuming that the cadmium particles are present in the mercury particle gates. This overestimates the integrals in both photo peaks originating from mercury and cadmium. However, due to

the different shape of angular cross section function in the two nuclei, the overestimation is slightly less for cadmium.

The extreme of overestimating the photo peak originating from mercury and a correct integration of the photo peak originating from cadmium should also be investigated. This is shown in figure 6.18.

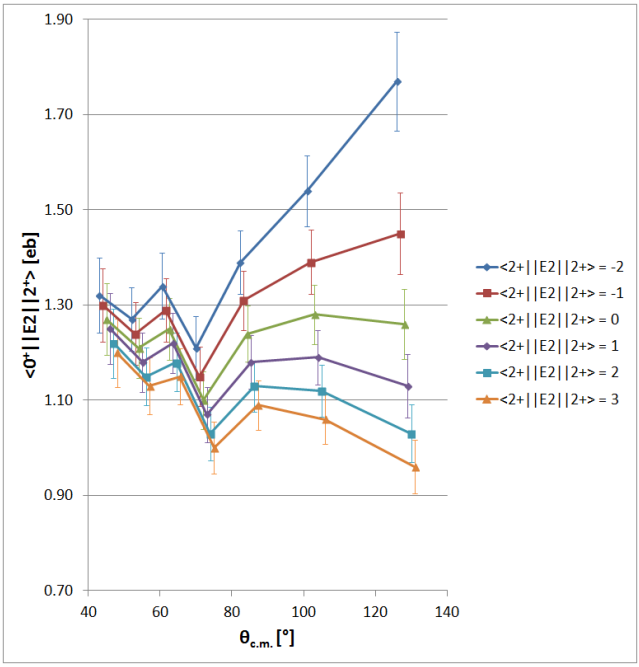

Figure 6.18: $\langle 0^+_{g.s.} \| E2 \| 2^+_1 \rangle$ for the seven angular ranges, assuming different integer values of $\langle 2^+_1 \| E2 \| 2^+_1 \rangle$. Only the photo peak originating from mercury is supposed to be overestimated.

6.1.5.5 The contribution of the cadmium particles

Demanding the $\langle 0^+_{g.s.} \| E2 \| 2^+_1 \rangle$ matrix element in ^{182}Hg to remain constant over the full c.m. angular range for the extraction of the correct $\langle 2^+_1 \| E2 \| 2^+_1 \rangle$ matrix element, gives different results in the three cases shown in the figures. It is therefore crucial to know what the contribution of cadmium particles amounts to when gating on the mercury particles in strips 12 to 15. Figure 6.10 already showed the decrease in cadmium contribution when demanding exactly one

detected particle. Integrating the $2_1^+ \rightarrow 0_{g.s.}^+$ photo peak from mercury around 352 keV using both a wide and narrow integration window can provide an estimation of the cadmium contribution. Hereby the wide window (320 - 375 keV) is assumed to include both observed $2_1^+ \rightarrow 0_{g.s.}^+$ transitions coincident with a detected mercury particle (and hence a good Doppler correction) or a detected cadmium particle (and hence a wrong Doppler correction). The latter gives rise to the broad bump in the spectrum on which the properly Doppler corrected photo peak is standing. On the other hand, a narrow integration window (342 - 358 keV) considering the wrongly Doppler corrected bump underneath as the background on which the true photo peak is built, contains only the observed $2_1^+ \rightarrow 0_{g.s.}^+$ transitions in coincidence with the detection of a mercury particle. The same procedure can be applied when the detected particle in strips 12 to 14 is assumed to be cadmium, and the Doppler correction is performed for the corresponding mercury particle, of which the trajectory has been reconstructed from the kinematics. Figure 6.19 shows this spectrum demanding a coincidence with exactly one particle and in coincidence with any amount of particles.

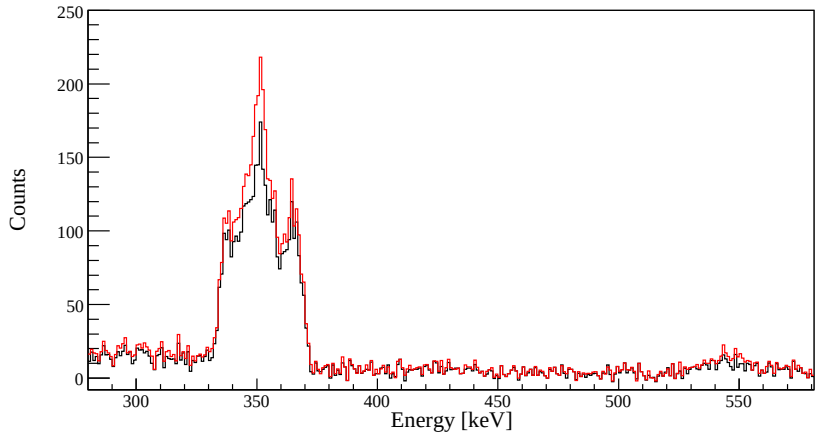

Figure 6.19: γ-ray spectrum around 352 keV coincident with exactly one particle (black) and any amount of particles (red), assuming the detection of a cadmium particle in strips 12 to 14 and Doppler-corrected for mercury.

The relatively sharp peak around 352 keV originates from the assumption that the detected particle in strips 12 to 14 is cadmium. The other $2_1^+ \rightarrow 0_{g.s.}^+$ photo peak intensity is smeared out and hence due to a wrong Doppler correction, implying the detected particle in strips 12 to 14 is mercury. The integration of the γ rays employing the same wide window as described in the previous

case (320 - 375 keV) includes both observed $2_1^+ \rightarrow 0_{g.s.}^+$ transitions coincident with a detected cadmium particle (and hence a good Doppler correction for the reconstructed mercury particle) or a detected mercury particle (and hence a wrong Doppler correction). The narrow integration window (342 - 358 keV) using the wrongly Doppler corrected bump underneath as a broad background on which the sharp photo peak is built, contains only the observed $2_1^+ \rightarrow 0_{g.s.}^+$ transitions coincident with a detected cadmium particle.

The integration of these spectra, assuming the detected particle to be mercury or cadmium using a narrow or a wide integration window allows the cadmium to total ratio to be estimated, i.e. the ratio of observed $2_1^+ \rightarrow 0_{g.s.}^+$ transitions coincident with a cadmium particle in strips 12 to 14 versus the observed $2_1^+ \rightarrow 0_{g.s.}^+$ transitions coincident with any particle (cadmium or mercury) in these strips. The values given in table 6.21 demand the detection of one or more particles in the DSSSD, those in table 6.22 the detection of exactly one particle.

Detected particle	Integration window	Integral	cadmium/total ratio
Hg	wide (320 - 375 keV)	4021 (73)	
Hg	narrow (342 - 358 keV)	3491 (66)	13.2 (23)
Cd	wide (320 - 375 keV)	4008 (74)	
Cd	narrow (342 - 358 keV)	757 (66)	18.9 (17)

Table 6.21: The cadmium to total ratio can be estimated comparing the integrals of the observed $2_1^+ \rightarrow 0_{g.s.}^+$ transitions using narrow and wide integration windows. The values given in this table demand the detection of one or more particles in the DSSSD.

When comparing table 6.21 and 6.22, it is clear that demanding the detection of exactly one particle reduces the contribution of cadmium particles. Assuming all cadmium particles are detected and using the $\langle 0_{g.s.}^+ \| E2 \| 2_1^+ \rangle$ and $\langle 2_1^+ \| E2 \| 2_1^+ \rangle$ matrix elements of ^{182}Hg extracted from the analysis in the lower strip numbers, the contribution to the total $0_{g.s.}^+ \rightarrow 2_1^+$ excitation cross section in ^{182}Hg due to cadmium particles in strips 12 to 14 can be calculated to be 23.1 % (as has been derived from section 6.1.5.4). This number can be compared to the ratios rendered in the two tables. When assuming that the detected particle particle is mercury, performing the Doppler correction for mercury and considering the $2_1^+ \rightarrow 0_{g.s.}^+$ transition of ^{182}Hg, the cadmium to total ratio is determined

Detected particle	Integration window	Integral	cadmium/total ratio
Hg	wide (320 - 375 keV)	3434 (68)	
Hg	narrow (342 - 358 keV)	3152 (62)	8.2 (26)
Cd	wide (320 - 375 keV)	3430 (68)	
Cd	narrow (342 - 358 keV)	498 (60)	14.5 (18)

Table 6.22: Same table as table 6.21, but demanding the detection of exactly one particle in the DSSSD.

to be 8.2 (26). When looking at the same transition, but assuming that the detected particle particle is cadmium and performing the Doppler correction for the reconstructed mercury projectile, the cadmium to total ratio is extracted to be 14.5 (18). The amounts of wrongly Doppler-corrected γ rays under the sharp well Doppler-corrected peak are not in agreement in these two cases, suggesting that they depend on the magnitude of the Doppler shift. Hence, it can be advocated that the magnitude of Doppler shift has an influence on the amount of wrongly corrected γ rays still present in the properly Doppler corrected photo peak. This indicates that the fraction of contamination cannot be directly derived from this procedure. Another consequence of this is that the suggestion made in section 6.1.5.4 of having cadmium contamination in the photo peak at 352 keV (mercury photo peak), but not at 619 keV (cadmium photo peak), cannot be falsified.

6.1.5.6 Influence of the unknown matrix elements in ^{182}Hg

A further consideration has to be made looking at figures 6.16 to 6.18. When taking into account the contamination due to cadmium particles in the mercury gate in strips 12 to 15, an assumption had to be made about the $\langle 0^+_{g.s.} \| E2 \| 2^+_1 \rangle$ and $\langle 2^+_1 \| E2 \| 2^+_1 \rangle$ matrix elements in ^{182}Hg, and they were taken from the two-particle analysis in the lower strip numbers, the diagonal matrix element having a relatively high uncertainty. However, by including the one-particle analysis, figure 6.16 suggests a $\langle 2^+_1 \| E2 \| 2^+_1 \rangle$ matrix element in ^{182}Hg of around -1. The influence of this matrix element on the excitation cross section becomes larger when going to higher c.m. angles, and the detection of the contaminating cadmium covers much higher c.m. angles than the detected mercury particles. A positive diagonal matrix element causes the excitation cross section curve

to increase, a negative one causes it to decrease, and this effect becomes stronger with increasing c.m. angle. Hence, a negative $\langle 2_1^+ \| E2 \| 2_1^+ \rangle$ matrix element causes the cadmium to total ratio to become lower. Assuming a lower contamination, the first four points in figure 6.16 (representing the one-particle analysis in strips 15 to 12) would have to increase, because higher transitional matrix elements in ^{182}Hg would be necessary to reproduce the γ-ray intensities. This is due to the lower cadmium-induced excitation. As a consequence, when demanding the $\langle 0_{g.s.}^+ \| E2 \| 2_1^+ \rangle$ matrix element to remain stable throughout the entire angular range, this would lead to an even higher $\langle 2_1^+ \| E2 \| 2_1^+ \rangle$ matrix element. This means that for the two last columns, the same assumptions were made as in figures 6.17 and 6.18.

This argument can also be reversed. The two-particle analysis in the lower strip numbers also allows a diagonal matrix element which is higher than 1. This would increase the contribution of cadmium in the excitation cross section of ^{182}Hg in strips 12 to 15, leading to a decrease of the transitional matrix elements in these four data points. Demanding the $\langle 0_{g.s.}^+ \| E2 \| 2_1^+ \rangle$ matrix element to remain quasi-constant over the full angular range would then produce a lower value than the one extracted from figure 6.16.

6.1.5.7 Conclusions

As a conclusion it can be stated that the analysis of the higher strip numbers shows a lack of necessary information for them to be included in the final GOSIA analysis. This information is summarized in the list below:

1. The amount of cadmium particles in the mercury gate covering strips 12 to 15 can be calculated. The demand of coincidence with exactly one particle should theoretically cancel out all cadmium, but the experimental data show that there is still cadmium present. The fraction of the remaining cadmium particles in the mercury gate however cannot be extracted.

2. The underlying amount of wrongly Doppler-corrected γ rays under the properly Doppler corrected photo peaks can not be correctly estimated, since it apparently depends on the magnitude of the Doppler shift.

3. The precise relative ratio of the diagonal and transitional matrix element in ^{182}Hg is unknown. This value has an influence on the contribution of cadmium particles to the $0_{g.s.}^+ \rightarrow 2_1^+$ excitation cross section in ^{182}Hg.

These unknown parameters in the analysis can cause different values for the $\langle 0_{g.s.}^+ \| E2 \| 2_1^+ \rangle$ and $\langle 2_1^+ \| E2 \| 2_1^+ \rangle$ matrix elements in ^{182}Hg to be obtained. Hence,

the one-particle analysis will be omitted, and only the analysis with two coincident particles will be used. This means that the final set of matrix elements remains the one presented in table 6.19.

6.2 The ^{184}Hg case

In this section, the analysis of the experiments on ^{184}Hg will be discussed. Since there are lots of parallels with the analysis of the ^{182}Hg isotope, in many cases there will be references to the methods described in the previous section.

6.2.1 Intensity of the observed transitions

The Coulomb-excitation data on ^{184}Hg consist of three experiments on different targets. During the 2008 campaign, data were acquired employing a 2.3 mg/cm^2 ^{120}Sn target and a 1.1 mg/cm^2 ^{107}Ag target. In 2009, Coulomb excitation was performed by a ^{184}Hg beam incident on a 2.0 mg/cm^2 ^{112}Cd target. Like in the ^{182}Hg case, a division into angular gates has been made in the DSSSD, where the range of the target is split up in three cuts and the ^{182}Hg projectile needs to be detected in the corresponding DSSSD angular range. Figure 6.20 shows the random-subtracted γ-ray spectrum, coincident with two identified particles, Doppler corrected for the mercury projectile and for the cadmium target.

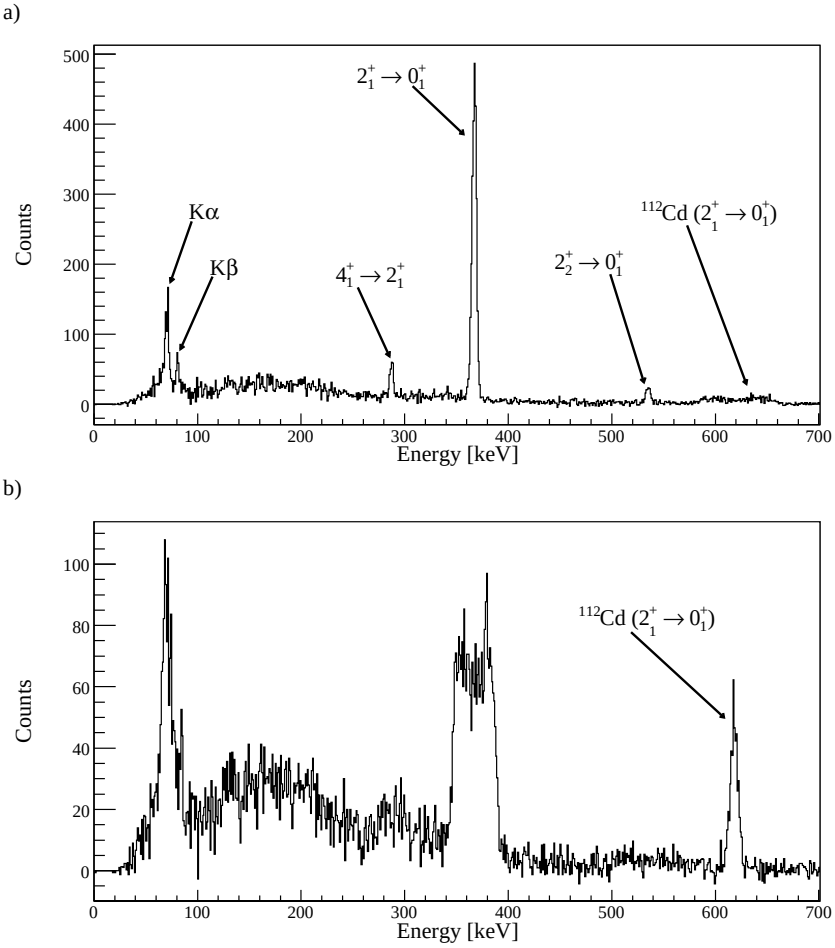

Figure 6.20: Random-subtracted γ-ray spectrum, coincident with two identified particles, Doppler corrected for the mercury projectile (a) and for the cadmium target (b). The spectra for the three particle angular cuts are not shown here. The photo peaks can be identified as the $2_1^+ \rightarrow 0_1^+$, the $4_1^+ \rightarrow 2_1^+$ and the $2_2^+ \rightarrow 0_1^+$ deexcitations. Also prompt X-rays are detected with an energy around 69 keV.

Figure 6.21 shows the corresponding spectra on the ^{107}Ag target. The relevant spectra obtained from the experiment on the ^{120}Sn target are shown in figure 6.22.

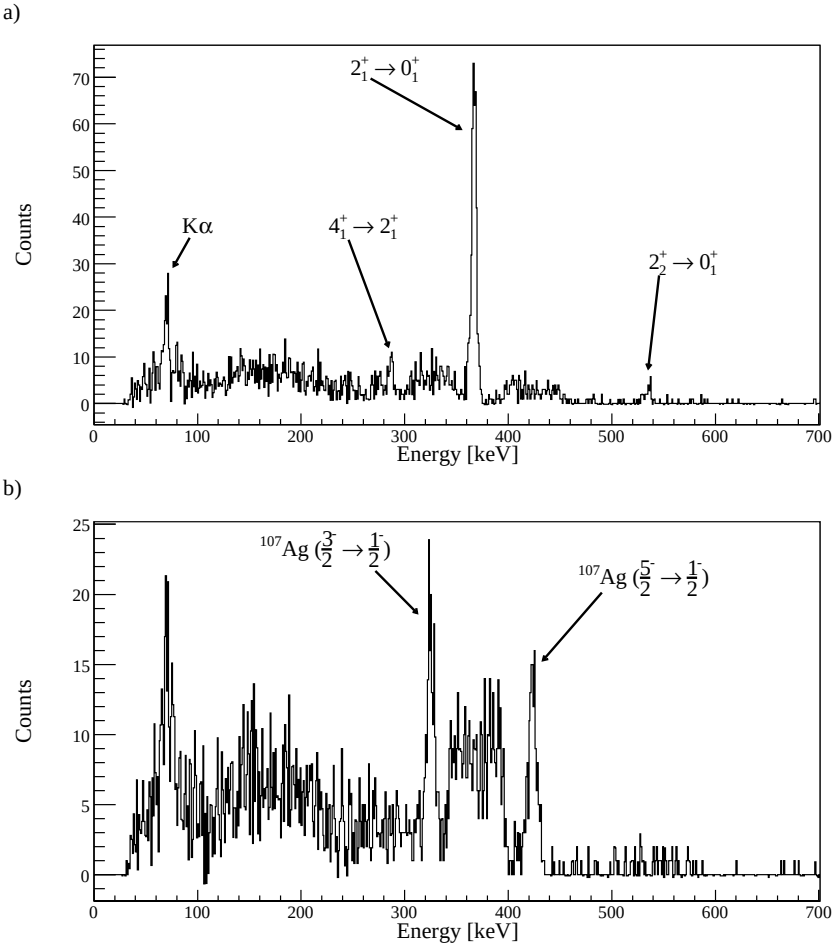

Figure 6.21: Random-subtracted γ-ray spectrum, coincident with two identified particles, Doppler corrected for the mercury projectile (a) and for the silver target (b). The same transitions are present here as in figure 6.20.

a)

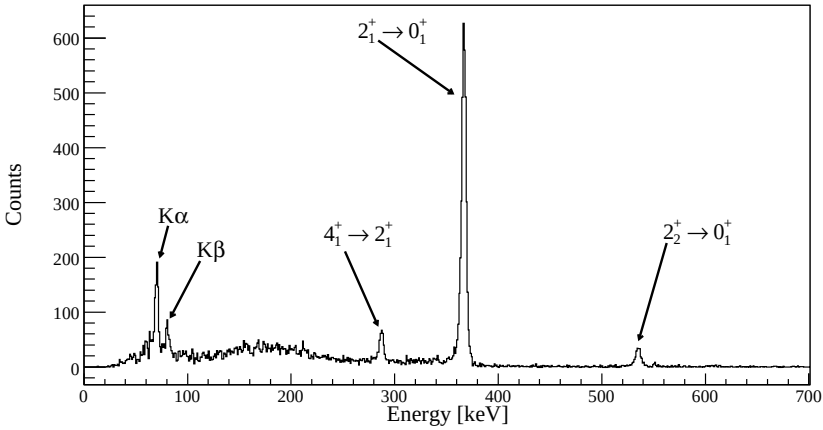

c)

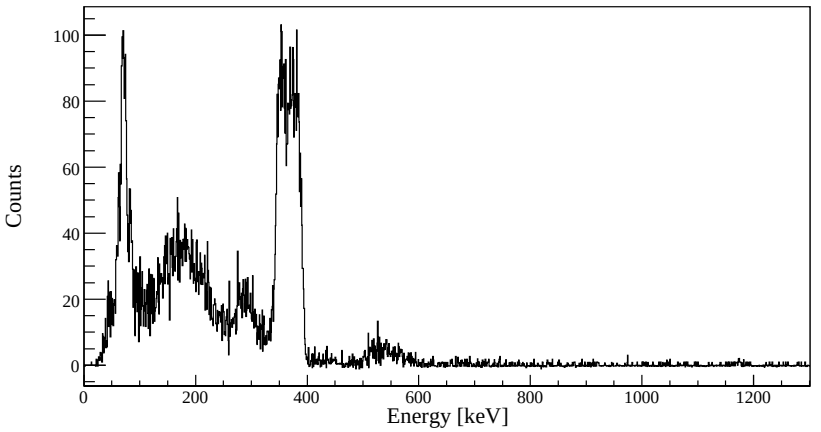

b)

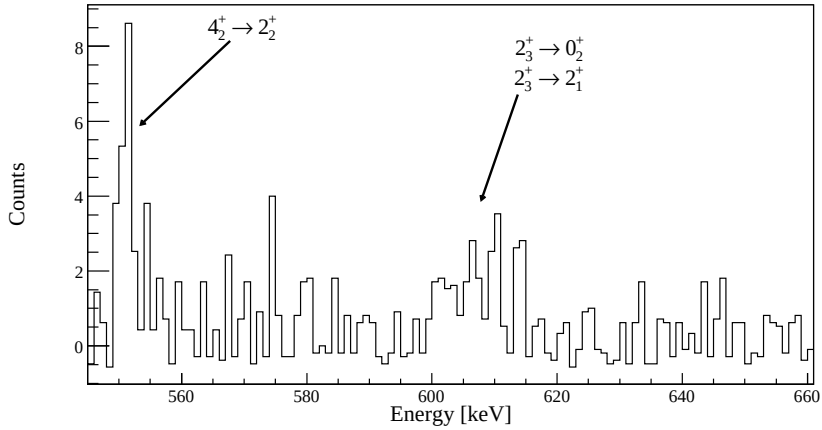

d)

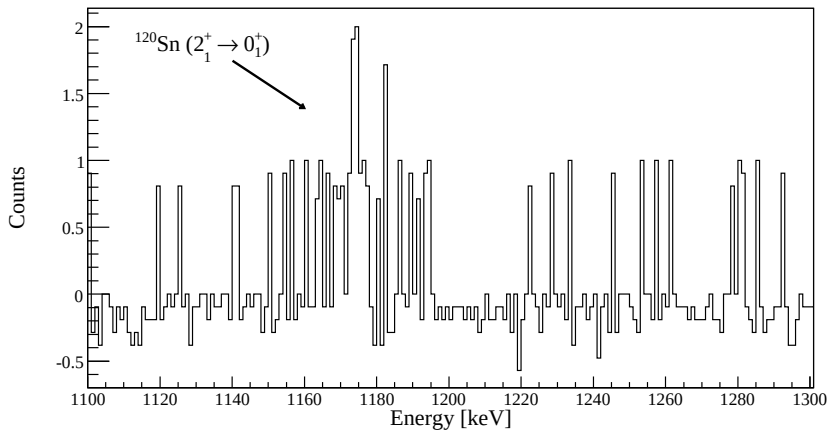

Figure 6.22: Random-subtracted γ-ray spectrum, coincident with two identified particles, Doppler corrected for the mercury projectile (a), enlarged around the energy range of 500-700 keV (b) for the visibility of the $4_2^+ \rightarrow 2_2^+$ transition and the $2_3^+ \rightarrow 0_2^+/2_3^+ \rightarrow 2_1^+$ doublet. Also the random-subtracted γ-ray spectrum, Doppler corrected for the tin target is shown (c), enlarged around 1171 keV (d), the energy of the $2_1^+ \rightarrow 0_1^+$ transition in ^{120}Sn.

A trace of the $2_1^+ \rightarrow 0_1^+$ transition in ^{120}Sn is present in spectrum 6.22.d. However, the normalization to the ^{120}Sn target is only useful when the total particle angular coverage can be divided in different ranges. For that purpose, the intensity of the $2_1^+ \rightarrow 0_1^+$ transition in ^{120}Sn is too weak, so it cannot be used and hence will be omitted in the further analysis.

The observed photo peak intensities are summarized in tables 6.23, 6.24, 6.25 and 6.26.

$I_i \rightarrow I_f$	E_γ [keV]	$\theta_{lab,t}[^\circ]$	$\theta_{c.m.}[^\circ]$	I_γ	$\epsilon_{\gamma,abs}[\%]$	$I_{\gamma,tot}$
$2_1^+ \rightarrow 0_1^+$	367	18.7 - 51.6	76.8 - 142.6	2532 (58)	10.59 (26)	23899 (803)
		43.6 - 51.6	76.8 - 92.8	1082 (39)		10213 (443)
		32.9 - 43.6	92.8 - 114.2	960 (35)		9061 (402)
		18.7 - 32.8	114.4 - 142.6	490 (25)		4625 (261)
$2_2^+ \rightarrow 0_1^+$	534	18.7 - 51.6	76.8 - 142.6	141 (21)	8.64 (45)	1631 (255)
		43.6 - 51.6	76.8 - 92.8	42 (13)		486 (156)
		32.9 - 43.6	92.8 - 114.2	56 (14)		648 (161)
		18.7 - 32.8	114.4 - 142.6	43 (9)		497 (102)
$4_1^+ \rightarrow 2_1^+$	287	18.7 - 51.6	76.8 - 142.6	193 (36)	12.25 (16)	1575 (296)
		43.6 - 51.6	76.8 - 92.8	98 (24)		800 (199)
		32.9 - 43.6	92.8 - 114.2	39 (22)		318 (183)
		18.7 - 32.8	114.4 - 142.6	56 (15)		457 (120)
K_α	≈69	18.7 - 51.6	76.8 - 142.6	529 (45)	12.81 (78)	4131 (433)
		43.6 - 51.6	76.8 - 92.8	207 (31)		1616 (259)
		32.9 - 43.6	92.8 - 114.2	218 (27)		1702 (237)
		18.7 - 32.8	114.4 - 142.6	104 (19)		812 (154)
K_β	≈80	18.7 - 51.6	76.8 - 142.6	76 (34)	15.10 (69)	503 (228)
		43.6 - 51.6	76.8 - 92.8	8 (24)		53 (161)
		32.9 - 43.6	92.8 - 114.2	27 (20)		179 (135)
		18.7 - 32.8	114.4 - 142.6	41 (13)		272 (86)

Table 6.23: Observed photo peak intensities I_γ (and I_X) are presented for the ^{184}Hg projectile when incident on the ^{112}Cd target for different angular ranges. Also the efficiency-corrected integrals are mentioned.

The K_α/K_β ratio of 8.2 (38) is not in agreement within 1 σ with the expected value of $\approx$ 3.6, but due to the large uncertainty this should not be worrisome.

$I_i \rightarrow I_f$	E_γ [keV]	$\theta_{lab,t}[^\circ]$	$\theta_{c.m.}[^\circ]$	I_γ	$\epsilon_{\gamma,abs}[\%]$	$I_{\gamma,tot}$
$2_1^+ \rightarrow 0_1^+$	619	18.7 - 51.6 43.6 - 51.6 32.9 - 43.6 18.7 - 32.8	76.8 - 142.6 76.8 - 92.8 92.8 - 114.2 114.4 - 142.6	477 (25) 198 (17) 176 (15) 103 (10)	8.03 (56)	5938 (519) 2465 (275) 2191 (245) 1282 (157)

Table 6.24: Observed photo peak intensities I_γ are presented for the ^{112}Cd target when the ^{184}Hg projectile is incident on it, and this for different angular ranges. Also the efficiency-corrected integrals are mentioned.

$I_i \rightarrow I_f$	E_γ [keV]	$\theta_{lab,t}[^\circ]$	$\theta_{c.m.}[^\circ]$	I_γ	$\epsilon_{\gamma,abs}[\%]$	$I_{\gamma,tot}$
$\underline{^{184}\text{Hg}}$						
$2_1^+ \rightarrow 0_1^+$	367	18.2 - 50.7	78.6 - 143.6	428 (22)	13.54 (33)	3162 (178)
$2_2^+ \rightarrow 0_1^+$	534			20 (7)	11.05 (58)	181 (61)
$4_1^+ \rightarrow 2_1^+$	287			40 (13)	15.65 (21)	256 (86)
K_α	$\approx$69			79 (16)	14.23 (87)	555 (117)
$\underline{^{107}\text{Ag}}$						
$\frac{3}{2}^- \rightarrow \frac{1}{2}^-$	325	18.2 - 50.7	78.6 - 143.6	113 (19)	14.54 (27)	777 (133)
$\frac{5}{2}^- \rightarrow \frac{1}{2}^-$	423			158 (14)	12.49 (41)	1265 (116)

Table 6.25: Observed photo peak intensities I_γ are presented for the ^{184}Hg projectile and the ^{107}Ag target for the total angular range.

$I_i \rightarrow I_f$	E_γ [keV]	$\theta_{lab,t}[^\circ]$	$\theta_{c.m.}[^\circ]$	I_γ	$\epsilon_{\gamma,abs}[\%]$	$I_{\gamma,tot}$
$2_1^+ \rightarrow 0_1^+$	367	18.2 - 50.7	78.6 - 143.6	3604 (63)	13.54 (33)	26622 (803)
		42.8 - 50.7	78.6 - 94.4	1472 (40)		10873 (400)
		32.1 - 42.7	94.6 - 115.8	1303 (38)		9625 (367)
		18.2 - 32.0	116.0 - 143.6	829 (30)		6124 (269)
$2_2^+ \rightarrow 0_1^+$	534	18.2 - 50.7	78.6 - 143.6	250 (18)	11.05 (58)	2263 (200)
		42.8 - 50.7	78.6 - 94.4	72 (10)		652 (97)
		32.1 - 42.7	94.6 - 115.8	95 (11)		860 (109)
		18.2 - 32.0	116.0 - 143.6	83 (10)		751 (97)
$4_1^+ \rightarrow 2_1^+$	287	18.2 - 50.7	78.6 - 143.6	276 (34)	15.65 (21)	1763 (219)
		42.8 - 50.7	78.6 - 94.4	86 (21)		549 (135)
		32.1 - 42.7	94.6 - 115.8	116 (21)		741 (134)
		18.2 - 32.0	116.0 - 143.6	75 (17)		479 (107)
$2_3^+ \rightarrow 0_2^+$ $2_3^+ \rightarrow 2_1^+$	608 and 616 doublet	18.2 - 50.7	78.6 - 143.6	14 (7)	8.08 (55)	173 (92)
$4_2^+ \rightarrow 2_2^+$	552	18.2 - 50.7	78.6 - 143.6	20 (7)	10.86 (60)	184 (67)
K_α	≈69	18.2 - 50.7	78.6 - 143.6	517 (42)	14.23 (87)	3633 (372)
		42.8 - 50.7	78.6 - 94.4	159 (27)		1117 (199)
		32.1 - 42.7	94.6 - 115.8	180 (25)		1265 (193)
		18.2 - 32.0	116.0 - 143.6	179 (21)		1258 (169)
K_β	≈80	18.2 - 50.7	78.6 - 143.6	182 (33)	16.77 (77)	1085 (202)
		42.8 - 50.7	78.6 - 94.4	66 (22)		393 (131)
		32.1 - 42.7	94.6 - 115.8	54 (19)		322 (115)
		18.2 - 32.0	116.0 - 143.6	62 (16)		370 (95)

Table 6.26: Observed photo peak intensities I_γ (and I_X) for the ^{184}Hg projectile on the ^{120}Sn target for different angular ranges.

The $\theta_{lab,t}$ angles are slightly smaller than in the experiment on the ^{112}Cd target, due to a larger distance to the DSSSD by 0.5 mm. When comparing with the experiment on the ^{112}Cd target, an increase for the γ-ray detection efficiency with a factor 23/18 is observed, due to 23 operational MINIBALL

cores compared to 18. For the K_α and K_β lines, the factor is only 20/18, since in three cores, a higher detection threshold is present. In these cores the X-rays are not observed. The intensities of the transitions in the ^{107}Ag nucleus target are presented here in a table, but will not be used in the analysis, the reason for this being addressed in appendix A.

Due to the low $0^+_{g.s.} \rightarrow 2^+_1$ excitation cross section in ^{120}Sn (section 3.3.4) and the low detection efficiency of the 1171 keV γ ray, no deexcitation in the target with satisfactory intensity has been observed. The ratio of K_α X-rays to K_β X-rays in table 6.26 amounts to 3.35 (71), which is in good agreement with the predicted value of ≈3.6.

Like in ^{182}Hg, there are clearly X-rays present that do not originate from heavy-ion vacancy creation induced by the collision of the ^{184}Hg projectile on the ^{112}Cd or ^{120}Sn target. Section 5.4 advocated that the remaining amount of X-rays arises from nuclear $E0$ transitions.

6.2.2 Intensity of the $\gamma - \gamma$ coincidences

6.2.2.1 Construction of the γ-ray spectra

The construction of the $\gamma_1 - \gamma_2$ coincidence spectra is done in the same way as in the ^{182}Hg case (section 6.1.2). Only the energy windows differ, for they are dependent on the energy of the $2^+_1 \rightarrow 0^+_{g.s.}$ transition, being 367 keV in ^{184}Hg. The gate for the central energy window is placed on the energies from 350 to 380 keV, for the lower energy window from 315 to 345 keV and for the higher energy window from 385 to 415 keV. The experiments on ^{182}Hg and ^{184}Hg on the ^{112}Cd target have the same windows for prompt and random coincidence with a particle, i.e. -900 to -600 ns and -1350 to 900 ns. Therefore, the random spectrum should be rescaled by a factor of $\frac{2}{3}$ in order to subtract it from the prompt spectrum. For the ^{184}Hg-on-^{120}Sn experiment, no downscaling on the random coincidences was enforced, so the prompt window was chosen to be -900 to 550 ns, and for the random window, the sum of the windows from -2025 to -900 and from -550 to 2000 have been selected. This yields a value for the ratio of both windows of ≈ 0.095. Furthermore, in all cases the time windows for prompt and random coincidence between two γ rays remain 0 to 300 ns and 400 to 700 ns. Due to low statistics, no $\gamma_1 - \gamma_2$ coincidence are discussed in the ^{184}Hg-on-^{107}Ag experiment.

6.2.2.2 Extraction of the singles integrals

Figure 6.23 shows the γ-ray spectra coincident with the $2_1^+ \rightarrow 0_{g.s.}^+$ γ transition at 367 keV for the three energy windows.

Only the $4_1^+ \rightarrow 2_1^+$ transition with an energy of 287 keV, and the K X-rays seem to be present. No sign of the $2_2^+ \rightarrow 2_1^+$ is observed. Table 6.27 shows the integrals of the transitions in the six spectra above, combined with their final integrals, which are calculated according to the procedure in section 4.6.

Target	Transition	E_γ [keV]	Int. centre	Int. left	Int. right	Total int.
^{112}Cd	$4_1^+ \rightarrow 2_1^+$	287	56 (11)	9 (9)	21 (5)	41 (13)
	K_α	69	52 (18)	10 (11)	14 (8)	40 (20)
^{120}Sn	$4_1^+ \rightarrow 2_1^+$	287	64 (10)	9 (6)	-3 (3)	61 (11)
	K_α	69	63 (16)	3 (7)	-9 (5)	66 (17)

Table 6.27: Integrals of the two observed transitions in the constructed coincidence spectra, together with the calculated total integral.

In order to convert these intensities to the full γ-ray spectrum, the same procedure as in section 6.1.2 is applied. The ratio $R_{4_1^+ \rightarrow 2_1^+}$ defined in equation 6.1 amounts to 0.21 (8) for the ^{112}Cd experiment and to 0.22 (5) for the experiment on the ^{120}Sn target.

Target	Transition	E_X [keV]	Integral in coincidence	Integral in full spectrum
^{112}Cd	K_α	69	40 (20)	188 (118)
^{120}Sn			66 (17)	299 (102)

Table 6.28: Calculation of the K_α intensities in the full γ-ray spectrum from the observed integrals in the coincidence spectra.

The observed amount of K_α X-rays in the full spectrum in the two experiments is 529 (45) (on the ^{112}Cd target) and 517 (42) (on the ^{120}Sn target). After subtraction from the heavy-ion K_α vacancy creation and the electron conversion from other observed transitions, 360 (49) and 328 (45) K_α's remain for the respective targets, which are attributed solely to nuclear processes. This subtraction also needs to be done in the integrals obtained from the coincidence spectra, yielding intensities of 29 (20) and 55 (17), which are then converted to the full γ-ray spectrum using the ratio $R_{4_1^+ \to 2_1^+}$, resulting in total integrals of 137 (107) and 247 (95) for the respective targets, originating from the $E0$ component of the $2_2^+ \to 2_1^+$ transition. By subtracting these intensities from the total amount of K_α X-rays resulting from nuclear processes (360 (49) and 328 (45)), intensities of 223 (118) and 82 (106) counts remain which are attributed to the $E0$ deexcitation of the 0_2^+ state.

It is necessary to correct the intensities of these two transitions for K_α branching and the fluorescence, because total deexcitation count rates are needed in the further analysis. For the integrals in the experiment on the ^{120}Sn target, the values also need to be increased by a factor $\frac{23}{20}$, since only 20 MINIBALL cores were operational for the detection of K_α X-rays, due to a higher detection threshold in three cores.

Table 6.29 presents the K_α integrals in the full γ-ray spectrum, deduced from the coincidence spectra, converted and corrected according to the considerations described above.

Target	Transition	Corrected integral in full spectrum
^{112}Cd	$E0(2_2^+ \to 2_1^+)$	192 (151)
	$E0(0_2^+ \to 0_1^+)$	314 (166)
^{120}Sn	$E0(2_2^+ \to 2_1^+)$	399 (155)
	$E0(0_2^+ \to 0_1^+)$	132 (171)

Table 6.29: Full γ-ray spectrum photo peak intensities derived from the coincidence spectra, after corrections.

Like in the ^{182}Hg case, due to the applied corrections, these integrals include non-fluorescent deexcitation and other electron paths than the K_α channel.

a)

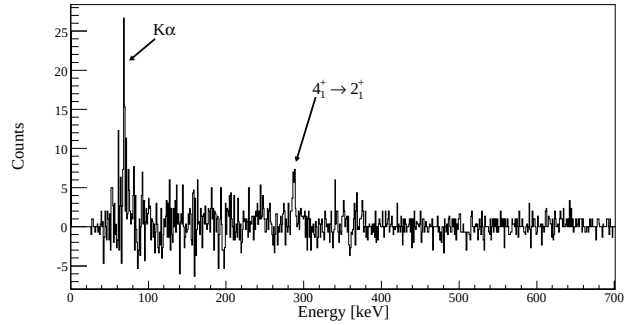

b)

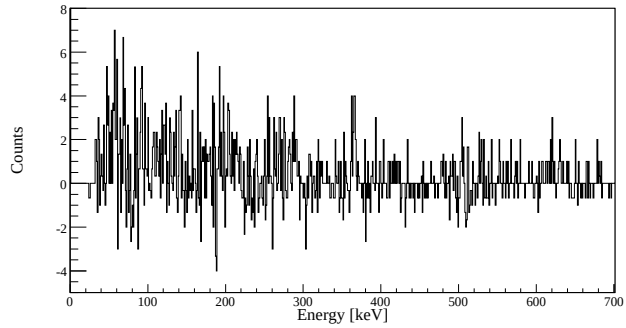

c)

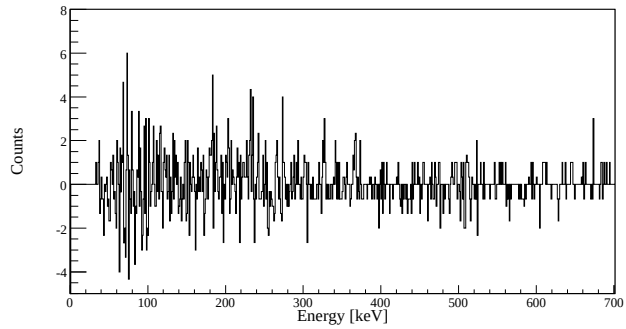

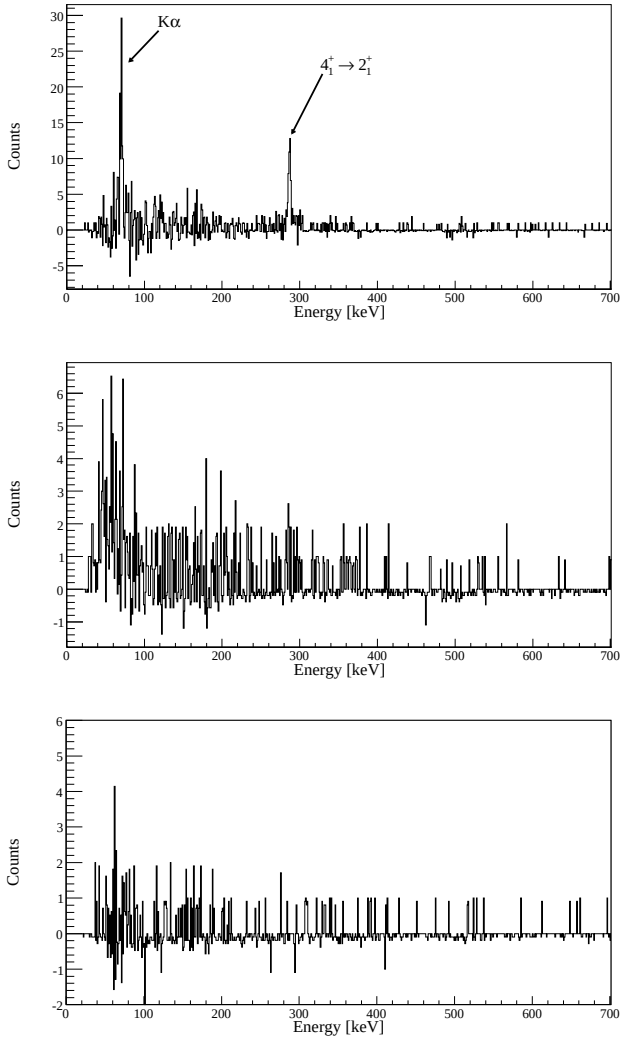

Figure 6.23: a) Spectrum of the γ rays coincident with a γ_1 ray around 367 keV (within the range 350 - 380 keV). b) and c) Idem, but the γ_1 ray energy window is slightly lower (within a range of 315 - 345 keV) or higher (within a range of 385 - 415 keV). The γ rays in these three spectra are Doppler corrected for the ^{184}Hg projectile. The spectra obtained with the ^{112}Cd target are presented in the left column, those obtained with the ^{120}Sn target in the right column.

6.2.3 Combined information on ^{184}Hg

6.2.3.1 Life times

In 1973, Rud et al. [Rud73] published life times of the yrast states with positive parity and even spin up to spin 6^+, including an upper limit for the yrast 8^+ state. The relevant life times for the further analysis of the Coulomb-excitation data are presented in table 6.30.

Nuclear state I^π	Life time τ [ps]
2_1^+	30 (7)
4_1^+	32.8 (34)
6_1^+	8.1 (31)

Table 6.30: Measured life times of the 2_1^+, 4_1^+ and 6_1^+ yrast states in ^{184}Hg from reference [Rud73].

In addition, Cole et al. proposed a life time of 0.9 (3) ns for the non-yrast 0_2^+ state [Col76].

Life times of positive parity yrast states with even spin in ^{184}Hg have been remeasured and published by L.P. Gaffney et al. [Gaf14]. They are presented here in table 6.31.

Nuclear state I^π	Life time τ [ps]
2_1^+	35.7 (15)
4_1^+	30.2 (10)
6_1^+	8.7 (4)

Table 6.31: Measured life times of the 2_1^+, 4_1^+ and 6_1^+ yrast states in ^{184}Hg from reference [Gaf14].

The values given in table 6.30 and table 6.31 are clearly in agreement. For the further analysis, the most recently obtained values of table 6.31 will be used, together with the known lifetime of the 0_2^+ state from reference [Col76].

6.2.3.2 Branching ratios and conversion coefficients

Branching ratios in ^{184}Hg have been published by Deng, Rud and Ma [Den95, Rud73, Ma86], which are summarized in table 6.32.

$\frac{I_i \to I_{f_1}}{I_i \to I_{f_2}}$	Ratio
$\frac{\gamma(2_2^+ \to 0_2^+)}{\gamma(2_2^+ \to 0_1^+)}$	<0.09
$\frac{\gamma(2_3^+ \to 2_1^+)}{\gamma(2_3^+ \to 0_2^+)}$	0.77 (30)
$\frac{\gamma(4_1^+ \to 2_1^+)}{\gamma(4_1^+ \to 2_2^+)}$	75.76 (1378)
$\frac{\gamma(4_2^+ \to 2_2^+)}{\gamma(4_2^+ \to 2_1^+)}$	1.54 (19)

Table 6.32: Measured branching ratios in ^{184}Hg from reference [Den95, Rud73, Ma86].

From a ^{184}Tl β decay experiment, Rapisarda et al. [Rap] have determined branching ratios and a conversion coefficient in ^{184}Hg that can be useful in the analysis of the Coulomb-excitation data. These most recently obtained results are in reasonable agreement with the values presented in table 6.32, so they will be used in the further analysis. Table 6.33 presents these values, which are compared to the branching ratios observed in the Coulomb-excitation data on the three experiments.

The observed branching ratios in the Coulomb-excitation experiments are in good agreement with the adopted values. Since the $2_2^+ \to 2_1^+$ is not observed, the $\frac{\gamma(2_2^+ \to 2_1^+)}{\gamma(2_2^+ \to 0_1^+)}$ branching ratio and the $\frac{e^-(2_2^+ \to 2_1^+)}{\gamma(2_2^+ \to 2_1^+)}$ conversion coefficient can be used to find a good estimation. Also the intensities of the unobserved $4_2^+ \to 2_1^+$ and $4_1^+ \to 2_2^+$ transitions can now be approximated.

$\frac{I_i \to I_{f_1}}{I_i \to I_{f_2}}$	Adopted ratio [Rap]	Coulomb excitation on ^{112}Cd	Coulomb excitation on ^{107}Ag	Coulomb excitation on ^{120}Sn
$\frac{\gamma(2_2^+ \to 2_1^+)}{\gamma(2_2^+ \to 0_1^+)}$	0.088 (20)	<0.34	<2.37	<0.19
$\frac{\gamma(2_2^+ \to 0_2^+)}{\gamma(2_2^+ \to 0_1^+)}$	0.082 (34)	<0.18	<1.29	<0.10
$\frac{\gamma(2_3^+ \to 2_1^+)}{\gamma(2_3^+ \to 0_2^+)}$	0.88 (28)	unknown	unknown	unknown
$\frac{\gamma(4_1^+ \to 2_1^+)}{\gamma(4_1^+ \to 2_2^+)}$	33.4 (234)	>9.29	>1.93	>13.29
$\frac{\gamma(4_2^+ \to 2_2^+)}{\gamma(4_2^+ \to 2_1^+)}$	1.33 (23)	unknown	unknown	>0.59
$\frac{e^-(2_2^+ \to 2_1^+)}{\gamma(2_2^+ \to 2_1^+)}$	23 (5)	>2.7	unknown	>6.5

Table 6.33: Comparison between the adopted branching ratios in ^{184}Hg from reference [Rap] and those observed in the Coulomb-excitation data.

6.2.3.3 Summary

In order to analyze the Coulomb-excitation data on ^{184}Hg, the information below will be used:

1. The extracted integrals from the Coulomb-excitation γ-ray spectra on the three targets that were employed. These intensities can be found in tables 6.23, 6.25 and 6.26. In some cases angular particle cuts are applied.
2. The extracted integrals of the $E0(2_2^+ \to 2_1^+)$ and $E0(0_2^+ \to 0_1^+)$ transitions in the total γ-ray spectrum. These can be found in table 6.29.
3. The life times of the 2_1^+, 4_1^+, 6_1^+ and 0_2^+ states, presented in table 6.31.
4. The measured branching ratios relevant for the further analysis and the conversion coefficient of the $2_2^+ \to 2_1^+$ transition, given in table 6.33.

6.2.4 GOSIA analysis

Like in the ^{182}Hg analysis, also here the GOSIA analysis is performed by including all information except for the life times, since they are expected to be reproduced by the Coulomb-excitation data. Again, a first estimation of the $\langle 0_1^+ \| E2 \| 2_1^+ \rangle$ matrix element is found by reducing the ^{184}Hg level scheme to the 0_1^+ and 2_1^+ states.

6.2.4.1 First approximation of $\langle 0_1^+ \| E2 \| 2_1^+ \rangle$

The $\langle 0_1^+ \| E2 \| 2_1^+ \rangle$ can be estimated by the absolute normalization of the $2_1^+ \rightarrow 0_{g.s.}^+$ γ transition in ^{184}Hg to the $2_1^+ \rightarrow 0_{g.s.}^+$ γ transition in ^{112}Cd, and this for three angular particle gates. No absolute normalization could be achieved for the experiment on the ^{120}Sn, since no satisfying intensity for its $2_1^+ \rightarrow 0_{g.s.}^+$ γ transition has been observed, due to the low excitation cross section to the 2_1^+ state in this nucleus. The experiment on the ^{107}Ag could be used neither, the reason for this being explained in appendix A.

Table 6.34 presents the observed integrals for both projectile and target, together with the target angles in the laboratory frame. The error bars have been increased according to the uncertainties in the γ ray efficiencies.

$\theta_{lab,t}[^\circ]$	$I_\gamma(2_1^+ \rightarrow 0_1^+)$ in ^{184}Hg	$I_\gamma(2_1^+ \rightarrow 0_1^+)$ in ^{112}Cd
43.6 - 51.6	1082 (47)	198 (22)
32.9 - 43.6	960 (43)	176 (20)
18.7 - 32.8	490 (28)	103 (13)

Table 6.34: The integrated photo peak intensities I_γ are given for the observed $2_1^+ \rightarrow 0_1^+$ transition in ^{184}Hg and in ^{112}Cd for the three angular particle gates.

Knowing the excitation cross section of the 2_1^+ state in ^{112}Cd, its expected $2_1^+ \rightarrow 0_1^+$ γ intensity can be calculated and compared to the one observed. The registered $2_1^+ \rightarrow 0_1^+$ γ-ray intensity in ^{184}Hg can then be used to determine the excitation cross section of its 2_1^+ state. Assuming a different $\langle 2_1^+ \| E2 \| 2_1^+ \rangle$ diagonal matrix element in ^{184}Hg, the calculated $\langle 0_1^+ \| E2 \| 2_1^+ \rangle$ transitional matrix element should remain constant throughout the three angular ranges.

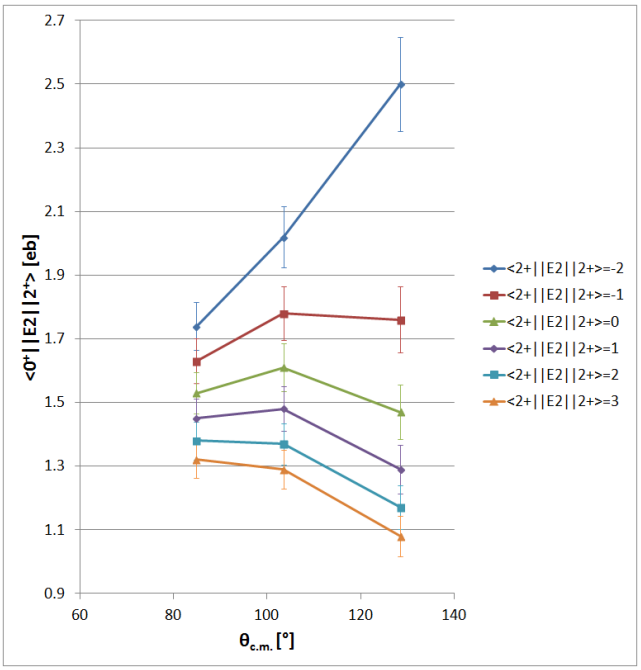

Figure 6.24: The $\langle 0^+_{g.s.} \| E2 \| 2^+_1 \rangle$ matrix element in ^{184}Hg for the three angular ranges, assuming different integer values of the $\langle 2^+_1 \| E2 \| 2^+_1 \rangle$ matrix element in this nucleus.

From figure 6.24, the $\langle 2^+_1 \| E2 \| 2^+_1 \rangle$ matrix element can be assumed to amount to value around -1, the $\langle 0^+_{g.s.} \| E2 \| 2^+_1 \rangle$ matrix element being approximately 1.7.

A GOSIA2 calculation of the reduced χ^2_ν per combination of $\langle 0^+_{g.s.} \| E2 \| 2^+_1 \rangle$ and $\langle 2^+_1 \| E2 \| 2^+_1 \rangle$ in ^{184}Hg is presented in figure 6.25. These reduced χ^2_ν's are the sum of the reduced χ^2_ν's in the projectile and in the target.

The errors on both matrix elements can be estimated by increasing the minimal total χ^2 by 1. This is addressed in figure 6.26.

These calculations result in $\langle 0^+_{g.s.} \| E2 \| 2^+_1 \rangle$ = 1.65 (15) and $\langle 2^+_1 \| E2 \| 2^+_1 \rangle$ = -1.3 (7).

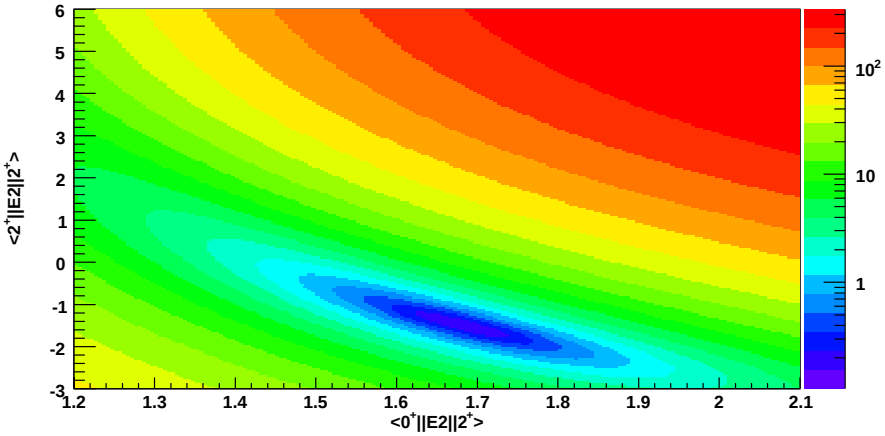

Figure 6.25: Reduced χ^2_ν surface assuming different values of the $\langle 0^+_{g.s.}\|E2\|2^+_1\rangle$ and the $\langle 2^+_1\|E2\|2^+_1\rangle$ matrix elements in ^{184}Hg.

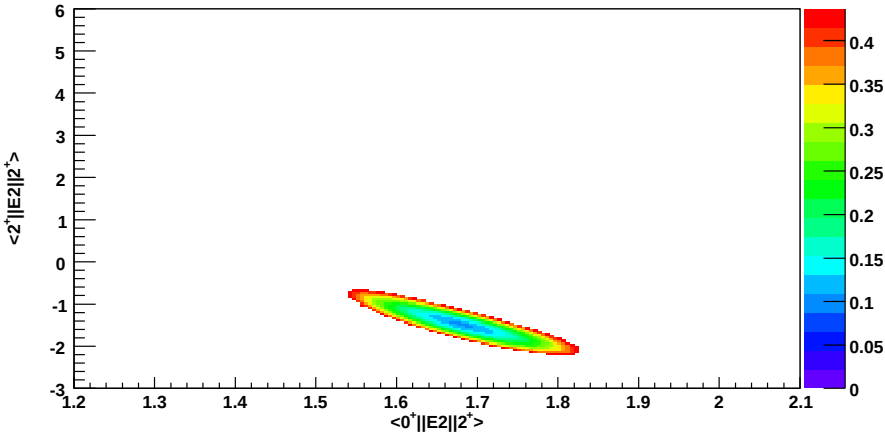

Figure 6.26: Reduced χ^2_ν surface with the condition $\chi^2 < \chi^2_{\rm min} + 1$, enabling 1σ uncertainties for $\langle 0^+_{g.s.}\|E2\|2^+_1\rangle$ and $\langle 2^+_1\|E2\|2^+_1\rangle$ to be estimated.

6.2.4.2 Further analysis in GOSIA1

The GOSIA1 analysis needs a specific input in order to estimate the $E2$ matrix elements. At first, the known life times are not included.

6.2.4.2.1 The energy level scheme

Table 6.35 gives the included nuclear levels in ^{184}Hg, together with their spins, parities and energies. The level scheme of ^{184}Hg is shown in figure 6.27.

I^π	Energy [keV]
0_1^+	0
2_1^+	367
0_2^+	375
2_2^+	534
4_1^+	653
2_3^+	983
6_1^+	994
4_2^+	1086

Table 6.35: Nuclear levels included in the GOSIA1 analysis.

Like in the analysis of ^{182}Hg, the observation of $E0$ transitions between the 2_2^+ and 2_1^+ states and the 0_2^+ and 0_1^+ states needs to be treated. Therefore two non-existing nuclear states with spin and parity 1^+ have been included at energies of 306 keV and 465 keV.

6.2.4.2.2 The matrix elements

The declared matrix elements in table 6.36 will be varied by GOSIA1 until a satisfying reproduction of the observed data has been achieved.

The 6_1^+ state is a buffer state in this analysis, since no deexcitations from it have been observed. The 2_3^+ is only coupled to the 0_2^+ and 2_1^+ state, since an unresolvable deexcitation doublet is observed to these two states, which have an energy difference of only 8 keV. Moreover, the branching ratio $\frac{\gamma(2_3^+ \to 2_1^+)}{\gamma(2_3^+ \to 0_2^+)}$ is known, so an estimation of the two channels can be made.

The two 1^+ states mentioned in the previous paragraph can be used to treat the deexcitation via electronic transitions, since GOSIA1 cannot include $E0$ decay

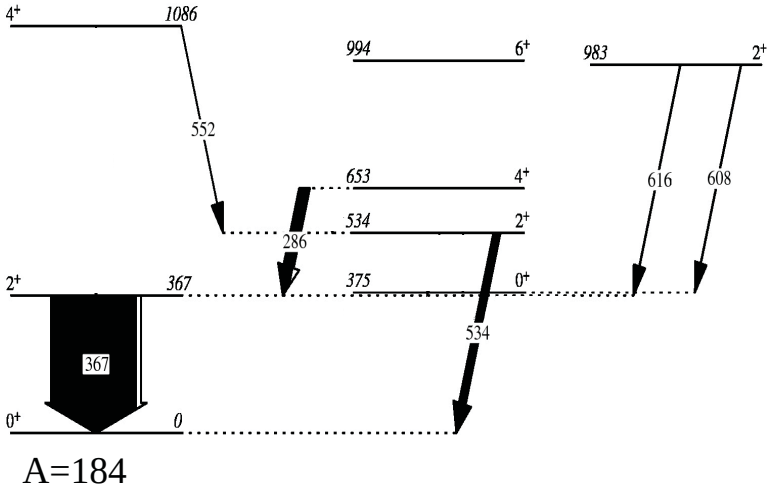

Figure 6.27: Scheme of the nuclear levels at low energy in ^{184}Hg. Black arrows indicate observed transitions in the total γ-ray spectrum of the Coulomb-excitation experiment, their relative thicknesses being related to their observed intensities in the ^{184}Hg-on^{112}Cd experiment, where the transitions were the most intense.

paths. The electrons will therefore be deviated via non-existing $M1$ transitions. In table 6.37, four extra matrix elements are declared.

The arguments for the use of $M1$ transitions replacing the $E0$ transitions in the GOSIA1 analysis were discussed for the ^{182}Hg case. Again, the energy difference between the 1_1^+ state and 0_2^+ state and the energy difference between the 1_2^+ state and 2_2^+ state exactly equal 69 keV, the energy of the K_α X-ray, making corrections for detection efficiency unnecessary.

The conversion coefficient and the known branching ratios, which are discussed in section 6.2.3.2, will also be included in the GOSIA1 analysis.

ME
$\langle 0_1^+ \| E2 \| 2_1^+ \rangle$
$\langle 0_1^+ \| E2 \| 2_2^+ \rangle$
$\langle 2_1^+ \| E2 \| 2_1^+ \rangle$
$\langle 2_1^+ \| E2 \| 0_2^+ \rangle$
$\langle 2_1^+ \| E2 \| 2_2^+ \rangle$
$\langle 2_1^+ \| E2 \| 4_1^+ \rangle$
$\langle 2_1^+ \| E2 \| 2_3^+ \rangle$
$\langle 2_1^+ \| E2 \| 4_2^+ \rangle$
$\langle 0_2^+ \| E2 \| 2_2^+ \rangle$
$\langle 0_2^+ \| E2 \| 2_3^+ \rangle$
$\langle 2_2^+ \| E2 \| 2_2^+ \rangle$
$\langle 2_2^+ \| E2 \| 4_1^+ \rangle$
$\langle 2_2^+ \| E2 \| 4_2^+ \rangle$
$\langle 4_1^+ \| E2 \| 4_1^+ \rangle$
$\langle 4_1^+ \| E2 \| 6_1^+ \rangle$
$\langle 2_1^+ \| M1 \| 2_2^+ \rangle$

Table 6.36: Matrix elements in ^{184}Hg that can be varied by GOSIA1 to reproduce the observed data. $E2$ matrix elements are expressed in units of eb, $M1$ matrix elements in units of μ_N.

ME
$\langle 0_1^+ \| M1 \| 1_1^+ \rangle$
$\langle 1_1^+ \| M1 \| 0_2^+ \rangle$
$\langle 2_1^+ \| M1 \| 1_2^+ \rangle$
$\langle 1_2^+ \| M1 \| 2_2^+ \rangle$

Table 6.37: Non-existing $M1$ matrix elements that are used to reproduce the $E0$ deexcitations.

6.2.4.2.3 Coulomb-excitation data

The Coulomb-excitation data are subdivided into nine different experiments. The first three experiments in the GOSIA1 input are the angular particle cuts with ^{112}Cd as the target nucleus, the fourth experiment covers the total angular particle detection range on that particular target. The fifth experiment gives the information obtained on the ^{107}Ag target, without any angular divisions. The sixth experiment contains the data when the ^{120}Sn target was used, and the last three experiments are the angular particle cuts on this target.

A relative normalization is obtained from the first three experiments. Since the particle detection efficiency can differ between the three angular cuts, GOSIA1 compares the three calculated deexcitation rates from the $2_1^+ \rightarrow 0_{g.s.}^+$ γ transition in ^{112}Cd in the three angular particle cuts to the observed integrals. The extracted normalization constants are then used as input for the further GOSIA1 analysis. Table 6.38 gives the integrals of the observed transitions in ^{184}Hg in the first three experiments. The errors on the γ ray detection efficiencies are included in the statistical error, as well as the statistical error on the observed transitions in ^{112}Cd. They all should be included in the uncertainties on the integrals in ^{184}Hg, since GOSIA1 does not allow errors for the γ ray efficiencies nor for the normalization constants to be declared.

$I_i \rightarrow I_f$	E_γ [keV]	$\theta_{lab,t}[^\circ]$	I_γ
$2_1^+ \rightarrow 0_1^+$	367	43.6 - 51.6	1082 (129)
$2_2^+ \rightarrow 0_1^+$	534		98 (27)
$4_1^+ \rightarrow 2_1^+$	287		42 (14)
$2_1^+ \rightarrow 0_1^+$	367	32.9 - 43.6	960 (116)
$2_2^+ \rightarrow 0_1^+$	534		39 (23)
$4_1^+ \rightarrow 2_1^+$	287		56 (15)
$2_1^+ \rightarrow 0_1^+$	367	18.7 - 32.8	490 (66)
$2_2^+ \rightarrow 0_1^+$	534		56 (16)
$4_1^+ \rightarrow 2_1^+$	287		43 (10)

Table 6.38: The integrated photo peak intensities I_γ are given for observed transitions in ^{184}Hg for the three angular particle gates.

In order to have an absolute normalization to the target, the value for the $\langle 0_1^+ \| E2 \| 2_1^+ \rangle$ matrix element in ^{184}Hg, inferred in section 6.2.4.1, will be included in the GOSIA1 analysis.

The integrals of the $E0(2_2^+ \rightarrow 2_1^+)$ and $E0(0_2^+ \rightarrow 0_1^+)$ transitions, extracted in section 6.2.2.2, will be included in the fourth experiment, since no angular particle cuts were made here. Analogously to the analysis of ^{182}Hg, a second data point for the $E0(0_2^+ \rightarrow 0_1^+)$ transition can be added. This procedure is explained in section 6.1.4.2.3. Table 6.39 gives the integrals serving as the GOSIA1 input for the fourth experiment.

$I_i \rightarrow I_f$	E_γ [keV]	$\theta_{lab,t}[^\circ]$	I_γ
$2_1^+ \rightarrow 0_1^+$	367	18.7 - 51.6	2532 (58)
$2_2^+ \rightarrow 1_2^+$	69		192 (151)
$0_2^+ \rightarrow 1_1^+$	69		200 (118)

Table 6.39: The integrated photo peak intensities I_γ and I_X are given for observed transitions in ^{184}Hg for the total angular particle range.

This fourth experiment is not normalized to any other, so no additional error due to the uncertainties in the $2_1^+ \rightarrow 0_{g.s.}^+$ γ transition in ^{112}Cd has to be added. Here, the $2_1^+ \rightarrow 0_{g.s.}^+$ γ transition in ^{184}Hg gives the integral to which the other transitions are normalized. Moreover, no uncertainties on the γ detection efficiency of the $2_1^+ \rightarrow 0_{g.s.}^+$ γ transition in ^{184}Hg have to be added, since the $E0$ integrals already have that efficiency error included by the way of constructing the coincidence spectrum and extracting the integrals.

Small incorrectnesses, due to the changing particle detection efficiency over the combined angular range of the fourth experiment, can be overcome by defining a limited azimuthal detection range for two of the three angular ranges within the total angular range of the fourth experiment. This procedure is explained for ^{182}Hg in section 6.1.4.2.3.

A detection limit for non-observed transitions of 30 counts has been included in this fourth experiment. The technical explanation about this in the input in GOSIA1 is the same as in the ^{182}Hg case and can be read in section 6.1.4.2.3.

For the fifth and sixth experiment, i.e. the total angular ranges with two identified particles on the ^{107}Ag and ^{120}Sn target, the same operations as in

the fourth experiment are applied: the changing particle detection efficiency is coped with by declaring a limited azimuthal detection range for two of the three angular ranges, and a detection limit of 30 counts for the non-observed transitions is maintained. For both experiments, the limited azimuthal detection range is based on the normalization to the transitions observed in the ^{107}Ag target, because the scarce excitation to the 2_1^+ state in ^{120}Sn could not provide reasonable intensities. This approximation can be justified, as the experiments on these two targets were performed in the same 2008 campaign. Again, the statistical errors on the γ detection efficiency of the $2_1^+ \rightarrow 0_{g.s.}^+$ γ transition in ^{184}Hg do not have to be taken into account, due to the method of constructing the γ - γ coincidence spectrum and the determination of the integrals. However, in the sixth experiment, this error is added to the uncertainties on the $4_2^+ \rightarrow 2_2^+$ and the $2_3^+ \rightarrow 0_2^+/2_3^+ \rightarrow 2_1^+$ intensities, since these count rates have not been inferred from the coincidence spectra, but directly from the total two-particle angular range.

The last three experiments are the three particle gates placed on the ^{120}Sn target, where the $2_1^+ \rightarrow 0_{g.s.}^+$, the $2_2^+ \rightarrow 0_{g.s.}^+$ and the $4_1^+ \rightarrow 2_1^+$ γ-ray intensities are declared. The uncertainties on the γ detection efficiency have to be taken into account, but no statistical errors on the target excitation have to be taken into consideration, since these three experiment are not normalized to one another, due to insufficient 2_1^+ state population in ^{120}Sn.

6.2.4.2.4 Results

Table 6.40 shows the resulting values for the matrix elements.

It is clear that the obtained value of $1.32^{0.01}_{0.06}$ eb for the $\langle 0_1^+ \| E2 \| 2_1^+ \rangle$ matrix element differs significantly from the value found in the first GOSIA2 analysis without higher-energy states, being $1.65^{0.15}_{0.15}$ eb. This is due to the fact that in order to obtain a stable solution, it was necessary in this analysis to run GOSIA2 again after the GOSIA1 analysis, with all matrix elements apart from the $\langle 0_1^+ \| E2 \| 2_1^+ \rangle$ and the $\langle 2_1^+ \| E2 \| 2_1^+ \rangle$ matrix elements serving as fixed input to reproduce the intensities of the transitions other than the $2_1^+ \rightarrow 0_{g.s.}^+$ transition. A significant decrease of the $\langle 0_1^+ \| E2 \| 2_1^+ \rangle$ matrix element was observed. The new $\langle 0_1^+ \| E2 \| 2_1^+ \rangle$ matrix element was then used as an input in GOSIA1, since no absolute normalization is present. This procedure has been repeated a few times until stable values for all matrix elements were achieved. This can be an indication of the importance of the nuclear states other than the 0_1^+ and 2_1^+ states and the matrix elements connecting them.

Like in the ^{182}Hg analysis, the inclusion of the unobserved 6_1^+ buffer state causes the $\langle 4_1^+ \| E2 \| 6_1^+ \rangle$ to have a large error bar. Big uncertainties are also observed

ME	Obtained value [eb or μ_N]
$\langle 0_1^+ \| E2 \| 2_1^+ \rangle$	$1.32^{0.01}_{0.06}$
$\langle 0_1^+ \| E2 \| 2_2^+ \rangle$	$-0.20^{0.01}_{0.01}$
$\langle 2_1^+ \| E2 \| 2_1^+ \rangle$	$0.81^{1.32}_{1.90}$
$\langle 2_1^+ \| E2 \| 0_2^+ \rangle$	$-5.07^{0.55}_{0.39}$
$\langle 2_1^+ \| E2 \| 2_2^+ \rangle$	$-0.30^{0.32}_{0.16}$
$\langle 2_1^+ \| E2 \| 4_1^+ \rangle$	$-3.25^{0.26}_{0.21}$
$\langle 2_1^+ \| E2 \| 2_3^+ \rangle$	$-0.80^{0.07}_{0.10}$
$\langle 2_1^+ \| E2 \| 4_2^+ \rangle$	$3.22^{0.20}_{0.16}$
$\langle 0_2^+ \| E2 \| 2_2^+ \rangle$	$1.23^{0.12}_{0.14}$
$\langle 0_2^+ \| E2 \| 2_3^+ \rangle$	$0.96^{0.09}_{0.10}$
$\langle 2_2^+ \| E2 \| 2_2^+ \rangle$	$1.52^{2.30}_{2.00}$
$\langle 2_2^+ \| E2 \| 4_1^+ \rangle$	$6.58^{0.45}_{0.32}$
$\langle 2_2^+ \| E2 \| 4_2^+ \rangle$	$-7.70^{0.43}_{0.40}$
$\langle 4_1^+ \| E2 \| 4_1^+ \rangle$	$-8.66^{2.13}_{0.89}$
$\langle 4_1^+ \| E2 \| 6_1^+ \rangle$	$0.10^{8.38}_{8.56}$
$\langle 2_1^+ \| M1 \| 2_2^+ \rangle$	$0.13^{0.01}_{0.01}$
$\langle 0_1^+ \| M1 \| 1_1^+ \rangle$	$0.10^{8.38}_{8.52}$
$\langle 1_1^+ \| M1 \| 0_2^+ \rangle$	$0.06^{0.01}_{0.11}$
$\langle 2_1^+ \| M1 \| 1_2^+ \rangle$	$0.10^{6.76}_{6.93}$
$\langle 1_2^+ \| M1 \| 2_2^+ \rangle$	$2.33^{0.15}_{0.11}$

Table 6.40: Matrix elements obtained from the GOSIA1 analysis without inclusion of the known life times.

in the $\langle 0_1^+ \| M1 \| 1_1^+ \rangle$ and $\langle 2_1^+ \| M1 \| 1_2^+ \rangle$ matrix elements, since the 1_1^+ and 1_2^+ non-existing auxiliary states only have one way of deexcitation, and the $M1$ excitation probability is small.

6.2.4.2.5 Comparison with known life times

The obtained matrix elements allow now for the life times of the 2_1^+ and 4_1^+ yrast states in ^{184}Hg to be calculated, and they can be compared to the known matrix elements given in table 6.31. A value for the life time of the 0_2^+ cannot be given, due to the big uncertainty on the $\langle 1_1^+ \| M1 \| 0_2^+ \rangle$ matrix element.

Nuclear state I^π	Life time τ [ps] from matrix elements	Known life time τ [ps]
2_1^+	33.2 (30)	35.7 (15)
4_1^+	27.8 (44)	30.2 (10)

Table 6.41: Comparison of the life times of the 2_1^+ and 4_1^+ yrast states in ^{184}Hg deduced from the matrix elements obtained from the Coulomb-excitation experiment to the known life times.

Since these values are in good agreement, the known life times can now be included in the GOSIA1 analysis.

6.2.4.3 Including the life times in GOSIA1

6.2.4.3.1 Obtained matrix elements

After inclusion of the known life times in GOSIA1, a more refined result is found. The physically relevant matrix element are presented in table 6.42

Analogous to the ^{182}Hg case, the inclusion of the life times decreases the error bars on the $\langle 0_1^+ \| E2 \| 2_1^+ \rangle$, $\langle 2_1^+ \| E2 \| 4_1^+ \rangle$ and $\langle 4_1^+ \| E2 \| 6_1^+ \rangle$ matrix elements.

In reference [Rap], the possibility of the presence of another state around 1086 keV has been advocated. This could explain the high value of the $\langle 2_2^+ \| E2 \| 4_2^+ \rangle$ matrix element, since only a 4_2^+ state has been taken into account by the GOSIA1 analysis.

It is also important to state that the obtained solution is independent of the sign of the $\langle 0_2^+ \| E2 \| 2_3^+ \rangle$ and $\langle 2_1^+ \| M1 \| 2_2^+ \rangle$ matrix elements.

Like in the analysis of the ^{182}Hg data, a starting value of $\delta = 1.85$ was introduced in GOSIA, extracted from known values in even-even nuclei in this region of the nuclear chart. Changing this value in GOSIA1 didn't cause relevant changes in the matrix elements.

The stability of the $\langle 0_1^+ \| E2 \| 2_1^+ \rangle$ can be checked by using GOSIA2 for the absolute normalization to the ^{112}Cd target, as explained for ^{182}Hg in section 6.1.4.4. No deviations from the value of $1.27^{0.03}_{0.03}$ eb are found.

ME	Obtained value [eb or μ_N]
$\langle 0_1^+ \| E2 \| 2_1^+ \rangle$	$1.27^{0.03}_{0.03}$
$\langle 0_1^+ \| E2 \| 2_2^+ \rangle$	$-0.21^{0.02}_{0.02}$
$\langle 2_1^+ \| E2 \| 2_1^+ \rangle$	$1.51^{1.80}_{1.18}$
$\langle 2_1^+ \| E2 \| 0_2^+ \rangle$	$-3.29^{0.82}_{0.79}$
$\langle 2_1^+ \| E2 \| 2_2^+ \rangle$	$-0.91^{0.14}_{0.14}$
$\langle 2_1^+ \| E2 \| 4_1^+ \rangle$	$-3.15^{0.06}_{0.06}$
$\langle 2_1^+ \| E2 \| 2_3^+ \rangle$	$-0.92^{0.28}_{0.28}$
$\langle 2_1^+ \| E2 \| 4_2^+ \rangle$	$3.74^{0.75}_{0.75}$
$\langle 0_2^+ \| E2 \| 2_2^+ \rangle$	$1.25^{0.28}_{0.28}$
$\langle 0_2^+ \| E2 \| 2_3^+ \rangle$	$1.02^{0.30}_{0.30}$
$\langle 2_2^+ \| E2 \| 2_2^+ \rangle$	$-2.61^{2.00}_{2.01}$
$\langle 2_2^+ \| E2 \| 4_1^+ \rangle$	$5.80^{0.51}_{0.51}$
$\langle 2_2^+ \| E2 \| 4_2^+ \rangle$	$8.20^{1.58}_{1.61}$
$\langle 4_1^+ \| E2 \| 6_1^+ \rangle$	$4.94^{0.14}_{0.10}$
$\langle 2_1^+ \| M1 \| 2_2^+ \rangle$	$-0.07^{0.01}_{0.01}$

Table 6.42: Physically relevant matrix elements obtained from the GOSIA1 analysis with inclusion of the known life times.

6.3 The ^{186}Hg case

6.3.1 Intensity of the observed transitions

In the Coulomb-excitation experiments aiming at investigating the ^{186}Hg isotope, three different targets were employed: a 2.0 mg/cm^2 ^{114}Cd target during the 2009 campaign, and a 1.1 mg/cm^2 ^{107}Ag target and 2.3 mg/cm^2 ^{120}Sn target during the 2008 campaign. For the ^{186}Hg-on-^{114}Cd data set, the particle scattering range in the DSSSD was divided into three angular cuts when gating on the target: annular strips 0 to 4 covering a low c.m. angular scattering range, strips 5 to 10 corresponding to an intermediate c.m. angular scope, and strips 10 to 14 matching a high c.m. set of angles. No angular gating has been applied to the experiments where ^{186}Hg was incident on the ^{107}Ag or on the ^{120}Sn target: there only the total angular spectrum with two identified particles has been used in the analysis.

The relevant spectra obtained from the three experiments are presented in figures 6.28, 6.29 and 6.30.

Due to its low intensity, the $2_1^+ \rightarrow 0_1^+$ transition in ^{120}Sn observed in spectrum 6.30.d will not be used in the further analysis.

Table 6.43 summarizes the observed intensities in the ^{186}Hg-on-^{114}Cd experiment.

$I_i \rightarrow I_f$	E_γ [keV]	$\theta_{lab,t}[^\circ]$	$\theta_{c.m.}[^\circ]$	I_γ	$\epsilon_{\gamma,abs}[\%]$	$I_{\gamma,tot}$
$2_1^+ \rightarrow 0_1^+$	405	18.7 - 51.6	76.8 - 142.6	1622 (49)	10.02 (30)	16191 (693)
and	and	43.6 - 51.6	76.8 - 92.8	607 (31)		6059 (359)
$4_1^+ \rightarrow 2_1^+$	403	32.9 - 43.6	92.8 - 114.2	599 (29)		5979 (344)
	doublet	18.7 - 32.8	114.4 - 142.6	416 (24)		4153 (274)
K_α	≈69	18.7 - 51.6	76.8 - 142.6	122 (33)	12.81 (78)	953 (263)

Table 6.43: The integrated photo peak intensities I_γ (or I_X) are given for the observed $2_1^+ \rightarrow 0_1^+/4_1^+ \rightarrow 2_1^+$ doublet in ^{186}Hg when incident on the ^{114}Cd target for the total angular range and the three particle gates. Also K_α X-rays are present.

The amount of K_β X-rays could not be estimated due to low statistics and large uncertainties induced by the random events and the background at this low energy.

The integrated photo peak intensities for transitions observed in ^{114}Cd are addressed in table 6.44.

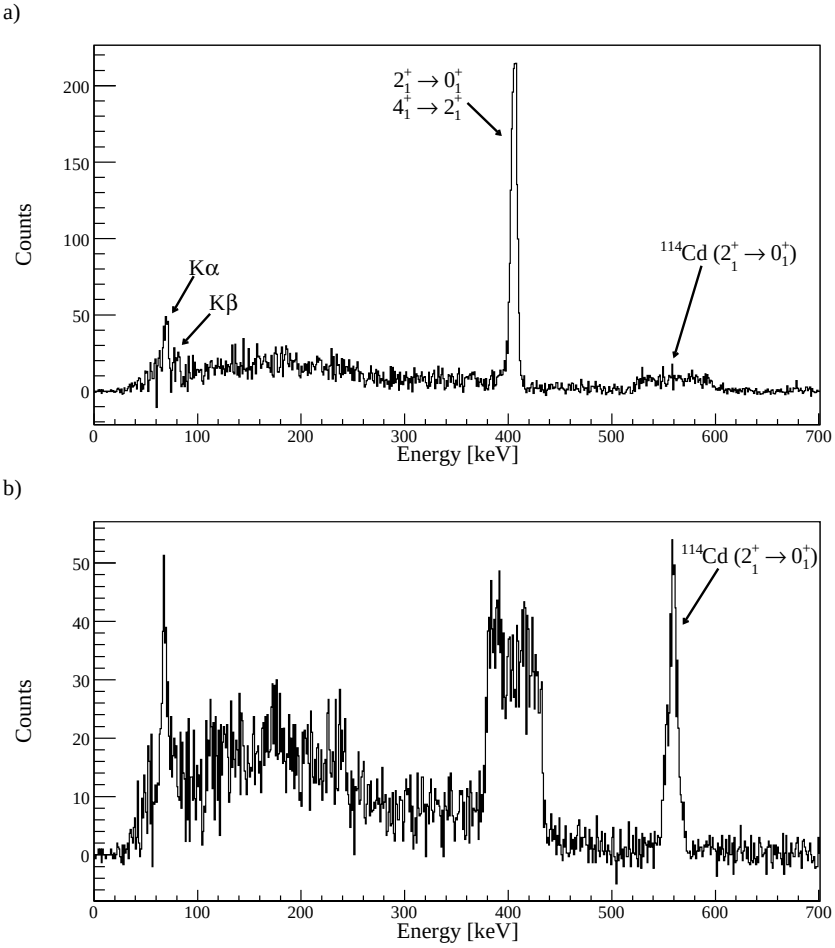

Figure 6.28: Random-subtracted γ-ray spectrum, coincident with two identified particles, Doppler corrected for the mercury projectile (a) and for the cadmium target (b). The spectra for the three particle angular cuts are not shown here. The sharp γ peak in (a) can be identified as the $2_1^+ \rightarrow 0_1^+/4_1^+ \rightarrow 2_1^+$ doublet, where the first transition has an energy of 405 keV, and the second an energy of 403 keV. Also prompt X-rays are detected with an energy around 69 keV.

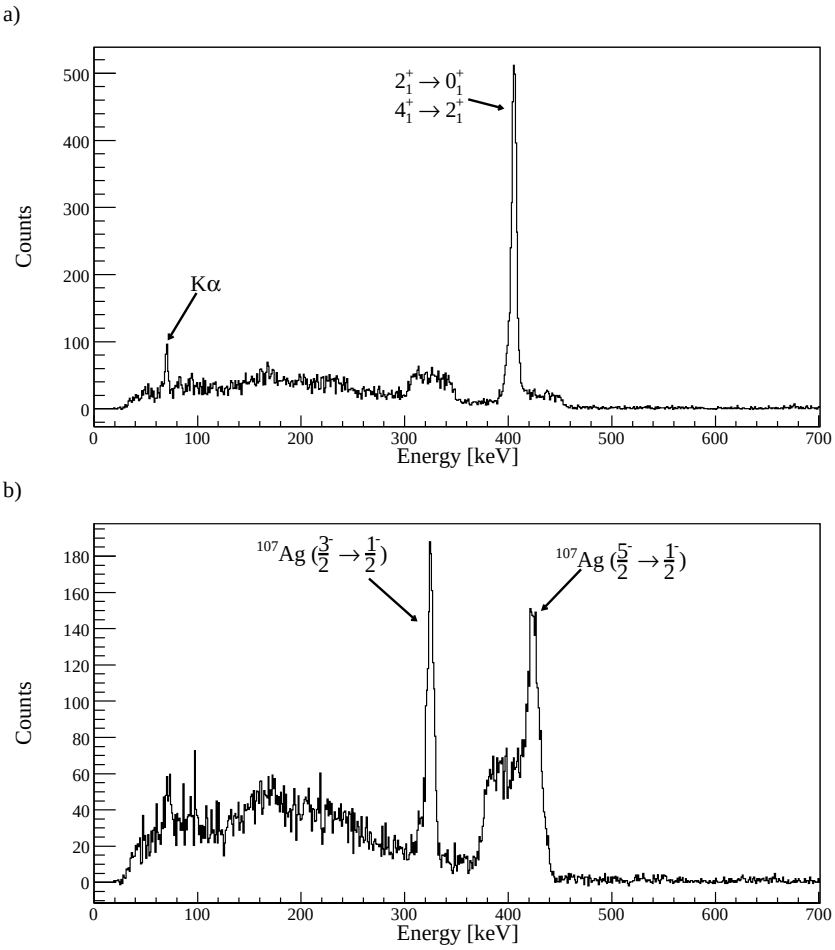

Figure 6.29: Random-subtracted γ-ray spectrum, coincident with two identified particles, Doppler corrected for the mercury projectile (a) and for the silver target (b). The same photo peaks are observed here as in figure 6.28.

a)

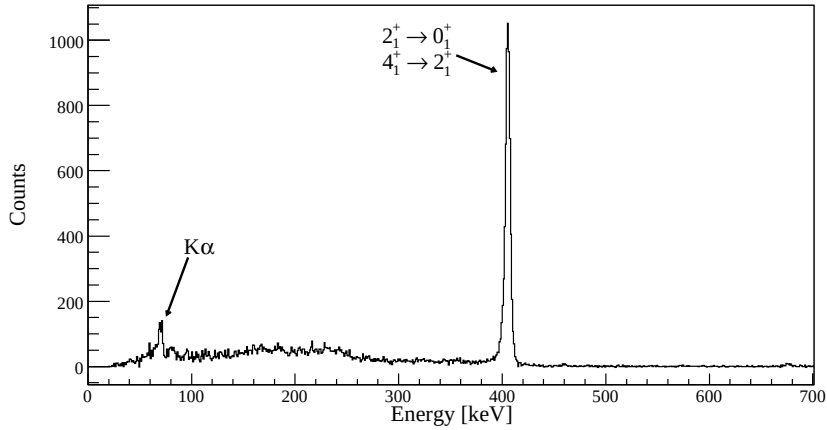

c)

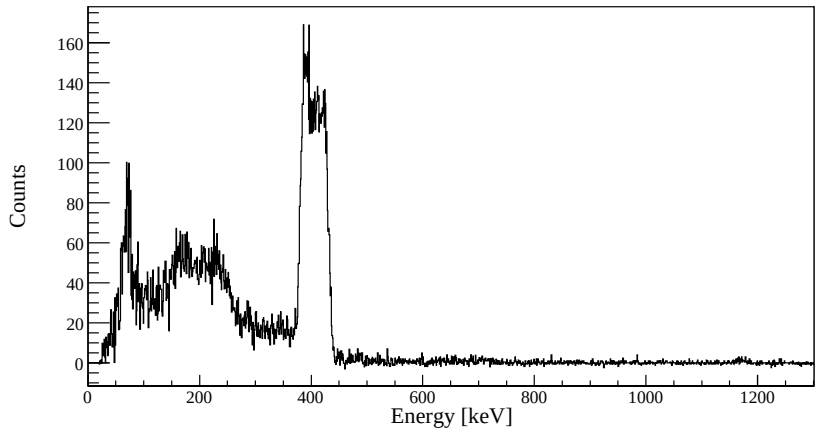

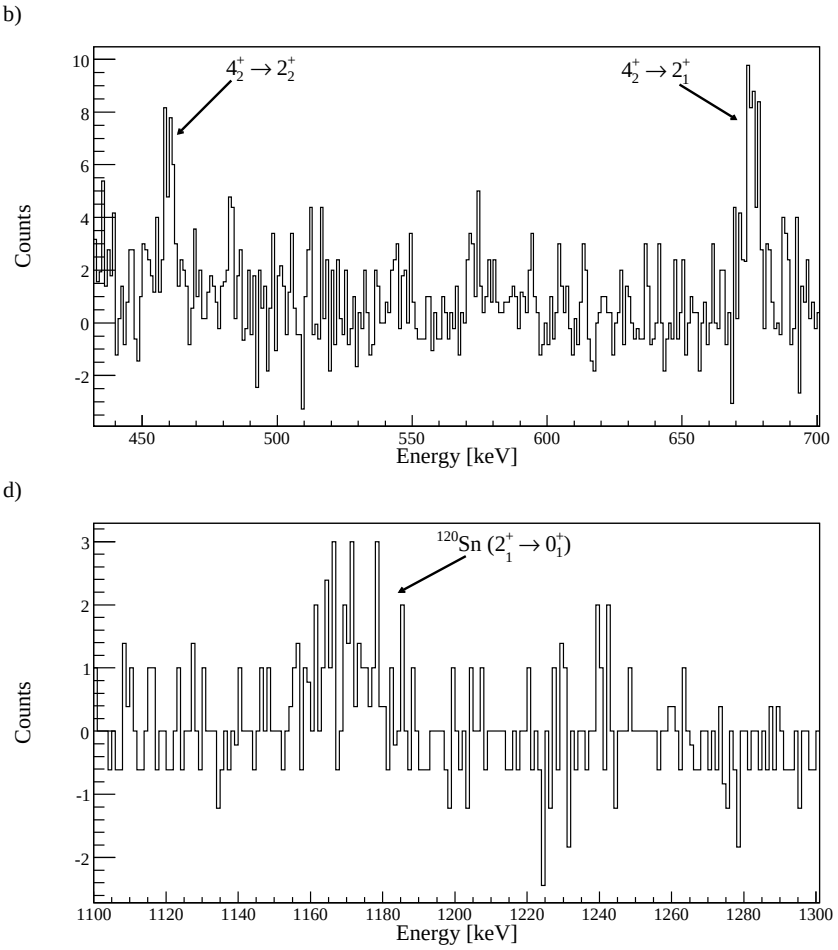

Figure 6.30: Random-subtracted γ-ray spectrum, coincident with two identified particles, Doppler corrected for the mercury projectile (a), enlarged around the energy region of the $4_2^+ \rightarrow 2_2^+$ (at 459 keV) and the $4_2^+ \rightarrow 2_1^+$ (at 675 keV) transitions (b). Also the random-subtracted γ-ray spectrum, Doppler corrected for the tin target is shown (c), enlarged around 1171 keV (d), the energy of the $2_1^+ \rightarrow 0_1^+$ transition in ^{120}Sn.

$I_i \rightarrow I_f$	E_γ [keV]	$\theta_{lab,t}[^\circ]$	$\theta_{c.m.}[^\circ]$	I_γ	$\epsilon_{\gamma,abs}[\%]$	$I_{\gamma,tot}$
$2_1^+ \rightarrow 0_1^+$	558	18.7 - 51.6 43.6 - 51.6 32.9 - 43.6 18.7 - 32.8	76.8 - 142.6 76.8 - 92.8 92.8 - 114.2 114.4 - 142.6	567 (27) 230 (17) 196 (16) 142 (13)	8.45 (48)	6709 (498) 2721 (257) 2319 (235) 1680 (177)

Table 6.44: The integrated photo peak intensities I_γ are given for the observed $2_1^+ \rightarrow 0_1^+$ transition in ^{114}Cd for the total angular range and the three particle gates.

The intensities observed in the ^{186}Hg-on-^{107}Ag experiment are presented in table 6.45.

$I_i \rightarrow I_f$	E_γ [keV]	$\theta_{lab,t}[^\circ]$	$\theta_{c.m.}[^\circ]$	I_γ	$\epsilon_{\gamma,abs}[\%]$	$I_{\gamma,tot}$
^{186}Hg						
$2_1^+ \rightarrow 0_1^+$	405 and	18.2 - 50.7	78.6 - 143.6	3356 (68)	12.80 (39)	26218 (956)
$4_1^+ \rightarrow 2_1^+$	403 doublet					
$4_2^+ \rightarrow 2_1^+$	675			46 (9)	9.84 (80)	467 (99)
K_α	≈ 69			253 (38)	14.23 (87)	1778 (285)
^{107}Ag						
$\frac{3}{2}^- \rightarrow \frac{1}{2}^-$	325	18.2 - 50.7	78.6 - 143.6	1396 (53)	14.54 (27)	9604 (404)

Table 6.45: Observed photo peak intensities I_γ (or I_X) are presented for the ^{186}Hg projectile and the ^{107}Ag target for the total angular range.

No integrated intensity for the $\frac{5}{2}^- \rightarrow \frac{1}{2}^-$ transition in ^{107}Ag has been given, because its energy of 423 keV is too close to the energy of the $2_1^+ \rightarrow 0_1^+$ transition

in ^{186}Hg at 405 keV. Furthermore, the observed intensity of the $\frac{3}{2}^- \rightarrow \frac{1}{2}^-$ in ^{107}Ag will not be used in the analysis, as stated in appendix A.

Table 6.46 gives the observed intensities in the ^{186}Hg-on-^{120}Sn experiment. The K_α/K_β ratio is found to equal 2.88 (81), in good agreement with the predicted value of ≈ 3.6.

$I_i \rightarrow I_f$	E_γ [keV]	$\theta_{lab,t}[^\circ]$	$\theta_{c.m.}[^\circ]$	I_γ	$\epsilon_{\gamma,abs}[\%]$	$I_{\gamma,tot}$
$2_1^+ \rightarrow 0_1^+$	405 and	18.2 - 50.7	78.6 - 143.6	6474 (89)	12.80 (39)	50577 (1681)
$4_1^+ \rightarrow 1_1^+$	403 doublet					
$4_2^+ \rightarrow 2_1^+$	675			58 (11)	9.84 (80)	589 (126)
$4_2^+ \rightarrow 2_2^+$	459			27 (13)	11.95 (46)	226 (113)
K_α	≈ 69			423 (53)	14.23 (87)	2973 (416)
K_β	≈ 80			173 (42)	16.77 (77)	1031 (252)

Table 6.46: The integrated photo peak intensities I_γ (or I_X) are given for the experiment where ^{186}Hg was incident on the ^{120}Sn target for the total angular range.

6.3.2 Intensity of the $\gamma - \gamma$ coincidences

6.3.2.1 Construction of the γ-ray spectra

For the construction of the γ-ray spectra coincident with the $2_1^+ \rightarrow 0_{g.s.}^+$ transition in ^{186}Hg at an energy of 405 keV, the same method has been applied as in the ^{182}Hg and ^{184}Hg cases. The produced spectra are of great interest in this particular case, since the intensity of the $4_1^+ \rightarrow 2_1^+$ transition at an energy of 403 keV can be extracted only by this procedure. The central energy window covers γ-ray energies between 380 and 420 keV, the lower window between 335 and 375 keV, and the higher window between 425 and 465 keV. For the experiments employing the ^{114}Cd and the ^{107}Ag target, a time window from -900

to -600 ns was chosen for the prompt coincidences with a particle, and a time window from -1350 to 900 ns was defined as the random-coincidence window. The random window should then be rescaled by a factor $\frac{2}{3} \approx 0.667$ in order to subtract it from the prompt window. In the ^{186}Hg-on-^{120}Sn experiment, the prompt window was defined from -900 to 625 ns, the random window remaining the same. This renders a scaling factor of ≈ 0.611. The time windows for prompt and random coincidence between two γ rays remain 0 to 300 ns and 400 to 700 ns.

6.3.2.2 Extraction of the singles integrals

The γ ray spectra coincident with the $2_1^+ \rightarrow 0_{g.s.}^+$ γ transition in ^{186}Hg at 405 keV for the three energy windows are shown in figures 6.31, 6.32 and 6.33.

Only the $4_1^+ \rightarrow 2_1^+$ transition with an energy of 403 keV seems to be present. Since the γ- ray on which is gated, can also be the $4_1^+ \rightarrow 2_1^+$ transition at 403 keV, the corresponding γ ray in the coincidence spectrum can also be the $2_1^+ \rightarrow 0_{g.s.}^+$ transition. Later in this section, this will be corrected for, enabling for the doublet in the singles γ-ray spectra to be resolved. It is clear that the γ rays originating from this transition can also be present when gating on the lower-energy window. These are due to Compton scattering, where one of the two coincident γ rays has a lower energy. In the ^{186}Hg-on-^{107}Ag case, an intensity is also observed when gating on the higher-energy window. This can be explained by the tail of the Doppler-broadened $\frac{5}{2}^- \rightarrow \frac{1}{2}^-$ transition at 423 keV in the target, being present in the energy window on which is gated. The observed photo peak in the coincidence spectrum then originates from simultaneous excitation of the projectile and the target to their respective 2_1^+ and $\frac{5}{2}^-$ states. The trace of K X-rays can be attributed to the K-vacancy creation phenomenon, so there is no excess of coincident K rays. Table 6.47 gives the integrals of the transitions in the twelve spectra above, combined with their final integrals, which are calculated according to the procedure in section 4.6. The remaining X-rays that were observed in the total γ-ray spectra (tables 6.43, 6.45 and 6.46) will hence be attributed to the $E0(0_2^+ \rightarrow 0_1^+)$ transition, after subtraction of the X-rays originating from K-vacancy creation and conversion from observed deexcitations.

For the ^{182}Hg and ^{184}Hg cases, the ratio $R_{4_1^+ \rightarrow 2_1^+}$ was defined in equation 6.1, in order to convert the intensities in the coincidence spectra to the full γ-ray spectrum. This ratio was chosen to be the intensity ratio of the $4_1^+ \rightarrow 2_1^+$ transition in the coincidence spectrum and in the full γ-ray spectrum. Since in the ^{186}Hg case, no $4_1^+ \rightarrow 2_1^+$ can be resolved from the $2_1^+ \rightarrow 0_{g.s.}^+ / 4_1^+ \rightarrow 2_1^+$ doublet in the full γ-ray spectrum, another strategy has to be searched for.

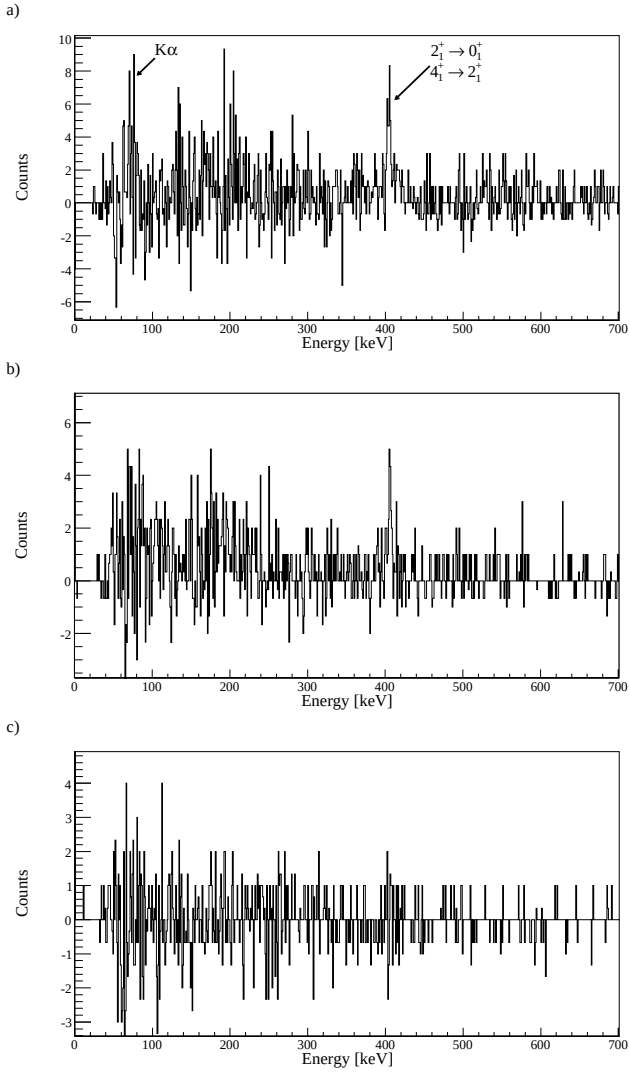

Figure 6.31: a) Spectrum of the γ rays coincident with a γ_1 ray around 405 keV (within the range of 380 - 420 keV), obtained with the ^{114}Cd target. b) and c) Idem, but the γ_1-ray energy window is slightly lower (within a range of 335 - 375 keV) or higher (within a range of 425 - 465 keV). The γ rays in these three spectra are Doppler corrected for the ^{186}Hg projectile.

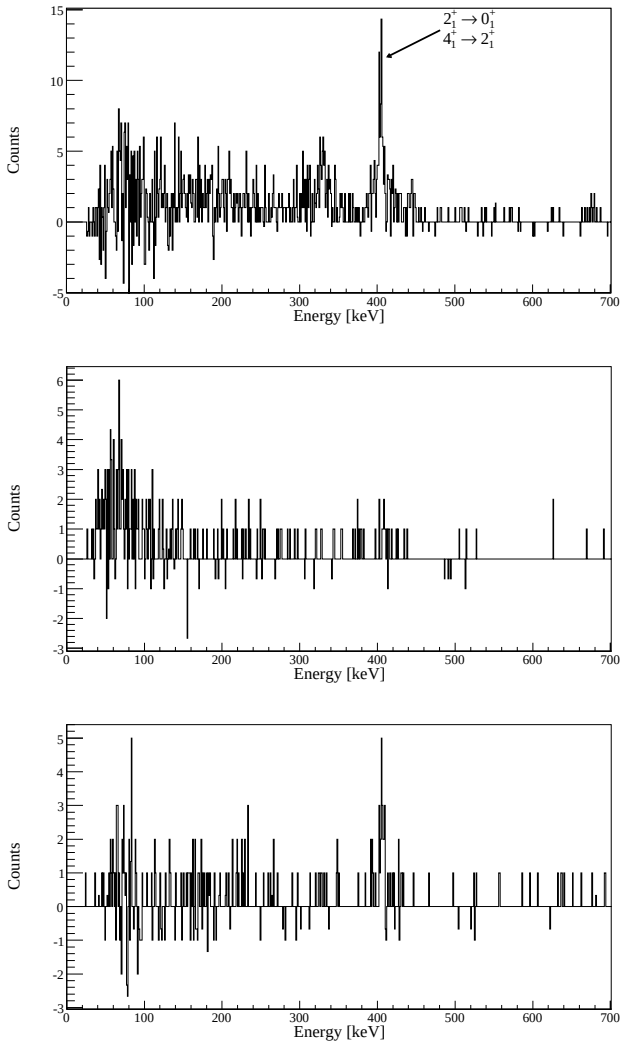

Figure 6.32: Same as figure 6.31, but obtained with the ^{107}Ag target.

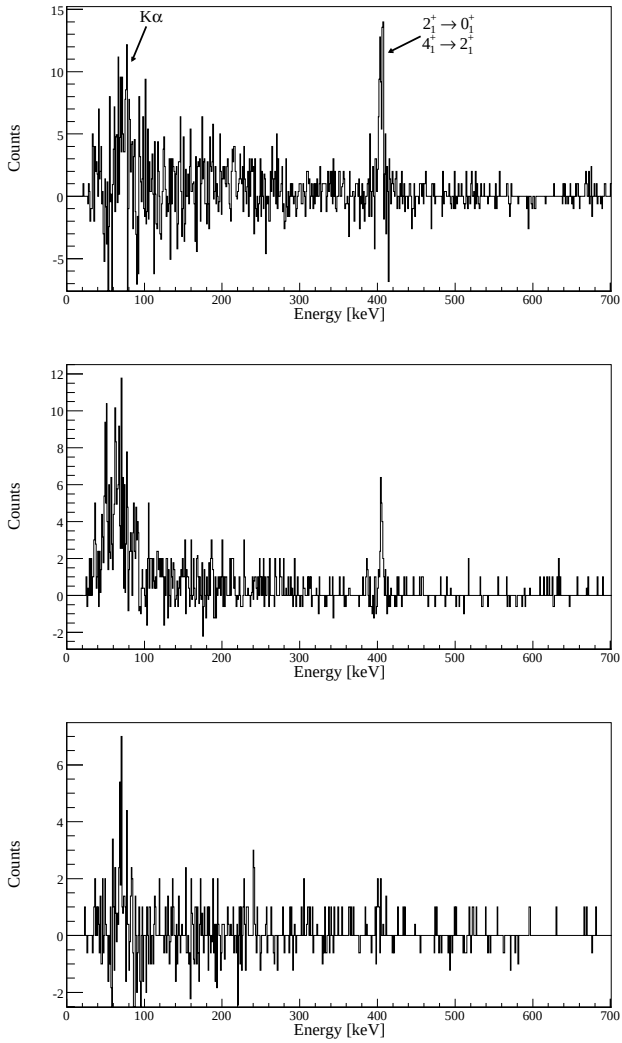

Figure 6.33: Same as figure 6.31, but obtained with the ^{120}Sn target.

Target	Transition	E_γ [keV]	Int. centre	Int. left	Int. right	Total int.
^{114}Cd	$4_1^+ \rightarrow 2_1^+$	403	58 (13)	25 (10)	4 (5)	44 (15)
^{107}Ag		and	86 (15)	10 (5)	27 (6)	68 (16)
^{120}Sn		405	102 (17)	22 (8)	3 (5)	90 (18)

Table 6.47: Integrals of the observed $4_1^+ \rightarrow 2_1^+$ transition in the constructed coincidence spectra, together with the calculated total integral.

As has been advocated in section 4.6.2, the coincidence spectrum, and the detection of exactly two particles in the full γ-ray spectrum identified as projectile and target, can cause the calculated intensity and the observed intensity to differ, as is observed in the ^{182}Hg, ^{184}Hg and ^{188}Hg cases. This problem can be overcome by comparing the intensity of the $2_1^+ \rightarrow 0_{g.s.}^+$ in the full γ-ray spectrum coincident with two identified particles and the intensity in the full γ-ray spectrum coincident with any amount of particles. The ratio of these two intensities can then be added as a factor for the extraction of full γ-ray intensities out of the intensities observed in the coincidence spectrum. However, when applying this procedure in the ^{182}Hg, ^{184}Hg and ^{188}Hg cases to the $4_1^+ \rightarrow 2_1^+$ transition in the coincidence spectrum, the calculated $4_1^+ \rightarrow 2_1^+$ full γ-ray intensity always differs slightly from the one observed. This is due to the different shape of the excitation cross section for exciting the 4_1^+ state (i.e. a two-step excitation) or the 2_1^+ state (which is mainly a one-step process). Indeed, the spectra demanding exactly two identified particles have a smaller angular range than those demanding any amount of particles, and the excitation cross sections for populating a certain nuclear state are dependent on the selected angular range. Therefore, the correction factor

$$F_{corr} = \frac{I_{4_1^+ \rightarrow 2_1^+, obs.}}{I_{4_1^+ \rightarrow 2_1^+, calc.}} \tag{6.5}$$

has been calculated for the ^{182}Hg, ^{184}Hg and ^{188}Hg cases on any ^{112,114}Cd or ^{120}Sn target. A weighted average of these values was adopted and applied as an additional correction factor in the ^{186}Hg case.

As a last correction, in order to resolve the $2_1^+ \rightarrow 0_{g.s.}^+$ and the $4_1^+ \rightarrow 2_1^+$ transitions, all events which have two coincident γ rays around 400 keV are only counted once. This procedure selects the $4_1^+ \rightarrow 2_1^+$ events coincident with

a $2_1^+ \rightarrow 0_{g.s.}^+$ transition. Table 6.48 presents the derived $4_1^+ \rightarrow 2_1^+$ intensities in the full γ-ray spectrum (with two identified particles).

Target	Transition	E_γ [keV]	Integral in coincidence	Integral in full spectrum
^{112}Cd	$4_1^+ \rightarrow 2_1^+$	403	22 (11)	61 (30)
^{107}Ag			34 (11)	138 (48)
^{120}Sn			45 (13)	158 (48)

Table 6.48: Calculation of the $4_1^+ \rightarrow 2_1^+$ intensities in the full γ-ray spectrum from the observed integrals in the coincidence spectra.

6.3.3 Combined information on ^{186}Hg

6.3.3.1 Life times

Proetel et al. [Pro74] measured life times for the yrast 2_1^+, 4_1^+, 6_1^+ and 8_1^+ states in ^{186}Hg. Life times for the 0_2^+ and 2_2^+ states were estimated by Joshi et al. [Jos94]. The values relevant for this analysis are presented in table 6.49.

Nuclear state I^π	Life time τ [ps]
2_1^+	26 (4)
0_2^+	<75
2_2^+	69 (39)
4_1^+	13 (4)
6_1^+	7 (3)

Table 6.49: Measured life times of the 2_1^+, 0_2^+, 2_2^+, 4_1^+ and 6_1^+ states in ^{186}Hg from [Pro74, Jos94].

Life times for the even-spin yrast states up to the 10_1^+ state can be found in [Gaf14]. Table 6.50 shows the obtained values up to the 6_1^+ state. Since some of the values differ strongly from the values given in table 6.49, the results for the 2_1^+, 4_1^+ and 6_1^+ states in ^{186}Hg will be adopted solely from the last table.

Nuclear state I^π	Life time τ [ps]
2_1^+	24 (3)
4_1^+	5.6 (20)
6_1^+	9.1 (4)

Table 6.50: Measured life times of the 2_1^+, 4_1^+ and 6_1^+ states in ^{186}Hg from [Gaf14].

6.3.3.2 Branching ratios and conversion coefficients

Branching ratios and conversion coefficients characterizing nuclear states in ^{186}Hg have been determined in more than one experiment. The National Nuclear Data Center [NND] provides values which are weighted averages from [Col77], [Ber77] and [Del94] for the states lying relatively low in energy. They are summarized in table 6.51.

The $\frac{\gamma(4_2^+ \to 2_2^+)}{\gamma(4_2^+ \to 2_1^+)} = 0.38\ (21)$ derived from the Coulomb-excitation experiment on the ^{120}Sn target can be considered to be in reasonable agreement with the known value.

6.3.3.3 Summary

The following information will be utilized in order to analyze the Coulomb-excitation data:

1. The extracted integrals from the Coulomb-excitation γ-ray spectra on the three employed targets. These intensities can be found in tables 6.43, 6.45 and 6.46. In the ^{186}Hg-on-^{120}Sn case, three angular particle cuts are applied.

$\frac{I_i \to I_{f_1}}{I_i \to I_{f_2}}$	Ratio
$\frac{\gamma(2_2^+ \to 2_1^+)}{\gamma(2_2^+ \to 0_1^+)}$	5.56 (56)
$\frac{\gamma(2_2^+ \to 0_2^+)}{\gamma(2_2^+ \to 0_1^+)}$	0.83 (44)
$\frac{\gamma(4_1^+ \to 2_2^+)}{\gamma(4_1^+ \to 2_1^+)}$	0.050 (13)
$\frac{\gamma(4_2^+ \to 2_2^+)}{\gamma(4_2^+ \to 2_1^+)}$	0.16 (2)
$\frac{\gamma(4_2^+ \to 4_1^+)}{\gamma(4_2^+ \to 2_1^+)}$	0.058 (2)
$\frac{e^-(2_2^+ \to 2_1^+)}{\gamma(2_2^+ \to 2_1^+)}$	3.5 (5)

Table 6.51: Measured branching ratios and one conversion coefficient in ^{186}Hg from [NND].

2. The extracted integrals of the $4_1^+ \to 2_1^+$ transition in the total γ-ray spectra, for the three experiments on the three targets. These can be found in table 6.48.

3. The life times of the 0_2^+ and 2_2^+ states (given in table 6.49), and those of the 2_1^+, 4_1^+ and 6_1^+ states (presented in table 6.50).

4. The measured branching ratios relevant for the further analysis and the conversion coefficient of the $2_2^+ \to 2_1^+$ transition, given in table 6.51.

6.3.4 GOSIA analysis

The analysis strategy used in the ^{182}Hg and ^{184}Hg cases will also be applied to the ^{186}Hg isotope. All information will be employed, except for the life times, which are expected to be reproduced by the Coulomb-excitation data. A preliminary value for the $\langle 0_1^+ \| E2 \| 2_1^+ \rangle$ matrix element is found by reducing the ^{186}Hg level scheme to the 0_1^+ and 2_1^+ states.

6.3.4.1 First approximation of $\langle 0_1^+ \| E2 \| 2_1^+ \rangle$

A first approximation of the $\langle 0_1^+ \| E2 \| 2_1^+ \rangle$ matrix element can be inferred from the absolute normalization of the $2_1^+ \rightarrow 0_{g.s.}^+$ γ transition in ^{186}Hg to the $2_1^+ \rightarrow 0_{g.s.}^+$ γ transition in ^{114}Cd, and this for the three angular particle gates. A normalization to the ^{120}Sn target could not be used in this analysis, since excitation to the 2_1^+ state in ^{120}Sn was scarce. Normalizing to the ^{107}Ag target was not useful for reasons addressed in appendix A.

Table 6.52 gives the extracted integrals for both projectile and target, together with the target angles in the laboratory frame. The statistical errors have been increased according to the uncertainties on the γ-ray efficiencies. The fact that the $4_1^+ \rightarrow 2_1^+$ is also included in the photo peak of the $2_1^+ \rightarrow 0_1^+$ transition, is neglected here.

$\theta_{lab,t}[^\circ]$	$I_\gamma(2_1^+ \rightarrow 0_1^+)$ in ^{186}Hg	$I_\gamma(2_1^+ \rightarrow 0_1^+)$ in ^{114}Cd
43.6 - 51.6	607 (36)	230 (22)
32.9 - 43.6	599 (34)	196 (20)
18.7 - 32.8	416 (27)	142 (15)

Table 6.52: The integrated photo peak intensities I_γ are given for the observed $2_1^+ \rightarrow 0_1^+$ transition in ^{186}Hg and in ^{114}Cd for the three angular particle gates.

The $\langle 0_1^+ \| E2 \| 2_1^+ \rangle$ transitional matrix element in ^{186}Hg can be calculated in each angular range, when assuming different values for the $\langle 2_1^+ \| E2 \| 2_1^+ \rangle$ diagonal matrix element. The calculated $\langle 0_1^+ \| E2 \| 2_1^+ \rangle$ matrix element should then remain constant over the different angular ranges. From figure 6.34, the $\langle 2_1^+ \| E2 \| 2_1^+ \rangle$

matrix element can be considered to be about 0, the $\langle 0^+_{g.s.} \| E2 \| 2^+_1 \rangle$ matrix element being approximately 1.3.

GOSIA2 can also calculate the reduced χ^2_ν per combination of $\langle 0^+_{g.s.} \| E2 \| 2^+_1 \rangle$ and $\langle 2^+_1 \| E2 \| 2^+_1 \rangle$ in ^{186}Hg. This is addressed in figure 6.35. These reduced χ^2_ν's are the sum of the reduced χ^2_ν's in the projectile and the target.

Errors on both matrix elements can be estimated by increasing the minimal total χ^2 by 1. This is treated in figure 6.36. These calculations result in $\langle 0^+_{g.s.} \| E2 \| 2^+_1 \rangle = 1.35\ (20)$ and $\langle 2^+_1 \| E2 \| 2^+_1 \rangle = 0.4\ (15)$.

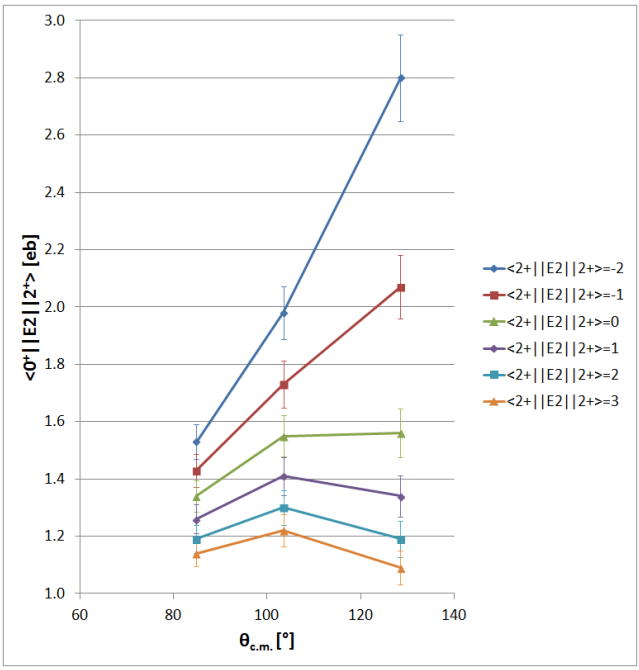

Figure 6.34: $\langle 0^+_{g.s.} \| E2 \| 2^+_1 \rangle$ for the three angular ranges, assuming different integer values of $\langle 2^+_1 \| E2 \| 2^+_1 \rangle$.

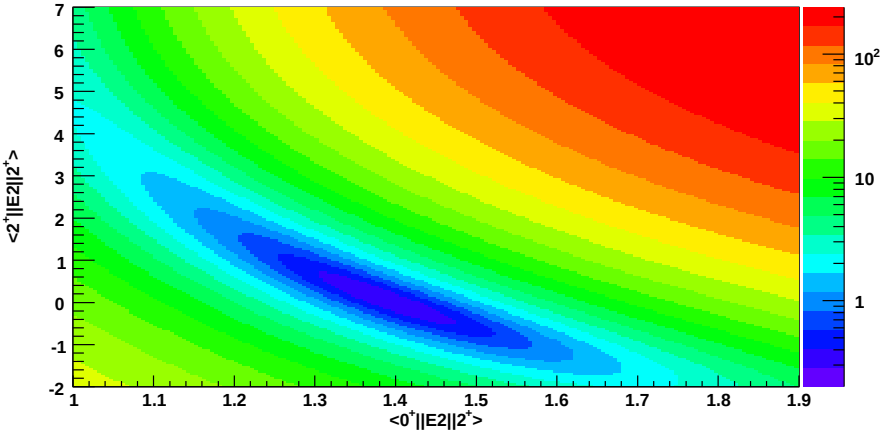

Figure 6.35: Reduced χ^2_ν surface assuming different values of the $\langle 0^+_{g.s.} \| E2 \| 2^+_1 \rangle$ and $\langle 2^+_1 \| E2 \| 2^+_1 \rangle$ in ^{186}Hg.

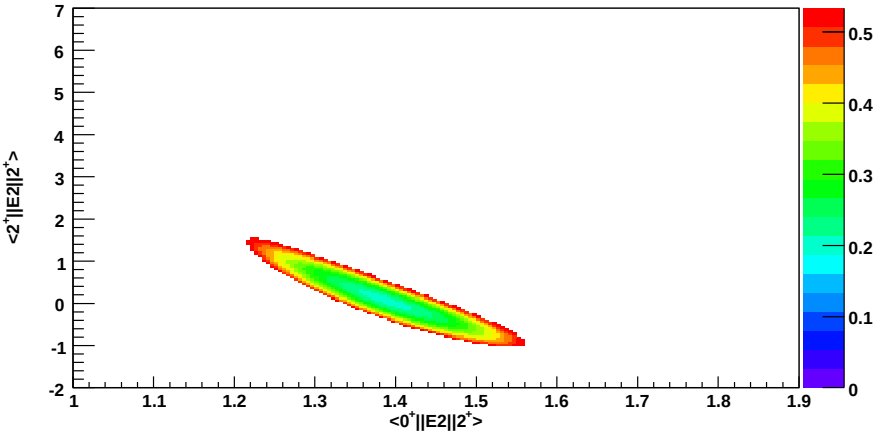

Figure 6.36: Reduced χ^2_ν surface with the condition $\chi^2 < \chi^2_{\min} + 1$, enabling 1σ uncertainties for $\langle 0^+_{g.s.} \| E2 \| 2^+_1 \rangle$ and $\langle 2^+_1 \| E2 \| 2^+_1 \rangle$ to be estimated.

6.3.4.2 Further analysis in GOSIA1

This section treats the input in the GOSIA1 analysis.

6.3.4.2.1 The energy level scheme

Table 6.53 presents the included nuclear levels, together with their spins, parities and energies. The level scheme of ^{186}Hg is shown in figure 6.37.

I^π	Energy [keV]
0_1^+	0
2_1^+	405
0_2^+	523
2_2^+	621
4_1^+	808
4_2^+	1080
6_1^+	1165

Table 6.53: Nuclear levels included in the analysis of ^{186}Hg.

Also a 1^+ state has been declared at an energy of 454 keV. This is necessary for the treatment of the $E0$ transition between the 0_2^+ and the 0_1^+ states, observed in the Coulomb-excitation experiments. The $E0$ transition between the 2_2^+ and the 2_1^+ states has not been included because there was no sign of populating the 2_2^+ state in the experiments performed. However, the conversion coefficient is known to have a value of 3.5 (5). In the GOSIA analysis, this path is added to the $\frac{\gamma(2_2^+ \to 2_1^+)}{\gamma(2_2^+ \to 0_1^+)}$ branching ratio. This can be done, since the $2_2^+ \to 2_1^+$ deexcitation modus is so small that it is not expected to be observed in the experiments, even with inclusion of the $E0$ deexcitations.

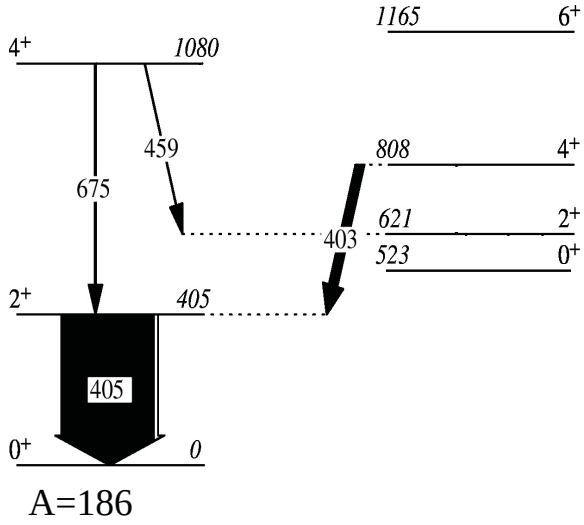

Figure 6.37: Scheme of the nuclear levels at low energy in ^{186}Hg. Black arrows indicate observed γ rays in the total spectrum of the ^{186}Hg-on-^{120}Sn Coulomb-excitation experiment, their relative thicknesses being related to their observed intensities.

6.3.4.2.2 The matrix elements

GOSIA1 varies the declared matrix elements in order to reproduce the observed data. Table 6.54 shows which matrix elements are used in the calculations.

The 6_1^+ is a buffer state, since no excitations to it were observed in the Coulomb-excitation experiments. The only levels that were populated are the 2_1^+, the 0_2^+, the 4_1^+ and the 4_2^+ states.

The $E0(0_2^+ \rightarrow 0_1^+)$ transition will be replaced by a non-existing $M1$ transition, since $E0$ transitions can not be defined in GOSIA. The declaration of two addition matrix elements is necessary, as presented in table 6.55. No corrections for the efficiency are necessary, as the energy difference between the 1_1^+ state and 0_2^+ states equals 69 keV, exactly the energy of the K_α X-ray in mercury.

ME
$\langle 0_1^+ \| E2 \| 2_1^+ \rangle$
$\langle 0_1^+ \| E2 \| 2_2^+ \rangle$
$\langle 2_1^+ \| E2 \| 2_1^+ \rangle$
$\langle 2_1^+ \| E2 \| 0_2^+ \rangle$
$\langle 2_1^+ \| E2 \| 2_2^+ \rangle$
$\langle 2_1^+ \| E2 \| 4_1^+ \rangle$
$\langle 2_1^+ \| E2 \| 4_2^+ \rangle$
$\langle 0_2^+ \| E2 \| 2_2^+ \rangle$
$\langle 2_2^+ \| E2 \| 2_2^+ \rangle$
$\langle 2_2^+ \| E2 \| 4_1^+ \rangle$
$\langle 2_2^+ \| E2 \| 4_2^+ \rangle$
$\langle 4_1^+ \| E2 \| 4_1^+ \rangle$
$\langle 4_1^+ \| E2 \| 4_2^+ \rangle$
$\langle 4_1^+ \| E2 \| 6_1^+ \rangle$
$\langle 4_2^+ \| E2 \| 4_2^+ \rangle$
$\langle 2_1^+ \| M1 \| 2_2^+ \rangle$
$\langle 4_1^+ \| M1 \| 4_2^+ \rangle$

Table 6.54: Matrix elements in ^{186}Hg that can be varied by GOSIA1 to reproduce the observed data.

ME
$\langle 0_1^+ \| M1 \| 1_1^+ \rangle$
$\langle 1_1^+ \| M1 \| 0_2^+ \rangle$

Table 6.55: Two non-existing $M1$ matrix elements, used to replace the $E0$ deexcitation.

The known life times of the 0_2^+ and 2_2^+ states, addressed in section 6.3.3.1, will also be included in the GOSIA1 analysis, together with the known branching ratios (including the conversion coefficient) from section 6.3.3.2.

6.3.4.2.3 Coulomb-excitation data

The input for the GOSIA1 analysis from the Coulomb-excitation experiment consists of six different experiments: the first three are the particle angular cuts into which the data on the ^{114}Cd target have been subdivided. The three last ones are the total angular ranges on the ^{114}Cd, the ^{107}Ag and the ^{120}Sn target. The normalization constants obtained from the comparison between the calculated and the observed count rates of the $2_1^+ \rightarrow 0_{g.s.}^+$ γ transition in ^{114}Cd allow GOSIA1 to normalize the first three experiments relatively to one another.

The integrals of the $2_1^+ \rightarrow 0_{g.s.}^+$ γ transition in ^{114}Cd, given in the last column of table 6.52, are used by GOSIA1 for the calculation of the three normalization constants. The intensities of the $2_1^+ \rightarrow 0_{g.s.}^+/4_1^+ \rightarrow 2_1^+$ γ doublet in ^{186}Hg included in GOSIA1 are given in table 6.56.

$I_i \rightarrow I_f$	E_γ [keV]	$\theta_{lab,t}[^\circ]$	I_γ
$2_1^+ \rightarrow 0_1^+$	405	43.6 - 51.6	607 (68)
and	and	32.9 - 43.6	599 (70)
$4_1^+ \rightarrow 2_1^+$	403	18.7 - 32.8	416 (52)

Table 6.56: The integrated photo peak intensities I_γ are given for observed $2_1^+ \rightarrow 0_{g.s.}^+$ γ transition in ^{186}Hg for the three angular particle gates.

Like in the previous cases, the error bars on the integrals are larger compared to those presented in table 6.43, because also the statistical error on the $2_1^+ \rightarrow 0_{g.s.}^+$ γ transition in ^{114}Cd has to be included, due to the absence of error bars on the normalization constants. The uncertainties on the γ detection efficiency for both projectile and target are included as well.

Since no absolute normalization to the target is performed in the GOSIA1 analysis, the value of the $\langle 0_1^+ \| E2 \| 2_1^+ \rangle$ matrix element derived in section 6.3.4.1 will also be included.

For the last three experiments, the intensities observed in tables 6.45 and 6.46 are given as input to the GOSIA1 analysis. No errors on the γ-ray detection efficiency have to be added, since the integrals of the $4_1^+ \rightarrow 2_1^+$ transition

already have that error included by the way the intensities are extracted from the coincidence spectra. However, these errors need to be included in the uncertainties of the $4_2^+ \rightarrow 2_1^+$, $4_2^+ \rightarrow 2_2^+$ and $0_2^+ \rightarrow 0_1^+$ intensities.

In the last three experiments, incorrectnesses due to the changing particle detection efficiency over the total angular range can be coped with by defining a limited azimuthal detection range for two of the three angular ranges within the total particle angular range. For ^{182}Hg, this is addressed in section 6.1.4.2.3. Since the excitation to the 2_1^+ state in ^{120}Sn was scarce, the change in particle detection efficiency for the last experiment was estimated to be the same as in the experiment on the ^{107}Ag target, where it was determined by looking at the intensities of its $\frac{3}{2}^+_- \rightarrow \frac{1}{2}^-_{g.s.}$ transition in the three angular ranges.

A detection limit of 30 counts has been included in the last three experiments, meaning that GOSIA1 can never calculate matrix elements in such a way that they would give rise to transitions with a higher count rate than 30 counts which are not declared as observed transitions in the analysis.

6.3.4.2.4 Results

Table 6.57 presents the relevant matrix elements from the GOSIA1 analysis.

ME	Obtained value [eb or μ_N]
$\langle 0_1^+ \| E2 \| 2_1^+ \rangle$	$1.47^{0.25}_{0.26}$
$\langle 0_1^+ \| E2 \| 2_2^+ \rangle$	$\pm 0.05^{0.01}_{0.01}$
$\langle 2_1^+ \| E2 \| 2_1^+ \rangle$	$-1.94^{20.10}_{17.87}$
$\langle 2_1^+ \| E2 \| 0_2^+ \rangle$	$1.83^{10.54}_{9.36}$
$\langle 2_1^+ \| E2 \| 2_2^+ \rangle$	$-1.02^{2.52}_{1.37}$
$\langle 2_1^+ \| E2 \| 4_1^+ \rangle$	$-3.41^{0.25}_{0.22}$
$\langle 2_1^+ \| E2 \| 4_2^+ \rangle$	$1.86^{0.04}_{0.04}$
$\langle 0_2^+ \| E2 \| 2_2^+ \rangle$	$4.51^{5.33}_{0.79}$
$\langle 2_2^+ \| E2 \| 4_1^+ \rangle$	$5.28^{1.30}_{0.60}$
$\langle 2_2^+ \| E2 \| 4_2^+ \rangle$	$1.99^{0.17}_{0.11}$

Table 6.57: Matrix elements obtained from the GOSIA1 analysis.

Like in the ^{184}Hg, the value of the $\langle 0_1^+ \| E2 \| 2_1^+ \rangle$ matrix element differs from the one obtained in section 6.3.4.1. When starting the analysis with GOSIA1, it was clear that this matrix element started to increase. When a stable solution was found, the procedure described in section 6.3.4.1 was repeated: the $\langle 0_1^+ \| E2 \| 2_1^+ \rangle$ and $\langle 2_1^+ \| E2 \| 2_1^+ \rangle$ matrix elements were allowed to vary, while the other obtained matrix elements were defined as fixed input in order to reproduce the observed transitions other than the $2_1^+ \rightarrow 0_{g.s.}^+$ transition. These two steps were performed a few times, until a stable value for the $\langle 0_1^+ \| E2 \| 2_1^+ \rangle$ matrix element was found.

6.3.4.2.5 Extracted life times

The life times of the 2_1^+ and 4_1^+ yrast states in ^{186}Hg can now be calculated. They are compared to the known values in table 6.58.

Nuclear state I^π	Life time τ [ps] from matrix elements	Known life time τ [ps]
2_1^+	17 (6)	24 (3)
4_1^+	5 (1)	5.6 (20)

Table 6.58: Comparison of the life times of the 2_1^+ and 4_1^+ yrast states in ^{186}Hg deduced from the matrix elements obtained from the Coulomb-excitation experiment to the known life times.

The comparison shows that the values are in good agreement. The known life times can now be included in the GOSIA analysis.

6.3.4.3 Including the life times in GOSIA1

6.3.4.3.1 Obtained matrix elements

The physically relevant matrix element, obtained from the GOSIA1 analysis with inclusion of the life times, are presented in table 6.59.

ME	Obtained value [eb or μ_N]
$\langle 0_1^+ \| E2 \| 2_1^+ \rangle$	$1.24^{0.10}_{0.07}$
$\langle 0_1^+ \| E2 \| 2_2^+ \rangle$	$\pm 0.05^{0.01}_{0.01}$
$\langle 2_1^+ \| E2 \| 2_1^+ \rangle$	$-2.44^{11.29}_{10.93}$
$\langle 2_1^+ \| E2 \| 0_2^+ \rangle$	$1.37^{9.53}_{10.03}$
$\langle 2_1^+ \| E2 \| 2_2^+ \rangle$	$0.41^{1.35}_{2.50}$
$\langle 2_1^+ \| E2 \| 4_1^+ \rangle$	$-3.40^{0.24}_{0.21}$
$\langle 2_1^+ \| E2 \| 4_2^+ \rangle$	$3.91^{0.08}_{0.08}$
$\langle 0_2^+ \| E2 \| 2_2^+ \rangle$	$4.45^{3.48}_{0.77}$
$\langle 2_2^+ \| E2 \| 4_1^+ \rangle$	$5.26^{1.29}_{0.54}$
$\langle 2_2^+ \| E2 \| 4_2^+ \rangle$	$4.18^{0.34}_{0.23}$
$\langle 4_1^+ \| E2 \| 6_1^+ \rangle$	$4.25^{5.99}_{0.56}$

Table 6.59: Physically relevant matrix elements obtained from the GOSIA1 analysis with inclusion of the known life times.

As explained for ^{182}Hg in section 6.1.4.4, the stability of the $\langle 0_1^+ \| E2 \| 2_1^+ \rangle$ can be checked by using GOSIA2 for the absolute normalization to the ^{114}Cd target. When applying this procedure, the value of $1.24^{0.10}_{0.07}$ eb can be maintained.

6.4 The ^{188}Hg case

6.4.1 Intensity of the observed transitions

Three targets were used for the experiments on the ^{188}Hg isotope: a 2.0 mg/cm^2 ^{114}Cd target, a 1.1 mg/cm^2 ^{107}Ag target and a 2.3 mg/cm^2 ^{120}Sn target. Since the statistics on ^{114}Cd target were high, the particle scattering range in the DSSSD was divided into five angular cuts: annular strips 0 to 2, strips 3 to 5, strips 6 to 8, strips 9 to 11 and strips 12 to 14. For the experiment on the ^{107}Ag target only the entire angular range of the DSSSD was taken into account, due to low statistics. The particle scattering range was divided into three gates for the experiment employing the ^{120}Sn target: a low angle c.m. range summing the γ-ray spectra gating on annular strips 0 to 4, an intermediate angle range combining strips 5 to 9, and a high angle range covering strips 10 to 14. It is important to notice, when comparing the γ-ray intensities between the experiments on the ^{114}Cd and on the ^{120}Sn target, that the statistics are higher in the latter case. The reason why the particle angular range is only divided into three angular cuts is due to the fact that this experiment will mainly serve to identify the $4_1^+ \rightarrow 2_1^+$ transition, which has less statistics than the main $2_1^+ \rightarrow 0_{g.s.}^+$ transition, which will be characterized by the absolute normalization using the ^{114}Cd target.

Figures 6.38, 6.39 and 6.40 show the relevant spectra obtained with the three targets that were used.

The $2_1^+ \rightarrow 0_1^+$ transition in ^{120}Sn is observed in spectrum 6.40.d. It will not be used in the further analysis however, since the absolute normalization to the target nucleus is only useful when a division in particle angular cuts is applied. The observed intensity of the $2_1^+ \rightarrow 0_1^+$ transition in ^{120}Sn is too weak for this purpose.

The observed intensities of the transitions in ^{188}Hg when incident on the ^{114}Cd target are summarized in table 6.60.

$I_i \to I_f$	E_γ [keV]	$\theta_{lab,t}[^\circ]$	$\theta_{c.m.}[^\circ]$	I_γ	$\epsilon_{\gamma,abs}[\%]$	$I_{\gamma,tot}$
$2_1^+ \to 0_1^+$	413	18.7 - 51.6	76.8 - 142.6	12386 (131)	9.91 (31)	124964 (4145)
		47.1 - 51.6	76.8 - 85.8	2646 (61)		26696 (1043)
		41.7 - 47.1	85.8 - 96.6	2934 (64)		29602 (1133)
		35.3 - 41.7	96.6 - 109.4	2728 (61)		27523 (1063)
		27.6 - 35.2	109.6 - 124.8	2509 (58)		25314 (991)
		18.7 - 27.5	125.0 - 142.6	1569 (46)		15830 (683)
K_α	≈69	18.7 - 51.6	76.8 - 142.6	803 (83)	12.81 (78)	6270 (753)
		47.1 - 51.6	76.8 - 85.8	128 (43)		1702 (350)
		41.7 - 47.1	85.8 - 96.6	99 (42)		773 (331)
		35.3 - 41.7	96.6 - 109.4	160 (38)		1249 (306)
		27.6 - 35.2	109.6 - 124.8	213 (34)		1663 (282)
		18.7 - 27.5	125.0 - 142.6	113 (27)		882 (215)

Table 6.60: The integrated photo peak intensities I_γ (or I_X) are given for the observed $2_1^+ \to 0_{g.s.}^+$ transition in ^{188}Hg when incident on the ^{114}Cd target for the total angular range and the five particle gates. Also K_α X-rays are present.

The $4_1^+ \to 2_1^+$ transition could not be estimated, since its 592 keV photo peak is contaminated by the Doppler-broadened $2_1^+ \to 0_{g.s.}^+$ transition in ^{114}Cd at an energy of 558 keV. Also the amount of K_β X-rays could not be estimated due to low statistics and large uncertainties induced by the random events and the background at this low energy. As already stated in section 5.4, the X-rays in the spectrum are attributed solely to conversion from observed transition and the heavy-ion induced K-vacancy creation.

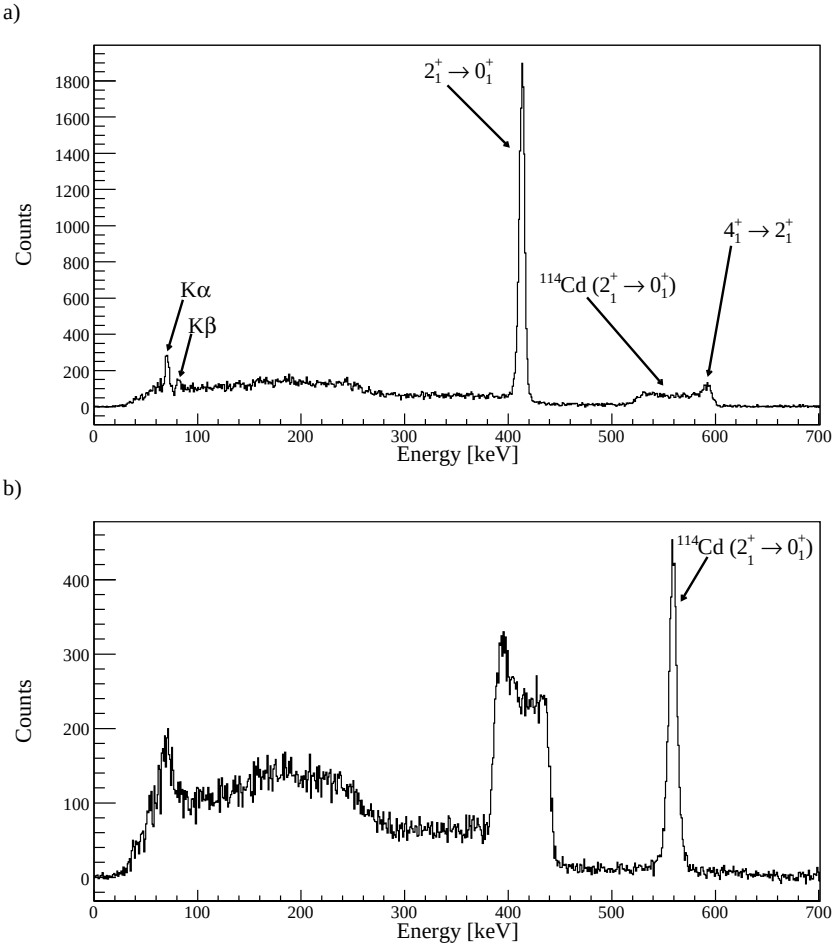

Figure 6.38: Random-subtracted γ-ray spectrum, coincident with two identified particles, Doppler corrected for the mercury projectile (a) and for the cadmium target (b). The spectra for the five particle angular cuts are not shown here. The sharp photo peaks in (a) can be identified as the $2_1^+ \rightarrow 0_1^+$ and the $4_1^+ \rightarrow 2_1^+$ transitions. However, the integration of the latter one in spectrum a is problematic, due to the contamination of the Doppler broadened ^{114}Cd photo peak. Prompt X-rays are detected with an energy around 69 keV, which are considered to be solely originating from atomic K-vacancy creation and conversion of observed transitions, as has been advocated in section 5.4.

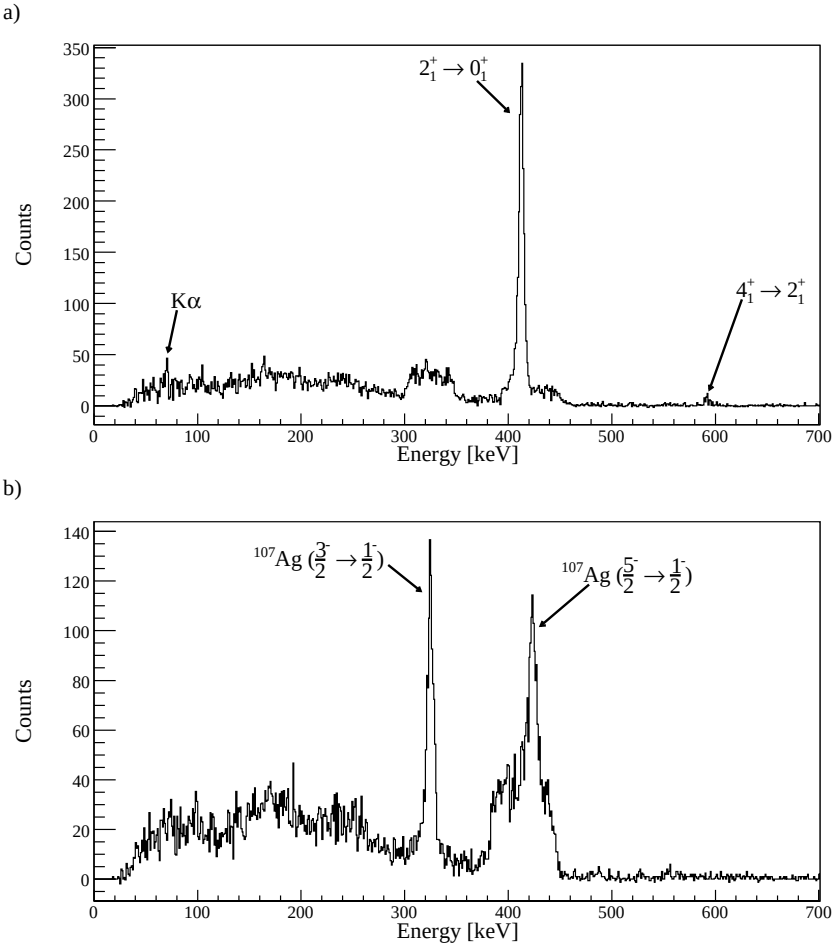

Figure 6.39: Random-subtracted γ-ray spectrum, coincident with two identified particles, Doppler corrected for the mercury projectile (a) and for the silver target (b). The same transitions are present here as in figure 6.38.

a)

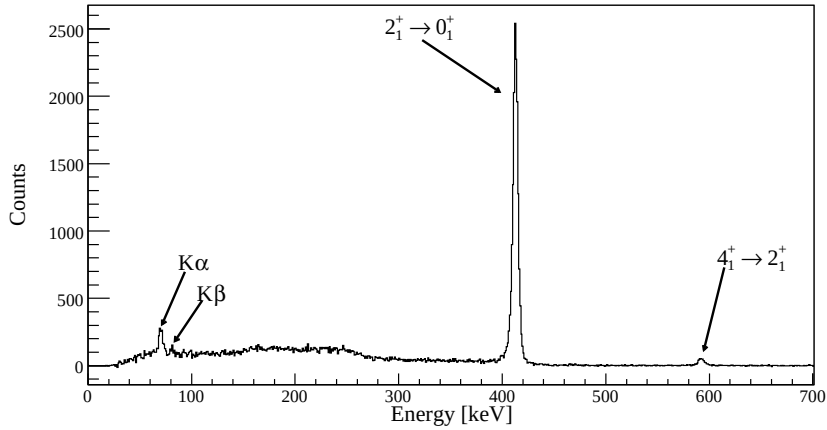

c)

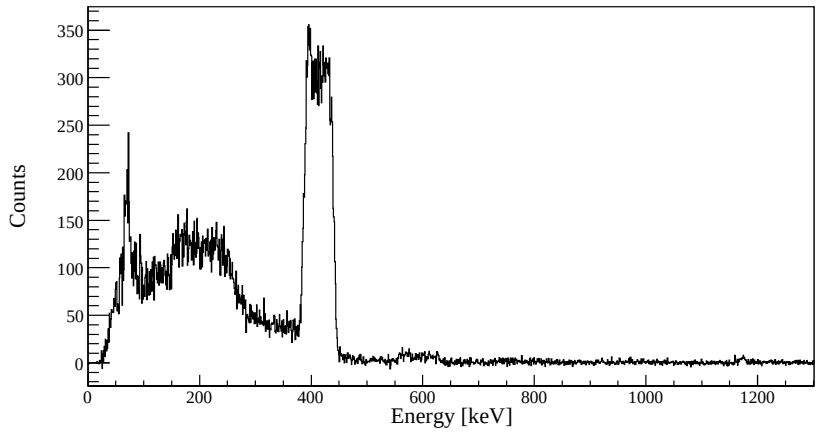

b)

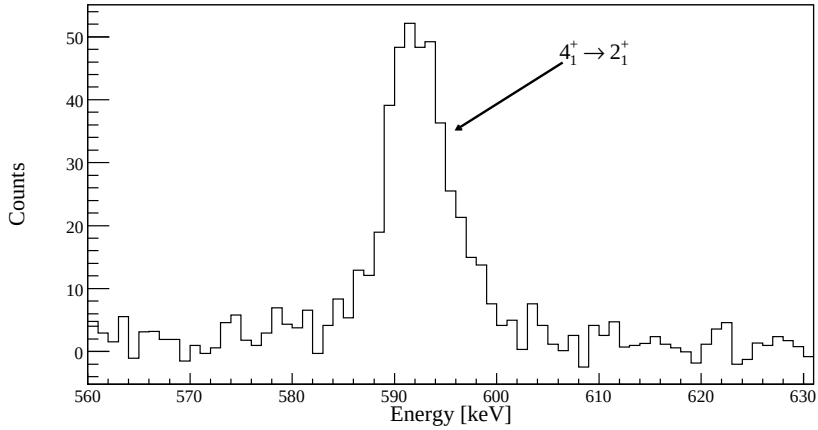

d)

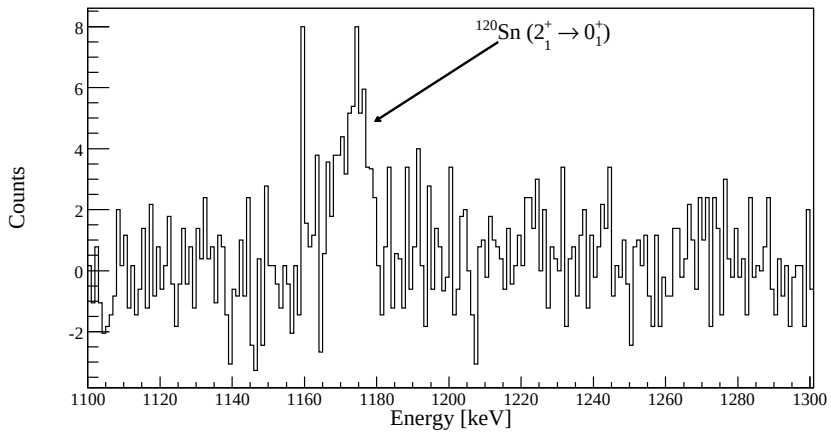

Figure 6.40: Random-subtracted γ-ray spectrum, coincident with two identified particles, Doppler corrected for the mercury projectile (a), enlarged around 592 keV (b) for the visibility of the $4_1^+ \rightarrow 2_1^+$ transition. Also the random-subtracted γ-ray spectrum, Doppler corrected for the tin target is shown (c), enlarged around 1171 keV (d), the energy of the $2_1^+ \rightarrow 0_1^+$ transition in ^{120}Sn.

The integrated photo peak intensities for transitions observed in ^{114}Cd are given in table 6.61.

$I_i \rightarrow I_f$	E_γ [keV]	$\theta_{lab,t}[^\circ]$	$\theta_{c.m.}[^\circ]$	I_γ	$\epsilon_{\gamma,abs}[\%]$	$I_{\gamma,tot}$
$2_1^+ \rightarrow 0_1^+$	558	18.7 - 51.6 47.1 - 51.6 41.7 - 47.1 35.3 - 41.7 27.6 - 35.2 18.7 - 27.5	76.8 - 142.6 76.8 - 85.8 85.8 - 96.6 96.6 - 109.4 109.6 - 124.8 125.0 - 142.6	4698 (77) 1210 (39) 1074 (37) 1001 (36) 869 (32) 543 (26)	8.45 (48)	55588 (3290) 14317 (935) 12708 (848) 11844 (795) 10282 (698) 6425 (481)

Table 6.61: The integrated photo peak intensities I_γ are given for the observed $2_1^+ \rightarrow 0_1^+$ transition in ^{114}Cd for the total angular range and the five particle gates.

The observed intensities in the ^{188}Hg-on-^{107}Ag experiment are addressed in table 6.62.

$I_i \rightarrow I_f$	E_γ [keV]	$\theta_{lab,t}[^\circ]$	$\theta_{c.m.}[^\circ]$	I_γ	$\epsilon_{\gamma,abs}[\%]$	$I_{\gamma,tot}$
^{188}Hg						
$2_1^+ \rightarrow 0_1^+$	413	18.2 - 50.7	78.6 - 143.6	2025 (55)	12.67 (40)	15989 (663)
$4_1^+ \rightarrow 2_1^+$	592			48 (11)	10.49 (67)	458 (107)
K_α	≈ 69			98 (25)	14.23 (87)	689 (179)
^{107}Ag						
$\frac{3}{2}^- \rightarrow \frac{1}{2}^-$	325	18.2 - 50.7	78.6 - 143.6	985 (43)	14.54 (27)	6776 (321)

Table 6.62: Observed photo peak intensities I_γ (or I_X) are presented for the ^{188}Hg projectile and the ^{107}Ag target for the total angular range.

No integrated intensity for the $\frac{5}{2}^- \rightarrow \frac{1}{2}^-$ transition in ^{107}Ag has been given, since its energy of 423 keV is too close to the energy of the $2_1^+ \rightarrow 0_1^+$ transition

in ^{188}Hg at 413 keV. Moreover, the observed intensity of the $\frac{3}{2}^- \rightarrow \frac{1}{2}^-$ in ^{107}Ag will not be of any use in the analysis, as stated in appendix A.

The integrated photo peak intensities observed in the experiment with the tin target are given in table 6.63.

$I_i \rightarrow I_f$	E_γ [keV]	$\theta_{lab,t}[^\circ]$	$\theta_{c.m.}[^\circ]$	I_γ	$\epsilon_{\gamma,abs}[\%]$	$I_{\gamma,tot}$
$2_1^+ \rightarrow 0_1^+$	413	18.2 - 50.7	78.6 - 143.6	15786 (139)	12.66 (40)	124636 (4070)
		42.8 - 50.7	78.6 - 94.4	5855 (87)		46230 (1606)
		32.1 - 42.7	94.6 - 115.8	6068 (86)		47912 (1652)
		18.2 - 32.0	116.0 - 143.6	3863 (68)		30502 (1098)
$4_1^+ \rightarrow 1_1^+$	592	18.2 - 50.7	78.6 - 143.6	451 (29)	10.49 (67)	4299 (392)
		42.8 - 50.7	78.6 - 94.4	130 (18)		1239 (193)
		32.1 - 42.7	94.6 - 115.8	198 (18)		1887 (207)
		18.2 - 32.0	116.0 - 143.6	123 (15)		1172 (157)
K_α	≈ 69	18.2 - 50.7	78.6 - 143.6	916 (87)	14.23 (87)	6437 (729)
		42.8 - 50.7	78.6 - 94.4	456 (60)		3205 (462)
		32.1 - 42.7	94.6 - 115.8	287 (52)		2017 (383)
		18.2 - 32.0	116.0 - 143.6	173 (38)		1216 (275)
K_β	≈ 80	18.2 - 50.7	78.6 - 143.6	140 (58)	16.77 (77)	835 (350)

Table 6.63: The integrated photo peak intensities I_γ (or I_X) are given for the observed $2_1^+ \rightarrow 0_{g.s.}^+$ and $4_1^+ \rightarrow 2_1^+$ transitions and K_α X-rays in ^{188}Hg when incident on the ^{120}Sn target for the total angular range and the three particle gates. Also the K_β X-rays are given for the entire angular particle range.

The K_α/K_β ratio is found to be 3.84 (170), in good agreement with the predicted value of ≈ 3.6.

6.4.2 Intensity of the $\gamma - \gamma$ coincidences

6.4.2.1 Construction of the γ-ray spectra

The spectra of γ rays coincident with the $2_1^+ \rightarrow 0_{g.s.}^+$ transition in ^{188}Hg at an energy of 413 keV have been constructed in the same way as in the previous cases. The central energy window covers γ-ray energies between 400 and 430 keV, the lower window between 365 and 395 keV, and the higher window between 435 and 465 keV. For the experiments on the ^{114}Cd and the ^{107}Ag targets, the same time windows are chosen for the prompt and random coincidences with a particle, being -900 to -600 ns and -1350 to 900 ns. The random window should then be rescaled by a factor $\frac{2}{3} \approx 0.667$ before subtracting it from the prompt window. For the experiment on the ^{120}Sn target, the prompt window has been defined from -900 to 625 ns, whilst the random window has remained the same. This yields a scaling factor of ≈ 0.611. The time windows for prompt and random coincidence between two γ rays remain 0 to 300 ns and 400 to 700 ns.

6.4.2.2 Extraction of the singles integrals

Figure 6.41 shows the γ ray spectra coincident with the $2_1^+ \rightarrow 0_{g.s.}^+$ γ transition in ^{188}Hg at 413 keV for the three energy windows.

Only the $4_1^+ \rightarrow 2_1^+$ transition with an energy of 592 keV, and the K X-rays seem to be present. No other transitions are observed. Table 6.64 shows the integrals of the transitions in the nine spectra above, combined with their final integrals, which are calculated according to the procedure in section 4.6.

After subtraction from the conversion of the observed $4_1^+ \rightarrow 2_1^+$ transition in the coincidence spectra and the heavy-ion induced K_α vacancy creation, the following K_α X-rays are left: -4 (33) for the ^{188}Hg-on-^{114}Cd experiment and -7 (27) for the ^{188}Hg-on-^{120}Sn experiment. X-rays originating from a purely nuclear process thus seem to be absent. Hence, there is no necessity to convert any intensities to the total γ-ray spectrum.

Moreover, since all K_α X-rays in the total γ-ray spectrum, after subtraction of the conversion of observed transitions, are suggested to originate solely from the heavy-ion induced K_α vacancy creation, no $E0$ transitions are present in the data set.

No trace is found of the $0_2^+ \rightarrow 2_1^+$ γ transition, which lies at an energy of 411 keV. This is important to know, since the presence of this transition in the coincidence spectrum would imply that the observed $2_1^+ \rightarrow 0_1^+$ γ transition at

Target	Transition	E_γ [keV]	Int. centre	Int. left	Int. right	Total int.
^{114}Cd	$4_1^+ \rightarrow 2_1^+$	592	51 (16)	23 (8)	2 (3)	39 (17)
	K_α	69	32 (27)	4 (21)	-9 (12)	35 (32)
^{107}Ag	$4_1^+ \rightarrow 2_1^+$	592	19 (5)	1 (1)	-1 (1)	19 (5)
^{120}Sn	$4_1^+ \rightarrow 2_1^+$	592	123 (15)	4 (7)	1 (4)	121 (16)
	K_α	69	47 (24)	17 (13)	-5 (6)	41 (25)

Table 6.64: Integrals of the two observed transitions in the constructed coincidence spectra, together with the calculated total integral.

an energy of 413 keV in the full γ-ray spectrum would also contain counts that originate from the $0_2^+ \rightarrow 2_1^+$ γ transition.

a)

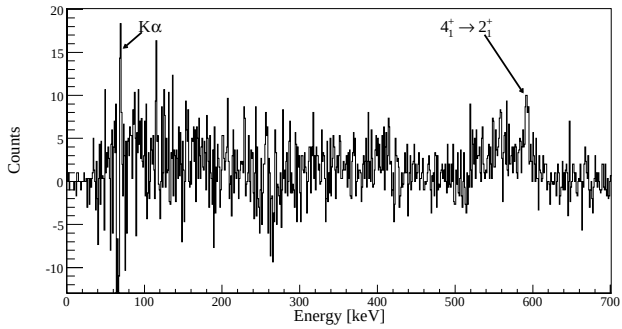

b)

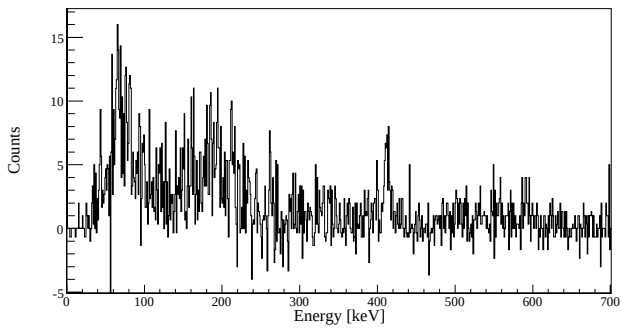

c)

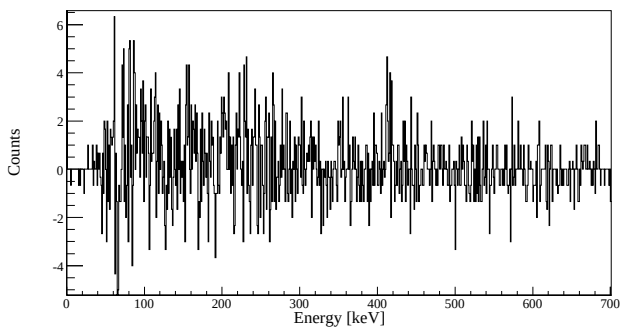

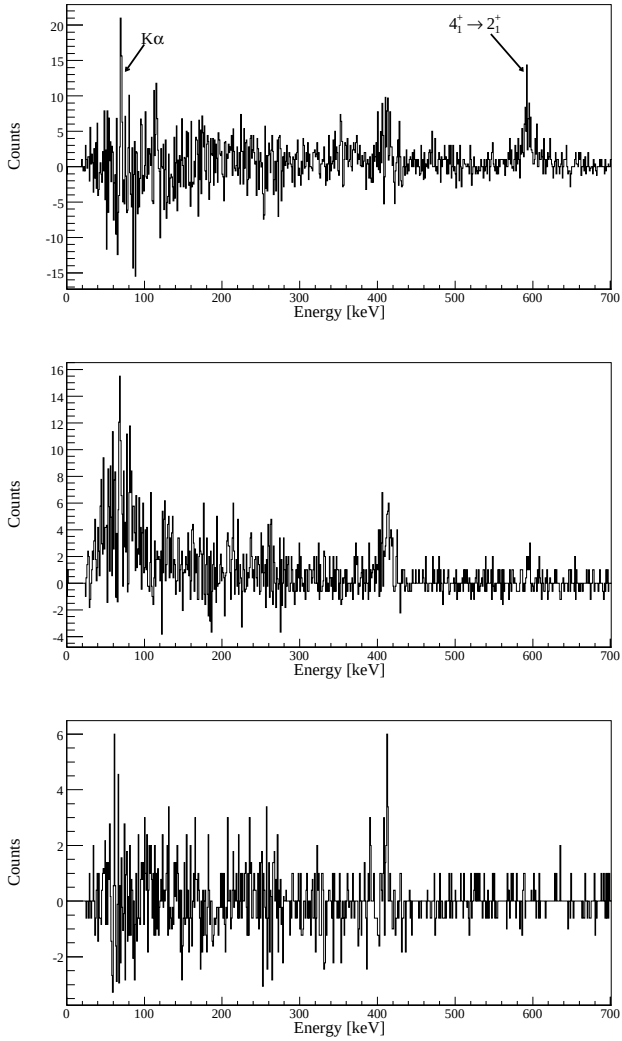

Figure 6.41: a) Spectrum of the γ rays coincident with a γ_1 ray around 413 keV (within the range 400 - 430 keV). b) and c) Idem, but the γ_1 ray energy window is slightly lower (within a range of 365 - 395 keV) or higher (within a range of 435 - 465 keV). The γ rays in these three spectra are Doppler corrected for the ^{188}Hg projectile. The spectra obtained with the ^{114}Cd target are presented in the left column, those obtained with the ^{120}Sn target in the right column.

6.4.3 Combined information on ^{188}Hg

6.4.3.1 Life times

The experiment described in [Gaf14] also provides a life time for the 2_1^+ state in ^{188}Hg of 28.3 (134) ps [Gaf]. In 1994, Joshi et al. [Jos94] suggested life times for the 0_2^+ and 2_2^+ states. A summary of these values is presented in table 6.65.

Nuclear state I^π	Life time τ [ps]
2_1^+	28.3 (134)
0_2^+	294 (65)
2_2^+	203 (45)

Table 6.65: Measured life times of the 2_1^+, 0_2^+ and 2_2^+ states in ^{188}Hg from [Gaf, Jos94].

6.4.3.2 Branching ratios and mixing ratios

In 1984, Cole et al. [Col84] have extracted branching ratios and a mixing ratio in ^{188}Hg, which are addressed in table 6.66.

6.4.3.3 Summary

The Coulomb-excitation data on ^{188}Hg will be analyzed using the following information:

1. The extracted integrals from the Coulomb-excitation γ-ray spectra on the three employed targets. These intensities can be found in table 6.60, 6.62 and 6.63. In some cases angular particle cuts are applied.
2. The life times of the 0_2^+ and 2_2^+ states, presented in table 6.65. The life time of the 2_1^+ state will not be included, since the further analysis can provide an independent value.
3. The measured branching ratios relevant for the further analysis and the E2/M1 mixing ratio of the $2_2^+ \rightarrow 2_1^+$ transition, given in table 6.66.

$\frac{I_i \to I_{f_1}}{I_i \to I_{f_2}}$	Ratio
$\frac{\gamma(0_2^+ \to 2_1^+)}{e^-(0_2^+ \to 0_1^+)}$	<0.72
$\frac{\gamma(2_2^+ \to 0_1^+)}{\gamma(2_2^+ \to 2_1^+)}$	1.32 (24)
$\frac{\gamma(4_2^+ \to 2_1^+)}{\gamma(4_2^+ \to 4_1^+)}$	8.33 (81)
$\frac{\gamma(4_2^+ \to 2_1^+)}{\gamma(4_2^+ \to 2_2^+)}$	1.05 (8)
$\delta(\frac{\langle I^\pi \Vert E2 \Vert I^\pi \rangle}{\langle I^\pi \Vert M1 \Vert I^\pi \rangle})$	Ratio
$\delta(\frac{\langle 2_1^+ \Vert E2 \Vert 2_1^+ \rangle}{\langle 2_1^+ \Vert M1 \Vert 2_1^+ \rangle})$	2 (1)

Table 6.66: Measured branching ratios and one mixing ratio in ^{188}Hg from [Col84].

6.4.4 GOSIA analysis

Since the measured life time of the 2_1^+ state in ^{188}Hg has an error bar of approximately 50%, it will not be used in the analysis of the Coulomb-excitation data. An independent value for this life time can be obtained from the Coulomb-excitation data, including all other information available: the life times of the 0_2^+ and 2_2^+ states, and the branching ratios and mixing ratio presented in table 6.66. A first estimation of the $\langle 0_1^+ \Vert E2 \Vert 2_1^+ \rangle$ matrix element is found by reducing the ^{188}Hg level scheme to the 0_1^+ and 2_1^+ states.

6.4.4.1 First approximation of $\langle 0_1^+ \| E2 \| 2_1^+ \rangle$

A first estimation of the $\langle 0_1^+ \| E2 \| 2_1^+ \rangle$ matrix element can be obtained by the absolute normalization of the $2_1^+ \rightarrow 0_{g.s.}^+$ γ transition in ^{188}Hg to the $2_1^+ \rightarrow 0_{g.s.}^+$ γ transition in ^{114}Cd, and this for the five angular particle gates. An absolute normalization to the ^{120}Sn target was not possible in this experiment, since no $2_1^+ \rightarrow 0_{g.s.}^+$ γ transition in the target could be extracted, due to the low excitation cross section to the 2_1^+ state. Appendix A explains why the ^{107}Ag target was not useful to perform an absolute normalization.

Table 6.67 presents the observed integrals for both projectile and target, together with the target angles in the laboratory frame. The error bars have been increased according to the uncertainties in the γ-ray efficiencies.

$\theta_{lab,t}[^\circ]$	$I_\gamma(2_1^+ \rightarrow 0_1^+)$ in ^{188}Hg	$I_\gamma(2_1^+ \rightarrow 0_1^+)$ in ^{114}Cd
47.1 - 51.6	2646 (103)	1210 (79)
41.7 - 47.1	2934 (112)	1074 (72)
35.3 - 41.7	2728 (105)	1001 (67)
27.6 - 35.2	2509 (98)	869 (59)
18.7 - 27.5	1569 (68)	543 (41)

Table 6.67: The integrated photo peak intensities I_γ are given for the observed $2_1^+ \rightarrow 0_1^+$ transition in ^{188}Hg and in ^{114}Cd for the five angular particle gates.

When assuming different values for the $\langle 2_1^+ \| E2 \| 2_1^+ \rangle$ diagonal matrix element in ^{188}Hg, the $\langle 0_1^+ \| E2 \| 2_1^+ \rangle$ transitional matrix element in ^{188}Hg can be calculated in each angular range. A correct estimation of the $\langle 2_1^+ \| E2 \| 2_1^+ \rangle$ matrix element should lead to a calculated $\langle 0_1^+ \| E2 \| 2_1^+ \rangle$ matrix element remaining constant over the different angular ranges.

From figure 6.42, the $\langle 2_1^+ \| E2 \| 2_1^+ \rangle$ matrix element can be inferred to be close to 1, the $\langle 0_{g.s.}^+ \| E2 \| 2_1^+ \rangle$ matrix element being approximately 1.3.

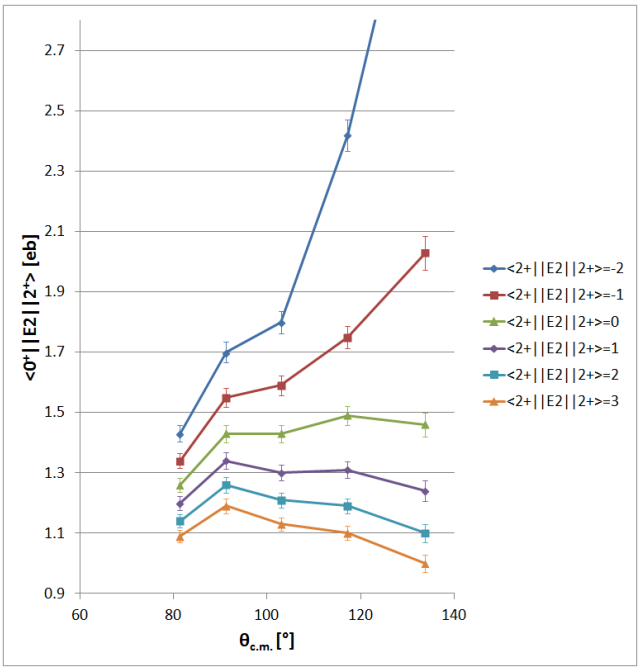

Figure 6.42: $\langle 0^+_{g.s.} \| E2 \| 2^+_1 \rangle$ for the five angular ranges, assuming different integer values of $\langle 2^+_1 \| E2 \| 2^+_1 \rangle$.

The reduced χ^2_ν per combination of $\langle 0^+_{g.s.} \| E2 \| 2^+_1 \rangle$ and $\langle 2^+_1 \| E2 \| 2^+_1 \rangle$ in ^{188}Hg can be calculated using GOSIA2. This is shown in figure 6.43. These reduced χ^2_ν's are the sum of the reduced χ^2_ν's in ^{188}Hg and in ^{114}Cd.

By increasing the minimal total χ^2 by 1, errors on both matrix elements can be estimated. This is treated in figure 6.44.

These calculations result in $\langle 0^+_{g.s.} \| E2 \| 2^+_1 \rangle = 1.27\ (8)$ and $\langle 2^+_1 \| E2 \| 2^+_1 \rangle = 0.5\ (7)$.

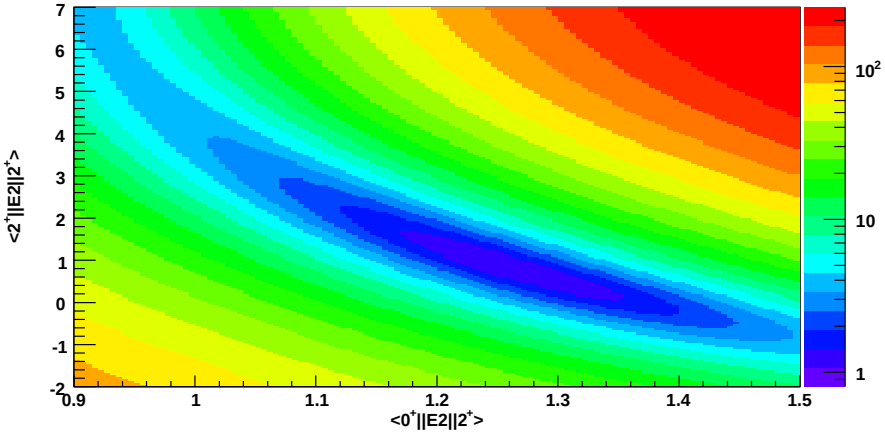

Figure 6.43: Reduced χ^2_ν surface assuming different values of the $\langle 0^+_{g.s.} \| E2 \| 2^+_1 \rangle$ and $\langle 2^+_1 \| E2 \| 2^+_1 \rangle$ in ^{188}Hg.

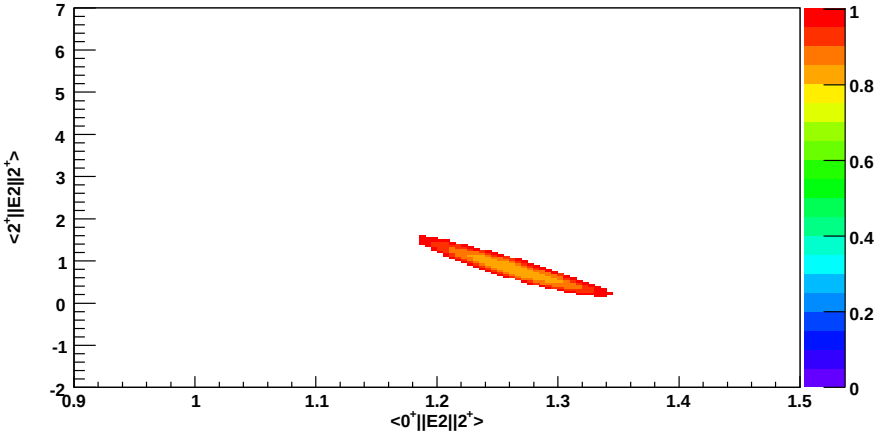

Figure 6.44: Reduced χ^2_ν surface with the condition $\chi^2 < \chi^2_{\min} + 1$, enabling 1σ uncertainties for $\langle 0^+_{g.s.} \| E2 \| 2^+_1 \rangle$ and $\langle 2^+_1 \| E2 \| 2^+_1 \rangle$ to be estimated.

6.4.4.2 Further analysis in GOSIA1

This section treats the input in the GOSIA1 analysis.

6.4.4.2.1 The energy level scheme

Table 6.68 gives the included nuclear levels, together with their spins, parities and energies. The level scheme of ^{188}Hg is shown in figure 6.45.

Also one non-existing nuclear state with spin and parity 1^+ has been included at an energy of 755 keV. This is necessary for the treatment of the possible $E0$ transition between the 0_2^+ and the 0_1^+ states, although there is no trace of the 0_2^+ population in the Coulomb-excitation experiment. Since the life time of the 0_2^+ is known (table 6.65), and the main deexcition path is known to be to the 0_1^+ state (table 6.66), the $E0$ transition needs to be included. The $E0$ transition between the 2_2^+ and the 2_1^+ states has not been included since the conversion coefficient is unknown. Moreover, there is no sign of population of the 2_2^+ state in the Coulomb-excitation experiment, and it can decay via many ways, including a mixed M1/E2 path to the 2_1^+ state. Including the $E0$ decay path to the analysis without any additional information would complicate the further analysis thoroughly.

I^π	Energy [keV]
0_1^+	0
2_1^+	413
0_2^+	824
2_2^+	881
4_1^+	1005
4_2^+	1208

Table 6.68: Nuclear levels included in the analysis of ^{188}Hg.

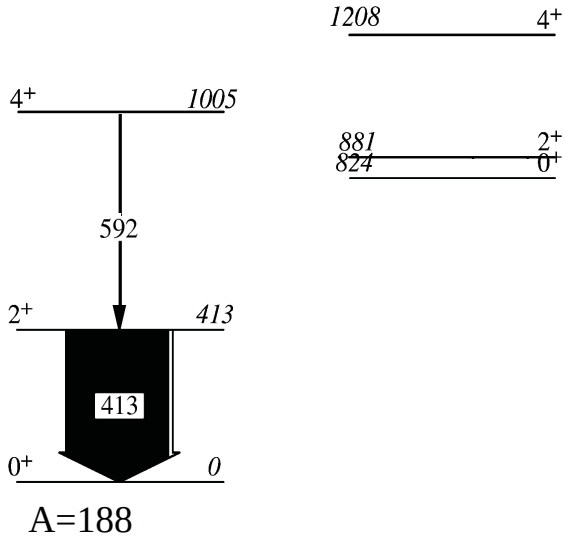

Figure 6.45: Scheme of the nuclear levels at low energy in ^{188}Hg. Black arrows indicate observed γ rays in the total spectrum of the ^{188}Hg-on-^{120}Sn Coulomb-excitation experiment, their relative thicknesses being related to their observed intensities.

6.4.4.2.2 The matrix elements

The declaration of matrix elements allows GOSIA1 to vary them in order to reproduce the observed data. Table 6.69 shows which matrix elements are used in the calculations.

Since only depopulation of the 2_1^+ and 4_1^+ states is observed in the Coulomb-excitation data, the GOSIA1 calculation is expected only to give information on the $\langle 0_1^+ \| E2 \| 2_1^+ \rangle$, $\langle 2_1^+ \| E2 \| 2_1^+ \rangle$ and $\langle 2_1^+ \| E2 \| 4_1^+ \rangle$ matrix elements (and perhaps the $\langle 4_1^+ \| E2 \| 4_1^+ \rangle$ matrix element, depending on the statistics). The 2_1^+ state only decays to the 0_1^+ ground state, and no branching ratios from the 4_1^+ state are known, so no additional matrix elements can be calculated by GOSIA1. However, the absence of population of some states, together with known branchings and life times, can give upper limits for certain matrix elements.

ME
$\langle 0_1^+ \| E2 \| 2_1^+ \rangle$
$\langle 0_1^+ \| E2 \| 2_2^+ \rangle$
$\langle 2_1^+ \| E2 \| 2_1^+ \rangle$
$\langle 2_1^+ \| E2 \| 0_2^+ \rangle$
$\langle 2_1^+ \| E2 \| 2_2^+ \rangle$
$\langle 2_1^+ \| E2 \| 4_1^+ \rangle$
$\langle 2_1^+ \| E2 \| 4_2^+ \rangle$
$\langle 0_2^+ \| E2 \| 2_2^+ \rangle$
$\langle 2_2^+ \| E2 \| 2_2^+ \rangle$
$\langle 2_2^+ \| E2 \| 4_1^+ \rangle$
$\langle 2_2^+ \| E2 \| 4_2^+ \rangle$
$\langle 4_1^+ \| E2 \| 4_1^+ \rangle$
$\langle 4_1^+ \| E2 \| 4_2^+ \rangle$
$\langle 4_2^+ \| E2 \| 4_2^+ \rangle$
$\langle 2_1^+ \| M1 \| 2_2^+ \rangle$

Table 6.69: Matrix elements in ^{188}Hg that can be varied by GOSIA1 to reproduce the observed data.

The $E0(0_2^+ \rightarrow 0_1^+)$ transition will be replaced by a non-existing $M1$ transition, since GOSIA does not include $E0$ transitions. The declaration of two addition matrix elements is necessary, as presented in table 6.70. Again, no correction for the efficiency is needed, as the energy difference between the 1_1^+ state and 0_2^+ states equals 69 keV, which is the energy of the K_α X-ray in mercury.

The known branching ratios and mixing ratio from section 6.4.3.2 will also be included in the GOSIA1 analysis, together with the life times of the 0_2^+ and 2_2^+ states from section 6.4.3.1.

ME
$\langle 0_1^+ \| M1 \| 1_1^+ \rangle$ $\langle 1_1^+ \| M1 \| 0_2^+ \rangle$

Table 6.70: Two non-existing $M1$ matrix elements, used to replace the $E0$ deexcitation.

6.4.4.2.3 Coulomb-excitation data

The input for the GOSIA1 analysis from the Coulomb-excitation experiment consists of nine different experiments: the first five are the particle angular cuts into which the data have been subdivided, when ^{188}Hg is incident on the ^{114}Cd target. The sixth one is the total angular range on the ^{107}Ag target. The run on the ^{120}Sn target can also be divided in three angular cuts, which are the last three experiments of the GOSIA1 input. The first five experiments only contain the $2_1^+ \rightarrow 0_{g.s.}^+$ γ transition in ^{188}Hg, since in the Doppler-corrected spectrum for ^{188}Hg, the $4_1^+ \rightarrow 2_1^+$ γ transition at 592 keV is overlapping with the Doppler-broadened peak of the $2_1^+ \rightarrow 0_{g.s.}^+$ γ transition in ^{114}Cd at 558 keV. However, the integral of the latter can be extracted in the Doppler-corrected spectrum for ^{114}Cd, because the intensity of the Doppler-broadened peak of the $4_1^+ \rightarrow 2_1^+$ γ transition in ^{188}Hg is very small. The last four experiments each contain the $2_1^+ \rightarrow 0_{g.s.}^+$ and $4_1^+ \rightarrow 2_1^+$ γ transitions in ^{188}Hg.

For the first five experiments, GOSIA1 compares the calculated and the observed count rates of the $2_1^+ \rightarrow 0_{g.s.}^+$ γ transition in ^{114}Cd, in order to link the five angular particle cuts to each other with five relative normalization factors. This is necessary, since differences in particle detection efficiency over the five angular ranges can be present.

The integrals of the $2_1^+ \rightarrow 0_{g.s.}^+$ γ transition in ^{114}Cd, given in the last column of table 6.67, are used by GOSIA1 to calculate the five normalization constants. The intensities of the $2_1^+ \rightarrow 0_{g.s.}^+$ γ transition in ^{188}Hg are presented in table 6.71.

The error bars on the integrals are larger compared to table 6.60, since also the statistical error on the $2_1^+ \rightarrow 0_{g.s.}^+$ γ transition in ^{114}Cd has to be included, due

$I_i \rightarrow I_f$	E_γ [keV]	$\theta_{lab,t}[^\circ]$	I_γ
$2_1^+ \rightarrow 0_1^+$	413	47.1 - 51.6	2646 (201)
$2_1^+ \rightarrow 0_1^+$		41.7 - 47.1	2934 (226)
$2_1^+ \rightarrow 0_1^+$		35.3 - 41.7	2728 (211)
$2_1^+ \rightarrow 0_1^+$		27.6 - 35.2	2509 (197)
$2_1^+ \rightarrow 0_1^+$		18.7 - 27.5	1569 (135)

Table 6.71: The integrated photo peak intensities I_γ are given for observed $2_1^+ \rightarrow 0_{g.s.}^+$ γ transition in ^{188}Hg for the five angular particle gates.

to the absence of error bars on the normalization constants. Also the errors on the γ detection efficiency for both projectile and target are included.

The value of the $\langle 0_1^+ \| E2 \| 2_1^+ \rangle$ matrix element derived in section 6.4.4.1 will be included in the GOSIA1 analysis, because no absolute normalization to the target is present.

From the sixth experiment, the intensities of the $2_1^+ \rightarrow 0_{g.s.}^+$ and $4_1^+ \rightarrow 2_1^+$ γ transitions in ^{188}Hg, when incident on the ^{107}Ag target, can be determined. These integrals cover the full experimental range and can be found in table 6.62. No additional error due to the statistical uncertainties in the excitation of the target has to be added, because this experiment is not normalized.

Due to the condition of always having two particles in coincidence, the particle detection efficiency can alter with changing particle angle. This can cause small incorrectnesses, since GOSIA1 treats the angular range of the sixth experiment to have the same particle detection efficiency throughout its entire angular range. A way to cope with this is to define a limited azimuthal detection range for two of the three angular ranges within the total angular range of the sixth experiment. The angular range with the highest particle detection efficiency is then defined to have a fully working particle detector with an azimuthal coverage of 360°, the other two angular ranges working with an azimuthal coverage that is lower. The integrals of the $\frac{3}{2}\,^{-}_{1} \rightarrow \frac{1}{2}\,^{-}_{g.s.}$ in three angular ranges are used to give an estimate of the deviation of constant particle detection efficiency.

The seventh to ninth experiments are the three particle cuts made when the ^{120}Sn target was used. The integrals of the $2_1^+ \rightarrow 0_{g.s.}^+$ and $4_1^+ \rightarrow 2_1^+$ γ transitions in ^{188}Hg can be found in table 6.63. Again, since no absolute normalization was performed, no additional statistical errors were needed.

A detection limit of 30 counts has been included in the experiments on the ^{107}Ag and ^{120}Sn targets, meaning that GOSIA1 can never calculate matrix elements in such a way that they would give rise to transitions with a higher count rate than 30 counts which are not declared as observed transitions in the analysis.

6.4.4.2.4 Results

The resulting values for the matrix elements are found in table 6.72.

ME	Obtained value [eb or μ_N]
$\langle 0_1^+ \Vert E2 \Vert 2_1^+ \rangle$	$1.31^{0.10}_{0.10}$
$\langle 0_1^+ \Vert E2 \Vert 2_2^+ \rangle$	$0.04^{0.01}_{0.01}$
$\langle 2_1^+ \Vert E2 \Vert 2_1^+ \rangle$	$1.01^{0.57}_{0.41}$
$\langle 2_1^+ \Vert E2 \Vert 2_2^+ \rangle$	$-0.16^{0.03}_{0.03}$
$\langle 2_1^+ \Vert E2 \Vert 4_1^+ \rangle$	$2.07^{0.08}_{0.08}$
$\langle 4_1^+ \Vert E2 \Vert 4_1^+ \rangle$	$0.78^{0.52}_{0.61}$
$\langle 2_1^+ \Vert M1 \Vert 2_2^+ \rangle$	$-0.03^{0.01}_{0.02}$

Table 6.72: Matrix elements obtained from the GOSIA1 analysis.

6.4.4.2.5 Extracted life times

A life time for the 2_1^+ state can be deduced from the $\langle 0_1^+ \Vert E2 \Vert 2_1^+ \rangle$ matrix element in table 6.72, since this state can only decay to the 0_1^+ ground state. The obtained life time amounts to 19.1 (29) ps, which is in agreement with the value of 28.3 (134) ps, addressed in table 6.65. This means that solely from the Coulomb-excitation experiment, a life time with much smaller uncertainty has been determined.

Also a life time for the 4_1^+ state can be determined. However, this state can deexcite to the 2_1^+ state as well as to the 2_2^+ state. Since no $\gamma(4_1^+ \rightarrow 2_1^+)/\gamma(4_1^+ \rightarrow 2_2^+)$ branching ratio is known, no much is known about the $\langle 2_2^+ \| E2 \| 4_1^+ \rangle$ matrix element. Since the $4_1^+ \rightarrow 2_2^+$ γ transition is not observed in the Coulomb-excitation data, GOSIA1 gives a range from 0 to 3.5 eb as an output for the $\langle 2_2^+ \| E2 \| 4_1^+ \rangle$ matrix element.

As addressed in section 2.8, the transition probability $T(E2) = \frac{1}{\tau}$ per possible decay channel can be calculated as:

$$T(E2) = 1.22 \cdot B(E2 : I_i \rightarrow I_f) \cdot E_\gamma^5, \tag{6.6}$$

with $T(E2)$ expressed in ps^{-1}, $B(E2 : I_i \rightarrow I_f)$ in e^2fm^4 and E_γ in MeV.

Comparing the energy differences from the $4_1^+ \rightarrow 2_1^+$ γ transition at 492 keV and the $4_1^+ \rightarrow 2_2^+$ γ transition at 124 keV, the first path is faster with a factor $\frac{0.492^5}{0.124^5} = 984$. This means that, even when the $\langle 2_2^+ \| E2 \| 4_1^+ \rangle$ matrix element has its largest possible value of 3.5 eb, the $4_1^+ \rightarrow 2_1^+$ path would still be approximately 300 times faster. Hence, the contribution of the $4_1^+ \rightarrow 2_2^+$ deexcitation path can be neglected for the calculation of the life time of the 4_1^+ state, yielding a value of 2.3 (2) ps.

The newly obtained life times are summarized in table 6.73.

Nuclear state I^π	Life time τ [ps]
2_1^+	19.1 (29)
4_1^+	2.3 (2)

Table 6.73: Life times of the 2_1^+ and 4_1^+ states in ^{188}Hg from the Coulomb-excitation experiment.

6.4.4.3 Absolute normalization to the ^{114}Cd target using GOSIA2

Section 6.4.4.1 treated the calculation of the $\langle 0_1^+ \| E2 \| 2_1^+ \rangle$ matrix element in ^{188}Hg by normalizing to the observed $2_1^+ \rightarrow 0_{g.s.}^+$ γ transition in the ^{114}Cd target, when the angular detection range for the particle was divided into five separate cuts. As a first-order, simplified approximation, only the $0_{g.s.}^+$ and 2_1^+ states

in ^{188}Hg were assumed to be present. When fixing now all matrix elements to the values found in table 6.72, except for the transitional $\langle 0_1^+ \| E2 \| 2_1^+ \rangle$ and diagonal $\langle 2_1^+ \| E2 \| 2_1^+ \rangle$ matrix elements, which are allowed to vary, a new reduced χ^2_ν surface can be calculated in GOSIA2. The reduced χ^2_ν surface with the condition $\chi^2 < \chi^2_{\min} + 1$ is shown in figure 6.46.

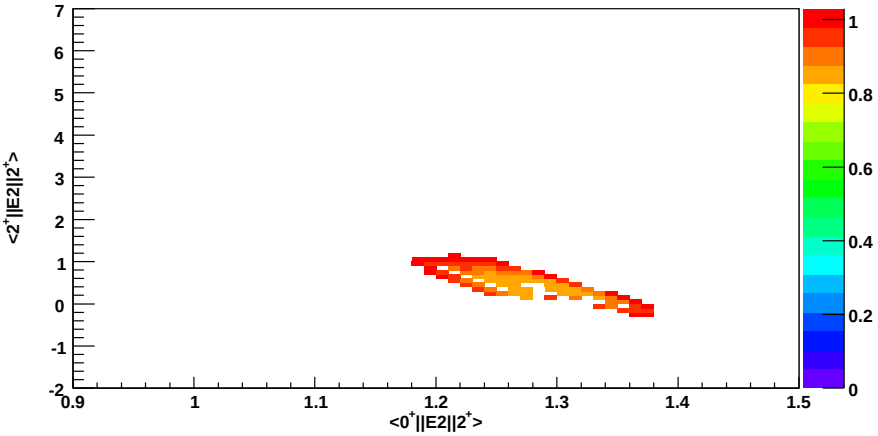

Figure 6.46: Reduced χ^2_ν surface with the condition $\chi^2 < \chi^2_{\min} + 1$, enabling error bars for $\langle 0^+_{g.s.} \| E2 \| 2^+_1 \rangle$ and $\langle 2^+_1 \| E2 \| 2^+_1 \rangle$ to be estimated. The matrix elements connecting the added states reproduce the observed transitions other than the $2^+_1 \rightarrow 0^+_{g.s.}$.

The values of $\langle 0_1^+ \| E2 \| 2_1^+ \rangle = 1.31^{0.10}_{0.10}$ and $\langle 2_1^+ \| E2 \| 2_1^+ \rangle = 1.01^{0.57}_{0.41}$ obtained with the GOSIA1 analysis are clearly in agreement with this GOSIA2 calculation.

Chapter 7

Interpretation and conclusions

7.1 Summary of the obtained data

Table 7.1 summarizes the relevant $E2$ matrix elements in the even-even $^{182-188}$Hg isotopes, obtained from the analysis performed in this work. The sign of the $E2$ matrix elements in this summarizing table may deviate from the ones found for the four isotopes in chapter 6. This is due to the fact that a set of signs for the $E2$ matrix elements in an isotope is not unique. An equivalent solution can be found when the signs of the transitional matrix elements are changed in such a way that the sign of the product of the matrix elements in a closed loop consisting of three transitional matrix elements remains unaltered. For example, when for a certain isotope the $\langle 0_1^+ \| E2 \| 2_1^+ \rangle$, $\langle 2_1^+ \| E2 \| 2_2^+ \rangle$ and $\langle 0_1^+ \| E2 \| 2_2^+ \rangle$ matrix elements are known, the sign of the $\langle 2_1^+ \| E2 \| 2_2^+ \rangle$ matrix element could be changed, and in order to find an equivalent solution, one of the two other matrix elements should change sign as well. In that case, the sign of the product of the three matrix elements remains the same. When other matrix elements are known, all other closed loops over three matrix elements should also be altered in order to remain the same product sign.

$\langle I_i \| E2 \| I_f \rangle$ [eb]	^{182}Hg	^{184}Hg	^{186}Hg	^{188}Hg
$\langle 0_1^+ \| E2 \| 2_1^+ \rangle$	$1.29^{+0.04}_{-0.03}$	1.27 (3)	$1.25^{+0.10}_{-0.07}$	1.31 (10)
$\langle 2_1^+ \| E2 \| 4_1^+ \rangle$	3.71 (6)	3.15 (6)	3.4 (2)	2.07 (8)
$\langle 0_1^+ \| E2 \| 2_2^+ \rangle$	-0.61 (3)	0.21 (2)	(±) 0.05 (1)	
$\langle 0_2^+ \| E2 \| 2_1^+ \rangle$	$-2.68^{+0.15}_{-0.13}$	3.3 (8)		
$\langle 0_2^+ \| E2 \| 2_2^+ \rangle$	-1.6 (2)	1.25 (28)	$\geq$ 3.7 (8)	
$\langle 2_1^+ \| E2 \| 2_2^+ \rangle$	-2.2 (4)	0.91 (14)		
$\langle 2_2^+ \| E2 \| 4_1^+ \rangle$	3.1 (3)	5.8 (5)	$-5.3^{+1.3}_{-0.5}$	
$\langle 2_1^+ \| E2 \| 2_1^+ \rangle$	$-0.04^{+1.30}_{-1.40}$	$1.5^{+1.8}_{-1.2}$		$1.0^{+0.6}_{-0.4}$
$\langle 2_2^+ \| E2 \| 2_2^+ \rangle$	$0.8^{+1.0}_{-0.6}$	-2.6 (20)		

Table 7.1: The reduced transitional and diagonal $E2$ matrix elements are presented for low-lying states in the even-even $^{182-188}$Hg isotopes. All error bars correspond to 1σ uncertainties. The (±) sign indicates that the sign of a matrix element could not be determined.

7.2 Two-state mixing

When two unperturbed states with the same spin J and parity π mix, the wave functions of the two resulting mixed states $|J_1^\pi\rangle$ and $|J_2^\pi\rangle$ can be written as linear combinations of the unperturbed states $|J_{\rm I}^\pi\rangle$ and $|J_{\rm II}^\pi\rangle$ [Dup90]:

$$\begin{aligned} |J_1^\pi\rangle &= \alpha_J |J_{\rm I}^\pi\rangle + \beta_J |J_{\rm II}^\pi \\ |J_2^\pi\rangle &= \beta_J |J_{\rm I}^\pi\rangle - \alpha_J |J_{\rm II}^\pi, \end{aligned} \tag{7.1}$$

where α_J and β_J are called the mixing amplitudes and $\alpha_J^2 + \beta_J^2 = 1$. The squares of the mixing amplitudes are the mixing probabilities, and they represent the fraction of mixing in a given state. This discussion will be limited to two coexisting bands, each with nuclear states having spins 0^+, 2^+, and 4^+, with increasing energy. When the pure intra-band (i.e. within the band) $E2$ matrix

elements are available, and the mixing amplitudes are known, the mixed $E2$ matrix elements can be calculated using formulae 7.1. This approach will provide a set of inter-band (i.e. connecting the two bands) and altered intra-band $E2$ matrix elements. It is assumed that inter-band, unperturbed transitions are non-existing. Figure 7.1 shows the mixing probabilities for the even-even $^{182-188}$Hg isotopes [Gaf14]. In order to calculate them, the variable moment of inertia model (VMI) was used to fit known level energies of rotational bands built upon the first two 0^+ states [Mar69].

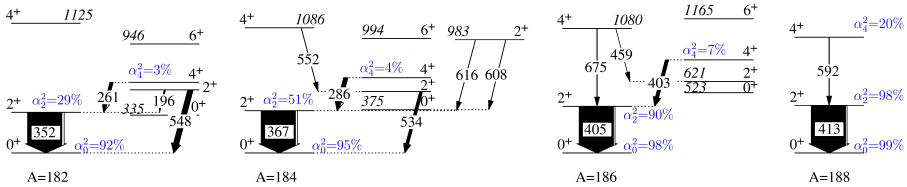

Figure 7.1: The low-lying energy levels of the even-even $^{182-188}$Hg isotopes are presented with experimentally obtained mixing probabilities α_J^2 of the unperturbed structure I. The transitions detected in the Coulomb-excitation experiments are represented by arrows, their thicknesses being related to the observed intensities.

In order for the $E2$ matrix elements connecting mixed states to be calculated, the intra-band $E2$ matrix elements connecting unperturbed states need to be estimated. The transitional $\langle 0_{\mathrm{I}}^+ \| E2 \| 2_{\mathrm{I}}^+ \rangle$ and $\langle 0_{\mathrm{II}}^+ \| E2 \| 2_{\mathrm{II}}^+ \rangle$, as well as for the diagonal $\langle 2_{\mathrm{I}}^+ \| E2 \| 2_{\mathrm{I}}^+ \rangle$ and $\langle 2_{\mathrm{II}}^+ \| E2 \| 2_{\mathrm{II}}^+ \rangle$ matrix elements have been fitted as a common, identical set for the four isotopes. The $\langle 2_{\mathrm{I}}^+ \| E2 \| 4_{\mathrm{I}}^+ \rangle$ and $\langle 2_{\mathrm{II}}^+ \| E2 \| 4_{\mathrm{II}}^+ \rangle$ matrix elements were then extrapolated from the $\langle 0_{\mathrm{I}}^+ \| E2 \| 2_{\mathrm{I}}^+ \rangle$ and $\langle 0_{\mathrm{II}}^+ \| E2 \| 2_{\mathrm{II}}^+ \rangle$ respectively, using the rotational model [Boh69]. Possible diagonal matrix elements of the 4^+ states have not been taken into account. Table 7.2 shows the results. A comparison between the experimentally obtained $E2$ matrix elements and those extracted from the two-state mixing calculation is shown in figure 7.2.

The two-state mixing calculations reproduce the experimental data rather well. This corroborates the assumption of two coexisting bands that mix when the energy difference between levels of the same spin and parity decreases. The unperturbed $\langle 0_{\mathrm{I}}^+ \| E2 \| 2_{\mathrm{I}}^+ \rangle$ is significantly smaller than the $\langle 0_{\mathrm{II}}^+ \| E2 \| 2_{\mathrm{II}}^+ \rangle$ matrix element, indicating a distinction in quadrupole collectivity of the two bands. Furthermore, an opposite sign of the diagonal matrix elements of the two unperturbed 2^+ states may suggest a weakly deformed oblate configuration for band I and a more deformed prolate shape for band II [Boh69]. As can

$\langle I_i \| E2 \| I_f \rangle$	band I	band II
$\langle 0^+ \| E2 \| 2^+ \rangle$	1.2	3.3
$\langle 2^+ \| E2 \| 2^+ \rangle$	1.8	-4.0
$\langle 2^+ \| E2 \| 4^+ \rangle$	1.9	5.3

Table 7.2: The calculated intra-band $E2$ matrix elements connecting unperturbed states will be used to perform the two-state mixing calculations. The matrix elements are given in units of eb.

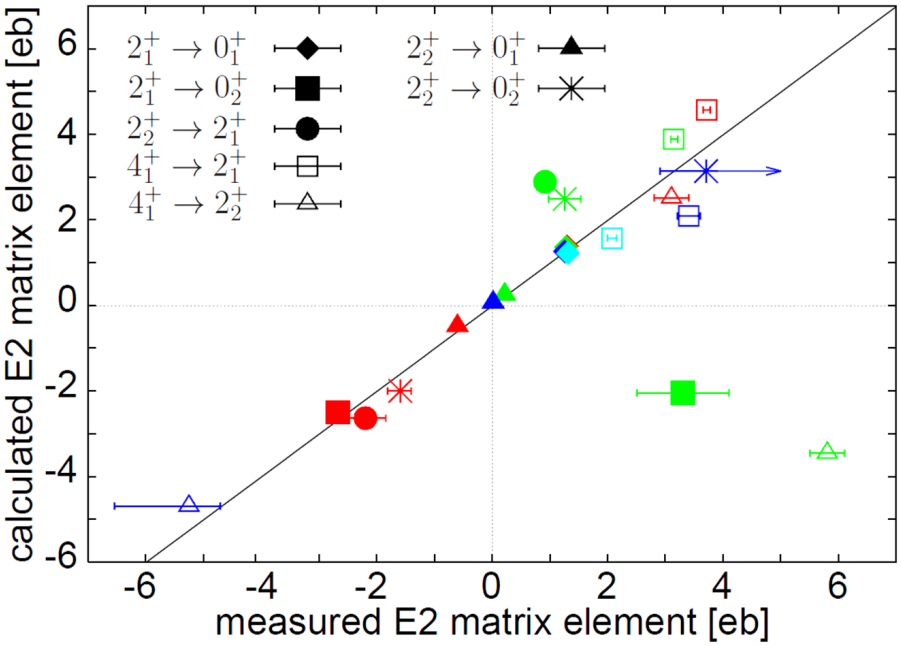

Figure 7.2: The $E2$ matrix elements determined in this work are compared to the ones originating from the two-state mixing calculations for ^{182}Hg (red), ^{184}Hg (green), ^{186}Hg (dark blue), and ^{188}Hg (light blue).

be seen in figure 7.1, the two-state mixing calculation suggests that the 2_1^+ state evolves from an almost pure I-structure nature in ^{188}Hg to a configuration dominated by structure II in ^{182}Hg. However, the energy of the 2_1^+ state and the $\langle 0_1^+ \| E2 \| 2_1^+ \rangle$ matrix element hardly change. This can be explained by the small mixing in the 0^+ states, which is also reflected in the small value of the $\langle 0_1^+ \| E2 \| 2_2^+ \rangle$ matrix element (figure 7.2). Also interesting to note is the change of sign of this matrix element when going to lighter mercury isotopes and the nice reproduction of this evolution by the two-state mixing calculation, showing the sensitivity of this approach to the sign of the matrix element.

The experimental results disagree partially with the two-state mixing calculations for ^{184}Hg. The absolute values of the matrix elements are in reasonable agreement, while the signs are not.

7.3 Quadrupole sum rules

The set of known $E2$ matrix elements connecting a certain state I_0 to other states I_i in a nucleus can be used to construct a nuclear-model independent characterization of the nuclear shape of that I_0 state, involving quadrupole deformation parameters. This description is referred to as the quadrupole sum rules method [Kum72, Cli86]. Since the multipole operator $E\lambda$ is a spherical tensor, its zero-coupled products are rotationally invariant. These invariants provide information on the charge distribution of the nucleus in a certain state in its intrinsic frame. Moreover, the quadrupole deformation parameters are universal variables present in quadrupole collective models involving the General Bohr Hamiltonian (GBH) [Pro09]. The two invariants which will be used in this interpretation are:

$$\begin{aligned} \langle Q^2 \rangle &= \sqrt{5} \sum_i \langle I_0 \| E2 \| I_i \rangle \langle I_i \| E2 \| I_0 \rangle \\ \langle Q^3 \cos(3\delta) \rangle &= \sqrt{\frac{35}{2}} \sum_i \langle I_0 \| E2 \| I_i \rangle \langle I_i \| E2 \| I_j \rangle \langle I_j \| E2 \| I_0 \rangle, \end{aligned} \tag{7.2}$$

where I_i and I_j represent all possible states which are connected to the initial state I_0 via the $E2$ operator. Also the case where $i = j$ has to be taken into account in the summation. $\langle Q^2 \rangle$ is referred to as the sum of $E2$ matrix elements

(SSM), and $\langle Q^3 \cos(3\delta)\rangle$ as the sum of triple products of $E2$ matrix elements (STM). The deformation Q and triaxility δ are related to the overall deformation parameter β and the non-axiallity parameter γ, which are GBH collective model variables, via the relation [Wrz12]:

$$\begin{aligned} Q^2 &= \left(\frac{3ZR_0^2}{4\pi}\right)^2 \beta^2 \\ Q^3\cos(3\delta) &= \left(\frac{3ZR_0^2}{4\pi}\right)^2 \beta^3 \cos(3\gamma), \end{aligned} \tag{7.3}$$

where $R_0 = r_0 A^{\frac{1}{3}}$, r_0 being approximately 1.2 fm. It should be noted that Q and δ, in comparison with β and γ, describe the charge rather than the mass distribution.

From the experimentally obtained $E2$ matrix elements, the two deformation parameters could be calculated for the 0_1^+ ground states of the four ^{182,184,186,188}Hg isotopes, however, information on ^{186}Hg was too scarce to gain knowledge on the δ parameter. With the available experimental information, it was possible to estimate the triaxiality $\langle Q^3\cos(3\delta)\rangle$ for the 0_1^+ and 0_2^+ state in ^{182,184}Hg as well. When calculating these quadrupole deformation parameters for a 0^+ state (in this case 0_1^+ or 0_2^+), the summations in formulae 7.4 loop over all 2^+ states observed in the experiment. The terms of the summation can then be written as $\langle 0^+\|E2\|2_i^+\rangle\langle 2_i^+\|E2\|0^+\rangle$ and $\langle 0^+\|E2\|2_i^+\rangle\langle 2_i^+\|E2\|2_j^+\rangle\langle 2_j^+\|E2\|0^+\rangle$, where the indices i and j correspond to the 2+ states involved. For ^{188}Hg, only the 2_1^+ has been taken into account, as it was the only 2^+ state observed in the experiment. The experimental results are summarized in figure 7.3.

The ground states of the four isotopes can be interpreted as being weakly deformed ($\beta \approx 0.15$) and tending towards an oblate shape ($\langle\cos(3\delta)\rangle \approx -1$). Due to the lack of key matrix elements, no information on the nature of the deformation of the 0_1^+ ground state in ^{186}Hg, and of the excited 0_2^+ state in ^{186}Hg and ^{188}Hg can be given.

Figure 7.3 also shows calculations from beyond mean field (BMF) [Yao13] and interacting boson models (IBM) [Gar14, Gar09, Gar11]. The BMF calculations result in two coexisting bands with a considerable difference in moment of inertia: for $N \geq 106$, the level schemes show a ground-state band with weak deformation ($\beta \approx 0.20$), and an excited prolate band with stronger deformation

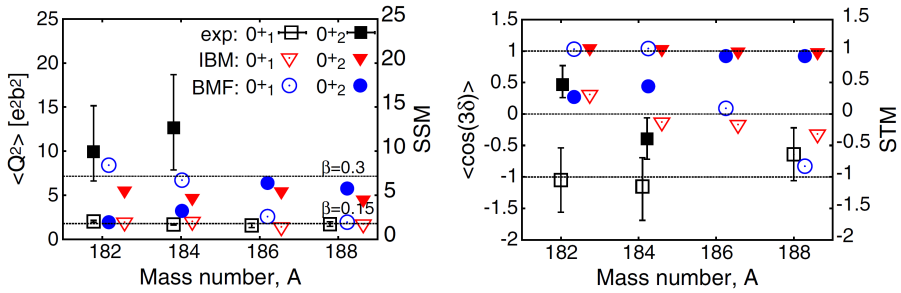

Figure 7.3: The experimentally obtained SSM and STM values for the 0_1^+ (open squares) and the 0_2^+ (full squares) states are presented for the four investigated mercury isotopes. They are compared to the BMF (blue) and IBM (red) calculations.

($\beta \approx 0.30$). In slightly lighter nuclei ($100 \leq N \leq 104$), the two bands cross: the ground state is calculated to be predominantly prolate, while the shape of the excited 0_2^+ state can be considered an almost equal mixture of an oblate and a prolate configuration. This is contradicted by the experimental data, as is shown in the left panel of figure 7.3: in ^{182,184}Hg, the calculated SSM values of the two 0^+ states are inverted with respect to the experimental ones. The disagreement is visible in the right panel of the figure as well. The IBM approach involves calculations using nucleon pair modes and takes into account the large open neutron shell from $N = 126$ down and beyond $N = 104$, together with the valence protons or proton holes, including proton-pair excitations across the $Z = 82$ major shell closure. The calculated SSM values are confirmed by the experiment (left panel), even though the STM sums only partially agree (right panel).

7.4 Conclusions and outlook

The experimentally obtained $E2$ transitional matrix elements in the even-even $^{182-188}$Hg isotopes have been compared to a two-state mixing calculation and two predictions involving beyond mean field calculations and an interacting boson-based approach. It was demonstrated that the magnitudes of the experimentally determined $E2$ transitional matrix elements can be explained as a result of two unperturbed coexisting structures with significantly different deformation. The interpretation of the data using the quadrupole sum rules formalism shows that the 0_1^+ ground states of the isotopes are weakly deformed and of oblate nature,

while the excited 0_2^+ states in ^{182,184}Hg correspond to a more deformed nuclear shape. The sums of squared matrix elements agree with the IBM calculations, while they are in partial disagreement with the results from the BMF approach. These final results support the premise of two coexisting configurations that mix when individual levels of the same parity and spin become close in energy.

In order to investigate the phenomenon of shape coexistence in this region of the nuclear chart, vigorous experimental techniques are available. The study of mean-square charged radii using laser spectroscopy can be extended to more exotic nuclei. Decay studies have the possibility to relate nuclear levels to one another and give insight in the possibly changing structure of mercury and adjacent nuclei. By Coulomb excitation at higher energies, nuclear states at higher excitation energies can be probed as well. Moreover, higher beam energies will enable for few-nucleon transfer reactions with these heavy beams to be performed. For example, producing an isomerically pure beam of the odd-mass mercury isotope ^{185}Hg using laser ionization, and performing a one-neutron transfer reaction feeding states in ^{186}Hg, might link the structure of the two different isomers with different bands in ^{186}Hg, providing more information on the underlying nuclear structure of these co-existing states. Also two-proton transfer reactions might be feasible. These challenges might be fulfilled by HIE-ISOLDE, located at CERN, where beam energies up to 10 MeV/u will be reached [Cat13].

Appendix A

The use of a ^{107}Ag target

This appendix describes the influence of the unknown quadrupole moment of the $\frac{3}{2}^-$ state at 325 keV in the ^{107}Ag target nucleus on the calculation of matrix elements in ^{32}Mg and ^{186,188}Hg projectiles in Coulomb excitation at REX-ISOLDE with MINIBALL.

We will only focuss on the $\frac{3}{2}^-$ state at 325 keV, since the intensity of the 424 keV transition cannot be extracted in the experiments on ^{186,188}Hg due to the overlap with the $2^+ \rightarrow 0^+$ transition in the projectile. The cross sections for excitation from the $\frac{1}{2}^-$ ground state in ^{107}Ag to the $\frac{3}{2}^-$ state for both projectiles are shown below, assuming three possible and realistic values of the diagonal matrix element $\langle \frac{3}{2}^- \| E2 \| \frac{3}{2}^- \rangle$ (which is proportional to the spectroscopic quadrupole moment): 0, -0.5 and 0.5. The 0^+ and 2^+ states discussed here always refer to the 0^+ ground state and the first excited 2^+ state of the projectile nucleus.

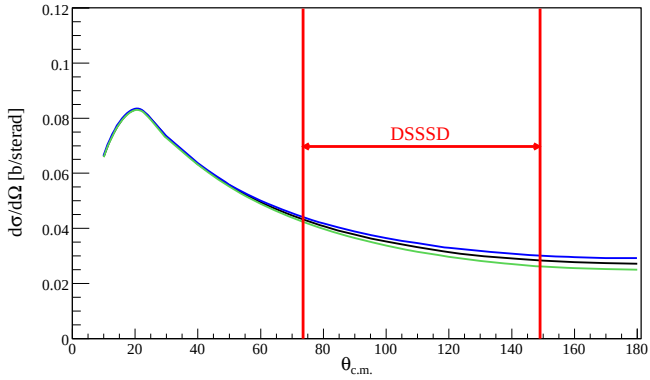

Figure A.1: Differential excitation cross section for the $\frac{3}{2}^-$ state in ^{107}Ag in a collision with a 2.86 MeV/u ^{32}Mg projectile, assuming a diagonal matrix element of 0 (black), 0.5 (blue) and -0.5 (green). The average energy was chosen for a target of 4.4 mg/cm^2 thickness. The detection range of the target by the DSSSD is marked with red lines.

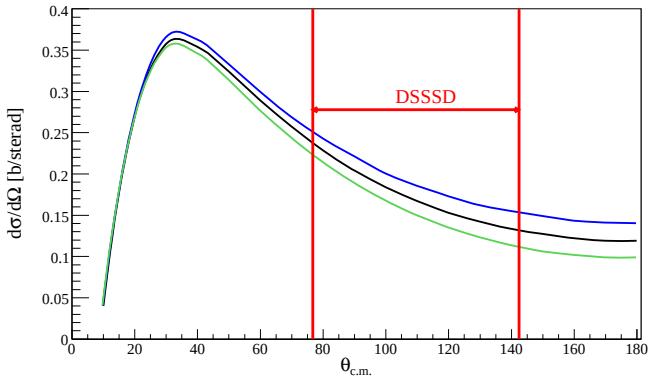

Figure A.2: Differential excitation cross section for the $\frac{3}{2}^-$ state in ^{107}Ag in a collision with a 2.85 MeV/u ^{188}Hg projectile, assuming a diagonal matrix element of 0 (black), 0.5 (blue) and -0.5 (green) The average energy was chosen for a target of 1.1 mg/cm^2 thickness. The detection range of the target by the DSSSD is marked with red lines.

For the ^{188}Hg case, it is clear that the diagonal matrix element has a considerable influence when integrating the detection cross section. Since the ^{188}Hg transitions are normalized to the $\frac{3}{2}^- \rightarrow \frac{1}{2}^-$ transition in ^{107}Ag, this will also affect the calculation of the transitional $\langle 0^+ \| E2 \| 2^+ \rangle$ and diagonal $\langle 2^+ \| E2 \| 2^+ \rangle$ matrix element in ^{188}Hg.

As an example, the results for ^{186,188}Hg assuming $\langle \frac{3}{2}^- \| E2 \| \frac{3}{2}^- \rangle = 0$ and $\langle \frac{3}{2}^- \| E2 \| \frac{3}{2}^- \rangle = -0.8$ are presented. The shown figures are χ^2 plots obtained by the minimization program GOSIA2. The reduced χ^2 surface is plotted as a function of the transitional $\langle 0^+ \| E2 \| 2^+ \rangle$ and diagonal $\langle 2^+ \| E2 \| 2^+ \rangle$ matrix element in ^{186,188}Hg with the condition that the normal χ^2 is smaller than $\chi^2_{min} + 1$, giving a confidence region for the individual parameters of 1 σ.

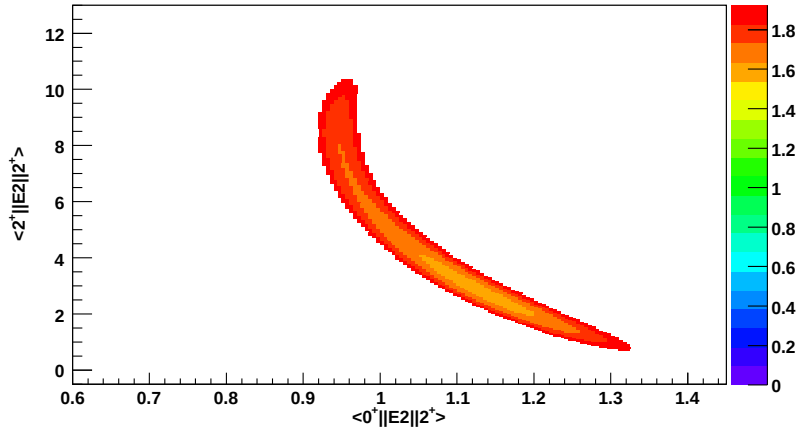

Figure A.3: Reduced χ^2 surface for the matrix elements in ^{188}Hg, assuming a diagonal matrix element $\langle \frac{3}{2}^- \| E2 \| \frac{3}{2}^- \rangle = 0$ in ^{107}Ag. The obtained results for ^{188}Hg are $\langle 0^+ \| E2 \| 2^+ \rangle = 1.13^{0.2}_{0.21}$ and $\langle 2^+ \| E2 | 2^+ \rangle = 2.9^{7.6}_{2.4}$.

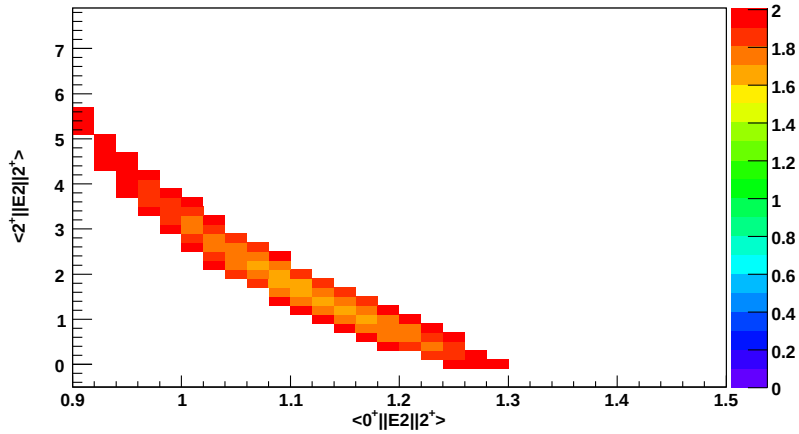

Figure A.4: Reduced χ^2 surface for the matrix elements in ^{188}Hg, assuming a diagonal matrix element $\langle \frac{3}{2}^- \| E2 \| \frac{3}{2}^- \rangle = -0.8$ in ^{107}Ag. The obtained results for ^{188}Hg are $\langle 0^+ \| E2 \| 2^+ \rangle = 1.14^{0.16}_{0.24}$ and $\langle 2^+ \| E2 \| 2^+ \rangle = 1.5^{4.5}_{1.5}$.

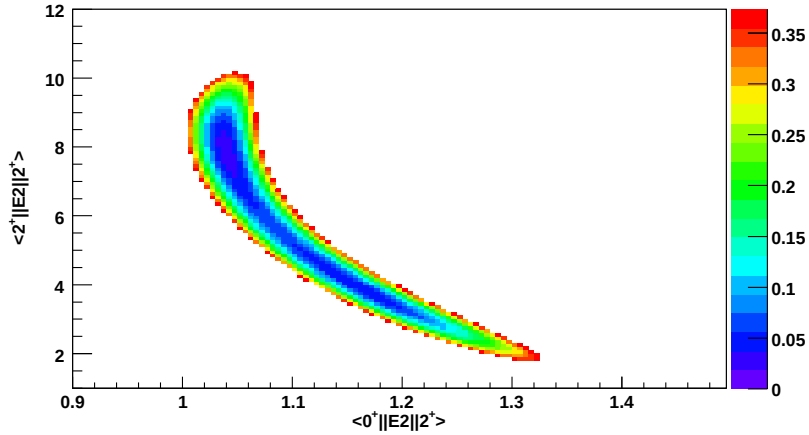

Figure A.5: Reduced χ^2 surface for the matrix elements in ^{186}Hg, assuming a diagonal matrix element $\langle \frac{3}{2}^- \| E2 \| \frac{3}{2}^- \rangle = 0$ in ^{107}Ag. The obtained results for ^{186}Hg are $\langle 0^+ \| E2 \| 2^+ \rangle = 1.17^{0.16}_{0.07}$ and $\langle 2^+ \| E2 \| 2^+ \rangle = 3.9^{6.3}_{2.1}$.

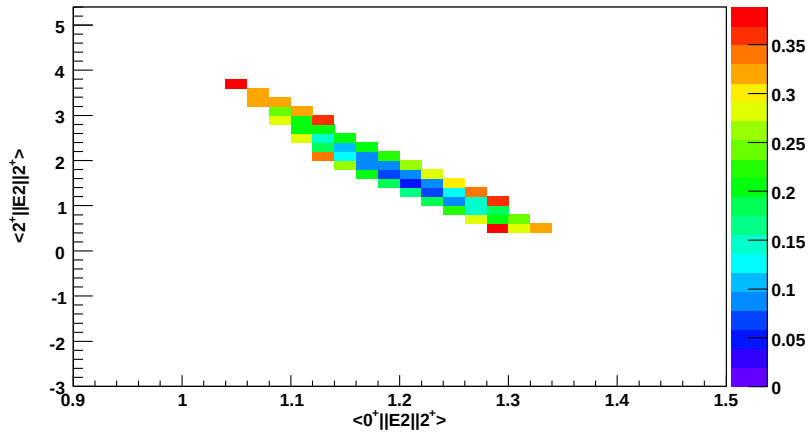

Figure A.6: Reduced χ^2 surface for the matrix elements in ^{186}Hg, assuming a diagonal matrix element $\langle \frac{3}{2}^- \| E2 \| \frac{3}{2}^- \rangle = -0.8$ in ^{107}Ag. The obtained results for ^{186}Hg are $\langle 0^+ \| E2 \| 2^+ \rangle = 1.22^{0.12}_{0.08}$ and $\langle 2^+ \| E2 \| 2^+ \rangle = 1.6^{2.2}_{1.2}$.

The change of the $\langle \frac{3}{2}^- \| E2 \| \frac{3}{2}^- \rangle$ matrix element in the target has a large influence on the diagonal matrix element in the mercury, and a minor influence on the transitional matrix element. This effect is clearly present in the ^{186}Hg case.

Compared to figure A.2, figure A.1 shows that the diagonal matrix element in ^{107}Ag hardly affects the integrated excitation cross section. Hence it will influence the calculation of the transitional matrix element in ^{32}Mg less than in the ^{186,188}Hg case.

Bibliography

[Ald75] K. Alder and A. Winther, *Electromagnetic excitation*, North-Holland Publishing Company Amsterdam (1975).

[Anh76] R. Anholt et al., Phys. Rev. A 16, 190 (1977).

[Anh82] R. Anholt et al., Z. Phys. A 308, 189 (1982).

[Beh79] H.-H. Behncke et al., Z. Phys. A 289, 333 (1979).

[Ber77] R. Bëraud et al., Nucl. Phys. A 284, 221 (1977).

[Boh69] A. Bohr and B.R. Mottelson, *Nuclear Structure*, W.A. Benjamin New York (1969).

[Bon72] J. Bonn et al., Phys. Lett. B 38, 308 (1972).

[Cas90] R.F. Casten, *Nuclear Structure from a Simple Perspective*, Oxford University Press (1990).

[Cat13] R. Catherall et al., Nucl. Instr. Met. Phys. Res., Sect. B 317, 204 (2013).

[Cli12] D. Cline, T. Czosnyka et al., Gosia user manual for simulation and analysis of Coulomb-excitation experiments (2012).

[Cli86] D. Cline, Ann. Rev. Nucl. Part. Sci. 36, 683 (1986).

[Col76] J.D. Cole et al., Phys. Rev. Lett. 37, 1185 (1976).

[Col77] J.D. Cole et al., Phys. Rev. C 16, 2010 (1977).

[Col84] J.D. Cole et al., Phys. Rev. C 30, 1267 (1984).

[Deb88] K. Debertin and R. G. Helmer, Gamma- and X-ray Spectrometry with Semiconductor Detectors, Elsevier (1988).

[Del94] J.P. Delaroche et al., Phys. Rev. C 50, 2332 (1994).

[Den95] J.K. Deng et al., Phys. Rev. C 52, 595 (1995).

[Dup90] P. Van Duppen, M. Huyse, and J. L. Wood, J. Phys. G Nucl. Part. 16, 441 (1990).

[Fir96] R.B. Firestone et al., *Table of Isotopes*, A Wiley-Sinterscience Publication (1996).

[Fos76] C. Foster et al., J. Phys. 9 No 11, 1943 (1976).

[Gaf] L.P. Gaffney, private communication.

[Gaf14] L.P. Gaffney et al., Phys. Rev. C 89, 024307 (2014).

[Gar09] J.E. García-Ramos and K. Heyde, Nucl. Phys. A 825, 39 (2009).

[Gar11] J.E. García-Ramos, V. Hellemans, and K. Heyde, Phys. Rev. C 84, 014331 (2011).

[Gar14] J.E. García-Ramos and K. Heyde, Phys. Rev. C 89, 014306 (2014).

[Gar73] J.D. Garcia et al., Rev. Mod. Phys. 45 No 2, 111 (1973).

[Gra09] T. Grahn et al., Phys. Rev. C 80, 014324 (2009).

[Gre77] J.S. Greenberg et al., Phys. Rev. Lett. 39 No 22, 1404 (1977).

[Hab98] D. Habs et al., Nucl. Instr. and Meth. B 139, 128 (1998).

[Ham75] J.H. Hamilton et al., Phys. Rev. Lett. 35, 562 (1975).

[Hey11] K. Heyde and J. L. Wood, Rev. Mod. Phys. 83, 1467 (2011).

[Jos94] P.K. Joshi et al., Intern. J. Mod. Phys. E 3, 757 (1994).

[Jul01] R. Julin et al., J. Phys. G 27, R109 (2001).

[Kum72] K. Kumar, Phys. Rev. Lett. 28, 249 (1972).

[Ma84] W.C. Ma et al., Phys. Lett. B 139, 276 (1984).

[Ma86] W.C. Ma et al., Phys. Lett. B 167, 277 (1986).

[Mar69] M.A.J. Mariscotti et al., Phys. Rev. 178, 1864 (1969).

[NND] J.K. Tuli and A. Sonzogni, Evaluated Nuclear Structure Data File, URL http://www.nndc.bnl.gov/.

[Ost02] A.N. Ostrowski et al., Nucl. Instr. and Meth. A 480, 448 (2002).

[Pro09] L. Prochniak and G. Rohozinski, J. Phys. G Nucl. Part. Phys. 36, 123101 (2009).

[Pro74] D. Proetel et al., Phys. Lett. B 48, 102 (1974).

[Rap] E. Rapisarda et al., to be published .

[Ric97] J.D. Richards et al., Phys. Rev. C56, 1389 (1997).

[Rin80] P. Ring and P. Schuck, *The Nuclear Many-Body Problem*, Springer-Verlag New York (1980).

[Rom00] C.M. Romo-Kröger, Nucl. Instr. and Meth. B 164-165, 349 (2000).

[Rom05] C.M. Romo-Kröger, Phys. Scripta T118, 9 (2005).

[Rud73] N. Rud et al., Phys. Rev. Lett. 31, 1421 (1973).

[Sch10] M. Scheck et al., Phys. Rev. C 81, 014310 (2010).

[SRI] J.F. Ziegler, J.P. Biersack, SRIM2003, URL http://www.srim.org/.

[Ulm86] G. Ulm et al., Z. Phys. A 325, 247 (1986).

[Wal06] J. Van de Walle, *Coulomb excitation of neutron rich Zn isotopes*, Ph.D. thesis (2006).

[War13] N. Warr et al., Eur. Phys. J. A. 20, 65 (2013).

[Wil80] W. Wilcke et al., At. Data and Nucl. Data Tables 25, 389 (1980).

[Woo92] J.L. Wood et al., Phys. Rep. 215 Nos 3 & 4, 101 (1992).

[Wrz] K. Wrzosek-Lipska, private communication.

[Wrz12] K. Wrzosek-Lipska et al., Phys. Rev. C 86, 064305 (2012).

[Yao13] J.M. Yao, M. Bender, and P. H. Heenen, Phys. Rev. C 87, 034322 (2013).